

Upwelling and Related Processes in the Banda and Northern Arafura Seas

Dissertation

with the aim of achieving a doctoral degree

at the Faculty of Mathematics, Informatics and Natural Sciences

Department of Earth Sciences

at Universität Hamburg

Submitted by

Abdul Basit

from Banyuwangi, Indonesia

Hamburg, 2019

Accepted as Dissertation at the Department of Earth Sciences

Day of oral defense: 21 January 2020

Reviewers: PD. Dr. Thomas Pohlmann

Dr. Bernhard Mayer

Chair of the Subject Doctoral Committee: Prof. Dr. Dirk Gajewski

Dean of Faculty of MIN: Prof. Dr. Heinrich Graener

Content

| | |
|---|-----|
| Abstract | V |
| Zusammenfassung..... | VII |
| 1. Introduction | 1 |
| 1.1 Motivation..... | 1 |
| 1.2 Research Aims | 4 |
| 1.3 Outlines | 4 |
| 2. The Banda and Arafura Seas (BAS) | 5 |
| 2.1 Geomorphology | 5 |
| 2.2 Monsoon System and its Influences on the BAS | 8 |
| 2.3 River Runoff..... | 9 |
| 2.4 Tides | 10 |
| 2.5 Residual Tidal Currents | 11 |
| 2.6 Indonesian Throughflow (ITF) | 12 |
| 2.7 The Adjacent Seas and their Influences on the BAS..... | 13 |
| 2.7.1 El Niño Southern Oscillation (ENSO) | 13 |
| 2.7.2 Indian Ocean Dipole..... | 14 |
| 2.7.3 The Evidence of ENSO and IOD Impacts on the BAS | 15 |
| 3. Methods and Data | 16 |
| 3.1 HAMSOM – Model Description | 16 |
| 3.2 Boundary Conditions..... | 18 |
| 3.3 Model Forcing | 19 |
| 3.4 Model Design | 19 |
| 3.5 The Three-Dimensional Dynamic Equation for Momentum Analysis..... | 21 |
| 3.6 Data for Validation | 22 |
| 4. VALIDATION | 23 |
| 4.1 Sea Surface Height (SSH) and Surface Currents | 23 |
| 4.2 Sea Surface Temperature (SST)..... | 27 |
| 4.3 Velocity | 29 |
| 4.4 TS-Diagram | 33 |

| | |
|---|-----|
| 5. Forcing and Hydrodynamic Conditions | 35 |
| 5.1 Forcing Conditions..... | 35 |
| 5.2 Seasonal Variability of Hydrodynamic and Physical Conditions in the BAS..... | 38 |
| 5.3 Tidal Motions and Momentum Balance around the Northern Arafura Sea | 45 |
| 5.4 Comparisons of Experimental Results during the South East Monsoon | 60 |
| 5.4.1 Sea Surface Properties | 60 |
| 5.4.2 Subsurface Properties | 65 |
| 5.4.3 Vertical Profile along the Section A..... | 68 |
| 5.4.4 Vertical Profile along the Section B..... | 74 |
| 5.4.5 Vertical Profile along the Section C | 78 |
| 5.5 Vertical Viscosity Coefficient | 82 |
| 5.6 Internal Tide and Mixing | 87 |
| 6. Momentum Analysis: The interaction of Tide and River Runoff with Wind-Driven Upwelling | 89 |
| 6.1 Interaction between Tidal Forcing and Wind-Driven Circulation during Wind-Driven Upwelling | 89 |
| 6.1.1 Horizontal Distribution of Momentum Balance | 89 |
| 6.1.2 Vertical Profile of Momentum Balance | 96 |
| 6.1.2.1 Section A | 96 |
| 6.1.2.2 Section B..... | 100 |
| 6.1.2.3 Section C | 105 |
| 6.2 Interaction between River Runoff and Tide-Wind Driven Circulation during Wind-Driven Upwelling | 109 |
| 7. Upwelling Variability in the Northern Arafura and Banda Seas | 115 |
| 7.1 Normal Condition..... | 115 |
| 7.2 La Niña | 117 |
| 7.3 El Niño | 120 |
| Conclusion | 121 |
| List of Abbreviations..... | 123 |
| List of Figure | 124 |
| References | 130 |
| Acknowledgments..... | 137 |
| A. Residual Tidal Currents Generation and Momentum Balance around the Northern Arafura Sea | 138 |

Abstract

The Banda and Arafura Seas (BAS) are part of the Eastern Indonesian Seas (EIS), a tropical sea located between the Pacific and Indian Oceans. The seas are known to have abundant fishery resources and be rich in marine biodiversity. Due to their locations, the seas are subject to monsoonal winds and thus their resources are seasonally variable. Relatively higher productivity is observed during the southeast monsoon, when SST is lower and SSS is higher than during the northwest monsoon. Due to the complex topography of the EIS and the relatively large river discharges, tidal forcing and river runoff play important roles in the physical processes around the BAS.

In this study, a three-dimensional baroclinic nonlinear numerical model—HAMBurg Shelf Ocean Model (HAMSOM)—is applied to investigate the effects of tidal forcing and river runoff on circulation during the upwelling period around the BAS by comparing different sensitivity runs from July 2004, i.e. “wind, river and tide” (WRT), “wind and tide” (WT), “wind and river” (WR), and “wind only” (WO) simulations. Furthermore, the role of adjacent oceans on upwelling intensity as associated with ENSO and IOD is investigated by running the WRT case over a 25-year period (1990–2014). The simulation results are validated with in-situ and altimeter data. Results show that seasonal variations in circulation, salinity, and temperature can be represented reasonably well by the model. Momentum analyses are further applied to explain the influence of tidal forcing and/or river runoff on wind-driven circulation during the upwelling period around the Northern Arafura Sea. Three vertical sections of this area (A, B and C) that represent pronounced upwelling signals are selected and investigated in detail.

The simulation results show that dry southeasterly winds (the southeast monsoon) generate upwelling around the BAS, and thus relatively low SST and high SSS are observed between May and October. Conversely, during the January–March period (i.e. the northwest monsoon), the wet northwesterly winds generate downwelling around the BAS. In addition, a subsurface salinity maximum of more than 34 within the thermocline layer is observed around the selected areas, indicating the influence of water masses from the Southern Pacific Ocean on the hydrodynamic conditions around the BAS area.

The important roles of tidal forcing and river runoff is indicated by the unrealistically high salinity maximum when both are excluded from the simulations. In contrast, the lower salinity maximum in the tide inclusion simulation indicates that tides enhance vertical mixing, mostly

occurring around the Halmahera and Seram Seas. Here, relatively strong currents (known as the eastern Indonesian throughflow) flow within the thermocline layer, bringing with them Southern Pacific Ocean water masses that enter the Aru Basin (part of the Northern Arafura Sea). By comparing the WRT and WT cases, this study suggests that the vertical mixing intensity in these areas is relatively strong, and thus the mixing generated by tidal forcing and the rough topography reaches the surface, bringing relatively fresh water down to the subsurface, and then eroding the salinity maximum within the thermocline layer.

The simulation results show that Ekman surface currents are the main factors inducing upwelling over the slopes of all selected sections. The simulation results also show that tidal forcing generally leads to upwelling being enhanced near the Northern and Southern Aru Islands (section A and section B). In section A, enhanced upwelling in the tide inclusion simulation is related to the cell circulation formation and separation flow induced by nonlinear interaction between tidal flows and topography conditions. In section B, enhanced upwelling is mainly associated with the modified pressure gradient force that increases onshore subsurface flow. In contrast, tidal forcing weakens upwelling over section C in general; this is mainly caused by the relatively low residual surface currents toward off the Papua Coast, which are strongly related to the enhanced vertical viscosity coefficient induced by tidally enhanced vertical mixing. Furthermore, simulation results show that river runoff enhances cross-shelf circulation, as observed in all the sections. This is mainly related to enhanced stratification, that leads in weaker vertical eddy coefficients and interfacial stress. By considering the same wind forcing in the river runoff inclusion and exclusion simulation, the vertical viscosity force in the surface layer in the river runoff inclusion is subsequently enhanced.

Long-term simulations found that the El Niño/La Niña events contribute to the enhancement/weakening of upwelling intensities induced mainly by local wind forcing across the Arafura and Banda Seas. It is also observed that positive/negative IOD events lead to enhanced/weakened upwelling.

Zusammenfassung

Die Banda- und die Arafurasee (BAS) sind Teil des Ostindonesischen Meeres (EIS), eines tropischen Meeres zwischen dem Pazifischen und dem Indischen Ozean. Beide Meere sind dafür bekannt, reich an Fischereiressourcen und mariner Artenvielfalt zu sein. Aufgrund ihrer Lage sind sie Monsunwinden ausgesetzt und ihre Ressourcen dadurch saisonabhängig. Eine relativ höhere Produktivität wird während des Südost-Monsuns beobachtet, wenn die Meeresoberflächentemperatur (SST) niedriger und der Meeresoberflächensalzgehalt (SSS) höher ist als während des Nordwest-Monsuns. Aufgrund der komplexen Topographie des EIS und der relativ großen Stromabflussmenge spielen diese sowie die Gezeiten eine wichtige Rolle in den physikalischen Prozessen rund um die BAS.

Diese Studie untersucht die Auswirkungen von Gezeiten und Stromabflüssen auf die Zirkulation während des Auftriebs (Upwelling) um die BAS. Dazu vergleicht ein nichtlineares, dreidimensionales, baroklines, numerisches Modell - das Hamburg Shelf Ocean Model (HAMSOM) - verschiedene Sensitivitätsläufe ab Juli 2004 durch Simulationen für "Wind, Fluss und Flut" (WRT), "Wind und Flut" (WT), "Wind und Fluss" (WR) und "nur Wind" (WO). Darüber hinaus wird die Rolle benachbarter Ozeane für die Intensität des Auftriebs im Zusammenhang mit *El Niño–Southern Oscillation* (ENSO) und *Indian Ocean Dipole* (IOD) untersucht, indem die WRT-Simulation über einen Zeitraum von 25 Jahren (1990–2014) durchgeführt wird. Die Simulationsergebnisse werden mit In-Situ- und Altimeterdaten validiert. Die Ergebnisse zeigen, dass saisonale Schwankungen von Zirkulation, Salzgehalt und Temperatur durch das Modell relativ gut dargestellt werden können. Darüber hinaus werden Impulsanalysen durchgeführt, um den Einfluss von Gezeiten und / oder Flussabflüssen auf die windgetriebene Zirkulation während der Auftriebsperioden um die nördliche Arafurasee zu erklären. Drei vertikale Schnitte dieses Bereichs (A, B und C), die ausgeprägte Auftriebssignale darstellen, werden ausgewählt und detailliert untersucht.

Die Simulationsergebnisse zeigen, dass trockene Südostwinde (der Südost-Monsun) rund um die BAS Auftrieb erzeugen und daher zwischen Mai und Oktober eine relativ niedrige SST und hohe SSS beobachtet werden. Umgekehrt erzeugen die feuchten Nordwestwinde während der Zeit von Januar bis März (d.h. während des Nordwest-Monsuns) ein Absinken (Downwelling) um die BAS. Zusätzlich wird um die ausgewählten Gebiete unter der Oberfläche ein Salzgehaltsmaximum von mehr als 34 innerhalb der thermoklinen Schicht beobachtet, was auf den Einfluss von Wassermassen aus dem südlichen Pazifik auf die hydrodynamischen Bedingungen um das BAS-Gebiet hinweist.

Die wichtige Rolle der Gezeiten und des Stromabflusses wird durch ein unrealistisch hohes Salzgehaltsmaximum angedeutet, wenn beide aus den Simulationen entfernt werden. Im Gegensatz dazu deutet das niedrigere Salzgehaltsmaximum in der Simulation mit Gezeiten darauf hin, dass Gezeiten die vertikale Vermischung verstärken, die hauptsächlich in der Halmahera- und Seramsee auftritt. Hier fließen relativ starke Strömungen (bekannt als ostindonesischer Durchstrom) innerhalb der Thermokline und bringen Wassermassen aus dem Südpazifik mit sich, die in das Arubecken (Teil der nördlichen Arafurasee) gelangen. Durch den Vergleich der WRT- und WT-Simulationen lässt sich feststellen, dass die vertikale Vermischungsintensität in diesen Bereichen relativ stark ist. Die Vermischung, die dort durch Gezeitenkräfte und raue Topographie erzeugt wird, erreicht die Oberfläche und relativ frisches Wasser gelangt unter die Oberfläche und erodiert das Salzgehaltsmaximum in der Thermokline.

Die Simulationsergebnisse zeigen, dass Ekman-Oberflächenströmungen die Hauptfaktoren sind, die den Auftrieb über den Gefällen aller ausgewählten Schnitte bewirken. Die Simulationsergebnisse zeigen auch, dass Gezeitenkräfte in der Nähe der nördlichen und südlichen Aru-Inseln im Allgemeinen zu einem verstärkten Auftrieb führen (Schnitt A und Schnitt B). In Schnitt A ergibt sich ein verstärkter Auftrieb in der Simulation mit Gezeiten durch die Bildung von Zirkulationszellen und die Trennung der Strömungen, die durch nichtlineare Wechselwirkung zwischen Gezeitenströmungen und Topographie verursacht werden. In Schnitt B ist ein verstärkter Auftrieb hauptsächlich mit der veränderten Druckgradientenkraft verbunden, die eine auflandige Strömung unter der Oberfläche verstärkt. Im Gegensatz dazu schwächen die Gezeitenkräfte allgemein den Auftrieb über Schnitt C ab; dies ist hauptsächlich auf die relativ geringen Oberflächenrestströmungen vor der Küste von Papua zurückzuführen, die in engem Zusammenhang mit dem erhöhten vertikalen Austauschkoefizienten stehen, der durch eine gezeiteninduziert erhöhte vertikale Vermischung hervorgerufen wird. Darüber hinaus zeigen die Simulationsergebnisse für alle Schnitte, dass der Stromabfluss die Zirkulation quer zum Schelf verstärkt. Dies hängt hauptsächlich mit einer stärkeren Schichtung zusammen, die zu schwächeren vertikalen Austauschkoefizienten und Grenzflächenspannungen führt. Durch die Berücksichtigung des gleichen Windantriebs in der Simulation mit und ohne Stromabfluss wird anschließend die vertikale Viskositätskraft in der Oberflächenschicht in der Simulation mit Stromabfluss erhöht.

Langzeitsimulationen ergaben, dass die Ereignisse von El Niño / La Niña zur Verstärkung / Abschwächung der Intensität des Auftriebs beitragen, die hauptsächlich durch lokale Windkräfte über der Arafura- und Bandasee verursacht wird. Es wird zudem beobachtet, dass positive / negative IOD-Ereignisse zu einem verstärkten / abgeschwächten Auftrieb führen.

1. Introduction

1.1 Motivation

The Banda and Arafura Seas (BAS) are known to have high abundance of fisheries resources as well as being rich in marine biodiversity. The annual fish potential in these areas is about 1 million ton/year, which is 16% of annual fisheries production potential in the Indonesian Seas, and contributes up to 30% of total Indonesian export of fishery products (Adisanjaya, 2010; Sulistiyo, 2013). From their annual fish production, it contributes to the country's income more than US\$ 800 million (CEA, 2016). Furthermore, these regions exhibit high productivity (can yield $1\text{gC}/\text{m}^2/\text{d}$) that sustains both small and large-scale fisheries. The in-situ observation shows that their primary production varied between $0.91\text{gC}/\text{m}^2/\text{d}$ (during the northwest monsoon) and $1.85\text{gC}/\text{m}^2/\text{d}$ (during the southeast monsoon) (Gieskes et al., 1990). The seasonal pattern of the high productivity in this area is also indicated by observing the chlorophyll-a concentration in the surface. From satellite-derived observation chlorophyll-a data (Figure 1), it is obvious that toward offshore, the concentration observed around the BAS during the southeast monsoon was higher than the concentration during the northwest monsoon (December- March), confirming the findings of Ilahude and Mandaris (1990) and Wetsteyn et al. (1990).

During the high productivity period, relatively low sea surface temperature (SST) and high sea surface salinity (SSS) are generally observed (Zijlstra et al., 1990), indicating the occurrence of upwelling around these areas. It is also concluded that the river runoff only contributes to a significant impact on the salinity field but not on the nutrient budget in offshore waters, and the upwelling is the main mechanism responsible for the relative high nutrients in the upper water column (Ilahude and Mardanis, 1990; Wetsteyn et al.; Zijlstra et al., 1990; Kämpf 2016). However, the river runoff could have significant impacts on the changes of the circulation system in the coastal ocean system of the BAS, influencing the amount of nutrients upwelled from the subsurface. The interaction between the river runoff and wind-driven circulation has been studied in some areas (Allen et. al, 1995; Lentz, 2001; Gan, 2008).

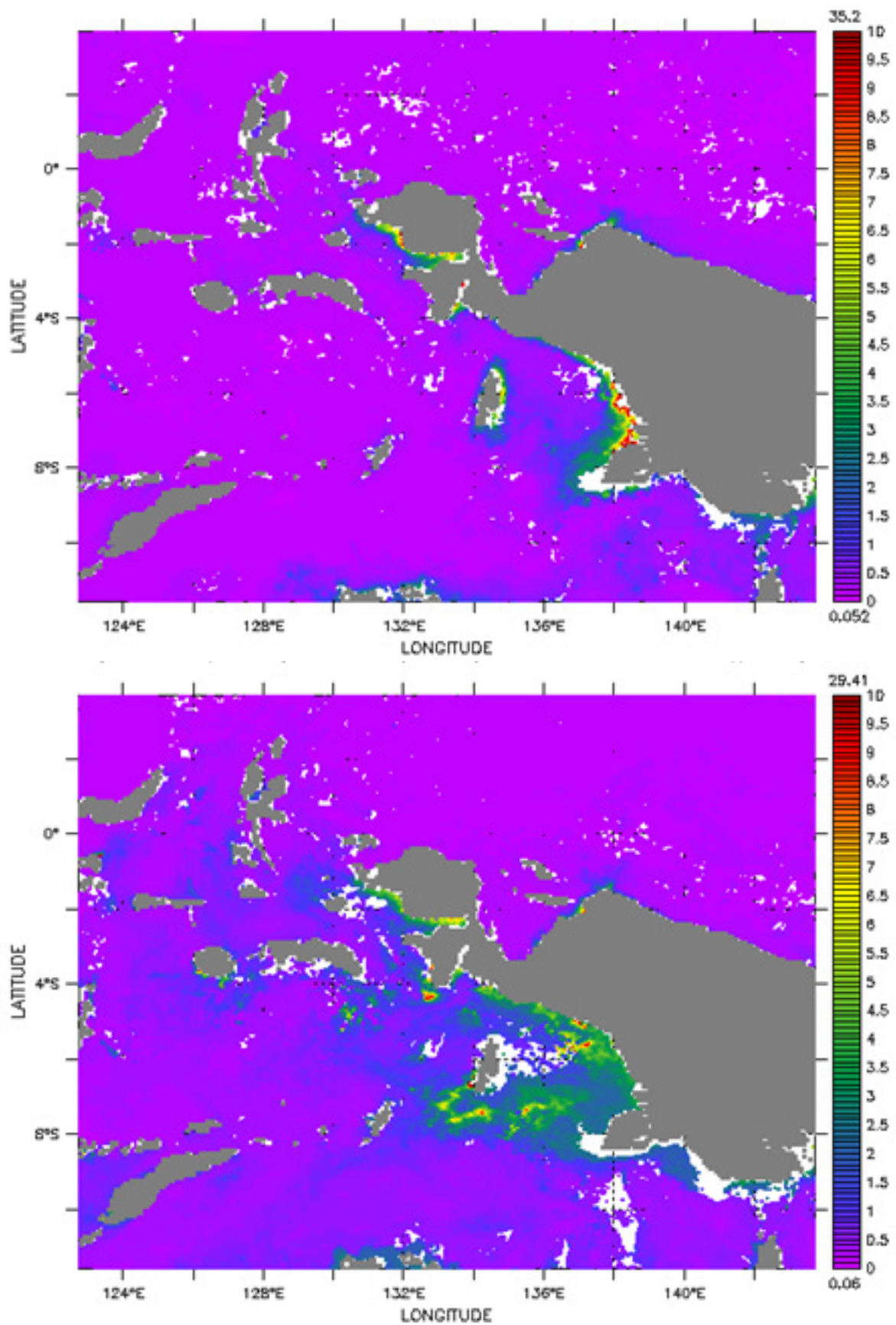


Figure 1: The horizontal distributions of chlorophyll-a (gC/m^3) derived from MODIS (<http://icdc.cen.uni-hamburg.de>) during the northwest monsoon (December 2004) (above) and during the southeast monsoon (July 2004) (below) around the Banda and Arafura Seas

The strong influence of monsoonal climate on the hydrodynamic conditions on the BAS has been observed by previous studies (Wyrski, 1961; Zijlstra et al., 1990; Gordon and Susanto, 2001; Kida and Richards, 2008; Iskandar, 2010; Kampf 2016). In general, their results reveal that the southeasterly winds prevail in this area during the southeast monsoon (May-October). Under the Coriolis force influence and the presence of the shelf-break connecting the Aru Basin (the eastern Banda Sea) and Sahul Shelf, the winds generally lead to the westward offshore surface currents, inducing upwelling and resulting in strong SST gradient with colder SST near the eastern boundary of the basin. Furthermore, Kida and Richards (2008) found that the shelf plays an important role on the cooling of the SST by preventing the relatively warm surface water of the Banda Sea to enter the Arafura Sea so that the cold SST is found in the northern Aru Basin. In this period, a relatively higher SSS at the eastern boundary, compared to the one in the western boundary, is generally observed. It was also observed that the relatively high salinity is highly associated to the water masses originating from the Southwestern Pacific Ocean (Zijlstra et al., 1990) confirming the role of the Aru Basin as a part of the eastern Indonesian throughflow (ITF) route (Gordon, 2005; Gordon et al., 2008, Sprintall et al., 2014). In contrast, during the northwest monsoon, northwesterly winds prevail in this area and generate the surface currents toward the Western Papua Coast. In this period, generally downwelling occurs and compared to the situation during the southeast monsoon, a relatively high SST and a low SSS are generally observed around the BAS. The differences of SST and SSS between the two seasons at their peaks are about 3°C and 0.5 respectively.

On time scales of a tidal cycle, some studies reveal that tide also plays an important role in the physical processes of the Indonesian Seas. It contributes to the cooling of the SST in the Indonesian Seas by between 0.6 and 1.5 °C, and generally erodes the salinity maximum of the Pacific inflow water along the main route of ITF (Koch-Larroy et al., 2007; Koch-Larroy et al., 2008). Furthermore, the tide could have a significant impact on the transport associated with the upwelling on the continental shelf. In particular, it has been shown that the tides could induce and strengthen the upwelling (XingGang et al., 2007; Wang et al., 2015). Therefore, application of explicit tidal forcing on the circulation model of the Indonesian Seas becomes important if upwelling is in the main focus of the study.

In addition, due to its location between the two Oceans, i.e Pacific and Indian Oceans, the hydrodynamic conditions of the Indonesian Seas are influenced by the air-sea interaction and the ocean dynamic from the two Oceans. Their impacts are generally propagated by Kelvin and

Rossby waves that can be identified by observing the interannual SST around the Indonesian Seas, as observed by Iskandar (2010).

The majority of the previous investigations of wind-driven upwelling around the Northern Arafura Sea did not address directly the effects of river runoff and tides on the circulation. However, due to the relatively high river discharge, the presence of shelf slope and influence of ITF around the research area, introducing river runoff and tidal forcing on the wind-driven circulation in a numerical simulation are important to obtain a better estimation so that the physical processes related to the upwelling phenomenon in the Northern Arafura and Banda Seas can be understood more accurately.

1.2 Research Aims

In this study, by using a high-resolution 3-D baroclinic, free surface model, HAMburg Shelf Ocean Model (HAMSOM) (Backhaus, 1985; Pohlmann, 1987, 1996a, 1996b), the following topics will be investigated:

1. The monsoon variability of the hydrodynamic conditions.
2. The impacts of river runoff, tidal forcing and the ITF on the wind-driven circulation during the upwelling period.
3. The role of adjacent oceans on the upwelling intensity associated with ENSO and IOD impacts.

1.3 Outlines

This dissertation is structured as follows: After this short introduction (Chapter 1), Geomorphology, monsoon system and the influence of adjacent seas of Banda and Arafura will be described in Chapter 2. In Chapter 3, the model design and data are briefly described, followed by the validation of simulation results with in-situ and satellite observations in Chapter 4. In Chapter 5, the discussion will be focused on the forcing and simulated hydrodynamic conditions. The momentum analysis related to the dynamical process will be discussed in Chapter 6. In Chapter 7, the inter-annual pattern during the upwelling period will be discussed. The summary and outlook will be presented in the last chapter.

2. The Banda and Arafura Seas (BAS)

2.1 Geomorphology

The Indonesian archipelago is known to have complex topographic features and very sharp sills (Figure 2.1). On one hand, sills are generally identified in the passages where the Pacific Ocean water masses mostly flow into the Indonesian Seas (Gordon, 2002; Gordon, 2005; Sprintall et al., 2014). In the western passage, the relative shallow sill at about 680 m depth, i.e., Dengkawang, which separates the Southern Makassar Strait and Flores Sea, is located at about 6°S, 119°E. In the eastern passage, the relative deep sill at around 1940 m depth, i.e. Lifamatola that controls the direct access of the Maluku Sea to the Banda Sea, is situated at about 2 °S, 127.5°E. Meanwhile, the shallower sill at about 580 m depth, i.e. Halmahera sill, is located at about 0° 129°E, which allows saline South Pacific lower thermocline water to enter the Seram Sea (Ilahude and Gordon, 1996a, b). On the other hand, sills are also found in the southern passages connecting the Indonesian Seas and Indian Ocean. There are three main passages, i.e., Lombok Strait, Ombai Strait and Timor Passage with a sill depth at about 250 m, 1800 m, and 1200 m respectively.

The Banda and Arafura Seas are located at the eastern part of the Indonesian Seas located between longitude 125°E – 132°E and latitude 9 °S and 3 °S (Figure 2.2). The Banda Sea is a deep sea (up to 7000 meter) fringed by larger islands (Seram and Buru) in the north, smaller islands in the east, i.e. Kai Islands, and in the south, i.e. Alor, Timor, Wetar, Babar, and Tanibar Islands. In this area, there are two deep basins, i.e. Banda and Weber Basins, separated by the Lesser Banda Arc. The Arafura Sea is located to the east of the Outer Banda Arc and between the Australian continent and Papua Island. It comprises mostly a large shelf (covering about 650,000 km²) ranging from 50 to 80 m depth over the Sahul Shelf and a deep part, the Aru Basin, with a depth of up to 3650 m. The shelf slopes are generally located at the Sahul Shelf edge connecting the Aru Basin and the Sahul Shelf. The detail topography condition in Sahul Shelf is shown in Figure 2.2.

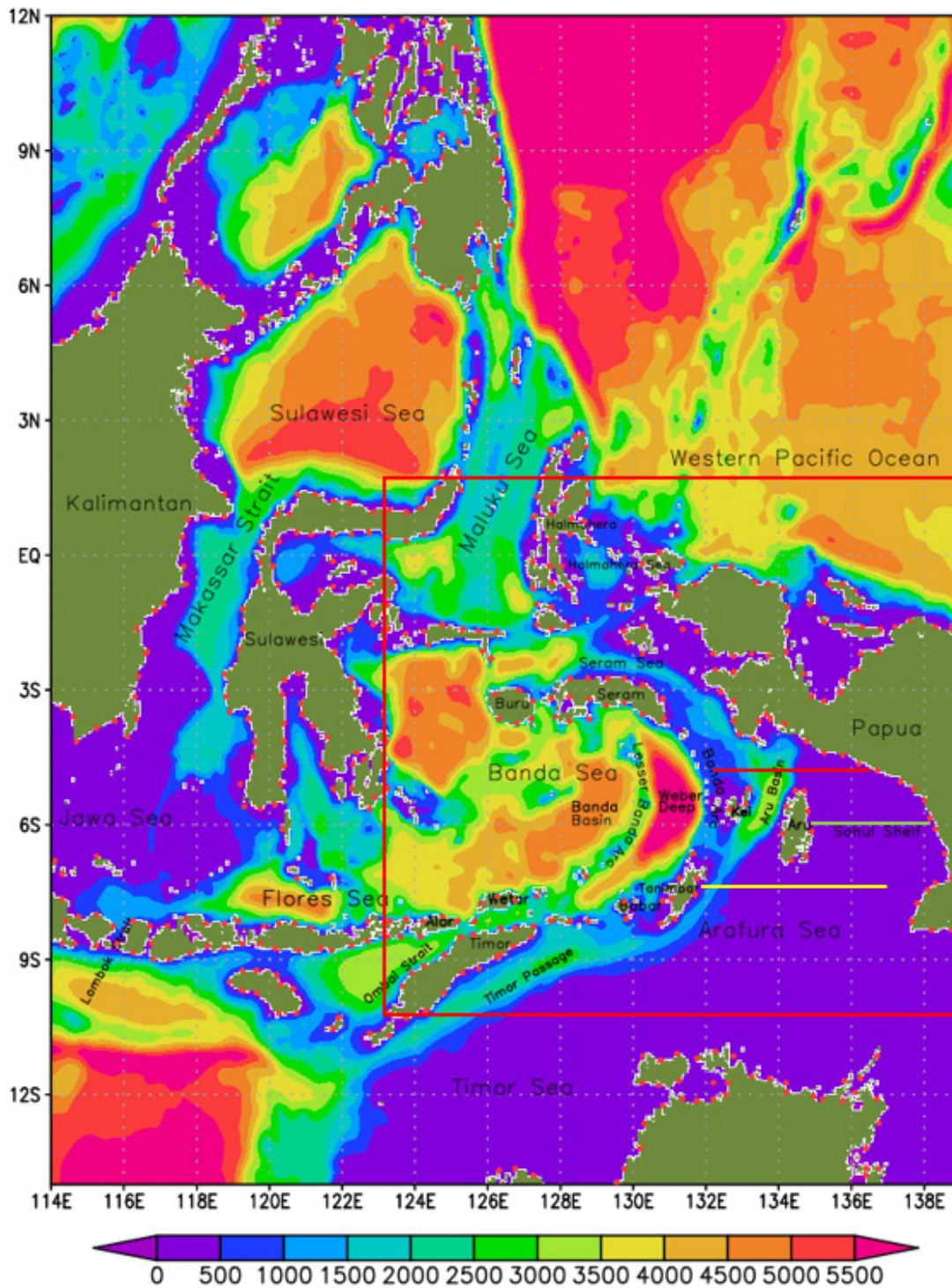


Figure 2. 1 : Topography (meters) of the model area. The red box with Red-line (Section A), Green-line (Section B), and Yellow-line (Section C) indicates the region this paper is mostly concerned with (in the section 5.3). The red solid circles represent the river locations.

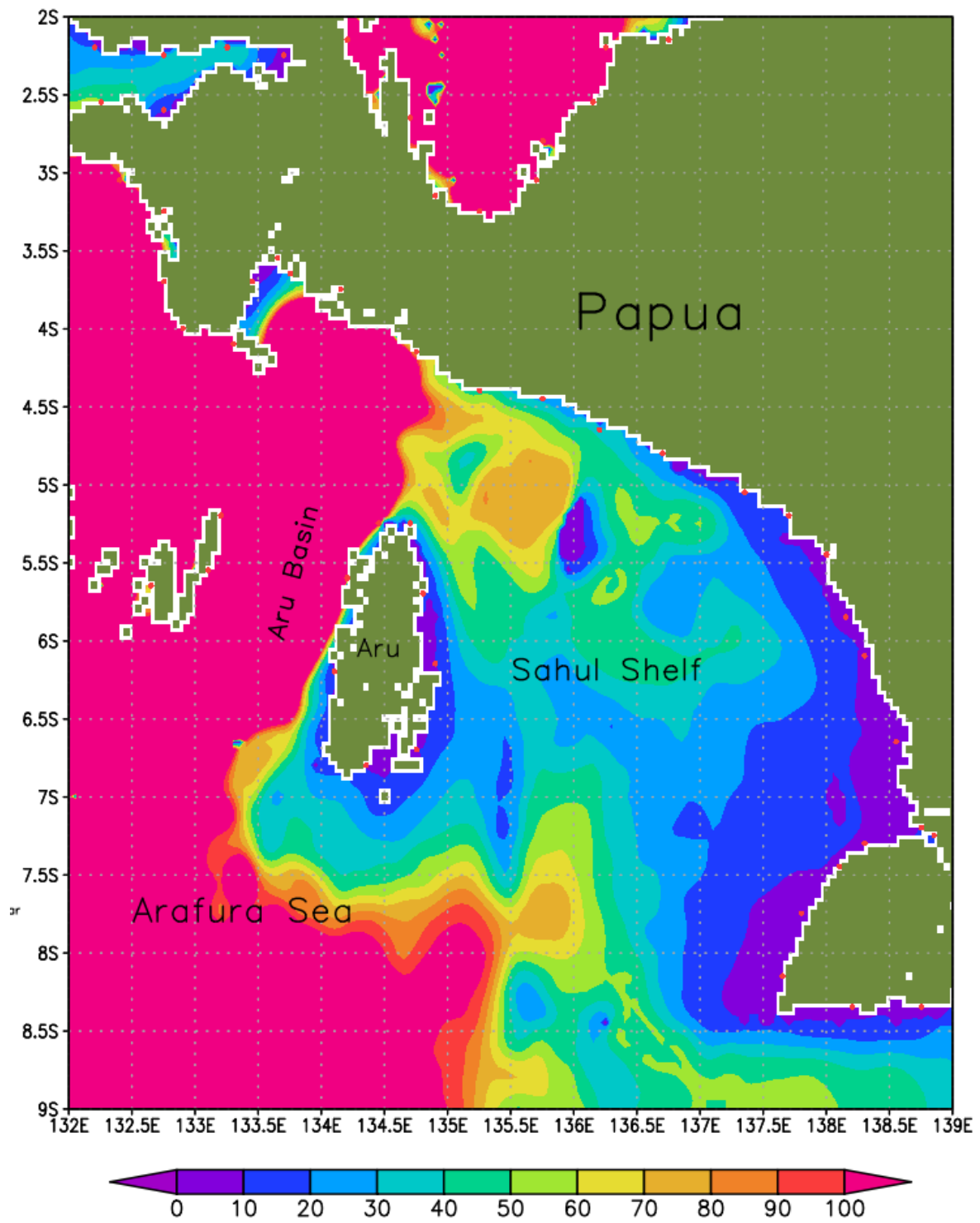


Figure 2. 2: Topography in the Sahul Shelf (meters)

2.2 Monsoon System and its Influences on the BAS

Situated between Australia and Asia continents, the Banda and Arafura Seas are mainly exposed to the monsoon (Wyrтки, 1961). Under normal conditions, when the southern hemisphere receives less solar radiation than the northern hemisphere, the air pressure over the Australian continent is higher than the pressure over the Asian continent during the period of May-October (Austral winter). As consequence of this, the prevailing winds blow northwestward from Australia and pass through the BAS, called then as the southeast monsoon. It reaches its full development in July/August (Wyrтки, 1961). In this season, the precipitation in the eastern Banda and Arafura Seas is relatively low and has a minimum in August at just below 100 mm/month (Aldrian and Susanto, 2003).

In contrast, the BAS is normally exposed to northwesterly winds during austral summer period (December - March) when the air pressure over Australia is lower than over Asia, called then as the northwest monsoon. It is fully developed in January (Wyrтки, 1961). The wind speed during the northwest monsoon in this area is generally lower compared to the wind speed during the southeast monsoon. In this season, a rainy season around the BAS is observed during this period. The eastern Banda and Arafura Seas exhibit a higher precipitation during this period compared to the other seasons, reaching a peak in January (Aldrian and Susanto, 2003).

In the period of November (the transition I) and April (the transition II), the wind speeds are relatively low and starting to change their directions.

It is observed that the circulation and physical conditions in the Banda and Arafura Seas show strong seasonal response to the monsoon climate forcing (Wyrтки, 1961; Gordon and Susanto, 2001; Kida and Richards, 2008). Wyrтки (1961) concluded that surface waters flow from the Flores Sea to the Banda Sea, and only part of these waters is exported into Indian Ocean via Timor Sea and Sulawesi Sea via Maluku Sea, resulting in downwelling in the Banda and Arafura Seas. In contrast, during the southeast monsoon, the surface waters from Banda Sea are transported partly to the south into Indian Ocean via Timor Sea and to the east into Flores Sea, resulting in an upwelling in the Banda and Arafura Seas. It is suggested that the wind stress curl plays an important role in inducing stronger upwelling in the Eastern Banda Sea (Gordon and Susanto 2001; Kida and Richards, 2008), as already suggested by Wyrтки (1961).

Furthermore, the monsoon also contributes to the seasonal variation of the ITF. In general, the total transport of the ITF during the northwest monsoon is lower than the transport during the southeast monsoon (Gordon et al., 2008; Mayer et al., 2010; Mayer and Damm, 2012; Shinoda et al., 2012). It is observed that the southward motions within the thermocline in the Makassar Strait reach their peak at about 0.68 m/s during the southeast monsoon while they are about 0.56 m/s during the northwest monsoon (Gordon et al., 2008). Mayer et al. (2010) suggested that the northwesterly winds induce waters to pile up into the Banda Sea, thus producing a northward-directed a barotropic gradient against the prevailing southward flow and subsequently reducing the total ITF volume transport.

2.3 River Runoff

Not many in-situ observational data providing accurate information about the numbers of rivers and their discharges are found for the Western Papua Coast. However, based on the Water GAP Global Hydrology Model (WHHM) simulation (Döll et al., 2003), it is estimated that there are at least 15 rivers located along the coast (Figure 2.1) with a maximum discharge varying between 500 and 3300 m³/s. Near the coastal ocean, the river runoff generally leads to the relatively low salinity which is persistently observed along the Western Papua Coast. Low sea surface salinities at less than 34 in the course of their two cruises during the northwest monsoon (February 1985) and during the southeast monsoon (August 1984) are found by Zijlstra and Baars (1990). In addition to freshening of the sea water, the runoff plays an important role in influencing wind-driven dynamics of the coastal ocean. Enhancement of vertical stratification by the freshwater input tends to reduce the mixed layer depth so that the efficiency of wind forcing near the surface is strengthened (Allen et. al, 1995; Lentz, 2001). Furthermore, it could enhance the cross-shelf circulation in the upper water column so that the surface Ekman current and compensating flow beneath the plume is enhanced (Gan, 2008). Moreover, the horizontal pressure gradient formed between the buoyant plume and the ambient seawater could alter the intensity of the wind driven circulation (Chao, 1988; Rennie et al., 1999).

2.4 Tides

The influences of semidiurnal and diurnal tides are generally observed in the Indonesian Seas (Ray et al., 2005; Robertson and Ffield, 2008; Robertson and Ffield, 2008). It was found that the primary semidiurnal tidal components (M_2 and S_2) enter from Indian Ocean into the Indonesian Seas through the Lombok, Ombai and Timor straits (Figures 6 and 7, Robertson and Ffield, 2008). From the Lombok Strait, the tidal wave passes northward into the Makassar Strait and westward into the Java Sea. From the Timor Strait, the tide passes eastward into the Arafura Sea, northwestward through the Banda Sea into the Maluka Sea and the Makassar Strait. The semidiurnal tides (M_2 and S_2) with a relative lower amplitude, compared to the tides from the Indian Ocean, also enter from Pacific Ocean into the Indonesian through the Makassar Strait and the Maluku and Halmahera Seas in which the semidiurnal tidal components from the two Oceans subsequently met (Robertson and Ffield, 2008). Meanwhile, the primary diurnal components (K_1 and O_1) with the relatively low amplitude compared to the primary semidiurnal tidal components enter from Pacific Ocean into the Indonesia Sea through Sulawesi and Halmahera Seas before they flow into Indian Ocean through Timor Sea (Robertson and Ffield, 2008).

Tides play a significant role by affecting the formation process of water masses and circulation of the Indonesian Seas for both open oceans as well as for coastal areas. The extensive shelves, rough topography and large tidal currents in the Indonesian Seas lead to an exceptionally high amount of tidal energy dissipation (Miller, 1966; Mihardja, 1991; Sjöberg and Stigebrandt, 1992; Ffield and Gordon, 1996). As the tidal currents interact with the sill or shelves, the tidal energy is dissipated by turbulent mixing (Sandstrom and Oakey, 1995; Klymak et al., 2012; Haren and Gostiaux, 2012). A relatively strong tidal mixing in the deep sea is generally observed around the Sulawesi Sea, Makassar Strait, and Halmahera Sea, having significant impacts on the water mass transformation of the ITF (Ffield and Gordon, 1996; Robertson and Ffield, 2005; Koch-Larroy, 2008).

Some studies show that the tides also contribute significantly to the cross-shelf circulation driven by alongshelf winds. In general, the circulation on the inner continental shelf depends strongly on vertical mixing and stratification (Allen et al., 1995; Lentz, 1995, Lentz, 2001; Austin and Lentz, 2002; Kirincich et al., 2005). Their results reveal that the stronger stratification allows the circulation to extend into the shallower water. Meanwhile, the tidal

currents would enhance vertical mixing, reduce stratification, and consequently weaken the efficiency of the winds to drive cross-shelf currents over the shallow regions so that the upwelling circulation tends to be shifted toward offshore (Castelao et al., 2010). Furthermore, the tides could induce stronger upwelling around the shelf (XingGang et al., 2007; Wang et al., 2015). Their findings show that the enhanced vertical mixing generates stronger density fronts and the subsequent lateral baroclinic pressure gradient that drive the bottom water to move from deep to shallow areas along the slope and move reversely in the upper layer so that relative strong upwelling is induced around the slope, compared to the non-tidal simulation. In this study for the first time, the interaction between tidal forcing and wind-driven circulation during the upwelling period around the Sahul Shelf will be discussed.

2.5 Residual Tidal Currents

Mean (residual) currents are important for the long-term movement of sea-floor sediments, fish larvae, and sea-water. Residual currents usually arise from meteorological forcing and horizontal density gradients, but can also be produced by tidal currents. Tidal residual currents could enhance the transportation of nutrients from the subsurface to the surface waters in the Northern Arafura Sea during the upwelling period (southeast monsoon), Tidal residual currents are generally induced by asymmetric tidal currents between ebb and flood over one cycle period, which are generated by nonlinear interactions between tidal flows and bottom topography, as also observed by Huthnance (1972, 1981), Zimmerman (1979), Robison (1981), Signel and Geyer (1991), Maze (1998), and Sheng and Wang (2004). They found that nonlinear terms in the momentum equations, i.e. quadratic bottom friction and advection, play an important role in generating residual currents. When stratification is added, the magnitude and structure of residual currents are modified by tide-induced front formation, internal tide generation, and the modification in internal and bottom friction due to stratification (Loder and Wright, 1985; Maas and Zimmerman, 1989a,b; Chen and Beardsley, 1995; Magaldi et al., 2008). Chen and Beardsley (1995) found that the vertical structure of the nonlinear term over the slope is significantly larger in the homogeneous case than in the stratified case. The contribution of the nonlinear advection term associated with baroclinic tidal currents flowing over a slope to the averaged momentum balance is also observed by Wunsch (1971) and Kurapov et. al, (2010). Furthermore, nonlinear terms' role in producing residual currents is also observed around a headland (Geyer and Signell, 1990; Signel and

Geyer 1991). It is found that residual currents directed away from the headland are generated when the advection term is larger than the friction term. The influence of stratification on residual currents around the headland is also observed by Lee and Beardsley (1999) and Magaldi et al. (2008).

2.6 Indonesian Throughflow (ITF)

The Indonesian Throughflow (ITF) is the only open pathway situated at low latitude connecting the two oceans, i.e. Pacific and Indian Oceans. Around 90% of the ITF water masses consists of North Pacific Subtropical Water (NPSW) transported through the Sulawesi Sea and the Makassar Strait named then as the western route, whereas the remaining (10%) South Pacific Subtropical Water (SPSW) is transported through the Halmahera and Seram Seas named then as the eastern route (Gordon, 2005; Gordon et. al., 2010, Sprintall et al., 2014). The NPSW and SPSW waters are generally characterized by a salinity maximum of 34.8 and 35.45, respectively (Wyrski, 1961). Then, they transit mainly into the Banda Sea and experience a significant transformation before being exported into Indian Ocean through the Lombok Strait, Ombai Strait and the Timor Passage (Gordon, 2005; Gordon et. al., 2010, Sprintall et al., 2014). It was suggested that vertical and horizontal mixing contributes to the transformation of incoming Pacific water (Field and Gordon, 1992; Gordon, 2005). Furthermore, it is observed that the tidal mixing contributes significantly to enhance the vertical mixing around the narrow strait, channel and sills of the Indonesian Seas, resulting in a reduced salinity maximum of the inflow waters along the ITF routes (Robertson and Field, 2005; Koch-Larrouy, 2007; Koch-Larrouy, 2008; Ray and Susanto, 2016).

In the Eastern Indonesian Seas (EIS), it is observed that the tidal mixing is mostly generated around the Halmahera and Seram Seas where the shallow sills and the narrow strait are located (Koch-Larrouy, 2007; Koch-Larrouy, 2008; Ray and Susanto, 2016). As a consequence of this, the thermocline SPSW waters are eroded so that their signature is no longer perceptible. Furthermore, it is suggested that the Aru Basin is a part of the eastern Indonesian throughflow (ITF) route advecting the upper thermocline water of the South Pacific through Halmahera and Seram seas before exiting into the Indian Ocean (Figure 1, Sprintall et. al., 2014). Therefore, introducing the tidal forcing in a numerical simulation is important to obtain a better estimation to understand the physical processes around the Aru Basin which is a part of the main research areas of this study.

2.7 The Adjacent Seas and their Influences on the BAS

On the inter-annual time scale, the physical and dynamical conditions in the Banda and Arafura seas are influenced by the ENSO and IOD phenomena.

2.7.1 El Niño Southern Oscillation (ENSO)

The interactions between sea and air occurring in the Indian and Pacific Oceans play an important role in influencing the Indonesian water conditions because the Indonesian Seas is located between these two oceans. The general mechanism of how the water masses from the Indian and Pacific Ocean enter and influence the Indonesian Seas is explained in the section 2.4 and 2.5.

In the equatorial Pacific, the trade winds blow normally from the east (Peru) to the west (Asia) (<https://www.pmel.noaa.gov/elNiño/what-is-el-Niño>). As a consequence of this, the warm surface water of the equatorial Pacific migrates to the West Pacific and, thus, the sea surface height in the west equatorial Pacific, close to the Indonesian waters, is higher by about 0.5 meter compared to the height in the east equatorial Pacific. Furthermore, this causes the subsurface water to upwell to the surface water, generally cooling the surface waters of Peru waters. This cold water generally brings a rich nutrient supply which is important for primary productivity and at the end for a high fishery field.

During El Niño, the normal easterly trade winds weaken and sometimes, the winds will switch and blow from the west to the east so that the thermocline deepens in the eastern Pacific Ocean while it shoals in the west (<https://svs.gsfc.nasa.gov/12601>). This generally reduces the upwelling intensity around the Peru Coast resulting in the higher SST and the lower primary productivity around the coast, the latter of which adversely affects fishery abundance. Furthermore, the eastward displacement of the atmospheric heat source overlaying the warmest water leads to substantial changes in the global atmospheric circulation. Under this condition, the high precipitation follows the warm water eastward and then causes flooding in Peru and drought in Indonesia and Australia.

In contrast, during La Niña, the easterly trade winds generally strengthen. This leads to a drop of SST in the Equatorial Pacific Ocean as a response to wind-driven upwelling intensification during this period around the eastern boundary (Peru). The enhanced upwelling also tends to enrich nutrients in the euphotic zone, subsequently resulting in the rise of primary productivity and fishery productions around the Peruvian Coast. In this period, flooding is generally found in Australia and Indonesia while Peru is threatened by droughts.

2.7.2 Indian Ocean Dipole

The Indian Ocean Dipole (IOD) is formed in the equatorial Indian Ocean as a result of the interaction between atmosphere and ocean that affect climate surrounding the Indian basin, including Indonesia (Saji et al., 1999). The IOD is characterized by anomalous cooling of SST in the tropical south-eastern Indian Ocean and anomalous warming of SST in the tropical western Indian Ocean. Furthermore, it is observed that there are significant changes in the surface wind field over the tropical Indian Ocean, especially in its zonal component over the equator during dipole mode periods, indicating the strong dependence between the wind field and the intensity of IOD (Saji, 1999). The intensity of IOD is parameterized by defining an index, known as dipole mode index (DMI), that represents the difference of SST anomaly between the two regions confined in $50^{\circ}\text{E} - 70^{\circ}\text{E}$, $10^{\circ}\text{S} - 10^{\circ}\text{N}$ and $90^{\circ}\text{E} - 110^{\circ}\text{E}$, $10^{\circ}\text{S} - \text{Equator}$. A positive index is characterized by the lower temperature of the eastern Indian ocean compared to the temperature of the western Indian Ocean and more easterly winds across the Indian Ocean while the reverse patterns are generally true for the negative index. The extreme events of IOD were identified in 1961, 1967, 1972, 1982, 1994, and 1997 (Saji, 1999).

Some studies show that IOD events are independent from ENSO (Saji, 1999; Ashok et. al., 2003). They found that there was a significant correlation between IOD and ENSO when those events occurred simultaneously, e.g. in 1972, 1982 and 1997, but these co-occurrences were only about 35% of total observation. They also found that ENSO events occur more frequently than IOD events. Therefore, it was suggested that ENSO and IOD occur as results of inherent internal modes limited specifically to the Indian and Pacific Ocean Basins.

2.7.3 The Evidence of ENSO and IOD Impacts on the BAS

Iskandar (2010) found that on the inter-annual scale, the SST in the Banda Sea is relatively low during El Niño and/or positive IOD events while the relatively high SST was observed during La Niña and/or negative IOD events. On one hand, it was suggested that the upwelling Kelvin waves induce the low SST in the Banda Sea during a positive IOD event. These waves are generated in the equatorial Indian Ocean, propagating along the southern coast of Sumatra and Java before entering into the Banda Sea through the Lombok Strait, Ombai Strait and the Timor Passage. On the other hand, the low (high) SST during the El Niño (La Niña) events was induced by upwelling (downwelling) caused by Equatorial Rossby waves partly scattering into the Indonesian Seas through the Halmahera, Maluku and Sulawesi Seas. This observation confirms Gordon and Susanto's (2001) findings. They found that the SST during the upwelling period during El Niño events is lower than the one during La Niña events even though the Ekman pumping during El Niño is observed to be weaker than it is during La Niña. As the Banda Sea responds to local wind forcing, in general, a stronger Ekman pumping induces a cooler SST and a shallower thermocline. However, this relationship is not applicable at ENSO scale. This indicates that the thermocline variations related to ENSO dynamics contribute to the SST inter-annual variation so that the shallower thermocline during the El Niño enhances the efficiency of SST cooling in the Banda Sea.

3. Methods and Data

3.1 HAMSOM – Model Description

A three-dimensional baroclinic nonlinear numerical model - HAMBURG Shelf Ocean Model (HAMSOM) - developed by Backhaus (1985) and his colleagues has been applied to simulate the circulation around the Banda and Arafura Seas. The model has been designed to allow simulations of oceanic, coastal and shelf sea dynamics. The basic frame of the HAMSOM model has been developed by Backhaus (1983, 1985). Some modifications and several applications of this model to simulate the hydrodynamic process in several shelf seas worldwide have been performed by Pohlmann (1987,1991, 1996a, 1996b, 2006), Huang (1995), Alaei et al. (2004), Putri(2005), Hein (2008), Hein (2013), Su and Pohlmann (2009), Ludewig (2015).

The HAMSOM applies the primitive equation with a free surface and utilizes two time-levels (Backhaus, 1985). Some approximations and simplifications are introduced to obtain the solutions (Backhaus, 1985). The fluid is incompressible, i.e. the density of a liquid remains almost constant as the pressure changes. Furthermore, the hydrostatic equilibrium is applied to the vertical momentum equation. In this condition, it is obtained that the acceleration of gravity is balanced by the vertical pressure gradient, as long as the vertical velocity scale is much less than the horizontal vertical scale (Cushman-Roisin and Beckers, 2011). Reynold stresses representing the effects of the unresolved scales on the resolved scales are parameterized assuming a Newtonian fluid. In addition, only the horizontal components of Coriolis acceleration are considered in the momentum equation.

In the HAMSOM numerical scheme, Z co-ordinates and an Arakawa C-grid are used to define the grid spacing vertically and horizontally. In this model, a semi-implicit numerical scheme is applied so that the run times of numerical simulations could be reduced significantly by allowing larger time steps as usually required for explicit formulations. These can be avoided by the semi-implicit scheme, but the accuracy is still comparable to explicit scheme. The implicit algorithm is applied to discretize the horizontal divergence terms in the continuity equation, the barotropic pressure and the vertical shear stress terms in the momentum equation, and the vertical diffusion terms in the transport equation of salinity and temperature. An explicit formulation is used for the horizontal diffusion terms, and the advective terms of the momentum equation and of the transport of temperature and salinity. In order to avoid

the linear numerical instability arising from a non-conservative approximation of inertia oscillations, a rotational matrix is introduced to the Coriolis and pressure gradient terms of momentum equation (Wais, 1985 in Backhaus, 1985; Backhaus, 2011).

In order to parameterize horizontal sub-grid-scale dynamical processes, a Smagorinsky Scheme is implemented to calculate non-constant coefficients of horizontal viscosity which depend on the horizontal shear stress. This scheme has also been applied by Hein (2008), Hein (2013), Mayer (2012). The Smagorinsky diffusion describes a nonlinear diffusion acting horizontally, depending on the u- and v-components. A Smagorinsky Scheme has been applied for the first time to parameterize horizontal sub-scale process in the HAMSOM when it is applied to the South China Sea by Hein (2008). This scheme yields a non-constant viscosity coefficient in a physical consistent manner. In this scheme, the velocity shears are defined locally and are computed by finite differences between neighboring grid points. The role of the Smagorinsky scheme in the simulation has been also discussed by Ludewig (2014). It is observed that the negligence of Smagorinsky diffusion leads to a stronger and partly overestimated local velocity components. The Smagorinsky equation is given by,

$$A_h = c \cdot dx \cdot dy \cdot \sqrt{\frac{\partial u^2}{\partial x} + \frac{1}{2} \left(\frac{\partial v}{\partial x} + \frac{\partial v}{\partial x} \right)^2 + \left(\frac{\partial v}{\partial y} \right)^2}$$

c is a dimensionless coefficient, which in this simulation is set to 0.5.

As implemented by Pohlmann (1996b), the approach of Kocherin (1987) is used to calculate the vertical turbulent viscosity coefficient. It is assumed that the coefficient is proportional to the root square of stratification and the vertical shear stress,

$$A_v = (c_{ML} \cdot h_{ML})^2 \cdot \sqrt{\left(\frac{\partial u}{\partial z} \right)^2 + \left(\frac{\partial v}{\partial z} \right)^2 + \frac{1}{S_M} \frac{g}{\rho} \frac{\partial \rho}{\partial z}}$$

Where $C_{ML} \approx 0.05$ (Kochergin's constant), h_{ML} is the depth of the turbulent mixed layer at the surface and the bottom, S_M is the Prandtl number. The turbulent mixed layer depth is determined by the Richardson number. In general, the vertical turbulent viscosity is enhanced by a stronger velocity shear. In contrast, the viscosity is generally weakened by the stronger vertical stability.

3.2 Boundary Conditions

At the surface and the sea bed, the kinematic and dynamic conditions specifying the flow velocity and the forces respectively are applied (Backhaus, 1985; Pohlmann, 1987; Huang 1995; Putri, 2005). The former condition implies the fluid particles directly at the free surfaces always to remain part of the free surface while there is no flow through the seabed so that the vertical component of particle velocity at this boundary is set to zero. The latter requires the stress to be continuous across the free surface which separates the two fluids while there is no heat and salt fluxes across the seabed/the traction and continuity of the heat flow perpendicular to the surface must hold at the bed (Huang, 1995; Hutter and Jöhnk, 2004). The wind stress at the surface and the stress at the bottom are represented by quadratic stress laws. At the surface, fluxes of momentum, heat and freshwater at the sea surface are determined by means of bulk formula by using meteorological parameters, i.e. 10 m wind speed, sea surface pressure, 2 m air temperature, sea surface temperature, 2 m relative humidity, total cloud cover and total precipitation. The net heat exchange consists of four terms: the net incoming short-wave radiation, the net incoming long-wave radiation, turbulent sensible heat flux, and turbulent latent heat flux. For the incoming solar radiation term, the bulk formulas from the COHERENS model (Coupled Hydrodynamical Ecological model for Regional Shelf seas) are applied (Luyten et al., 1999). The outgoing long-wave radiation is calculated by applying the Fung's bulk formula (Fung et al., 1984). And, the turbulent fluxes are parameterized according to Kondo (1975).

At the lateral solid boundaries, a semi-slip and zero flux condition is applied. The former is prescribed to calculate the horizontal momentum exchange in its standard form so that it gives half the velocity shear compared with the no-slip condition, while the latter was set to assume that no water masses were transported through the solid boundaries (Backhaus 1985; Pohlmann, 2006, Kämpf, 2009). Furthermore, daily river inflow is simulated by introducing temperature and salinity changes at the respective input grid cells (Pohlman, 2006). At the lateral open boundaries, the Neumann conditions which assume a zero gradient are employed for the transports. In contrast, the sea surface elevation is prescribed at the lateral open boundaries as a result of the inverse barometric effect, tidal elevations, river discharge effects

and the dynamical height (Backhaus 1985; Hein, 2013). Furthermore, as inflow conditions, temperature and salinity values are prescribed, while for outflow conditions, a Sommerfeld radiation is applied (Orlanski, 1976).

3.3 Model Forcing

The model is forced by various data sets containing the atmospheric conditions, river discharge and tidal elevation. Furthermore, water temperature and salinity prescribed at the lateral open boundaries. Altogether six meteorological forcing data, including atmospheric sea surface pressure, air temperature, specific humidity, U-Wind, V-Wind, and precipitation rate, are interpolated from National Centers for Environmental Prediction (NCEP) (Kalnay et al., 1996). The river discharge is obtained from the Water GAP Global Hydrology Model (WHHM) with the spatial resolution of 0.5° (Döll et al., 2003). Tidal forcing at the open ocean boundary is specified by using the Oregon State University (OSU) global inverse tidal model of TPXO.6.2, which solves the Laplace tidal equations with a grid resolution of 0.25° by 0.25° and assimilates data from tidal gauge observations and TOPEX/Poseidon satellite measurements (Egbert et al., 1994; Egbert and Erofeeva, 2002). This simulation applies 11 tidal components (M2, S2, K1, O1, Q1, P1, N2, K2, M4, MS4, Mn4) at the open ocean boundary.

3.4 Model Design

The regional model topography was derived from Shuttle Radar Topography Mission (SRTM) data with a 30-second grid resolution, which is roughly one kilometer. In this study, a grid size of 3 minutes has been used for the model simulation. Therefore, the original data has been averaged over 60 grid cells in x- and y- axis to obtain a 3-minute resolution.

To simulate the realistic circulation around the BAS, a nested model system has been set up and applied for a period of 25 years (1990 – 2014). The spin up period has been set to 5 years so that the simulation is not influenced by the initial conditions. The model domain ranges from 114° E to 139° E and from 14° S to 12° N, which is larger than the focused research areas (the BAS) (Figure 2.1). This aims to cover the in-situ observation areas used to validate the simulation (see chapter 4). Furthermore, this chosen domain is optimal to investigate the role of ITF to the focused research area by tracking and observing its flow and its physical characteristics (see in the section 4.4 and 5.2). Data of the Max-Planck-Institute Global Ocean/Sea Ice Model (MPI-OM) with a horizontal resolution of 24 min and 40 layers of increasing

thickness from top to bottom has been interpolated to generate finer resolution data, with a horizontal resolution of 3 min and 54 vertical layers, to obtain initial and boundary conditions for the local simulation. The MPI-OM is also driven by NCEP forcing (Marsland et al., 2003; Jungclaus et al., 2006). In this simulation, 54 layers represent the total depth of 6000 meters, with increasing thickness from top to bottom, thus more layers represent the mixed and thermocline layers compared to the deeper ocean.

In order to determine the influence of tides and rivers on the wind-induced upwelling, three additional experiments only for the 2004-year-period are performed to be compared with the control run (WRT) (Table 1). The three additional experiments are conducted by switching off the river discharge and the tidal forcing (WO), the river discharge only (WT) and the tidal forcing only (WR). WO is used to determine how wind forcing alone influences the physical and hydrodynamic conditions around the focused research area by excluding the tidal forcing and river discharge. The interaction between wind forcing and river discharge is investigated in the WR by excluding the tidal forcing in the simulation. To obtain information about the interaction between wind forcing and tide, the river discharge is switched off as performed in WT. The interaction between wind forcing and river discharge can be also investigated by comparing the WRT and WT cases while the interaction between wind forcing and tide can be also investigated by comparing the WT and WO cases. Some additional experiments are also designed to observe the nonlinear processes around the Sahul Shelf. As discussed in section 2.5, the residual currents can be induced by nonlinear interaction between tidal currents and topography. The other additional experiments have been designed by introducing tide as only driving force to the simulation for both barotropic (TOBT) and baroclinic (TOBC) modes. The roles of two primary nonlinear terms of momentum equations i.e. advection and quadratic bottom friction are also investigated by designing the simulation without advection (TOBT-NADV) and halved bottom friction (TOBT-Half).

| Experiments | Wind | River runoff | Tidal elevation |
|---|------|--------------|-----------------|
| Control run (WRT) | Y | Y | Y |
| No-River (WT) | Y | N | Y |
| No-Tide (WR) | Y | Y | N |
| Wind only (WO) | Y | N | N |
| Tide only-barotropic (TOBT) | N | N | Y |
| Tide only-barotropic-without advection term (TOBT-NAdv) | N | N | Y |
| Tide only-barotropic – with halved friction (TOBT-Half) | N | N | Y |
| Tide only-baroclinic (TOBC) | N | N | Y |

Table 1: Numerical experiment design

3.5 The Three-Dimensional Dynamic Equation for Momentum Analysis

The momentum balance equation will be examined to study interaction between tidal flow and bottom topography (Section 5.3 and Appendix A) and the dynamical processes of how tidal forcing and river runoff influence the wind-driven circulation during the upwelling period (Chapter 6). Defining that the x-axis is the cross-shelf axis (positive eastward) and the y-axis is the along-shelf axis (positive northward) in the local Cartesian coordinate system, the x and y momentum equations can be written as

$$\overbrace{\frac{\partial \vec{U}}{\partial t}}^{ACCEL} + \overbrace{\vec{U} \cdot \nabla_h \vec{U}}^{HADV} + \overbrace{w \cdot \frac{\partial \vec{U}}{\partial z}}^{VADV} - \overbrace{2\Omega \times \vec{U}}^{COR} = -\overbrace{\frac{1}{\rho} \nabla P}^{PGF} + \overbrace{A_h \nabla^2 \vec{U}}^{HVI} + \overbrace{\frac{\partial}{\partial z} \left(A_v \frac{\partial \vec{U}}{\partial z} \right)}^{VVI} \quad (6.1)$$

where,

ACCEL is acceleration; HADV is the horizontal nonlinear advection; VADV is the vertical nonlinear advection; ADV = VADV + HADV; COR is the coriolis force which is proportional in magnitude to the flow speed and directed perpendicular to the direction of the flow that acts to the left of

the flow in the southern hemisphere; PGF is the pressure gradient force; HVI is the horizontal viscous force; VVI is the vertical viscous force representing the vertical shear stress gradient (stress difference between the two layers divided by the vertical distance); in the surface, the stress (then called as surface stress) is proportional to the squared wind velocity; in the bottom, the stress (then called as bottom stress) is proportional to the squared water velocity near to the bottom; in the interior, the stress (then called as interfacial stress), is dependent on the vertical eddy viscosity and shear velocity as formulated by by $\tau_{xz} = \rho A_v \left(\frac{\partial u}{\partial z} - f v \right)$, with u is the velocity in the zonal direction and v is the velocity in the meridional direction; Ω is the angular frequency ($\Omega = 2\pi f = 7.2921 \times 10^{-5}$ rad/s); f is the Coriolis frequency; ρ_0 is the reference density, A_h is horizontal momentum diffusion coefficient; A_v is vertical turbulent viscosity coefficient. A_h and A_v have been already explained in more detail in section 3.1. In the following, the symbol of Δ will be used to represent the differences of momentum components between the two particular simulations.

3.6 Data for Validation

The satellite images of Sea Surface Temperature (SST) and Sea Surface Height (SSH) derived from the Moderate Resolution Imaging Spectro-radiometer Satellite (MODIS) and Archiving, Validation and Interpretation of Satellite Oceanographic (AVISO) data set are employed to validate the WRT simulation results. Furthermore, the in-situ observation data of International Nusantara Stratification and Transport project (INSTANT) (Sprintall et al., 2004) are used to validate the WRT simulation with respect to velocity. Furthermore, time series of the sea level of the WRT simulation are compared to the one made available from University of Hawaii Sea Level Center (<https://uhslc.soest.hawaii.edu/data/?rq>)

4. VALIDATION

4.1 Sea Surface Height (SSH) and Surface Currents

According to Figures 4.1 and 4.2, the simulation is able to reproduce the SSH variability reasonably well. This is indicated by the presence of the higher SSH near the Eastern Papua Coast in the simulation and satellite observation, generating the anti-cyclonic circulation around the coast during the southeast monsoon. However, it is found that the surface currents in some areas show significant magnitude and direction differences. For example, the surface currents along the Eastern Papua Coast flow during the southeast monsoon in the observation flow northwestward while the simulation currents tend to flow southeastward with relatively low intensity compared to the satellite observation. The study suggests that differences are caused by the influence of baroclinic terms that are not reasonably resolved in the calculation based on satellite observations. The presence of simulated northwest currents, also known as the New Guinea Coastal Current (NGCC), confirms the in-situ observation found by Kashino et. al. (2013). Subsequently, these currents meet the Mindanao Current (MC) near the Halmahera Island. Some water masses carried by these currents enter the Indonesian Seas and some of them flow eastward as well, known as the North Equatorial Counter Current (NECC). Furthermore, Mindanao and Halmahera Eddies (ME and HE) are formed at the retroreflection points of MC and NGCC, respectively. The ME and HE are respectively indicated by the lower SSH (cyclonic circulation) and the higher SSH (anti-cyclonic circulation) compared to the surrounding. The HE is located at around the Northern Halmahera Island while the ME is further north. In general, the seasonal variations of NECC and HE agree well with the observation conducted by Kuroda (2000), Ueki, et. al. (2003) and Kashino, et. al (2013). As their findings, the simulation results show that the HE tends to shift northwestward during the southeast monsoon, and southeastward during the northwest monsoon.

Furthermore, the simulation and observation results indicate that the lower SSH is observed in the EIS during the southeast monsoon. In this period, it is also shown that the SSH in the Indonesian Seas is relatively lower than the SSH around the Northern Papua Coast. In contrast, the higher SSH is observed in the EIS during the northwest monsoon compared to the SSH in the Western Indonesia Sea and around the Northeastern Papua Coast.

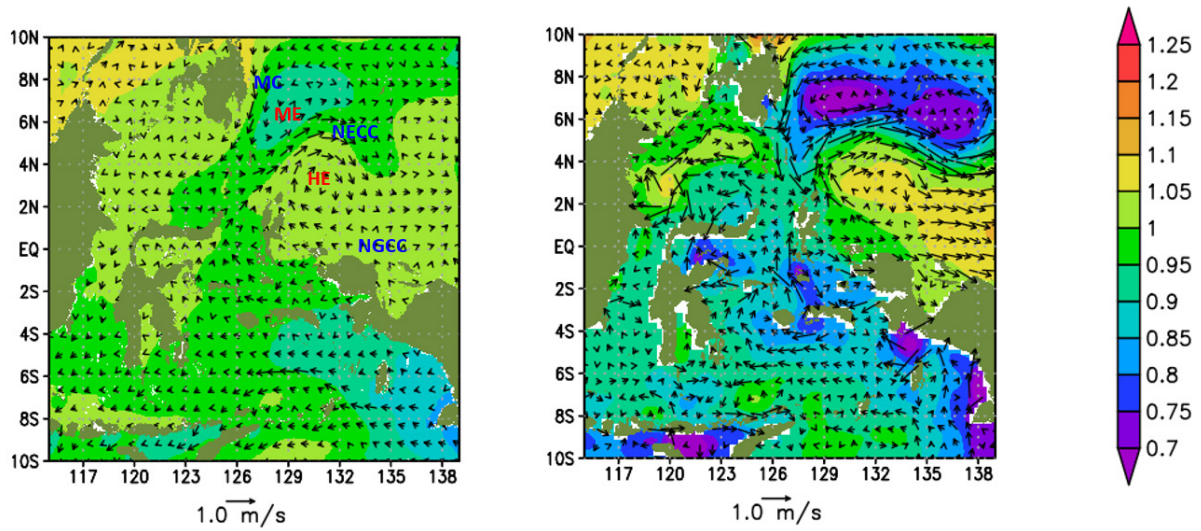


Figure 4.1: SSHs (meter) overlaid by baroclinic (left) and barotropic (right) surface currents (m/s) during the south-east monsoon reproduced by HAMSOM (left) and AVISO (right).

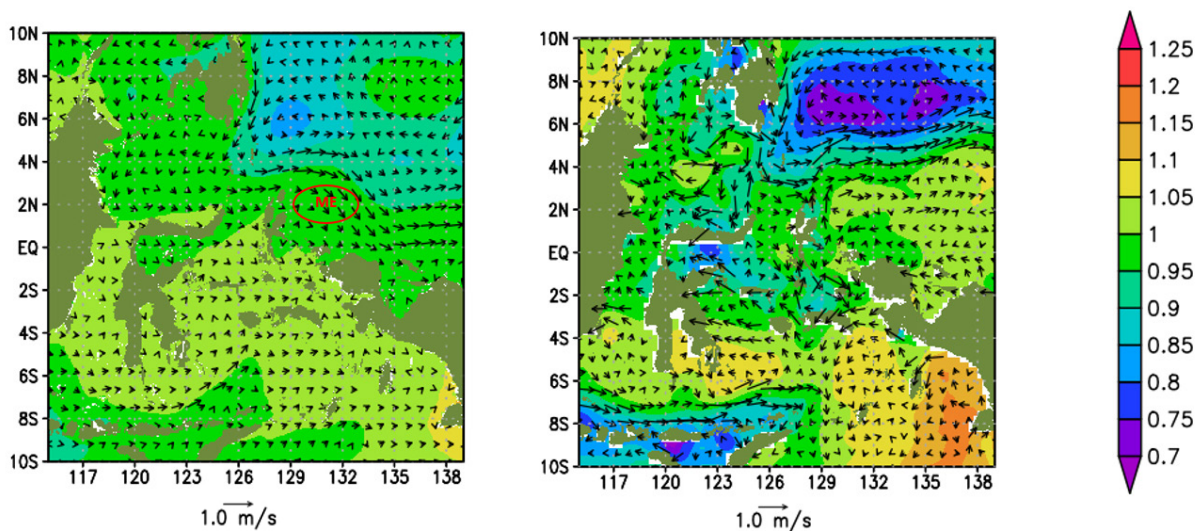


Figure 4.2: SSHs (meter) overlaid by baroclinic (left) and barotropic (right) surface currents during the north-west monsoon reproduced by HAMSOM (left) and AVISO (right).

In general, HAMSOM is also able to simulate the time series of tidal elevations in the model area reasonably well (Figure 4.3). The evaluation is done by comparing the HAMSOM and in-situ data for the Ambon tide gauge station (3.7° S 128.2° E) during the period between 1-31 July, 2004, taken from (<https://uhsic.soest.hawaii.edu/data/?rq>). The results show that semidiurnal character can be represented well by the model indicated by the strong correlation between the model and observation of about 0.82 – 0.92. However, for Ambon, the amplitude reproduced by the simulation tends to be higher than the one in the observational data. This is because the resolution model is too coarse, so it could not resolve well the narrow and shallow

area where the Ambon tide gauge station is located. The location is in the Inner Ambon Bay which is separated by narrow and shallow channels with about 800 m width and less than 50 m depth while the model resolution is 3' (about 5 km). Therefore, the tidal elevation reproduced by the model is taken near the coast Ambon directly facing the Banda Sea which is relatively wide and deep, which explains the relatively high amplitudes. It is known that the tidal amplitude tends to decrease as it enters the strait as observed by Medeiros and Kjerfve (1988). They found that the tidal choking occurs as the tide enters into the narrow strait resulting in decrease of its amplitude in a step-like manner.

In contrast, the tidal amplitude and the phase in the simulation, such as in the Tawau, is respectively underestimated and slightly shifted compared to the measured tidal amplitude. In this station, the simulation is able to resolve the bathymetry around the station so that the position taken from the simulation is nearly representing the observed measurement. Therefore, the study suggests that the underestimated tide amplitude and delayed phase of the simulation is associated to the semi implicit scheme applied in the numerical calculation. This scheme tends to damp the barotropic wave, but it is necessary to keep the model stable with longer time step.

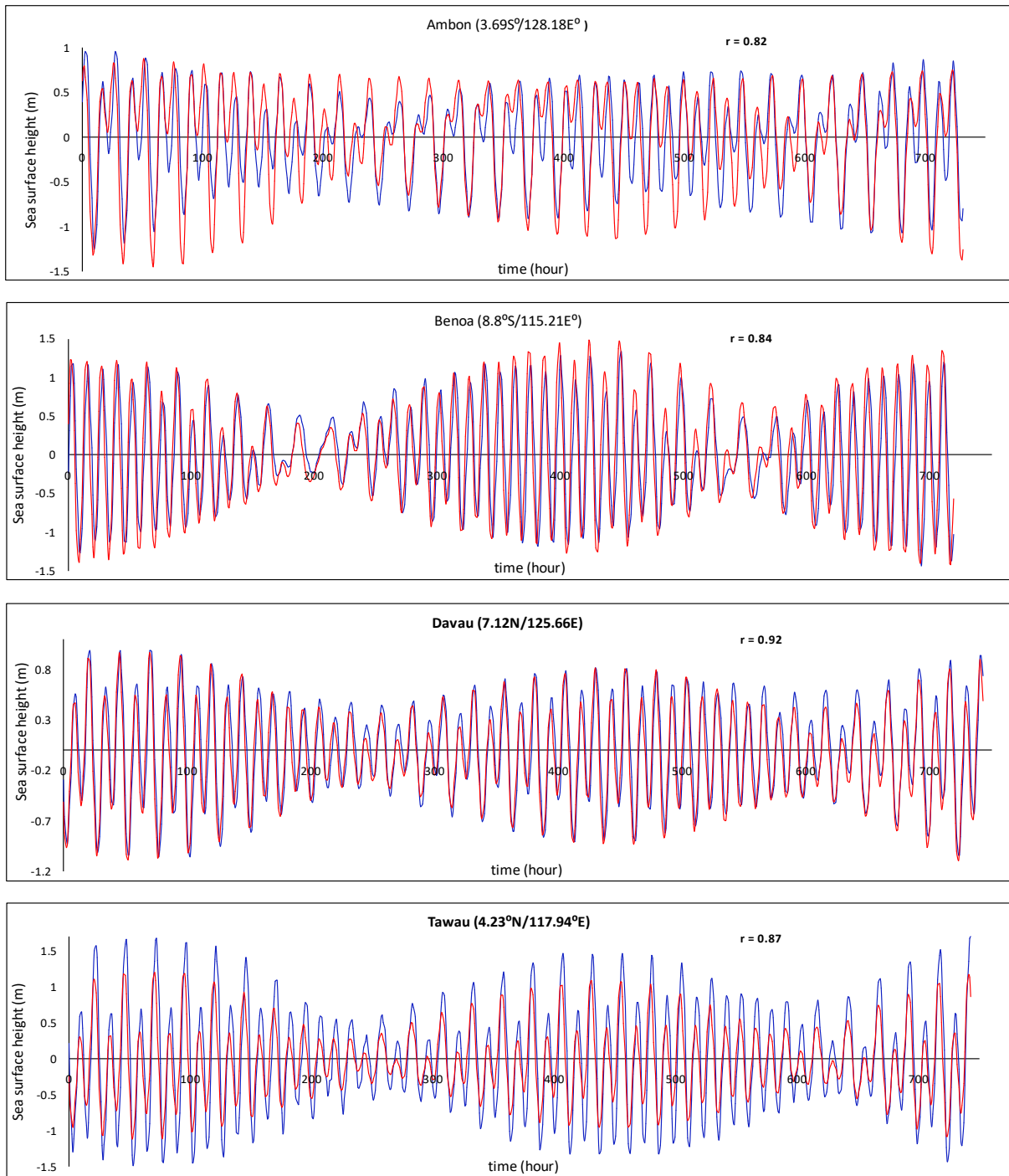


Figure 4.3: Time-series comparing measured tides (blue lines) with tides from the hydrodynamic model (red lines) at a) Ambon (July 2004) b) Benoa (September 2004) c) Davau (July 2004) d) Tawau (July 2004).

4.2 Sea Surface Temperature (SST)

In general, the monthly simulated SST derived from the HAMSOM model is in good agreement with the SST derived from MODIS (Figure 4.4). The results show seasonal patterns indicated by the relatively low temperature at 24 -25 °C during the southeast monsoon (July-August) and the relatively high temperature at 30 – 31 °C which occurs during the northwest monsoon (January-February). The correlation between the simulated and measured data in selected areas around the Banda and Northern Arafura Seas over 12 years (between 2003 and 2014) is about 0.72 - 0.92, indicating a good correlation. However, it is observed that the maximum and minimum temperatures of simulation are generally underestimated by the MODIS. The difference is associated to the relatively low spatial resolution of NCEP forcing ($2.5^{\circ} \times 2.5^{\circ}$, $1^{\circ} \approx 111$ km), applied to the model and the regional model, compared to the MODIS resolution (5.5 km \times 5.5 km).

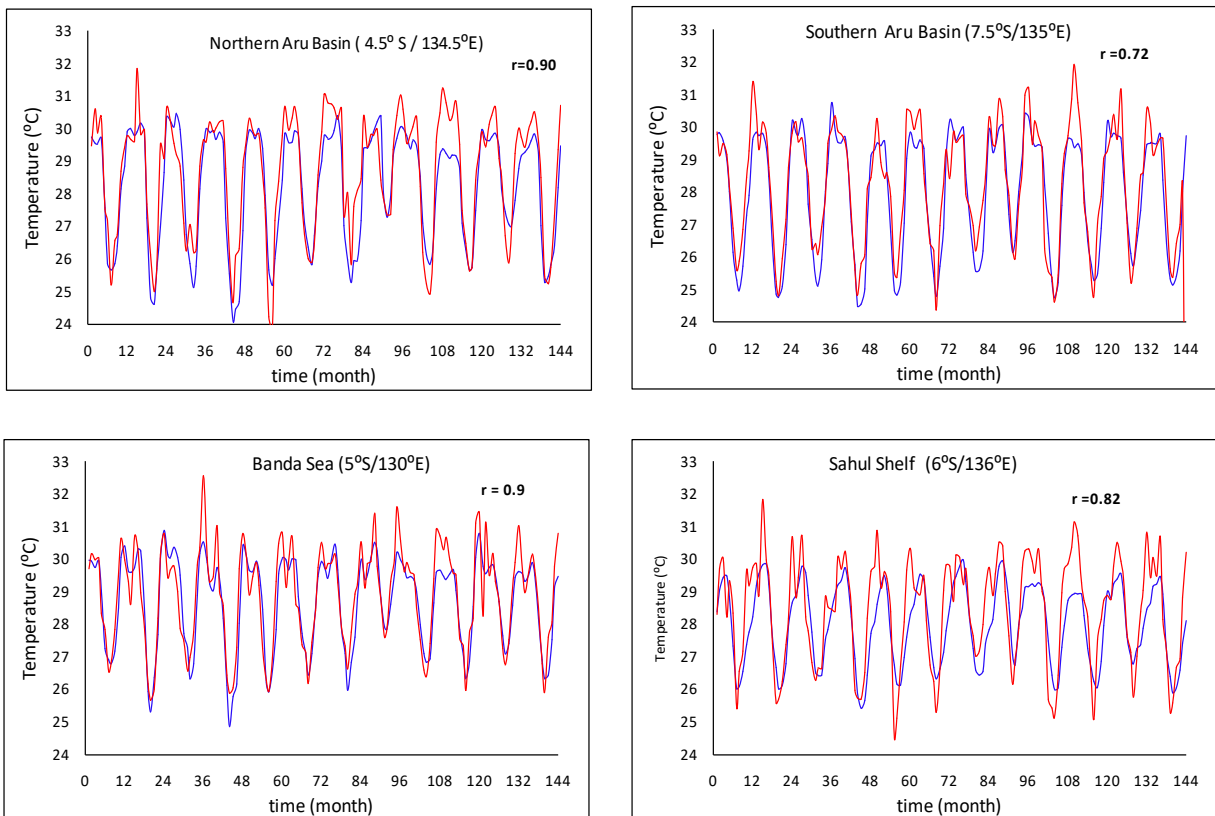


Figure 4.4: The values of SST (°C) from MODIS (red color) and HAMSOM simulation (blue color) in the period of between 2003 and 2014 in the Banda and Northern Arafura Seas

Similarly, the simulation is also able to reproduce the SST spatial variation that agree reasonably well with the spatial variation produced by Moderate Resolution Imaging Spectroradiometer Satellite (MODIS) (Kilpatrick, K. A., et al., 2015) (Figure 4.5). Some cold areas such as around the Northern Aru Basin and the Southern Seram Coast are observed during the southeast monsoon. However, the simulated SSTs such as in the southeastern part of the model region are overestimated compared to the MODIS SSTs. In contrast, the modeled SSTs in the other regions such as the Northern Aru Basin underestimate the observed SSTs. Again, the low resolution of forcing and boundary data most likely leads to an inaccuracy in the model results.

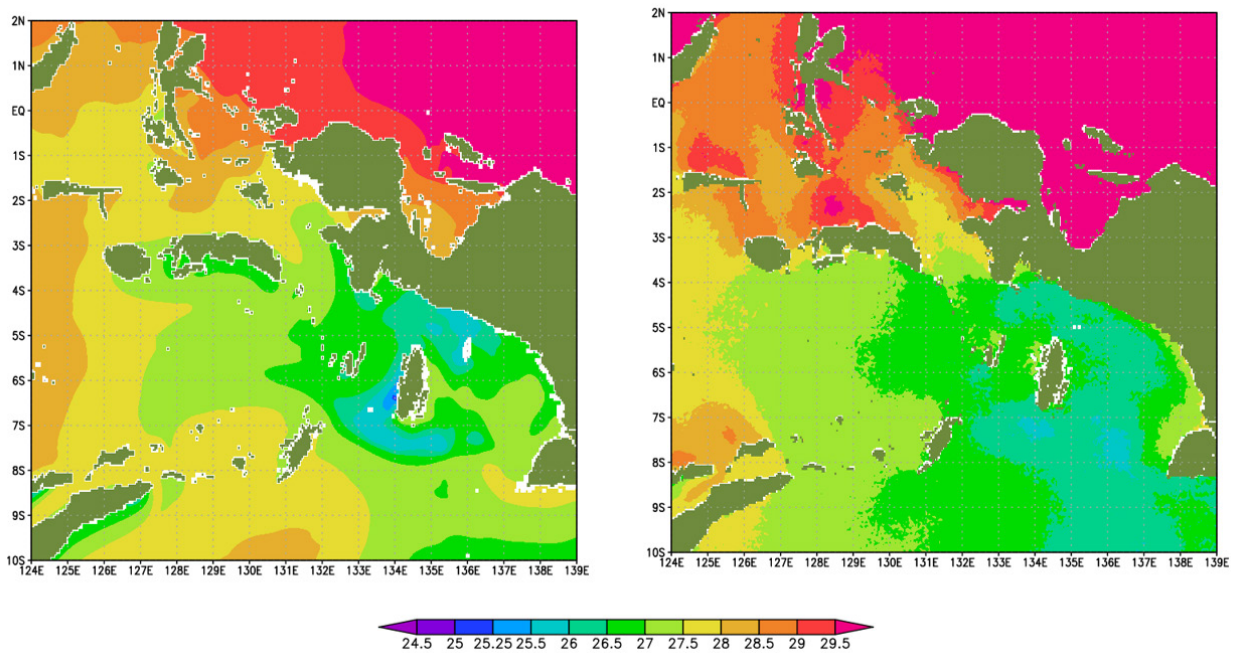


Figure 4.5: Averaged SST (°C) over the period 2003-2014 comparison between the HAMSOM (left) and MODIS (right) during southeast monsoon.

4.3 Velocity

The velocity is generally verified at four locations i.e. the Makassar Strait (2.86° S / 118.45° W), the Lombok Strait (8.4° S / 115.9° W), the Ombai Strait (8.53° S / 125° W) and the Timor Passage (11.37° S / 122.96° W) (Figures 4.6 and 4.7). The Makassar Strait is well known as the main gate where the Northwest Pacific Ocean water masses enter into the Indonesian Seas while the others are the exit gates where Indonesian water masses exit into the Indian Sea. The measured data are derived from the International Nusantara Stratification and Transport project (INSTAN) project (Sprintall et al., 2004). In general, the simulation results show an acceptable agreement with the findings from the observational data. However, it is identified that the correlation between the two data is smaller than it is for SST, as discussed previously. It is estimated that the velocity correlations between observation and simulation vary between 14 – 78 %. The reason for smaller correlation is that the velocities are measured at a certain location and also in a certain depth while the model's velocity represents the average velocity of a certain model grid cell with a finite depth range, i.e. layer thickness, which increases with depth. The corresponding layer thickness at the depth of 50 m and 150 m are 7 m and 22 m, respectively. As a consequence of this, the model's velocity tends to be underestimated in deeper regions and the correlation could be smaller. Meanwhile, both the simulated SST and the MODIS SST represent the average SST of a certain model grid cell, with a grid cell size of 21 km^2 and 30 km^2 , respectively. Therefore, the SST comparison shows a higher correlation compared to the velocity comparison. Furthermore, some results are shown to have relatively small correlation (14-20%). However, the simulated velocities are still accepted because they are mostly in the same direction as the observation velocities, and still shown to be capable of reproducing low and high variations.

In the meridional direction, the currents in the two layers in both the simulation and observation are generally directed to the southward. Some northward currents are mostly found during the transition periods in May/June and November/December. The simulation results also indicate that the intensities follow seasonal variations as found in the observational results. In the Makassar Strait, the current intensities both in the upper and lower layers from the two data sets during the southeast monsoon (July – October) are generally shown to be larger than the ones during the northwest monsoon (December - February). This indicates more thermocline water masses originating from the North Pacific Ocean entering into the

Indonesian Seas during the southeast monsoon than during northwest monsoon, as also suggested by Gordon and Susanto (2008), Mayer and Damm (2012). Similarly, in the three exit gates (the Lombok, Ombai Straits and Timor Passage), a higher intensity than during northwest monsoon in the two selected layers is generally observed during the southeast monsoon in both those data sets. Moreover, as also observed in the mooring data, the simulation shows that the intensity of velocity in the Lombok Strait is generally higher than the one in the other exit gates, while the intensity in Timor Passage is the lowest.

Similar to the meridional currents, in the zonal direction, the results indicate that the currents in the two selected layers in both observation and simulation during the southeast monsoon are generally higher than those during the northwest monsoon. In the Makassar Strait, the zonal currents in the two data sets are mostly directed to the west in the both selected layers and their magnitudes are relatively lower compared to the meridional currents. In the three exit gates, it is observed that the currents flow to the westward during the two seasons in both of the selected layers. Similar to the currents in the Makassar Strait, the meridional currents in the Lombok Strait in the two data sets are shown to be relatively higher than the zonal currents. In contrast, the zonal currents in the Ombai Strait and Timor Passage are relatively higher than the meridional currents. The results also indicate that except in the lower layer in the Ombai Strait, the zonal currents during the southeast monsoon are generally higher than they are during the northwest monsoon.

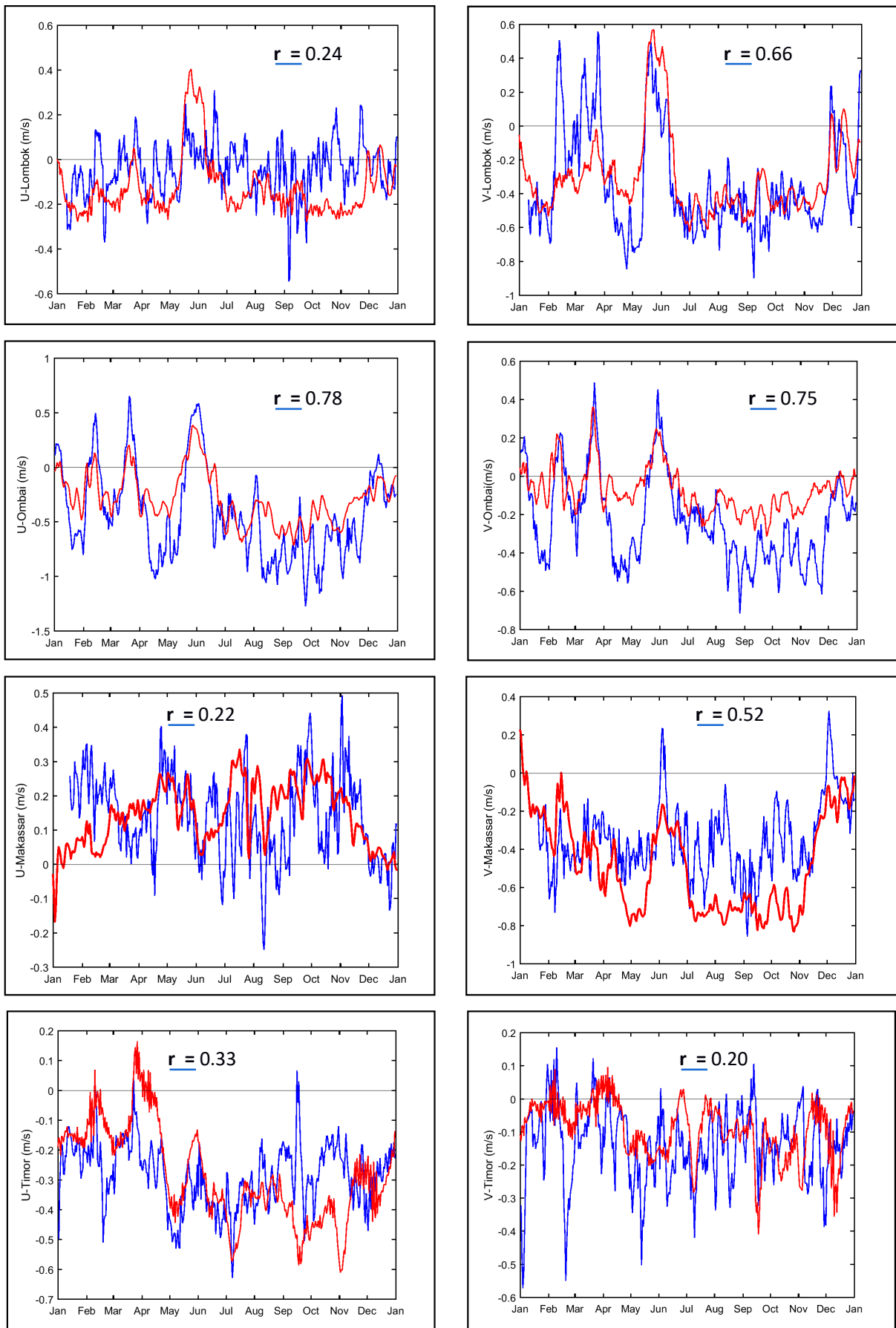


Figure 4.6: Comparison of HAMSOM simulation (red line) and INSTANT observation (blue line) of zonal and meridional velocities at 50 m depth in Lombok, Makassar, Ombai straits and Timor Passage.

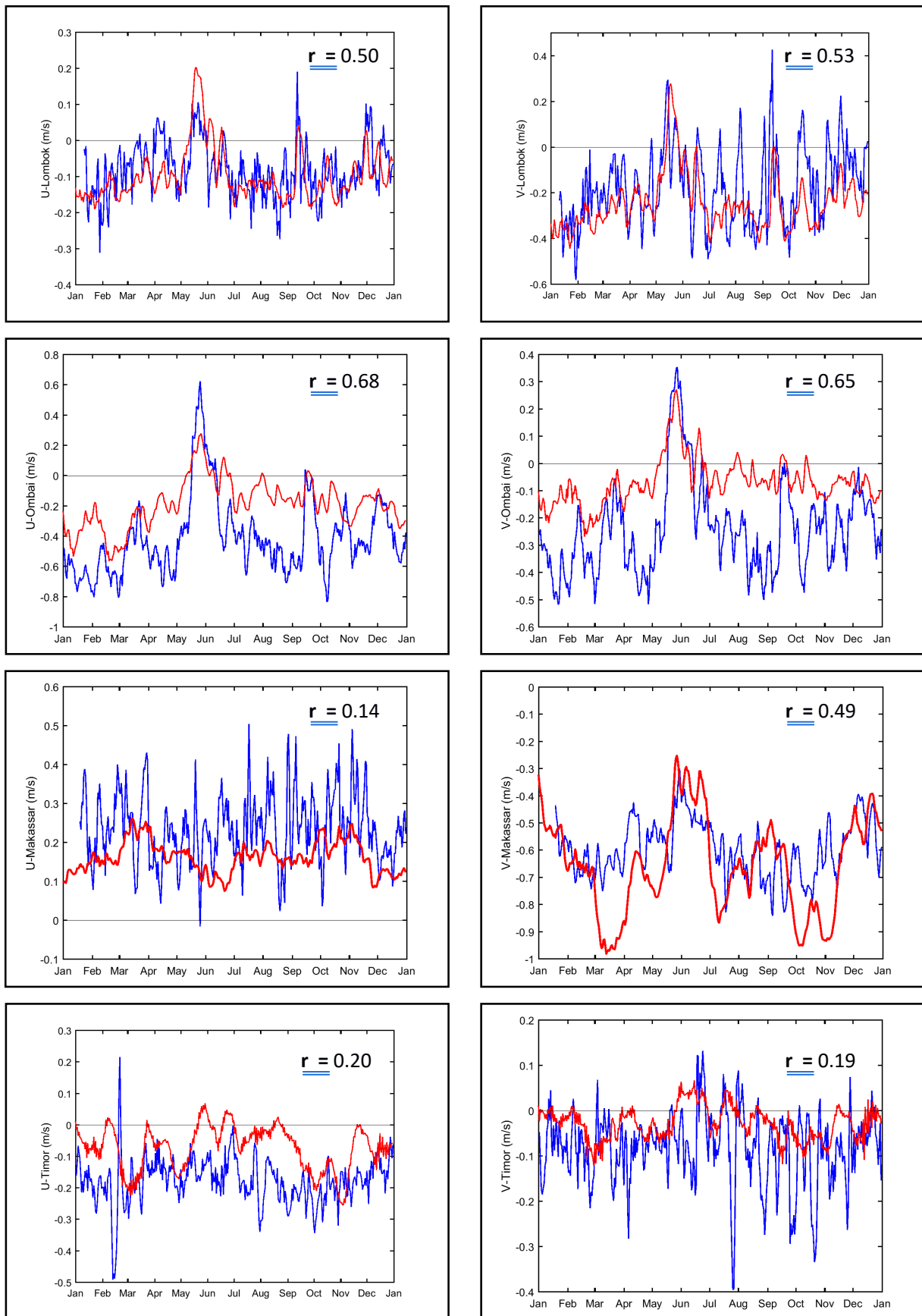


Figure 4.7: Comparison of HAMSOM simulation (red line) and INSTANT observation (blue line) of zonal and meridional velocities at 150 m depth in the Lombok, Makassar, Ombai Straits and Timor Passage

4.4 TS-Diagram

The four simulation experiments are compared to the global data of EN4 in the selected areas, i.e. the Halmahera Sea ($0-2^{\circ}$ S / $128-129^{\circ}$ E), Banda Sea ($4-6^{\circ}$ S / $125-130^{\circ}$ E), Makassar Strait ($0-4^{\circ}$ S / $118-120^{\circ}$ E) and the Aru Basin ($4-5^{\circ}$ S / $133-135^{\circ}$ E), by means of TS-diagram (Figure 4.8). In general, the simulated TS diagrams (the WRT case) are shown to have a good agreement with observations. The best fits are found in the Halmahera Sea and the Makassar Strait, with a deviation of less than 0.1. In the Banda Sea and the Aru Basin, the deviation is at about 0.2. The results indicate that the tidal exclusion forcing causes the salinity maximum to be overestimated by 0.2 – 0.6. The highest deviation is observed in the Halmahera Sea. Significant deviations of about 0.6 are also observed in the Banda Sea and the Aru Basin. The deviation is only at about 0.2 in the Makassar Strait. The eroded salinity maximum in the tide inclusion simulations indicates the generation of internal tidal mixing that enhances vertical mixing that mostly occurs in Halmahera and Sulawesi Seas (see also in the section 5.4). As consequence of this, deeper waters with relatively low salinity and temperature compared to the thermocline layers are upwelled and then mixed, resulting in a reduction of the salinity and temperature within the thermocline layers. Furthermore, the results show that fresh water at the surface plays an important role in stabilizing the surface water so that a better result is indicated in the WRT case than in the WT case. In particular, the mixing generated by tidal forcing, and rough topography reaches the surface to bring relatively fresh water down to the subsurface which subsequently erodes the salinity maximum within thermocline layer. The influence of river runoff is more obvious in the Northern Papua Coast, the Aru Basin, the Banda Sea and the Makassar Strait. This is not surprising because there are big rivers located in these areas. It also is shown that relatively fresh surface water only contribute relatively little to reduce the subsurface salinity when the tidal forcing is excluded from the simulation, as indicated by comparing between the WO and WR cases. The TS diagrams in both WR and WO are similar, namely their salinity maximum are overestimated by about 0.6 compared to the observations.

The study also suggests that the horizontal mixing also contributes to erode salinity maximum in the EIS so that salinity maximum in the Aru Basin, which mostly originate from Halmahera Sea is less than salinity maximum in the Halmahera Sea as observed in all simulation and global observation data (see Figures 4.8 and 5.8).

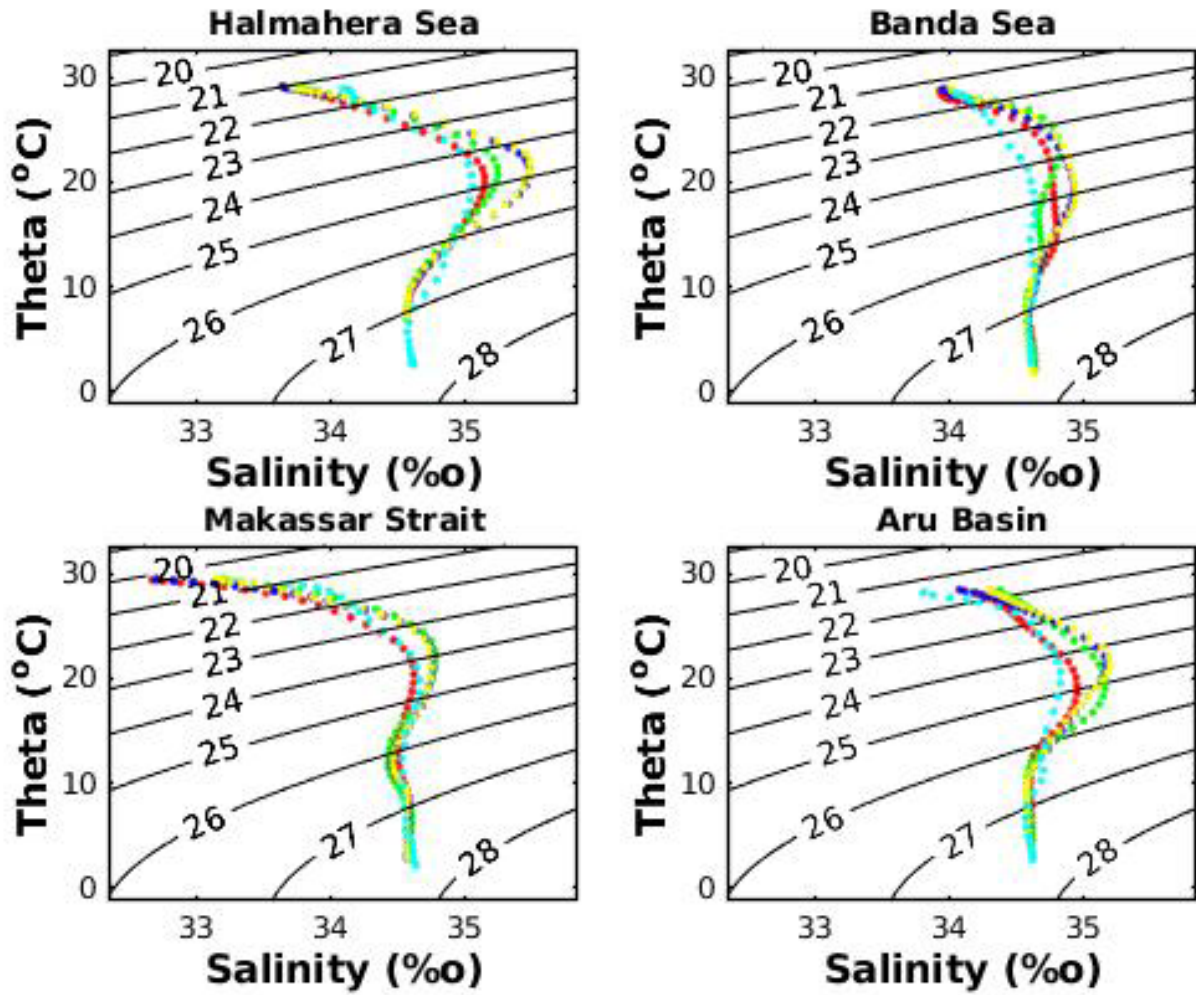


Figure 4.8: TS-diagram derived from HAMSOM simulations and global observation data (EN4) in the 2004 period in the selected areas: the WRT case (red), the WO case (yellow), the WR case (blue), the WT case (green) and the global data of EN4 (cyan).

5. Forcing and Hydrodynamic Conditions

In order to obtain general characteristics about the conditions of driving forces and the physical and dynamical conditions in the BAS, the monthly and seasonally average from the simulation results are described in the first two sections of this chapter (5.1 and 5.2). The tidal motion around the Northern Arafura Sea will be discussed in section 5.3. The simulation results obtained from the first four different runs (see Table I) are presented in section 5.4. The description will focus on the interactions of the river runoff and tidal forcing with the seasonal wind-driven upwelling around the Northern Arafura Sea. In section 5.5, the vertical viscosity coefficient in the first four different runs around the Northern Arafura Sea is discussed. Then, in section 5.6, the connection between internal tide and vertical mixing in deep water is presented.

5.1 Forcing Conditions

The results show that the Eastern Indonesian Seas (EIS) is generally exposed to south-easterly winds between May and October, giving way to what is called the “south-east monsoon” (Figures 5.1 and 5.2). The wind intensity tends to decrease toward the north-west. The southeast monsoon reaches its full development between July and August. During this period, the wind stress varies between 0.02 Nm^{-2} and 0.15 Nm^{-2} . It is also found that the eye wind, i.e. a stronger wind than its surrounding, is always found around the Southern Aru Island (Figure 5.2). The maximum of eye wind stress magnitude reaches about 0.15 Nm^{-2} . In contrast, the winds from north-west blow to south-east between December and March, which is then called the “north-west monsoon”. The wind stress during this period varies between 0.02 Nm^{-2} and 0.08 Nm^{-2} . The relatively strong wind with the wind stress at about 0.08 Nm^{-2} is observed around the Southern Makassar Strait and the Maluku Sea. In contrast, a relatively low-wind stress is observed around the Makassar Strait, Banda Sea and Northern Arafura Sea. In between those periods, relatively weak winds generally prevail starting to change their directions, which are called the “transition periods”. The wind stress during this period varies only between 0.02 Nm^{-2} and 0.06 Nm^{-2} .

The simulation results also show that a seasonal pattern is observed for evaporation and precipitation rate (Figure 5.3). In general, the evaporation rate during the southeast monsoon is higher than the one during the northwest monsoon. The evaporation rate varies

between 544 m³/s and 1,737 m³/s during the northwest monsoon while it varies between 1,594 m³/s and 4,054 m³/s during southeast monsoon. Minimum evaporation is observed at about 800 m³/s during the transition periods, i.e. in April (transition I) and November (transition II), when the wind speed is at a minimum rate while the maximum evaporation is found between July and August when the south-easterly wind blows at its maximum. In contrast, the precipitation during the southeast monsoon is generally less than during the northwest monsoon. The precipitation rate varies between 9,575 m³/s and 12,029 m³/s during the northwest monsoon, while it varies between 3,813 m³/s and 14,116 m³/s during southeast monsoon. The minimum precipitation is observed between July and August while the maximum is measured in April. It is also found that the evaporation rate around Banda Sea and Aru Basin during the full development of the southeast monsoon between July and August is smaller than the precipitation rate so that the ocean loses fresh water. In contrast, it is observed that the precipitation rate is generally higher than the evaporation rate during the other seasons so that the ocean gains fresh water.

Seasonal variation of river runoff is also observed, though with less variations. The river runoff varies between 10,952 m³/s and 13,410 m³/s during the northwest monsoon while it varies at between 11,088 m³/s and 13,747 m³/s during southeast monsoon (Figure 5.3). The highest river runoff is generally found at about 15,208 m³/s during the transition I period; while the lowest river runoff is observed at about 10,175 m³/s during the transition period II. It is also observed that the river runoff generally causes more freshwater flow into the sea, compared to the total evaporation and precipitation (P-E) (minus sign indicates the loss of fresh water). During the northwest monsoon, the river supplies about 59% of total freshwater input, while a larger contribution of about 81% is observed during the southeast monsoon. Between July and August, the river contribution peaks at about 96%. Meanwhile, the proportion of river runoff to the total amount of freshwater discharging into the sea during the transition I and II periods is about 56% and 68% respectively.

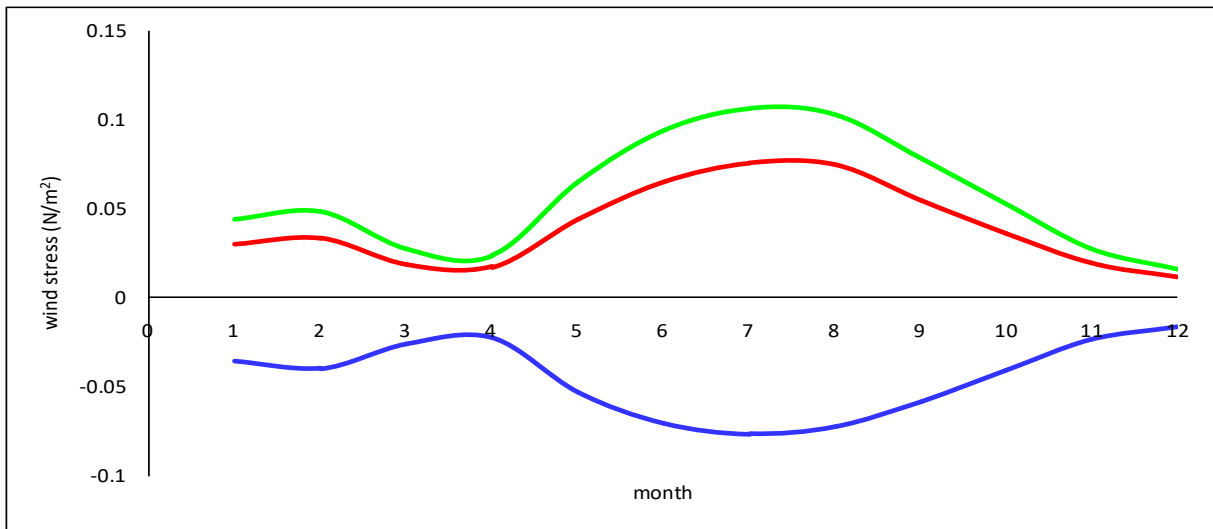


Figure 5.1: Monthly average wind stress (Nm^{-2}) in the Arafura and Banda Seas (BAS) (from 130°E - 137°E and from 4°S to 8°S) between January and December, derived from the NCEP data in the periods between 1990 and 2014: in zonal direction (blue line), in meridional direction (red line) and the resultant of zonal and meridional directions (light green line).

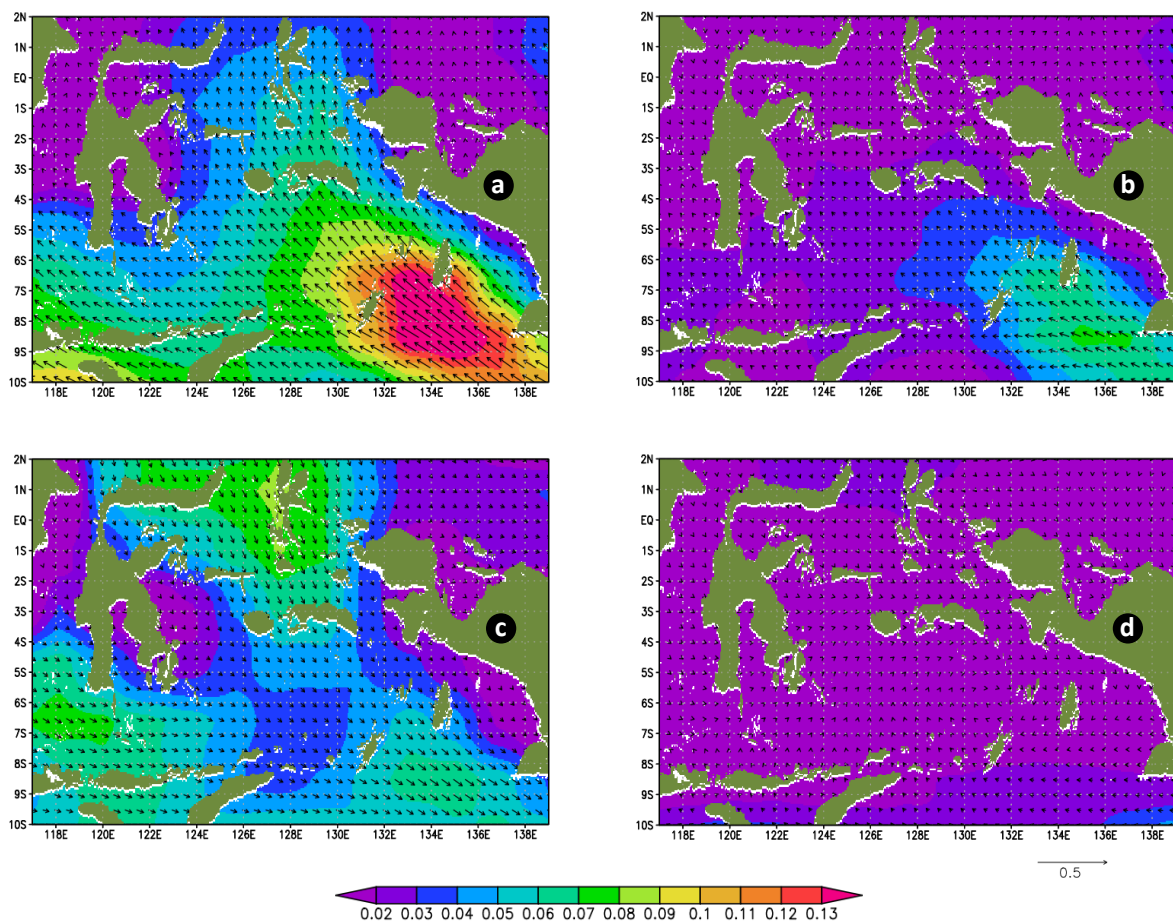


Figure 5.2: The horizontal distribution of seasonally average wind stress vectors (Nm^{-2}) and their magnitudes (background) derived from NCEP data in the periods between 1990 and 2014 during the; a) southeast monsoon (May-October), b) transition I (November), c) northwest monsoon (December-March) and transition II (April).

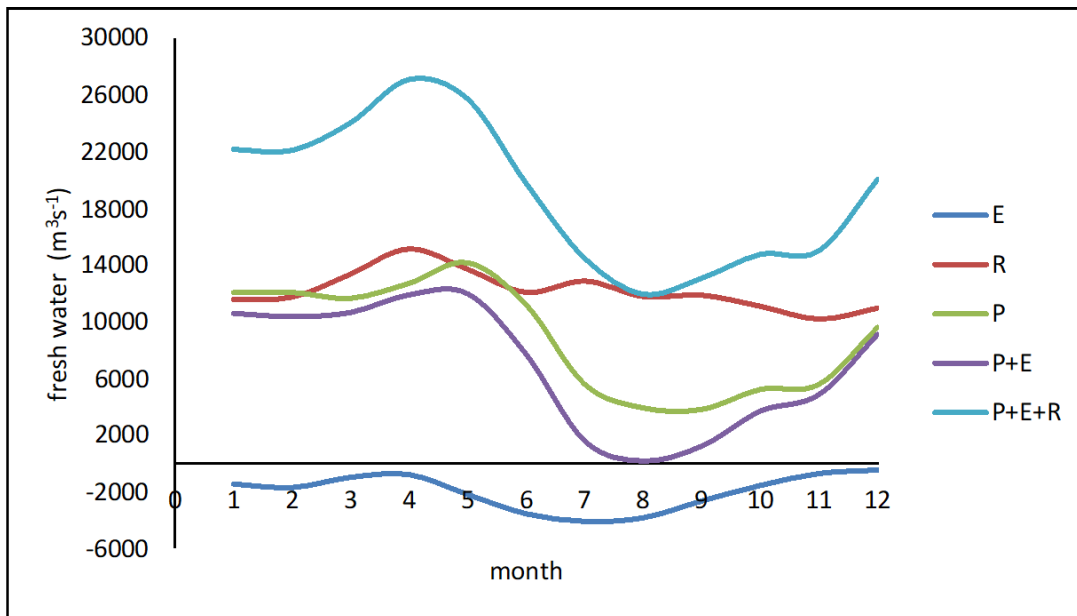


Figure 5.3: Monthly average of precipitation (P), evaporation (E) derived from NCEP data and river runoff (R) derived from WaterGAP Global Hydrology Model in the periods between 1990 and 2014 in the Arafura and Banda Seas (BAS) (from 130° E -137 ° E and from 4°S to 8°S): P(light green), E(blue), R(red), P+E (purple) and P+E+R (light blue).

5.2 Seasonal Variability of Hydrodynamic and Physical Conditions in the BAS

The monthly average of hydrodynamic and physical conditions around the BAS derived from the period 1990 to 2014 with the three main forcing factors (wind, river runoff and tide), named as the control run (the WRT case), will be discussed in this section. In general, the simulation results show that the SST in the Indonesian Seas is relatively warm, around 29.4°C during the northwest monsoon (December - March), while the SSS is relatively low, about 33.9 (Figure 5.4). The SST/SSS continues to increase/decrease and then reach its maximum/minimum at about 29.6 °C/33.4 in April when the winds start to change the direction to southeasterly winds. In the following period, the SST decreases and reaches its minimum at about 25.7°C in August while the SSS increases and reaches its maximum at about 34.3 in September. After this, the SST/SSS increases/decreases to reach its maximum/minimum in April/May.

During the northwest monsoon, the results show that the horizontal stratifications of the SST and SSS around the BAS are relatively low, varying from about 28.4°C to 29.5°C and from 33.5 to 34.1, respectively (Figure 5.5). The results also show that a relatively low SSS is observed in the western part of the research area. It is suggested that the lower salinity in the western area generally originates from Java and Sulu Seas bringing more fresh water.

Furthermore, it is observed that the surface currents during this period generally flow to eastward. In contrast, the relatively high stratification of the SST and the SSS in the BAS is observed during the southeast monsoon. In general, the SST increases from about 24.5°C to about 28.5°C toward the west while the SSS decreases from about 34.5 to about 33.5 toward the west (Figure 5.6). In this period, the surface currents in the BAS generally flow westward. The currents transport the surface waters toward Banda and Seram Seas. Relatively strong surface currents are observed around the Southern Aru Basin, where relatively strong winds blow. Surface currents increase from about 0.3 m/s in May to reach their peak of about 0.5 m/s in July. Furthermore, lower temperature and higher salinity compared to the surrounding areas, indicating a relatively high upwelling intensity in these areas, are observed around the Northern and the Southern Aru Basin during this period.

In addition, the obvious influence of river discharge is observed around the Digul River at the West Papua coast during all the season indicated by the low salinity around this area (Figure 5.6). These relatively fresh water masses are transported toward the Banda Sea during the southeast monsoon while the water masses are confined within 50 km from the coast during the northwest monsoon. Hence, far distance transport of the river discharge is mainly influenced by south-easterly wind blowing in this area. In contrast, the north-westerly winds are responsible that the river discharge is confined to the coast.

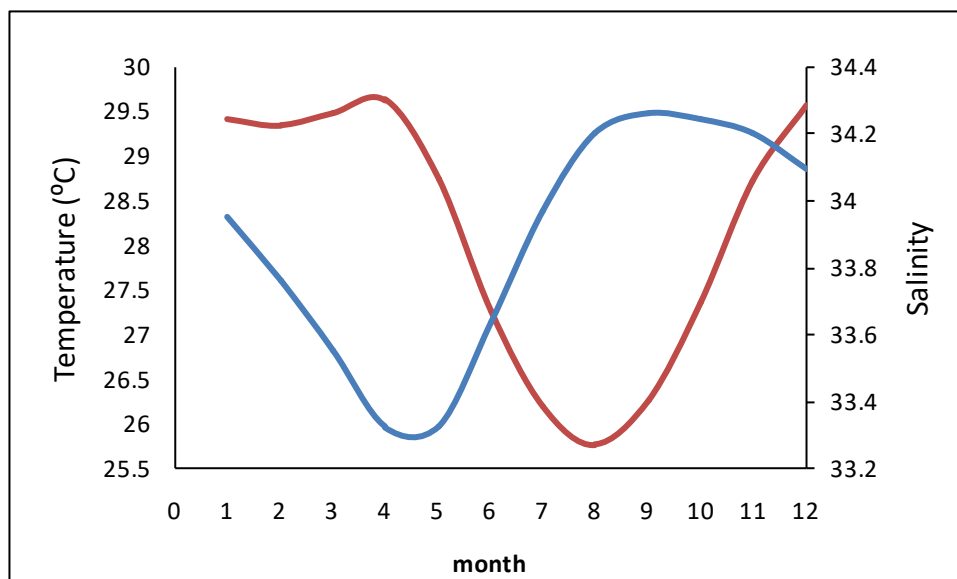


Figure 5.4: Monthly average SST (°C) (red) and SSS (blue) in the BAS (from 130° E - 137 ° E and from 4°S to 8°S) between January and December, derived from the HAMSOM simulation between 1990 and 2014.

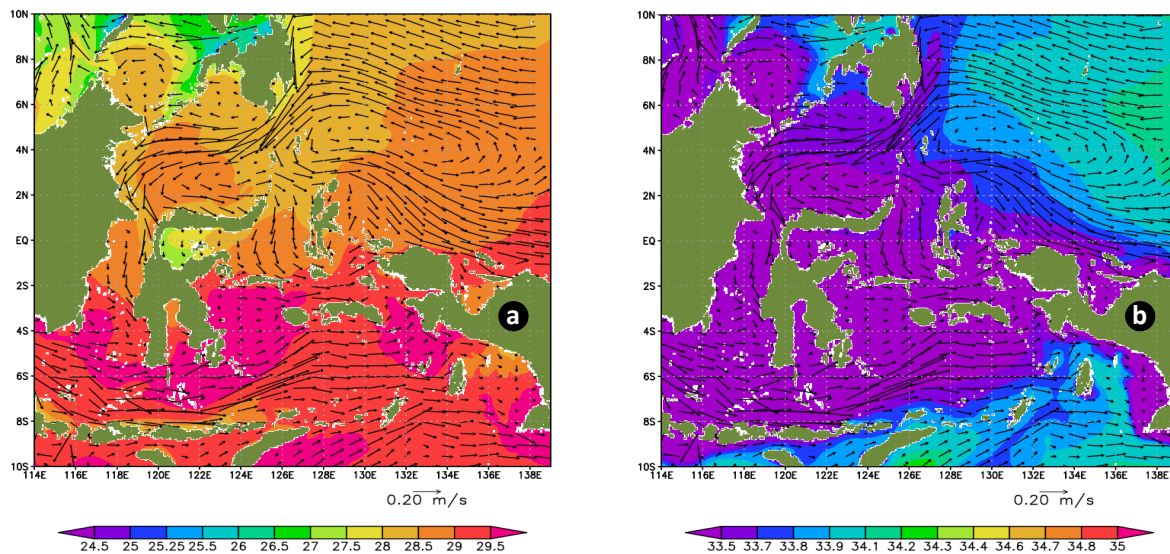


Figure 5.5: Horizontal distribution of average SST ($^{\circ}\text{C}$) and SSS (a and b) overlaid by surface currents during the northwest monsoon (February) in the BAS, derived from the HAMSOM simulation between 1990 and 2014

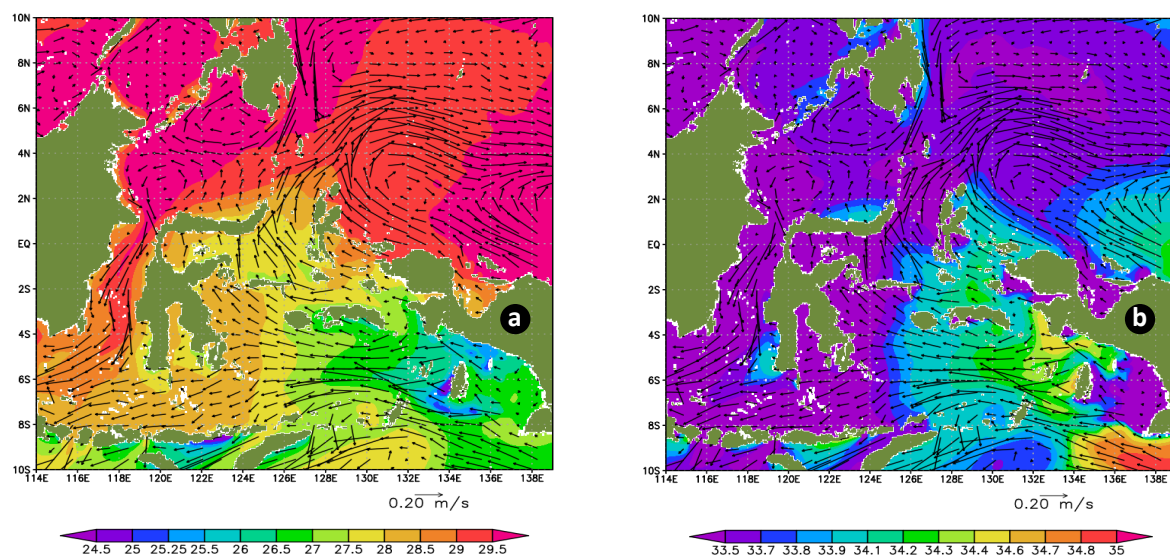


Figure 5.6: Horizontal distribution of average SST ($^{\circ}\text{C}$) and SSS (a and b) overlaid by surface currents during the southwest monsoon (July) in the BAS, derived from the HAMSOM simulation between 1990 and 2014.

The influence of North and South Western Pacific Oceans on the Indonesian Seas characteristics is observed in the thermocline layer, represented by the layer at 130 m depth. In this layer, relatively higher temperature and salinity values are generally found around the Northern Papua Coast than the surrounding area during the two monsoons derived from South Western Pacific Ocean (SWPO) (Figures 5.7 and 5.8). These water masses tend to flow

north-westward along the Papua Coast before most of them are retroflected to the east at the Northern Halmahera Island and parts of them are deflected into the Indonesian Seas through the Halmahera Sea, also known as the main gate of the eastern ITF. In general, the deflected currents are relatively higher during the southeast monsoon than they are during the northwest monsoon (Figures 5.9 and 5.10). It is also observed that water masses with relatively lower salinity and temperature originating from North Western Pacific Ocean enter into the Indonesian Seas through the Sulawesi Sea and then the Makassar Strait, also known as the main gate of the western ITF. These water masses are driven by relatively strong currents (at a speed more than 0.5 m/s). Similarly, the currents in the western ITF are generally higher during the southeast monsoon than during the northwest monsoon, confirming the findings of Gordon et al. (2008); Mayer and Damm (2012). As a consequence of this, during the southeast monsoon stronger currents flow from the Flores Sea into the Banda Sea rather than during the northwest monsoon. These two water masses generally meet in the Banda Sea before exiting into the Indian Sea, as observed by Gordon (2005).

The simulation results show that relatively high temperature and low salinity values in the subsurface waters (at about 130 m) of the Indonesian Seas, except in the Banda Sea, are generally observed during the northwest monsoon, compared to the situation during the southeast monsoon (Figures 5.7 and 5.8). Furthermore, relatively high salinity and temperature values in the EIS are found during the two seasons, indicating the influence of South Western Pacific Subtropical Salinity Maximum (SWPS). On one hand, the relatively high salinity in the EIS during the southeast monsoon originating from the South Western Pacific Ocean (SWPO) enters into the Indonesian Seas mostly through the Halmahera Strait and then flows into the Seram Sea and the Aru Basin, before exiting into the Indian Ocean. On the other hand, in addition to the lower influence of SPSW, the currents bringing cold and fresh water masses flowing from the Timor Sea to the Seram Sea through the Aru Basin lead to the relatively low salinity and low temperature during the northwest monsoon around the EIS, compared to the situations during the southeast monsoon. However, some of these currents will be deflected into the Banda Sea that cause the relatively higher salinity in the Banda Sea compared to its surrounding. Meanwhile, the lesser influence of SWPS during the northwest monsoon is also indicated by a lower transport (Figures 5.9 and 5.10) within the thermocline layers (at around 130 m depth) from the Pacific into the Indonesian Seas through the Halmahera Sea, compared to those during the southeast monsoon.

The simulation results also show that the salinity along the Indonesian eastern path is lower than the salinity before entering the Halmahera Sea (Figures 5.7 and 5.8). The study suggests that it is mainly caused by the strong vertical mixing occurring in the Halmahera Strait, as also observed by Field and Gordon (1992), Gordon (2005), Koch-Larroy et. al (2007). Furthermore, the horizontal mixing also contributes to the lower temperature and salinity in the EIS. A relatively lower temperature and salinity is observed while flowing from the Molluca Sea to the Seram Sea. As a consequence of this, it can be inferred that the observed salinity and temperature in the Seram Sea are lower than those in the Halmahera Sea. Similarly, it is observed that water masses from the Banda Sea, mostly originating from the North West Pacific also flow into the Aru Basin with lower temperature and salinity compared to the South West Pacific. Therefore, a lower temperature and salinity is observed around the Aru Basin, compared to the Halmahera and Seram Seas (see also Figure 4.8).

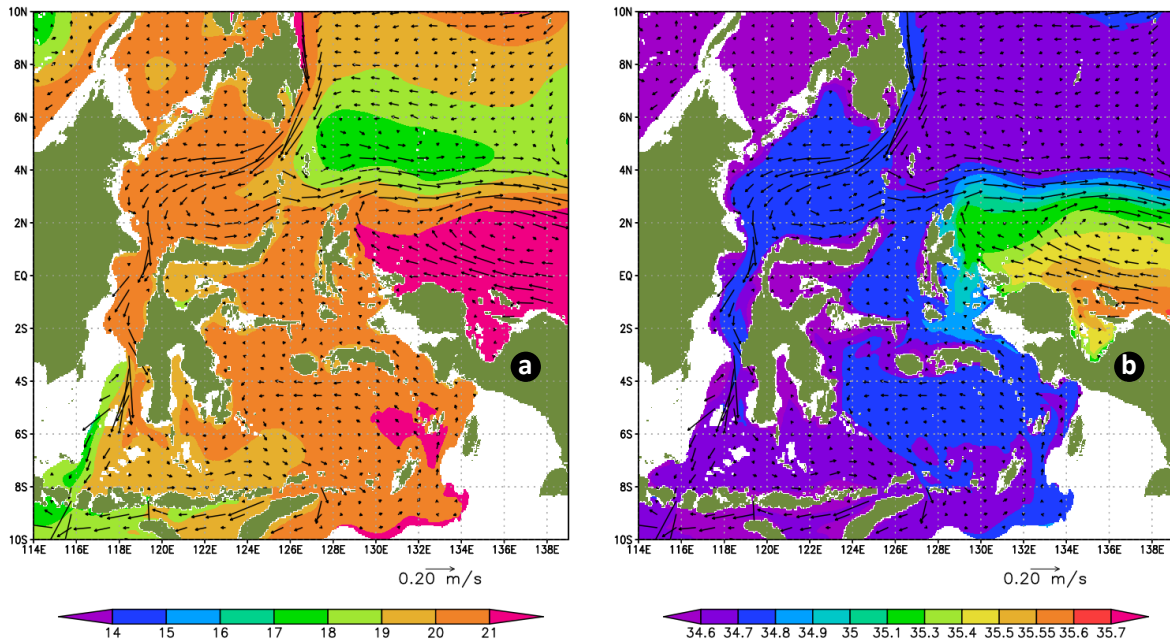


Figure 5.7: Horizontal distribution of average temperature (°C) (a) and salinity (b) overlaid by subsurface currents at about 130 m during the northwest monsoon (February) in the BAS, derived from the HAMSOM simulation between 1990 and 2014.

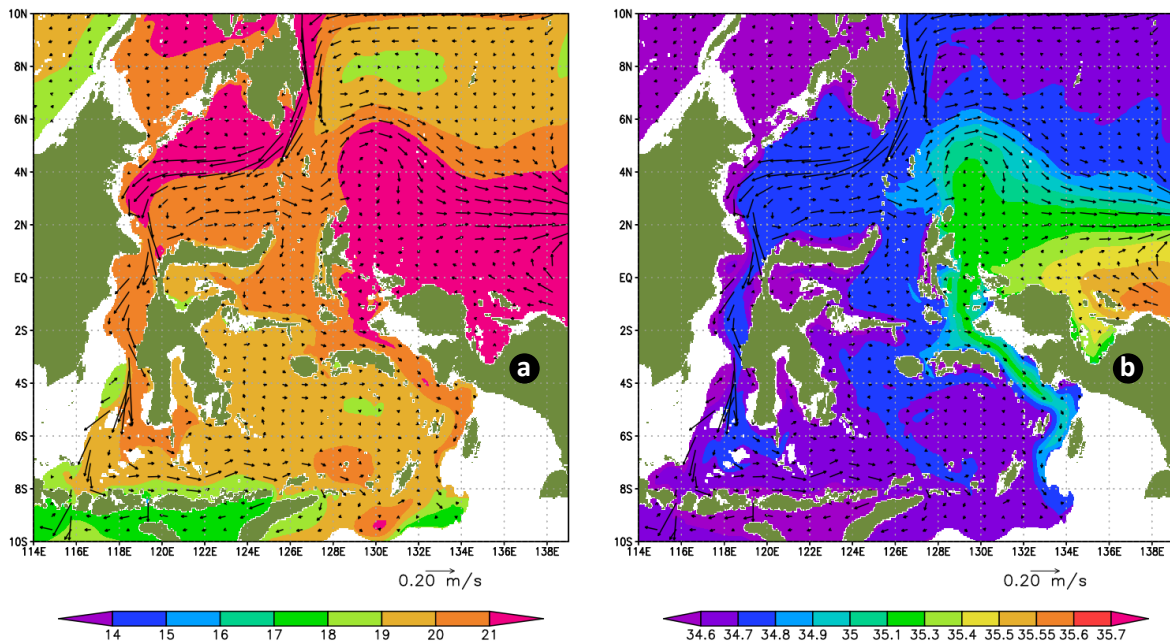


Figure 5.8: Horizontal distribution of average temperature (°C) (a) and salinity (b) overlaid by subsurface currents at about 130 m during the southeast monsoon (July) in the BAS, derived from the HAMSOM simulation between 1990 and 2014

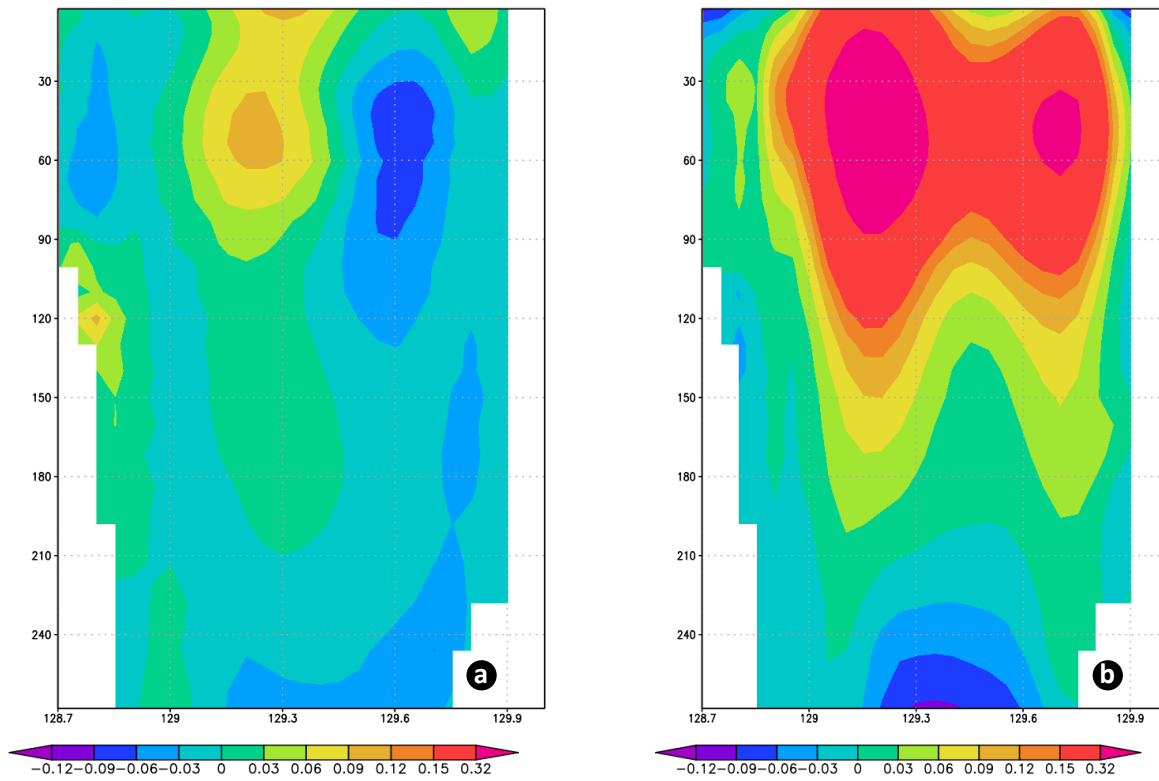


Figure 5.9: The vertical profile of average velocities (m/s) along the section of 0.5 °N and from 128.5 °E to 130°E for zonal (a) and meridional (b) flow directions during the northwest monsoon (February), derived from the HAMSOM simulation between 1990 and 2014

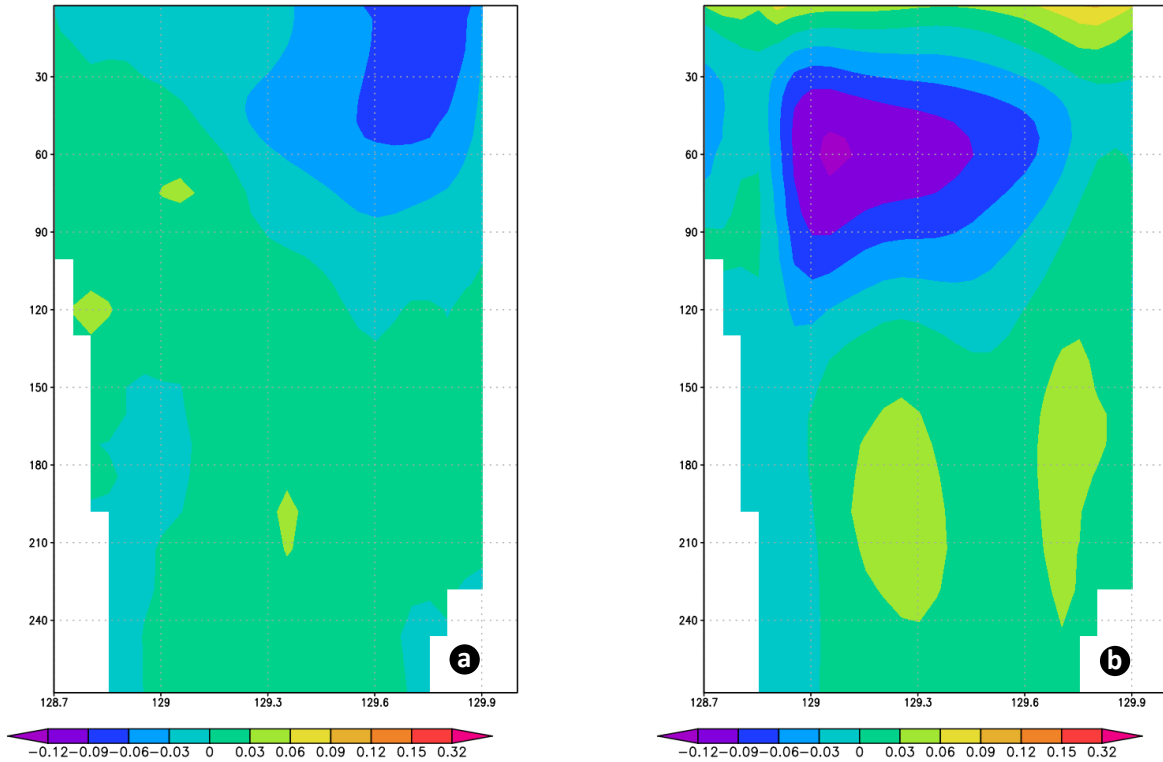


Figure 5.10: The vertical profile of average velocities (m/s) along the section of 0.5 °N and from 128.5 °E to 130°E for zonal (a) and meridional (b) flow directions during the southeast monsoon (July), derived from the HAMSOM simulation between 1990 and 2014.

5.3 Tidal Motions and Momentum Balance around the Northern Arafura Sea

Applying 11 tidal constituents, the horizontal distribution of surface currents in the barotropic mode at its maximum ebb and maximum flood are shown in Figure 5.11. The results show that, at the maximum flood (Figure 5.11a), relatively strong currents (reaching a maximum of 1.5 m/s) flow eastward from the Aru Basin to the Northern Sahul Shelf through the Aru Channel between the Northern Aru Islands and Papua (to the north) and the Southern Aru Islands (to the south). In contrast, at the maximum ebb (Figure 5.11b), relatively strong currents flow from around the western coast of Papua to the Aru Basin. Some of these water masses are directed to the northwest, passing along the western coast of Aru and across the Aru Channel before entering the Northern Aru Basin. The other currents flow westward, passing the western and southern coasts of Aru before entering the Southern Aru Basin. It is also found that the tidal currents across the continental slope of section A ($4.8^{\circ}\text{S}/134.6^{\circ}\text{E}$; Figure 5.13a) are stronger than those across the continental slope of section B ($7.35^{\circ}\text{S}/133.1^{\circ}\text{E}$; Figure 5.13c). The tidal surface currents across the continental slope of section A range from -1.2 m/s to 0.6 m/s, while across the continental slope of section B they are between -0.6 m/s and 0.3 m/s (Figures 5.13a and 5.13c). These results are generally similar to those of the baroclinic mode (Figures 5.11, 5.12 and 5.13).

However, it is also observed that stratification contributes to the modification of the intensity and duration of ebb and flood currents. In general, it is found that stratification reduces the tidal currents, as indicated by the peak-to-peak amplitude of tidal currents in the TOBC case being lower than in the TOBT case. It is found that, at some points, the peak-to-peak amplitude values differ between 0.1 m/s and 0.3 m/s between the TOBT and TOBC cases (Figures 5.13).

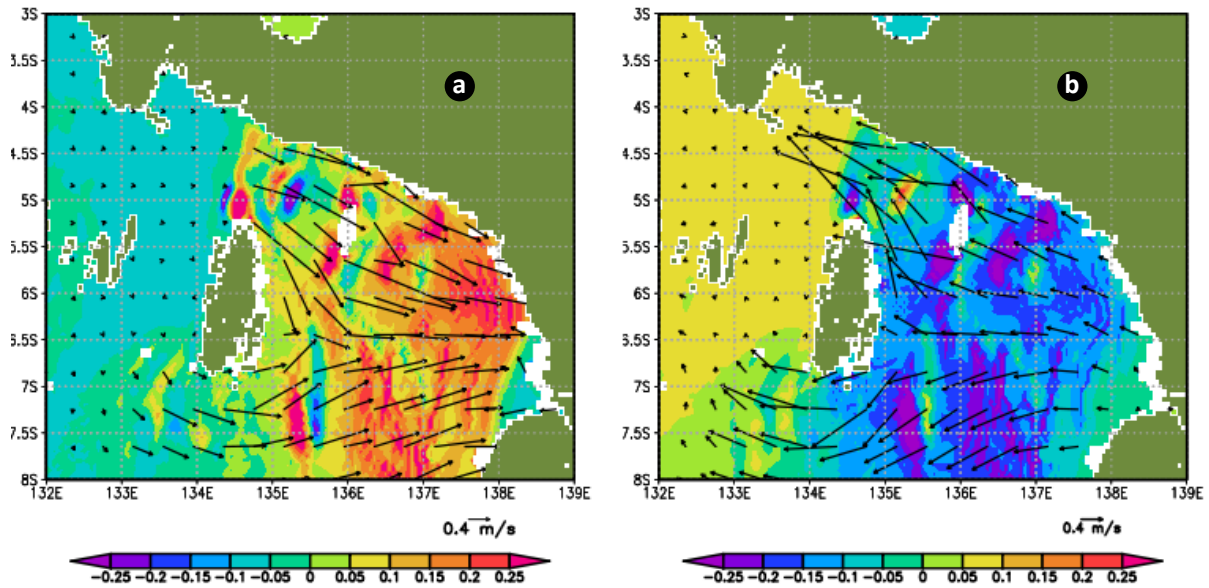


Figure 5.11: Tidal surface currents and w-velocity ($\times 10^{-3} \text{m/s}$) (the background) for barotropic mode (TOBT) around the Northern Arafura Sea at a) maximum flood and b) maximum ebb.

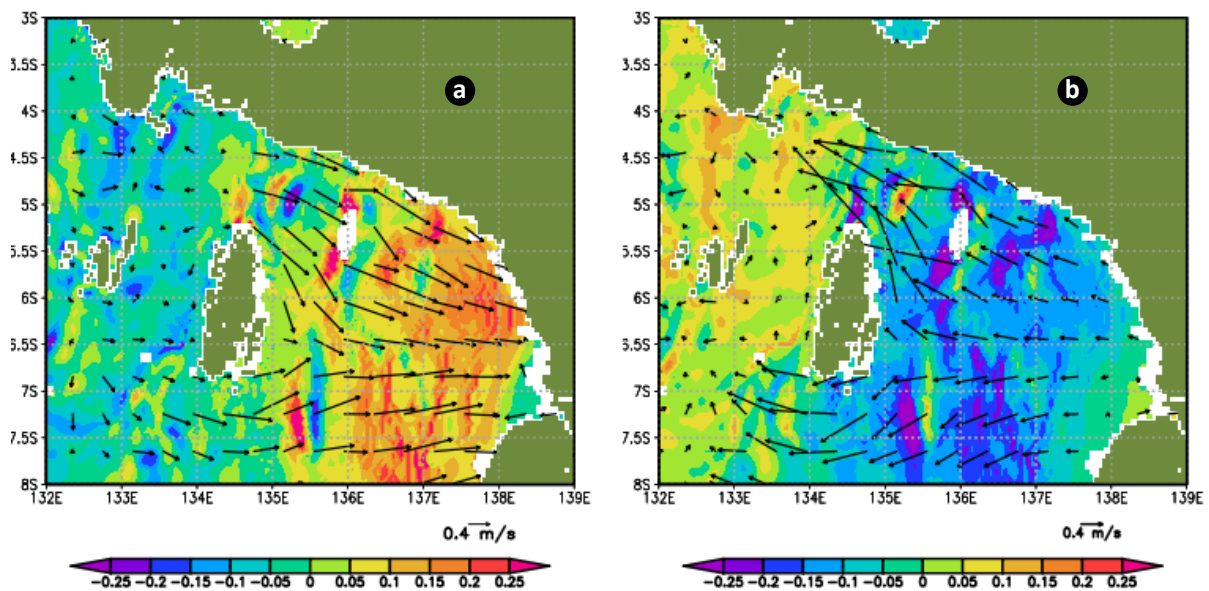


Figure 5.12: Tidal surface currents and w-velocity ($\times 10^{-3} \text{m/s}$) (the background) for baroclinic mode (TOBC) around the Northern Aru Arafura Sea at a) maximum flood and b) maximum ebb.

The results of the simulation also show that stratification contributes considerably to the modification of the magnitude and duration of ebb and flood currents, thereby resulting in modified residual currents. In the barotropic mode, the magnitude and duration of ebb currents (indicated by negative values) going zonally across the continental slope of section A ($4.8^{\circ}\text{S}/134.6^{\circ}\text{E}$) are significantly stronger and slightly longer-lasting than those of flood currents (indicated by positive values). Meanwhile, in the baroclinic mode, the magnitude and

duration of ebb currents are generally weaker and much shorter than those of flood currents (Figures 5.13a and 5.13b). In both modes, the duration of ebb currents going zonally across the continental slope of section B (7.5° S/ 133° E) is shorter than that of flood currents (Figures 5.13c and 5.13d). However, in the barotropic mode these ebb currents are significantly stronger than the flood currents; conversely, in the baroclinic mode they are significantly weaker. By averaging over 28 days, it is observed that the residual zonal currents in the upper layer crossing the continental slope of section A and B in the barotropic mode flow in the opposite direction of the residual zonal currents in the baroclinic mode, as discussed in Appendix A (see also Figures A.2a and A.2d). These patterns can also be identified through a comparison of the Coriolis term in the meridional direction, as shown in Figures A.5 and A.7 (for section A) and in Figures A.11 and A.13 (for section B). Furthermore, it is noted that the zonal residual surface currents across the continental slope of section A are generally greater than those around the continental slope of section B (Figures A.2a and A.3a).

Across the continental shelf of section C (6° S/ 137° E), the tidal currents are relatively strong, comparable to those across the continental slope of section A (Figures 5.13e and 5.13f). However, the difference in currents' magnitude and duration between ebb and flood periods along section C is less significant in both modes than those across section A. This indicates that bottom topography plays an important role in generating asymmetric patterns of tidal currents; the bottom topography of section A is relatively more complex than that of section C. The complexity of section A's bottom topography is indicated by the presence of steep slopes, a bump, and a headland (Figure 2.2).

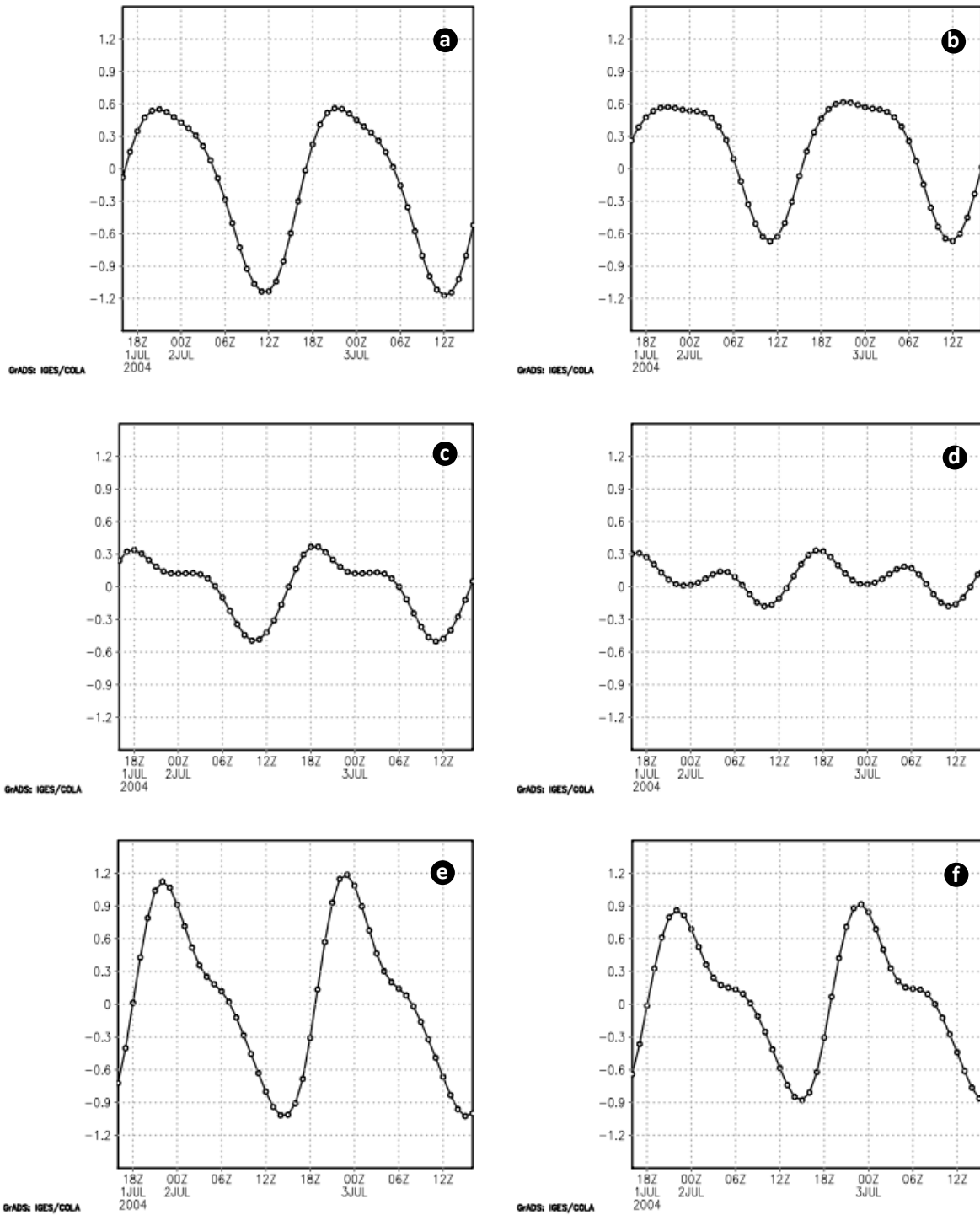


Figure 5.13: Zonal tidal currents (m/s) in the upper layer ($z=2$) at points: a) $4.8^{\circ}\text{S}/134.6^{\circ}\text{E}$ (section A), c) $7.35^{\circ}\text{S}/133.1^{\circ}\text{E}$ (section B), e) $6^{\circ}\text{S}/137^{\circ}\text{E}$ (section C) for the barotropic mode; b) $4.8^{\circ}\text{S}/134.6^{\circ}\text{E}$ (Section A), d) $7.35^{\circ}\text{S}/133.1^{\circ}\text{E}$ (section B), f) $6^{\circ}\text{S}/137^{\circ}\text{E}$ (section C) for the baroclinic mode

For TOBT case, the momentum balance at the surface layer of the Northern Arafura Sea is characterized by inertial-gravity wave equilibrium in which the local acceleration term (ACC) is balanced principally by the pressure gradient term (PGF) in the zonal direction and by the sum of the PGF and Coriolis (COR) terms in the meridional direction, as shown at selected points (Figure 5.14). The findings also show that, except for the COR term, the magnitude of each momentum component in the meridional direction is generally less than that in the zonal direction. Furthermore, it is observed that the nonlinear advection term (ADV) contributes more significantly to the modification of the inertial-gravity wave over the continental slope of section A compared to that over the continental slopes of section B and section C. Near the bottom, the vertical friction term is relatively larger than near the surface (Figure 5.15). It generally reaches a maximum/minimum when the tidal currents are at their minimum/maximum (Figures 5.13 and 5.15). The maximum/minimum tide also occurs when the local acceleration is zero (Figure 5.15). Vertical friction at the water surface over section C is also relatively high, a condition related to the relatively shallow depth of this region.

This study suggests that the relatively high ADV term over the continental slope of section A is related to the nonlinear interaction of the relatively stronger eastward tidal currents (see also Figure 5.20) flowing perpendicular to the steep continental slope connecting Papua Island (to the north) and the Northern Aru headland (to the south); see also Figure 2.2. The high ADV term is also induced by the presence of a bump near the shelf break (see also Figure 2.2). Furthermore, it is suggested that the high ADV is induced by nonlinear interaction between tidal currents and Northern Aru headland. Here, it is found that the ADV term is relatively higher than vertical friction term (VVI), indicating the separation flow which is identified mostly during the maximum ebb and flood periods (Figures 5.11, 5.16, 5.17, 5.18, and 5.19). In contrast, the separation flow does not occur in the Southern Aru Islands headland, as indicated by the advection term being relatively lower than the friction term. It is suggested that the relatively high friction term is due to relatively shallow depth of the Southern Aru Islands headland. These patterns are generally also observed in the baroclinic mode (figures not shown). These results confirm Signell and Geyer's (1991) findings that separation flow will occur around a headland if the ADV term is larger than the VVI or ACC term, leading to the PGF term being balanced by the ADV term rather than by the VVI or ACC term; otherwise (if VVI or ACC term > ADV term), the separation flow will not occur. In addition, it is observed that the ADV term has the same direction during the ebb and flood periods. By averaging over 28 days, it can therefore be seen

that the ADV term contributes significantly to the average momentum equation, as discussed in Appendix A (Figures A.4 and A.5). This study suggests that these nonlinear interactions are the main cause of the asymmetric pattern of tidal currents over the Northern Aru Headland over one tidal cycle. This situation, as will be discussed in Appendix A in depth, subsequently induces residual currents directed away from the headland (for horizontal distribution) and circulation cells along the slope (for vertical distribution).

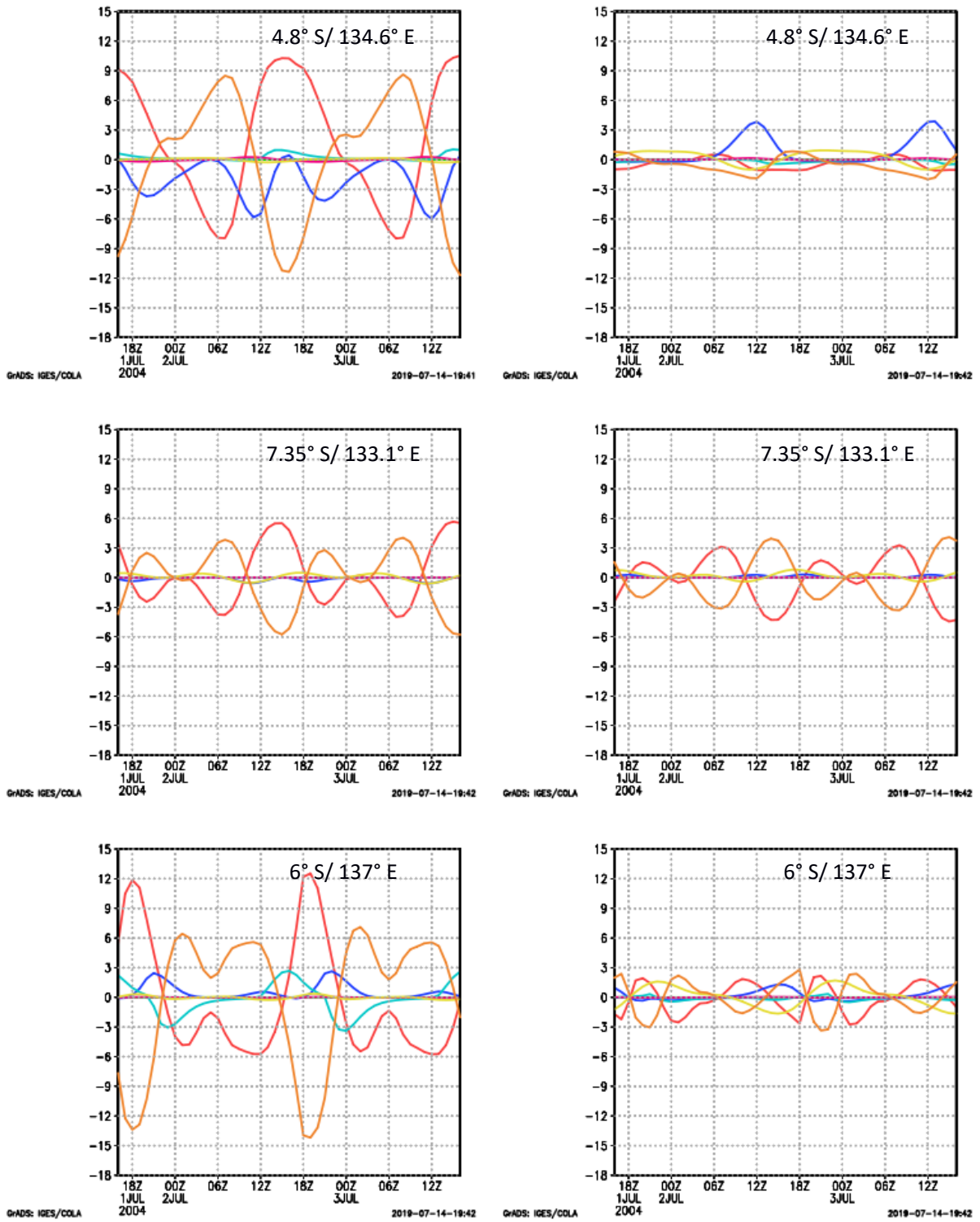


Figure 5.14: Momentum components in zonal(left) and meridional(right) directions at selected points during maximum flood at $z = 2$ for barotropic mode ($\times 10^{-3} \text{ ms}^{-2}$). Legend: Barotropic-PGF (Red), baroclinic-PGF (Green), ADV (Blue), VVI (light blue), COR (yellow), ACC (Orange).

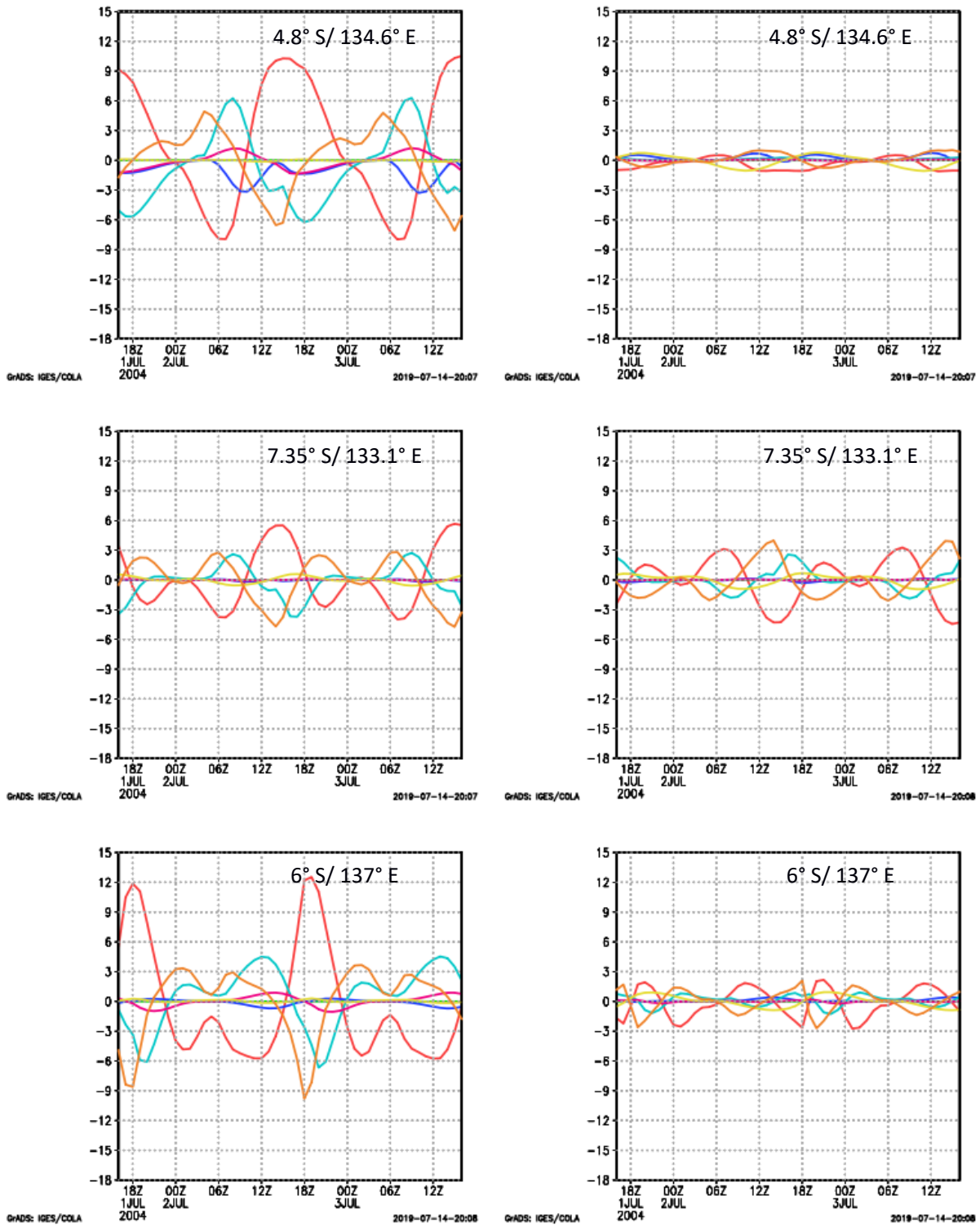


Figure 5.15: Momentum components in zonal(left) and meridional(right) directions at selected points during maximum flood at near bottom for barotropic mode ($\times 10^{-3} \text{ ms}^{-2}$). Legend: Barotropic-PGF (Red), baroclinic-PGF (Green), ADV (Blue), VVI (light blue), COR (yellow), ACC (Orange).

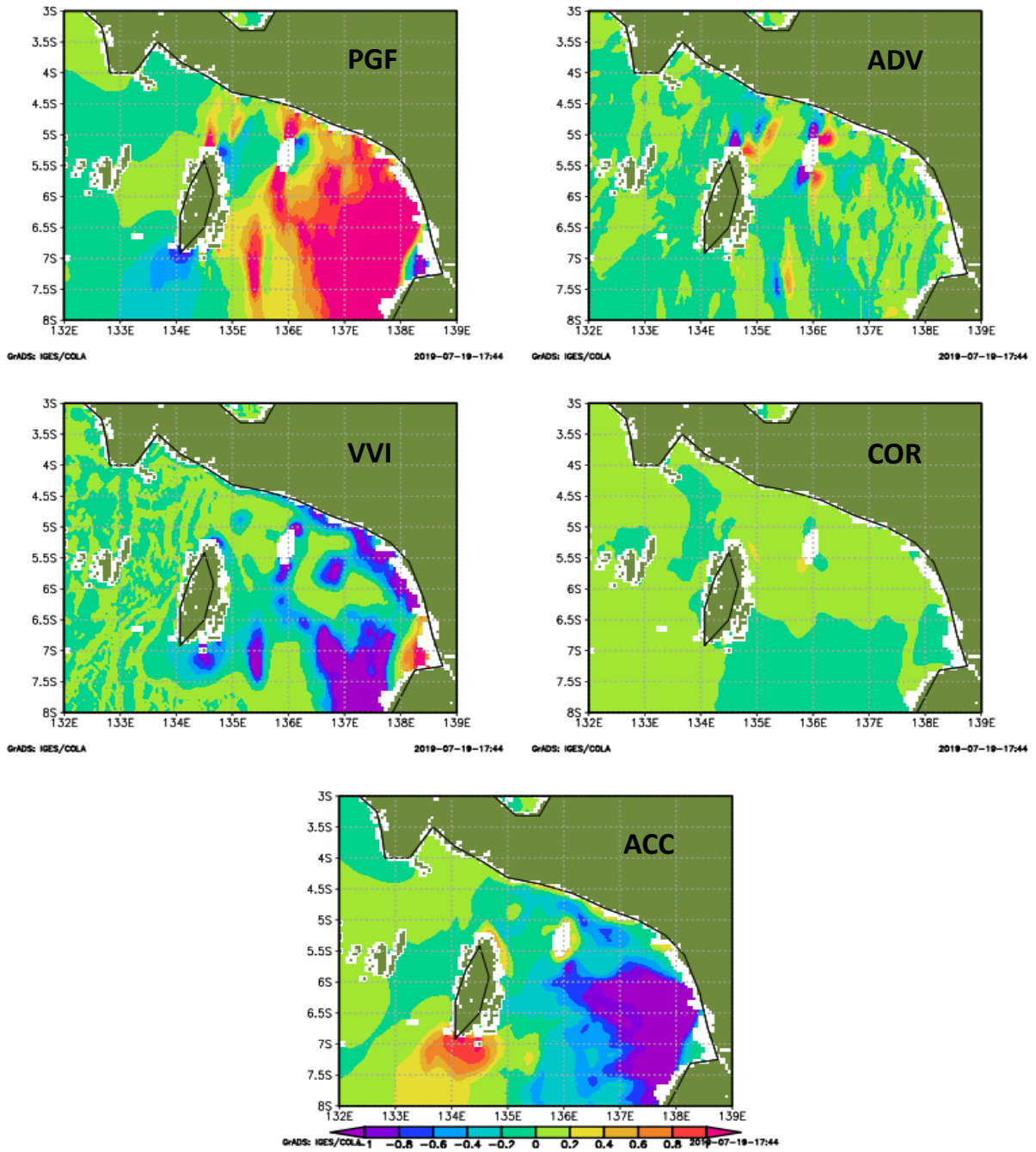


Figure 5.16: Momentum components around the Northern Arafura Sea in the zonal direction at maximum flood at $z = 2$ for the barotropic mode ($\times 10^{-2} \text{ ms}^{-2}$).

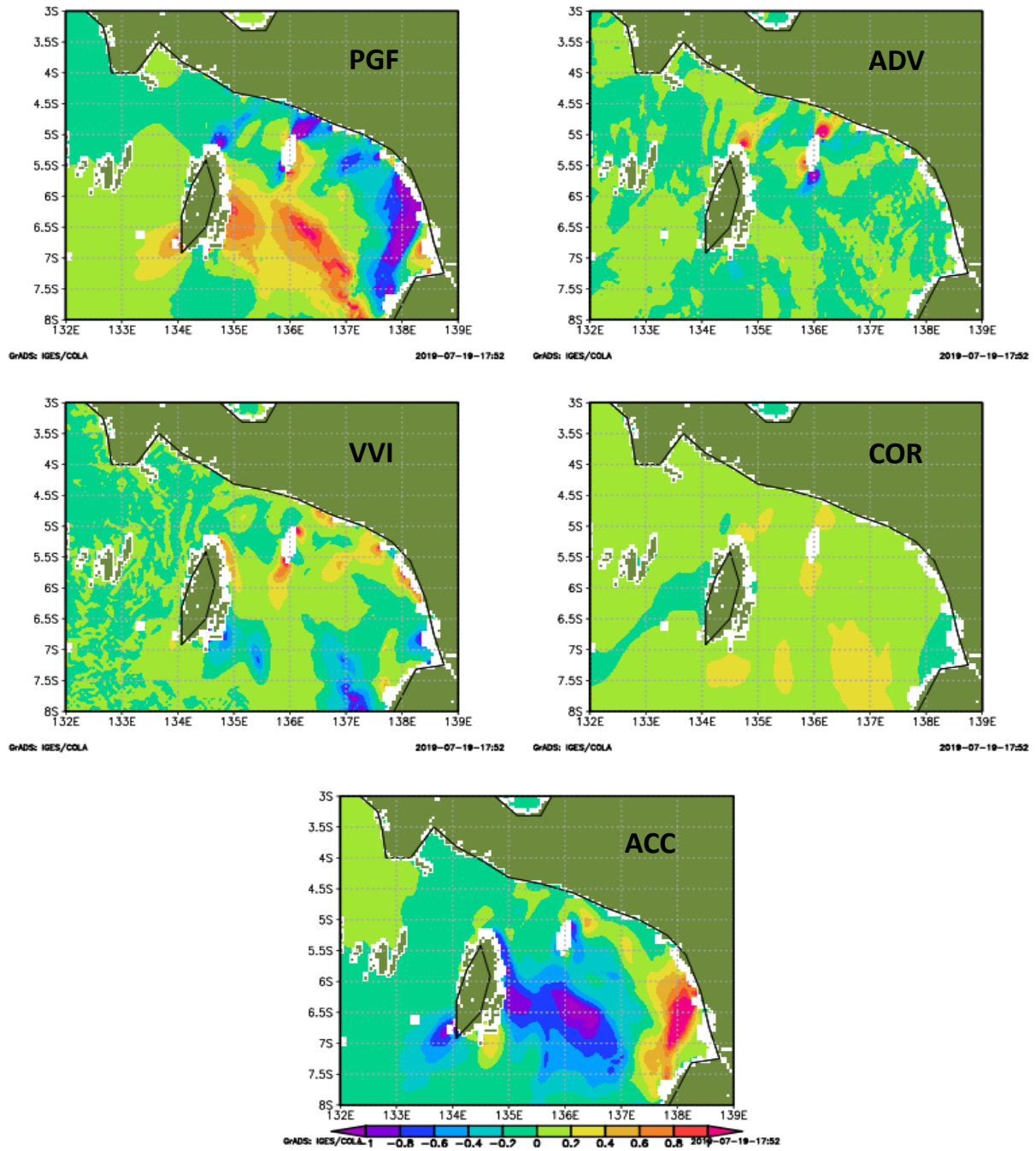


Figure 5.17: Momentum components around the Northern Arafura Sea in the meridional direction at maximum flood at $z = 2$ for the barotropic mode ($\times 10^{-2} \text{ ms}^{-2}$).

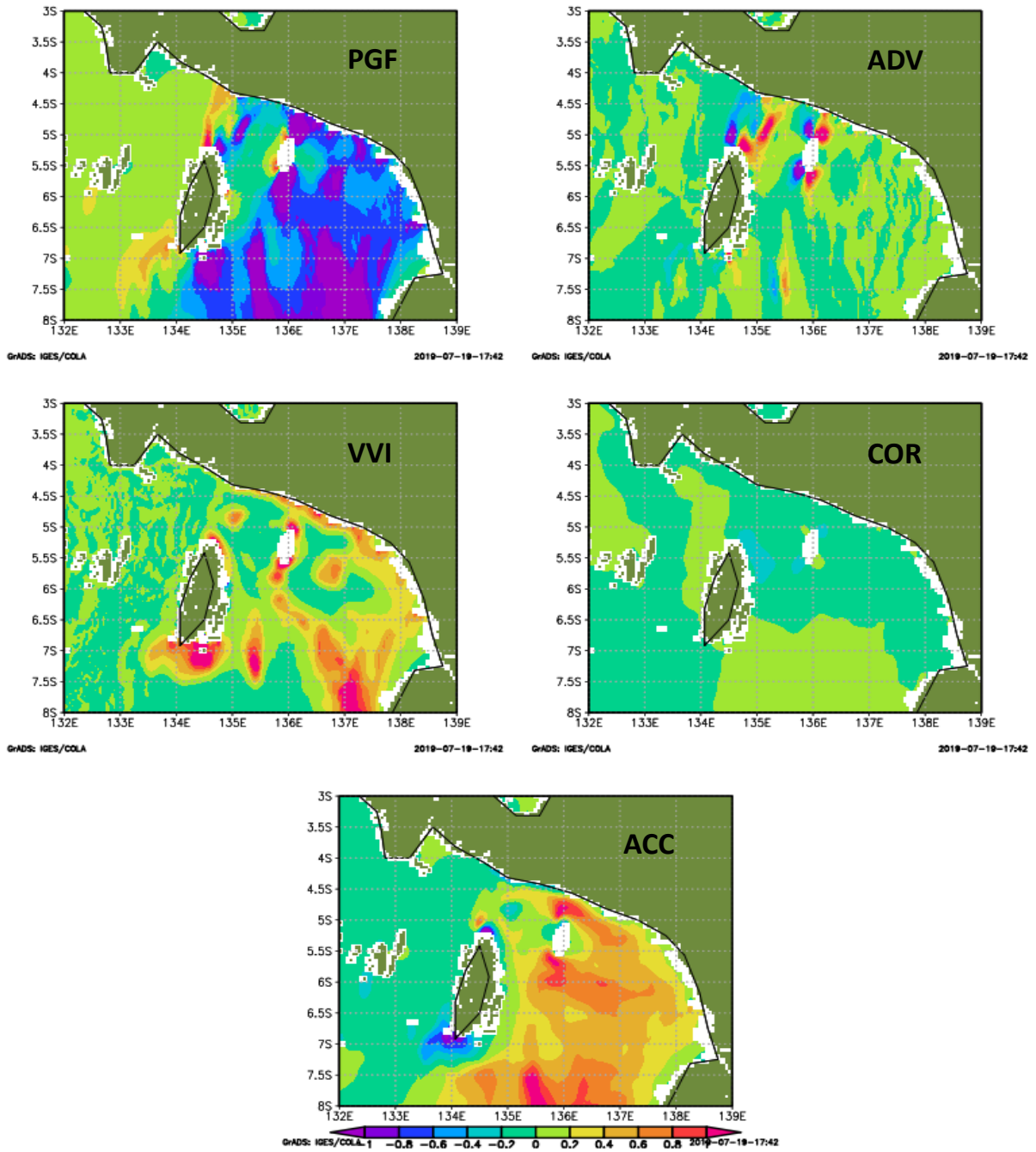


Figure 5.18: Momentum components around the Northern Arafura Sea in the zonal direction at maximum ebb at $z = 2$ for the barotropic mode ($\times 10^{-2} \text{ ms}^{-2}$).

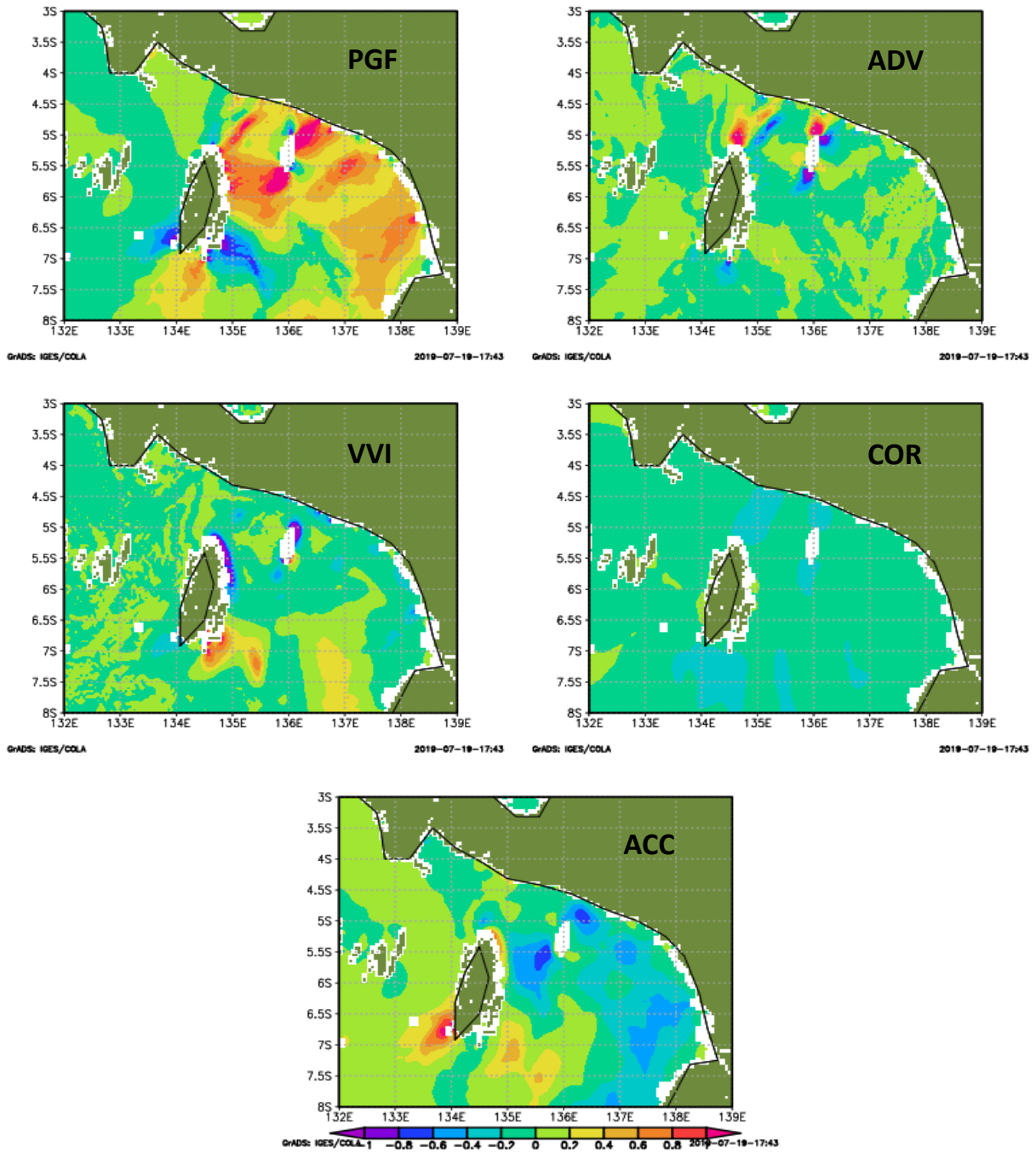


Figure 5.19: Momentum components around the Northern Arafura Sea in the meridional direction at maximum ebb at $z = 2$ for barotropic mode ($\times 10^{-2} \text{ ms}^{-2}$).

It is additionally observed that, as consequence of the climbing effect (flowing from deep to shallow water, the zonal tidal flow is rectified by the topography and forced up), relatively strong upwelling occurs around Northern (section A) and Southern (section B) Aru Islands in the TOBT and TOBC cases, where the relatively steep slope is located, during the flood period (Figures 5.20 and 5.21). In contrast, relatively strong downwelling is generated along the slopes during the ebb period. It is also found that the downwelling and upwelling centers in the TOBT are mostly concentrated on the continental slope of section A while relatively strong upwelling and downwelling (a ripple-like pattern) are also observed in the interior along section A in TOBC case. The results suggests that the ripple-like pattern along section A is not only influenced by the nonlinear interaction of the barotropic tide and bottom topography, but also by internal tide propagation that is caused mostly by the nonlinear interaction of the barotropic tide and sill around the Halmahera and Seram Seas (see also section 5.6). Due to the nonlinear interaction of tidal currents and bottom topography, an asymmetric pattern of tidal currents is generated over one tidal cycle around the slopes of sections A and B and forms circulation cells (Figures 5.25a and 5.26a). These circulation cells may contribute to the enhancement of upwelling intensity during wind-driven upwelling, as discussed in sections 5.4.3 and 5.4.4. It is also observed that the circulation cells around section A are significantly stronger than those in section B (Figures A.2a and A.3a). This study suggests that the relatively stronger circulation cells in section A can be attributed to relatively higher tidal currents and more complex bathymetric conditions.

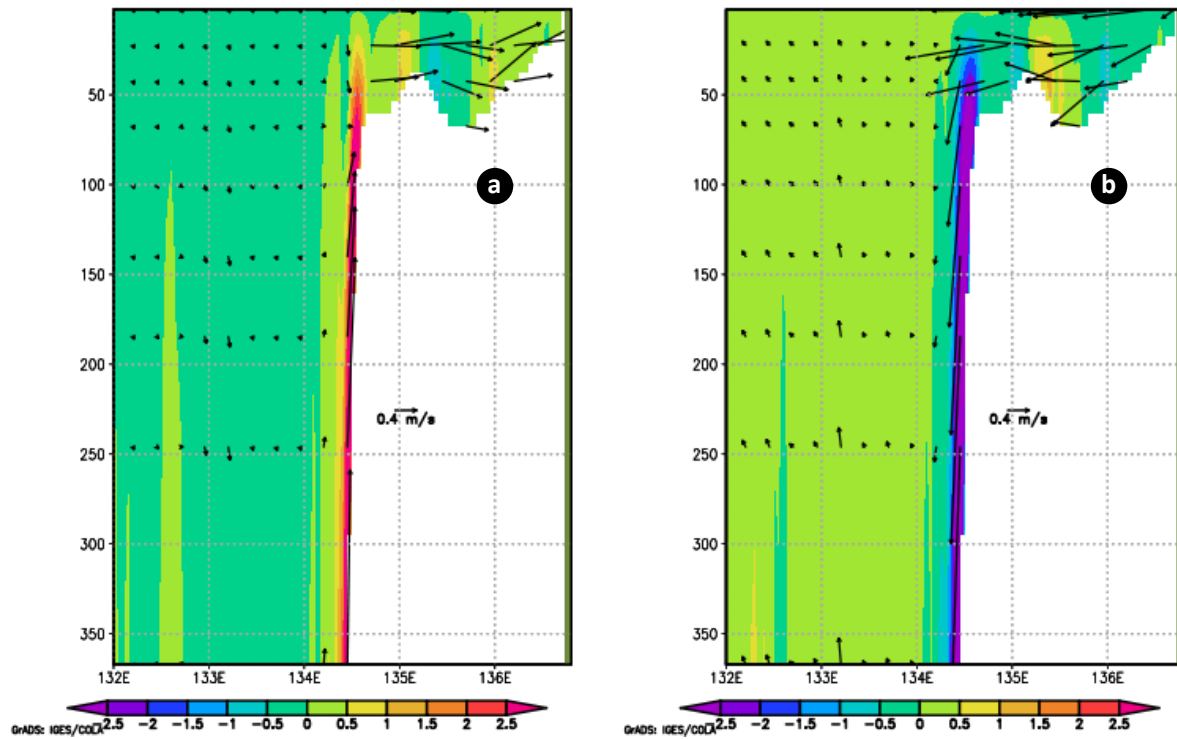


Figure 5.20: Vertical profile of u-w velocity, where u-velocity is in m/s and w-velocity is in $\times 10^{-3}$ (m/s). The background represents w-velocity ($\times 10^{-3}$ m/s) for barotropic mode (TOBT) around the Northern Aru Island (section A) at a) maximum flood and b) maximum ebb.

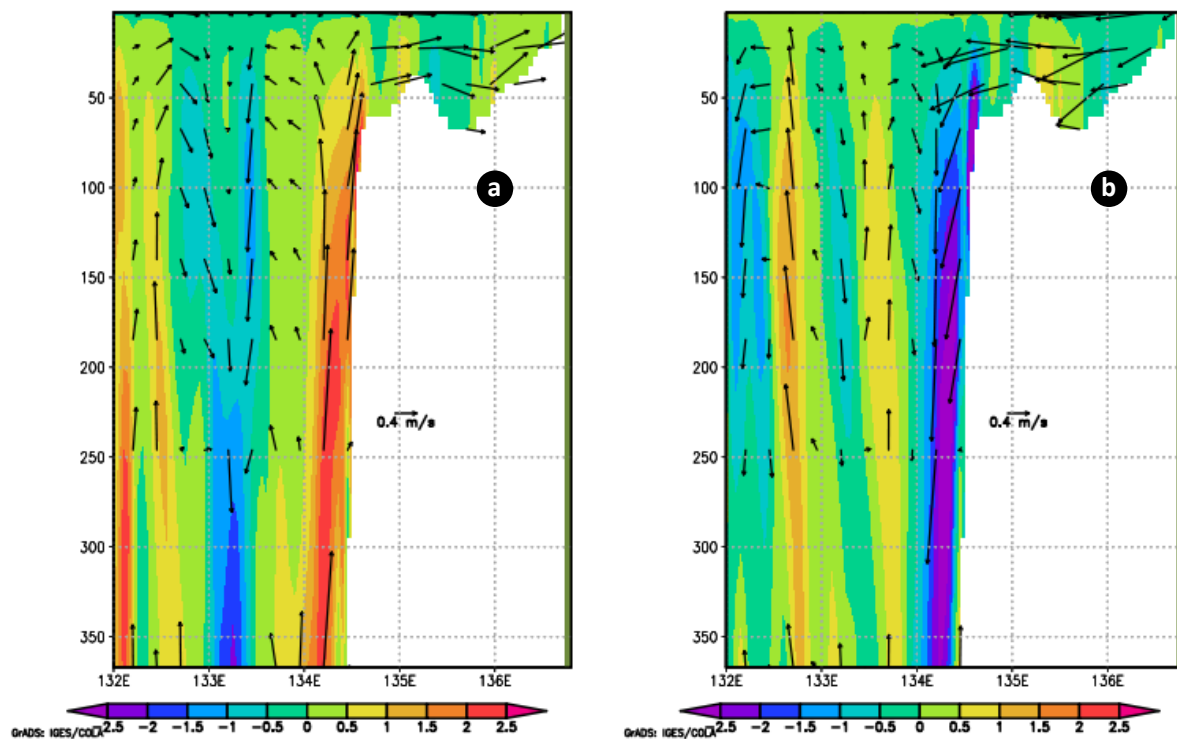


Figure 5.21: Vertical profile of u-w velocity, where u-velocity is in m/s and w-velocity is in $\times 10^{-3}$ (m/s). The background represents the w-velocity ($\times 10^{-3}$ m/s) for the baroclinic mode (TOBC) around the Northern Aru Island (section A) at a) maximum flood and b) maximum ebb.

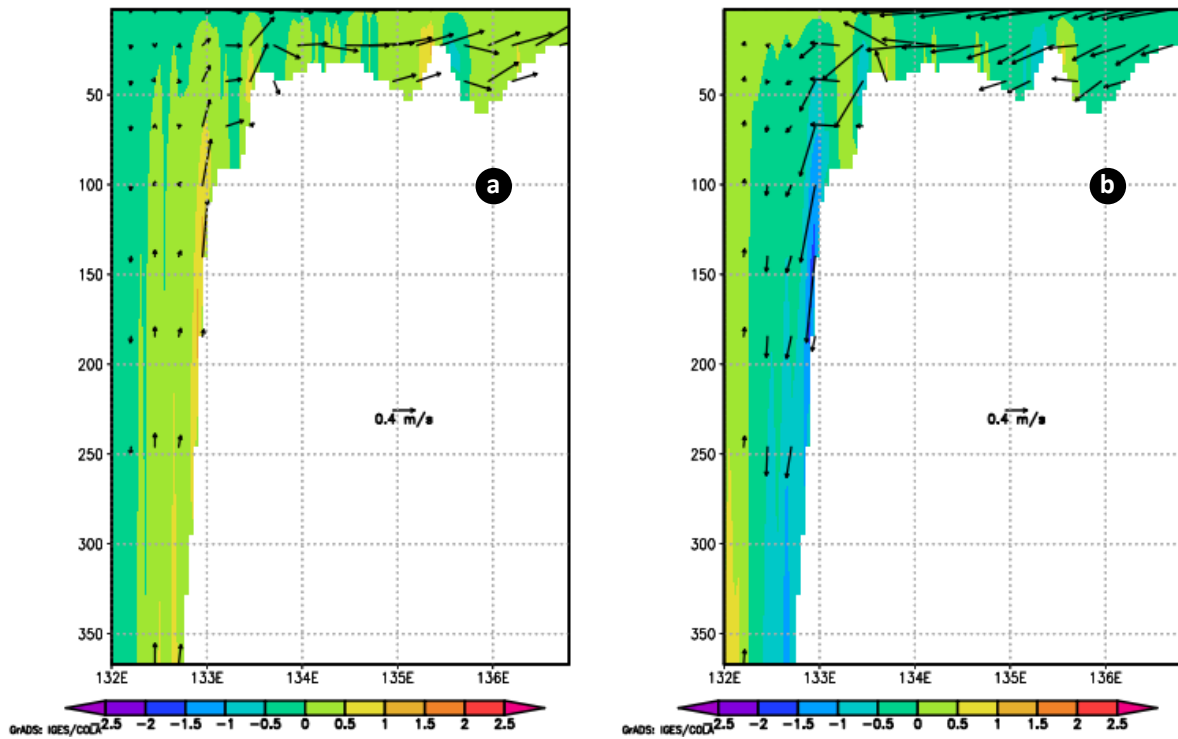


Figure 5.22: Vertical profile of u-w velocity, where u-velocity is in m/s and w-velocity is in $\times 10^{-3}$ (m/s). The background represents the w-velocity ($\times 10^{-3}$ m/s) for the barotropic mode (TOBT) around the Southern Aru Island (section B) at a) maximum flood and b) maximum ebb.

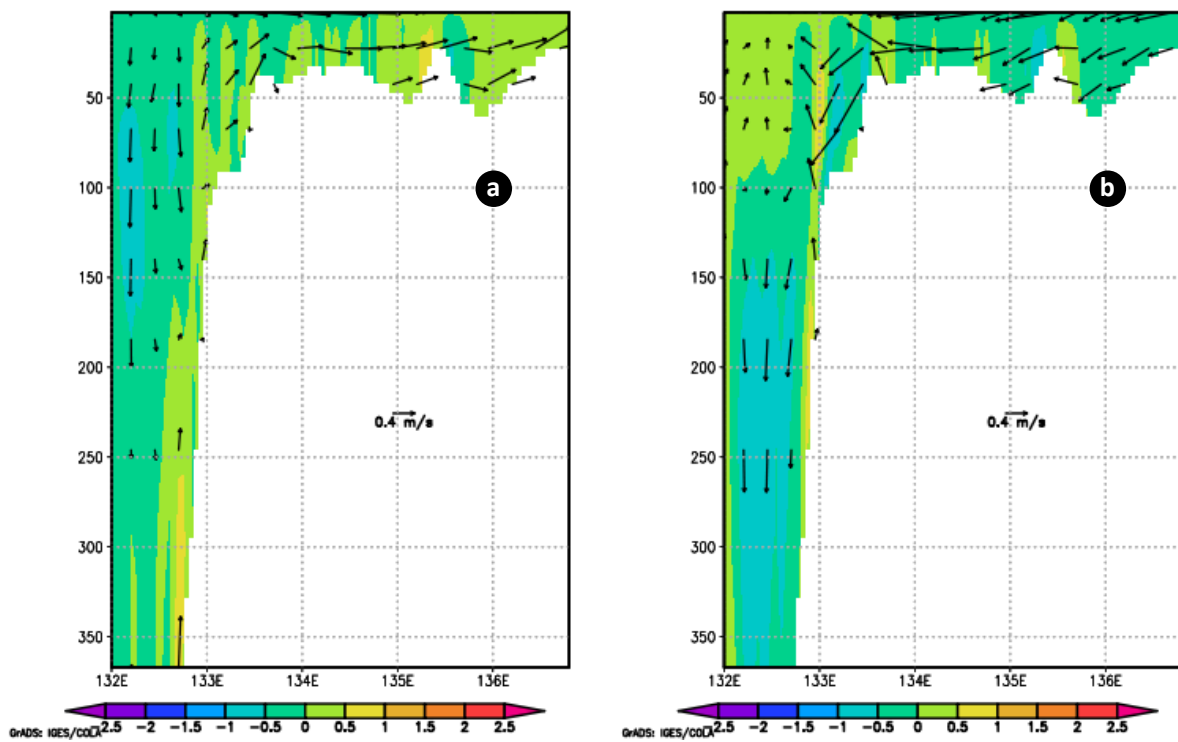


Figure 5.23: Vertical profile of u-w velocity, where u-velocity is in m/s and w-velocity is in $\times 10^{-3}$ (m/s). The background represents the w-velocity ($\times 10^{-3}$ m/s) for the baroclinic mode (TOBC) around the Southern Aru Island (section B) at a) maximum flood and b) maximum ebb.

5.4 Comparisons of Experimental Results during the South East Monsoon

In this section, the influences of tidal forcing and river runoff on the hydrodynamic conditions during the upwelling period are discussed by comparing four experiments, i.e. WRT, WO, WR and WT (see table I). The discussion will also focus more on three areas represented by three sections named A, B and C (Figures 1, 2.1, 3.5, 5.5 and 5.6), which shows pronounced upwelling during the period of July, 2004. The sections A and B are located in the Northern and Southern parts of the Aru Basin, which have relatively lower temperatures compared to their surrounding areas during the upwelling season. The section C represents the shallow shelf located between the Aru Basin and the Papua Islands, connecting the Northern and Southern parts of the Aru Basin.

5.4.1 Sea Surface Properties

At the surface, the horizontal distribution of currents, temperature and salinity around the Aru Basin derived from the experiments of WRT, WO, WR and WT (see table I) shows some similar patterns (Figure 5.24 and 5.25). Strong westward and northward surface currents are respectively observed in the Banda and Sulawesi Seas in all the experiments. The results also indicate that relatively warmer temperature and lower salinity is observed in the South Western Pacific Ocean compared to the other areas. When it comes to the surrounding areas of the Aru Basin, the results show that surface waters around sections A and B flow westward bringing new water masses into the Banda Sea. Furthermore, compared to the surrounding, a lower SST is generally observed around regions A and B during the southeast monsoon. On one hand, in section A, the lower SST is followed by a higher SSS. On the other hand, the low SST around section B seems not to be followed by a higher SSS, indicating the influence of river runoff to refresh the surface water. Furthermore, the relatively low salinity indicating the influence of river runoff is observed in all the experiments around the Southwestern Papua Coast.

However, some discrepancies are also observed. In the WRT case, it is observed that some surface currents flow from Seram Sea toward Western Ocean Sea through Halmahera Sea (Figure 5.24a). In contrast, the excluded river discharge and/or tide lead surface water coming from the South Western Pacific Ocean to enter into the Halmahera Sea and then to flow from the Seram Sea to the Banda Sea through the strait located between the Seram

and Papua Islands. Furthermore, the results obtained from the area around the Aru Basin show that the westward currents in region A in the WO case are smaller than in the other experiments, while the westward currents in region A in the WRT case are higher than those in the other experiments, which can be observed by comparing the current vectors among the figures of the experiment results (Figure 5. 24). By averaging the u-velocity in the region of $4.5 - 5^{\circ} \text{ S} / 132 - 135^{\circ} \text{ E}$, it is estimated that through the exclusion of tidal forcing, river runoff, or tidal forcing and river runoff from the simulation, the currents tend to weaken by about 0.068 (32%), 0.041 (20%) and 0.087 (40%) m/s respectively. In region B, the results show that the westward surface currents in the WO case are less than those in the WRT and WR cases, but higher than those in the WT case. By averaging the u-velocity in the region of $7.35 - 8^{\circ} \text{ S} / 133 - 136^{\circ} \text{ E}$, it is estimated that the excluded tidal forcing (the WR case) leads to a slight enhancement of the surface currents by about 0.01 m/s (4%) while the excluded river runoff (the WT case) tend to weaken by about 0.02 m/s (7.5%), compared to the WRT case. Furthermore, the excluded river runoff and tidal forcing in the region B lead to a slight increase of about 0.005 m/s (2%) in the surface currents. In the region C, the results indicate that the magnitude of the surface circulation in the tide simulations (WRT and WT cases) is less than the magnitude of the surface currents in the WO and WR cases. By averaging the magnitude of surface u-velocity in the region of $5.5 - 7^{\circ} \text{ S} / 135 - 138^{\circ} \text{ E}$, the average currents in the tide inclusion simulations is about 0.18 m/s while it is about 0.43 m/s in the tide exclusion simulations. This condition is the main factor responsible for a smaller SSS and higher SST in the tide inclusion simulations than the ones in the tide exclusion simulations.

Furthermore, the results show that the SST around regions A and B in the WRT case is lower than the one in the other experiments. This is indicated by relatively larger area with a cold tongue, i.e. the temperature of less than 25° C around those regions (Figure 5.24). In contrast, in the sections A and B, the SST in the WO case is higher than the others (see also in section 5.4.3). It is also observed that the SST in the WO case is higher than it is in the WR case, which indicates the role of river runoff for the upwelling of more subsurface water masses as also discussed in depth in sections 5.4.3 and 6.2. The influence of river runoff in cooling the SST around the region A and B can be also detected by comparing the cases of the WRT and WT. In region C, the SST in the WRT case is higher than the SST in the other experiments while the lowest SST of all is found in the WR case. In addition to the relatively lower residual currents, the relatively warmer SST in the tide exclusion simulation in the region C is mainly caused

by the less subsurface water transported from the region A into the region C as discussed in section 5.4.3. In terms of salinity, the results show that the SSS around regions A, B, and C in the WRT case is lower than the one in the other experiments. In contrast, the SSS in regions A, B and C in the WO case is higher than the SSS in the other experiments. The results also indicate that the SSS in these regions in the WT case is larger than it is in the WRT case. It is also shown in section 5.4.3 that the SSS in the regions A, B and C is not only influenced by the river runoff but also by the subsurface water masses in the Aru Basin.

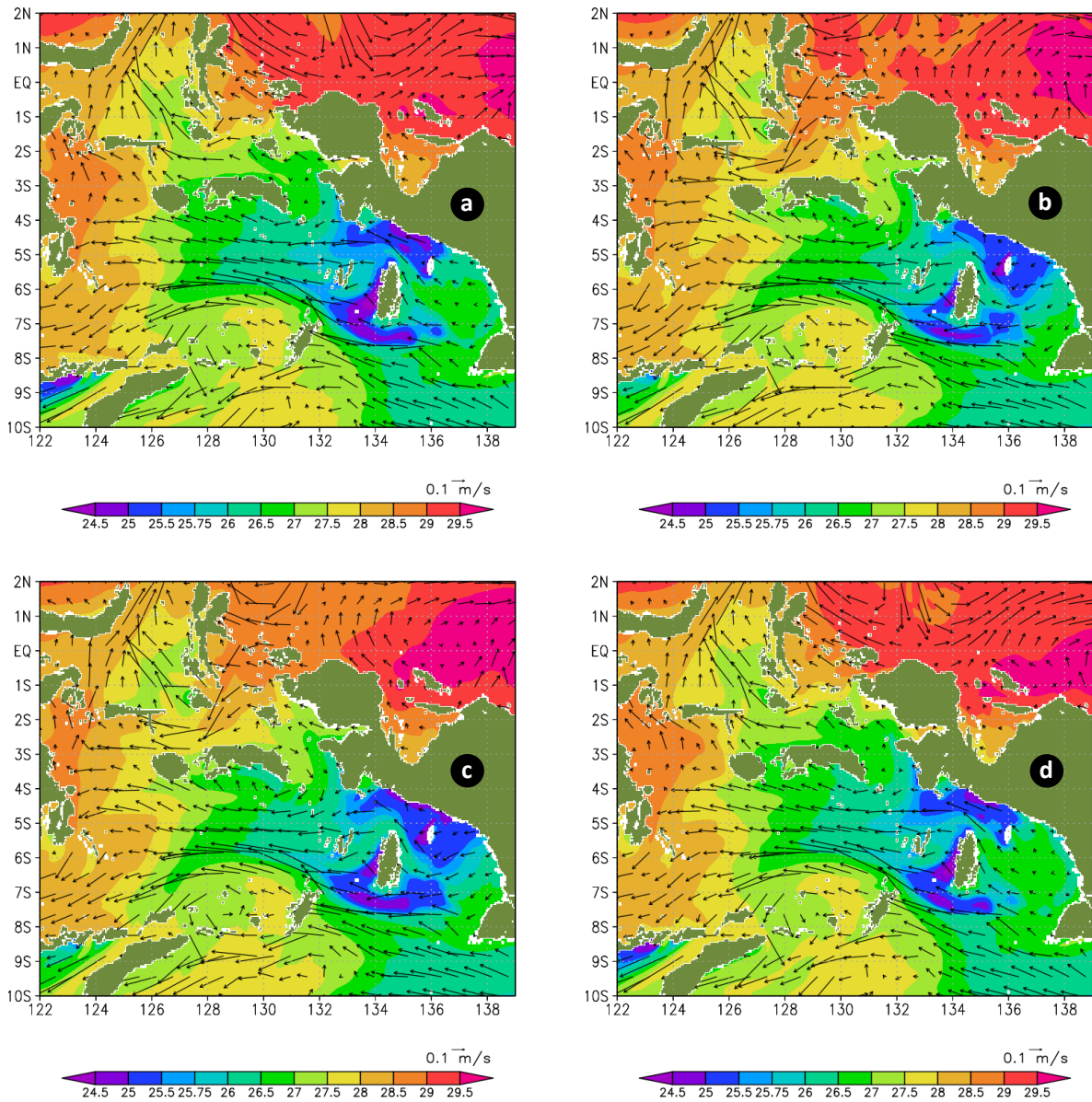


Figure 5.24: Surface currents and the SST ($^{\circ}\text{C}$) (the background) in the period of July 2004 for the cases of: a) the WRT; b) the WO; c) the WR; d) the WT.

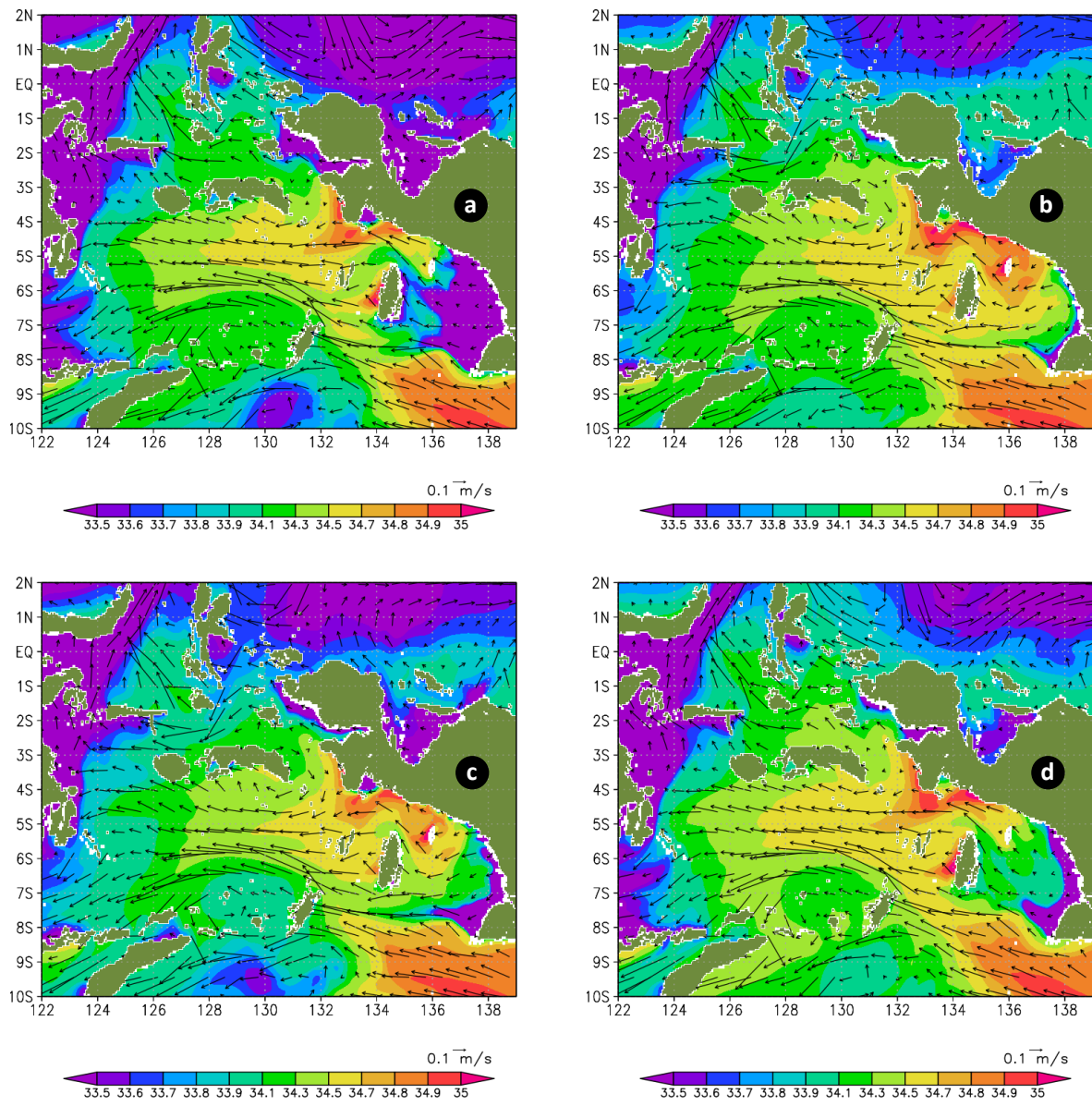


Figure 5.25: Surface currents and the SSS (the background) in the period of July 2004 for the cases of: a) the WRT; b) the WO; c) the WR; d) the WT.

5.4.2 Subsurface Properties

In the subsurface, the profiles are plotted at 130 m depth, representing the thermocline layer during the southeast monsoon (July 2004) where the relatively high salinity is generally located (Figures 5.26 and 5.27). The simulation indicates that the relatively strong currents flow from the Western Pacific Ocean to the Aru Basin through the Halmahera and Seram Seas. The currents generally bring relatively warmer and higher salinity than that in the Western Indonesian Seas. In the Halmahera Sea, the magnitude of currents in the tide inclusion simulation is generally smaller than in the tide exclusion simulation. In contrast, higher currents in the tide inclusion simulation are observed in the Seram Sea and the Aru Basin compared to those in the tide exclusion simulation.

The simulation results also show that higher salinity and warmer temperature in the thermocline layer is observed in the eastern research area compared to the western area (Figures 5.26 and 5.27). In the eastern area, the salinity is eroded toward the south, following the circulation direction. Furthermore, the tide inclusion simulation generally decreases the salinity by about 0.1 - 0.5 in the thermocline layer of the Indonesian Seas. However, the salinity in the WT case is observed to be higher in the Northern Aru Basin than in the WO case. It is suggested that the relatively higher salinity originates from the Halmahera Sea via the Seram Sea from the previous periods between May and June (not shown in the figure) transported by stronger currents in the WT case than that in the WO case. The river runoff (the WR case) also contributes to refreshing the salinity at this subsurface layer but not as much as in the tide inclusion simulation (the WT case). However, it is found that the influence of river runoff in this layer of the Eastern Indonesian Seas is more obvious when the tide and rivers (the WRT case) are applied together in the simulation (see also in section 4.4). In addition, the results show that more fresh water from the Molucca and Banda Seas enter into the Seram Sea in the tide inclusion simulation in this period (July 2004) than in the tide exclusion simulation. As consequence of this, a smaller salinity is observed in the Eastern Seram Sea compared to the Halmahera Sea and the Aru Basin.

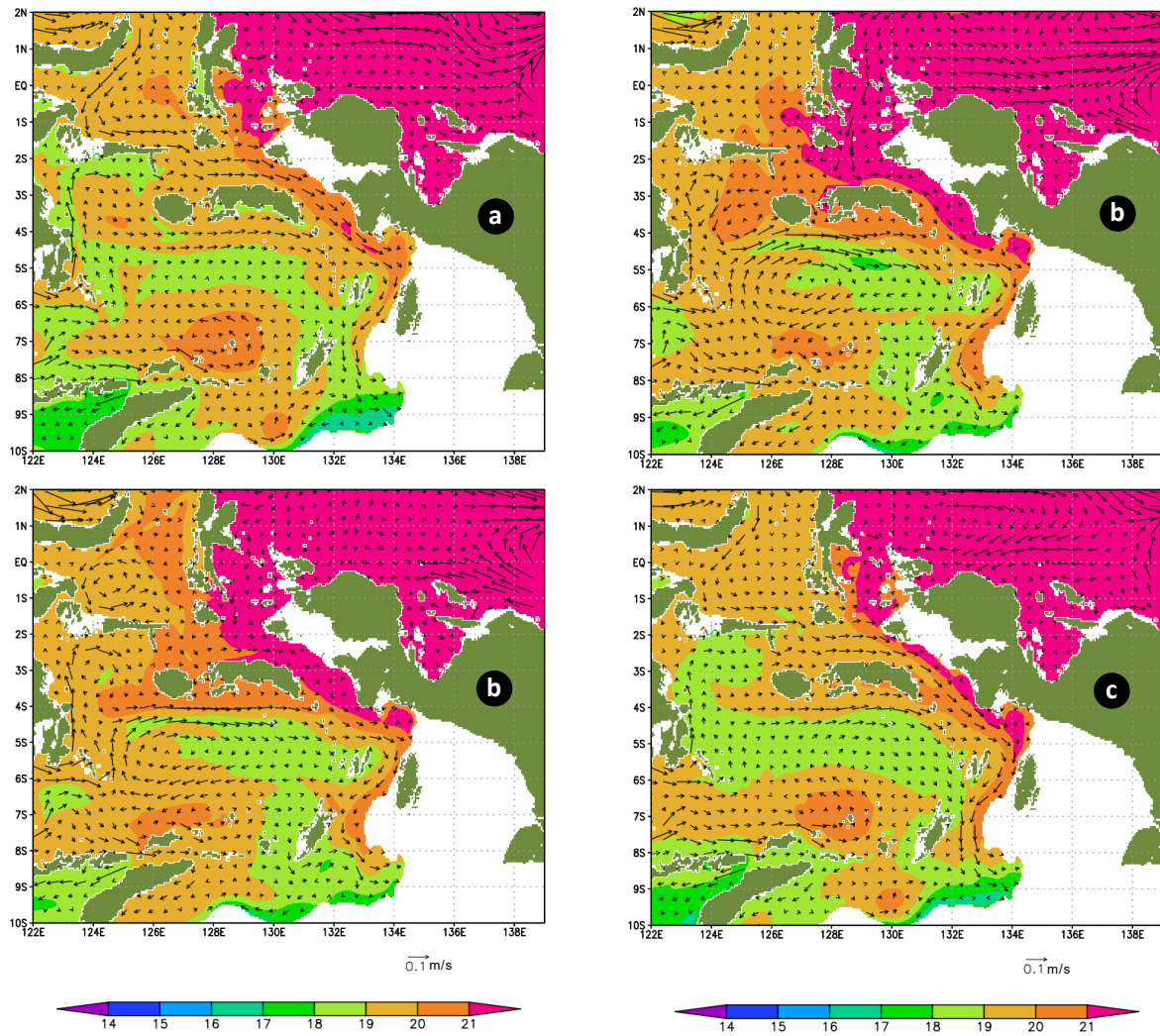


Figure 5.26: Subsurface currents and temperature ($^{\circ}\text{C}$) (the background) at 130 m depth in the period of July 2004 for the cases of: a) the WRT; b) the WO; c) the WR; d) the WT.

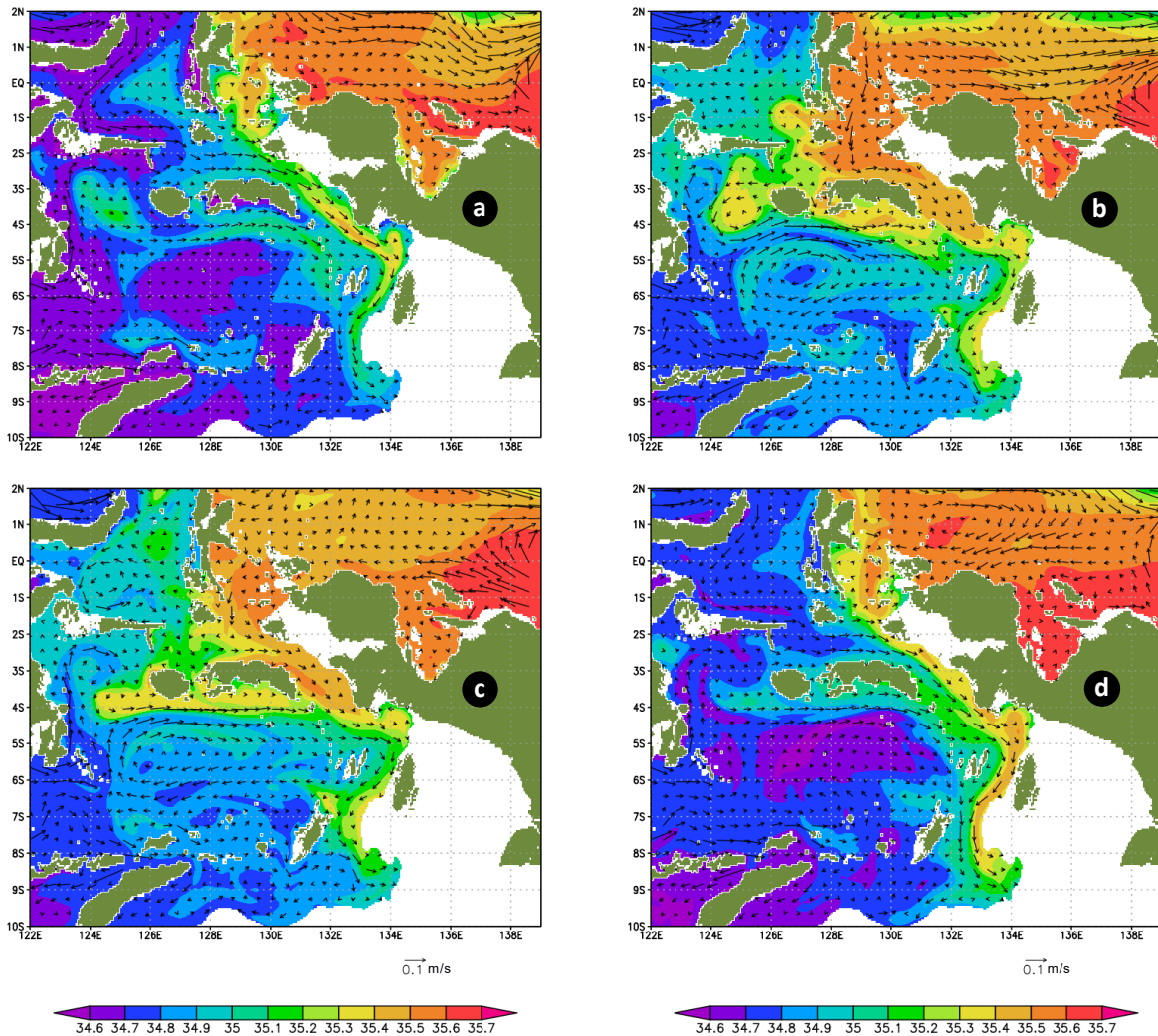


Figure 5.27: Subsurface currents and salinity (the background) at 130 m depth in the period of July 2004 for the cases of: a) the WRT; b) the WO; c) the WR; d) the WT.

Furthermore, an anti-cyclonic subsurface circulation around section A is generated in all cases, and the flow tends to be convergent resulting in waters pile-up and then inducing downwelling around the Northern Aru Basin (Figure 5.28). It is proposed that the anti-cyclonic circulation is mainly generated by the interaction between the bathymetry and the resultant currents between the ITF and geostrophic current induced mainly by sea surface slope toward offshore as an impact of the westward offshore surface currents. As consequence of this, it is suggested that the upwelling intensity around this area tends to weaken. Furthermore, the anti-cyclonic circulations observed in the tide exclusion simulation are generally stronger than those in the tide inclusion simulation. The study implies that compared to the circulation in the tide inclusion simulation (see also in the section 6.1.2.1), the stronger circulation is induced by the larger horizontal pressure gradient force in the tide exclusion simulation.

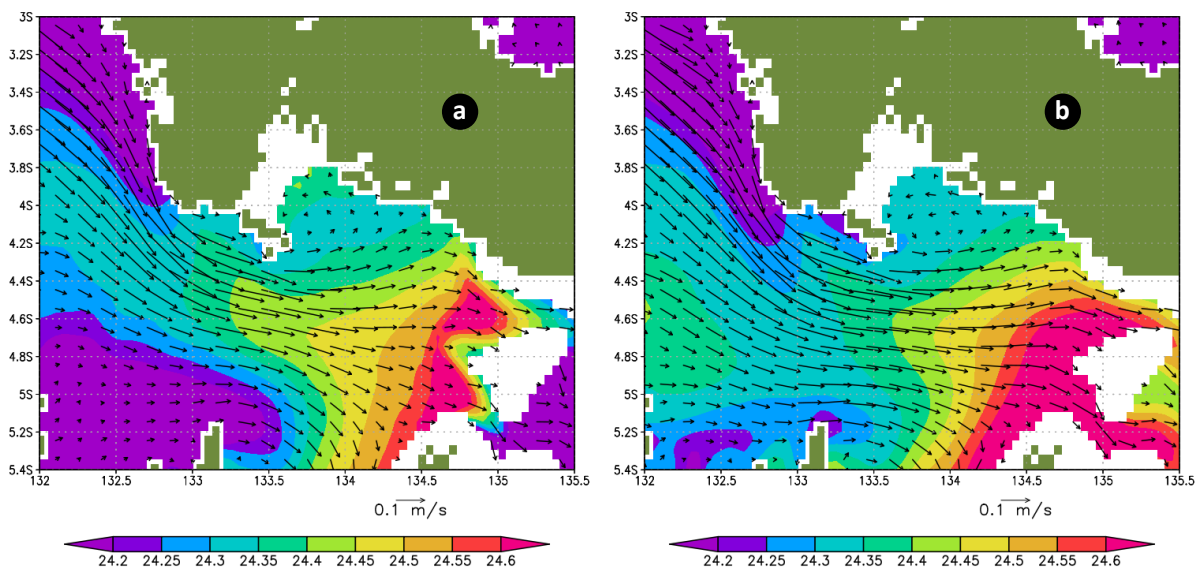


Figure 5.28: Subsurface currents and density ($+1000 \text{ kg/m}^3$) (the background) at 60 m depth in which the maximum velocities are generally found within the water column along the section A in the period of July, 2004 for the cases of: a) the WRT; b) the WR.

5.4.3 Vertical Profile along the Section A

As an impact of the southeasterly wind exposing the Northern Arafura Sea, a westward offshore within 20 m upper of water surface is generally observed in the section A in all experiments (Figure 5.29). With increasing depth in this layer, the current speed is reduced indicating the role of Ekman balance in influencing the circulation around this area. The upwelling signal in this layer is indicated by relatively colder and saltier water masses in the near coastal area than those toward offshore. Below this layer at between 20 and 150 m depth, eastward onshore currents with a relatively strong intensity of around 60 m depth are observed, and this structure is similar to the vertical velocity structure found around the Halmahera Sea (Figures 5.9 and 5.10). This subsurface condition confirms the influence of the Indonesian throughflow (ITF) around the Aru Basin, as discussed in section 5.4.2. As can be seen in the Figure 5.26, the ITF mainly originates from the Southwestern Pacific Ocean entering into the Indonesian Seas through the Halmahera and Seram Seas before entering into the Northern Aru Basin at section A. The evidence of the ITF influence is also indicated by the salinity maximum observed at around 120-130 m depth.

Moreover, the upward and downward motions are detected along this section (Figure 5.29). In general, the upwelling is also indicated by the upward-sloping isotherms toward onshore, and the reverse pattern is generally true. Such an upward slope is generally observed

above the Sahul Shelf Break while the downward gradient is mostly found at about 125 m depth in the middle of this section A even though the upwelling is generally observed around this area. This phenomenon suggests that the downward temperature gradient is associated to the intrusion of the Banda Sea water with relatively low temperature and salinity, compared to the water masses derived from SWPO, which also enter the Aru Basin (see also Figures 5.26 and 5.27).

However, some significant discrepancies are detected along section A among the four experiments. For the upper layers, their discrepancies have been discussed in the section 5.4.1. In the subsurface, the eastward currents in the simulation with tide are observed in deeper layers (between 20 m and 175 m depth) than the ones in the simulation without tide (between 20 m and 125 m depth) (Figure 5.29). However, the eastward onshore currents at the upper layers at around 60 m depth, where the maximum subsurface currents are located in the tide simulation, are smaller than those of the no-tide simulation while the reverse pattern is generally true for the surface water. It is suggested that the different subsurface currents in the two simulations are mainly caused by the different horizontal gradients of the SSH and density induced by different forcing applied in the two simulations. The study suggests that the enhanced vertical mixing generated by tidal forcing as found in the tide inclusion simulation plays an important role in modifying the gradients so that for both parameters the gradients observed in the tide simulation are smaller than the one in the no-tide simulation (see also in the section 6.1.2.1).

The simulation results also show that the upwelling intensity in the tide inclusion simulation is larger than it is in the tide exclusion simulation. As a consequence of this, relatively colder and saltier water from the lower layers can be upwelled to the surface. The study suggests that the upwelling-downwelling cells generated over the Sahul slope play an important role in upwelling more subsurface water to the upper layers around the Northern Aru Basin, subsequently causing the water temperature in the upper layers to be lower (Figure 5.29). The circulation cells are associated with residual currents induced by tidal forcing as indicated by a balance between pressure gradient force and non-linear advection terms of the momentum equation as discussed in section 6.1.2 and Appendix A. The simulation results show that the relatively strong upwelling in the tide inclusion simulations is still observed until 200 m depth. Stronger upwelling intensity in the tide simulation is also indicated by steeper upward-sloping isotherms toward onshore over the Sahul slope, which can be more obviously

be observed over the slope-edge between 100 m and 175 m depth. In the tide exclusion simulations, the upwelling with a relatively weaker intensity is only more concentrated in the upper layers around 100 m depth above the edge of the Sahul Shelf slope. Below this layer, the water masses tend to move downward with a weak intensity.

Furthermore, an upwelling intensity which is moderately stronger than the one in the no-river simulation (the WO/WT case) is found for the river simulation (the WR/WRT case) (Figure 5.29). This condition is indicated by more subsurface water which is upwelled to the upper layers (see also in Figure 5.24). It is observed that the river runoff causes the cold subsurface water layer in the river inclusion simulations to be about 5 m shallower than the one in the river exclusion simulations. In conclusion, this study showed that the enhanced upwelling is related to the enhanced offshore surface transport induced by the increased surface frictional force due to stronger stratification in the upper layer, as discussed in the section 6.2.

Confirming the horizontal distribution (Figures 5.25 and 5.27), in terms of salinity, the results show that the river discharge is refreshing not only the surface water but also the subsurface water so that the salinity at thermocline layers in the Aru Basin is eroded significantly (Figures 5.30a and 5.30d.). It is observed that a lower thermocline salinity is detected in the river runoff inclusion simulations of the WRT/WR case compared to the no-river simulations of the WT/WO cases. This fact indicates the occurrence of relatively strong vertical mixing around the EIS. It is also observed that the thermocline salinity in the WRT case is lower than for the other simulations, and the highest salinity maximum is observed in the WT case (see also in section 5.4.2). Furthermore, the results show that the lower thermocline salinity is found in the western part of section A, indicating the influence of water masses derived from the Banda Sea that generally have lower salinity.

In addition, a weakened vertical stratification of temperature and salinity in the tide simulations is observed around section A, compared to the one in the no-tide simulations. This is indicated by thicker layers of uniform temperature and salinity above the thermocline layer in the tide simulation (Figures 5.29 and 5.30). This weakened stratification is associated with an enhanced vertical mixing induced by internal tidal diffusion caused by the interaction between the bottom sill and tidal forcing that occurs mostly in the Halmahera and Seram Seas (see in the section 5.6). The enhanced vertical mixing is also observed over the continental slope of section A, indicated by a remarkable uniformity in salinity around the bottom slope (Figure 5.30).

Due to the specific bathymetric conditions, the hydrodynamics conditions in the subsurface waters of section A play an important role in influencing the hydrodynamic conditions on the Sahul Shelf. The simulation results show that relatively stronger subsurface currents in the excluded tide or/and river runoff simulation transport more water masses from the Aru Basin to the Sahul Shelf. These stronger subsurface currents generally transport water masses with relatively high salinity and low temperature. As a consequence of this, a relatively higher temperature and lower salinity is found within the water column of section C in the excluded tide or/and river runoff simulation.

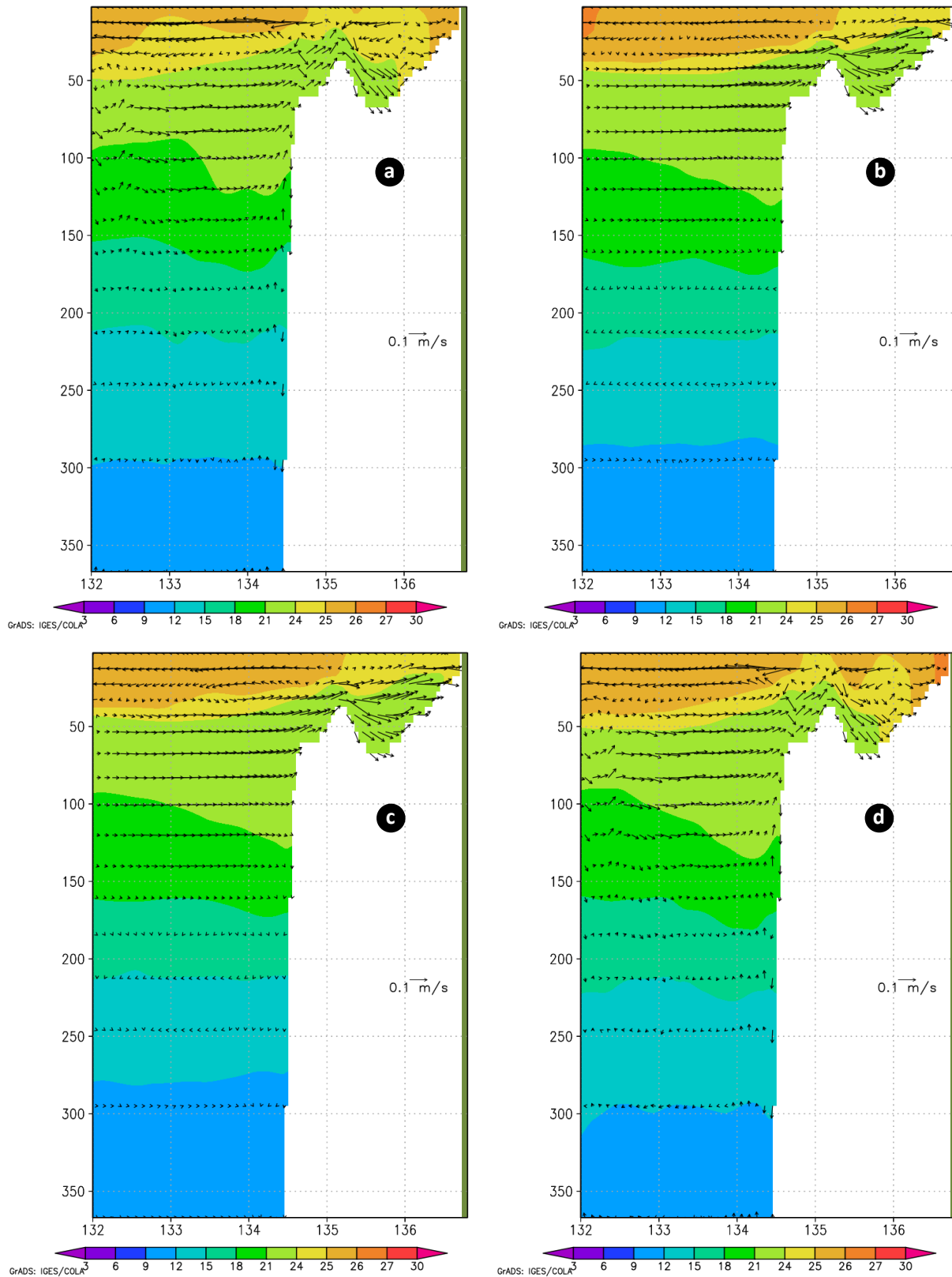


Figure 5.29: The vertical profile of u-w velocity (where u-velocity is in m/s and w-velocity is in $\times 10^{-3}$ m/s) and temperature ($^{\circ}\text{C}$) (the background) along the section A (4.8°S and 131°E - 136°E) in the period of July 2004 for the cases of: a) the WRT; b) the WO; c) the WR; d) the WT.

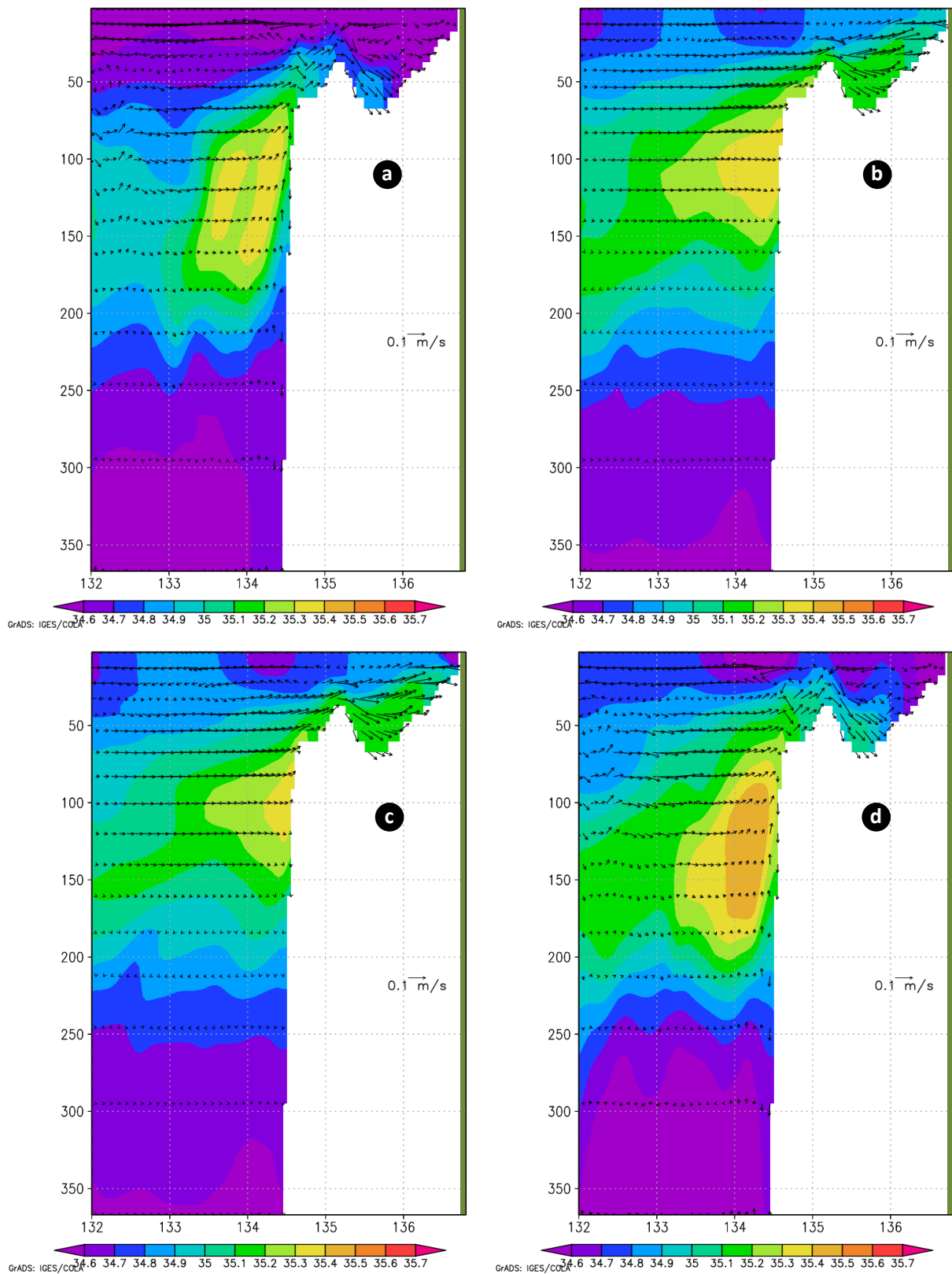


Figure 5.30: The vertical profile of u-w velocity (where u-velocity is in m/s and w-velocity is in $\times 10^{-3}$ m/s) and salinity (the background) along the section A (4.8° S and 131° E - 136° E) in the period of July 2004 for the cases of: a) the WRT; b) the WO; c) the WR; d) the WT.

5.4.4 Vertical Profile along the Section B

In section B, westward currents in the upper layer are generally observed from the surface to about 100 m depth (Figure 5.31). Compared to section A, the offshore currents in the section B are relatively high. In addition to the relatively higher wind stress inducing the relatively-higher Ekman transport in section B compared to the one in the section A, the high currents are also influenced by the geostrophic balance. This is induced by the relatively lower SSH in the Southern part of section B (Figure 4.1), as will be discussed in the section 6.1.2.2 in depth. The influence of geostrophic balance is also suggested as the main reason for the deeper offshore currents over the edge of the Sahul slope. It is predicted that the Ekman depth around this area is around 20 - 45 m. This generally should generate offshore currents within the Ekman layer compensated by the onshore subsurface currents just below it. However, the offshore currents are generally observed in the entire layer above 100 m depth. The results suggest that the strong geostrophic transport that brings relatively warmer and fresher water masses is the main factor in cancelling out the onshore transport (see also section 6.1.2.2). Below 100 m, the subsurface currents mostly flow south-westward following the eastern boundary conditions (see also the Figure 5.26). Therefore, the eastward onshore currents in this section are relatively small, compared to the ones in section A.

Upward-sloping isotherms in onshore direction are observed around the bottom slope that indicates the impacts of upwelling generated by the offshore surface transport and the ascending bottom topography. In the lower layers at between 125 m - 300 m, the downward-sloping isotherms in onshore direction are observed even though the water masses around this area tend to be moved upwards towards offshore. The characteristics of water mass around section B in the horizontal distribution are generally similar to these of the water masses around section A because the water masses at section B are generally the extension of water masses from section A. Therefore, similar to section A, the downward-sloping isotherms are related to the intrusion of the Banda Sea water masses into the area of the section B, which is mainly influenced by water masses derived from the SWPO. The salinity maximum in section B is generally smaller than it is in the section A located at about 125 m depth in all the experiments. This indicates that the vertical and horizontal mixing also occurs along the circulation pathway between sections A and B. The characteristics of salinity within the thermocline layer among the four experiments in the section A show similar patterns as in section A, where the weakening vertical stratification of temperature and salinity in the tide

inclusion simulations is also observed along the section B, compared to the one in the tide exclusion simulations (Figures 5.31 and 5.32).

In contrast to section A, by comparing the WRT and WR cases, it can be inferred that the tidal forcing in section B generally tends to weaken the offshore transport. However, similar to section A, relatively stronger upward motions in the tide simulation are observed around the bottom slope of the Sahul Shelf (Figure 5. 31). These simulation results indicate that the influence of geostrophic balance due to spatial variation of wind stress in the upper layers in the tide inclusion simulation is smaller than it is in the tide exclusion simulation (see also sections 5.1 and 6.1.2.2). The reduced influence of the geostrophic balance tends to enhance the effectiveness of surface Ekman transport in inducing more onshore subsurface flow, and the subsequent upwelling. Similarly, the upwelling intensity in the river runoff inclusion simulation (the WR/WRT case) is slightly stronger than the intensity in the river runoff exclusion simulation (the WO/WT case). It is observed that the river discharge contributes to the enhancement of the upward displacement of the subsurface water masses by about 5 m, which can be identified by comparing the vertical structure of temperature between the WRT and WT cases (Figure 5.31). As in the section A, it is suggested that the stronger upwelling intensity is caused by the enhanced offshore transport in the surface layer induced by the increased stratification in the surface water - as will be discussed in the section 6.2. Here, the circulation cells in tide inclusion simulations (WRT/WT case) over the continental slope of section B is not identified even though tidal forcing generates the cell (see Figure A.3d in Appendix A). The study suggests that the circulation cells are canceled out by the offshore subsurface currents around the slope induced by spatial variation of wind stress.

The increase in upwelling induced by the tide and river runoff is also indicated by temperature and salinity profiles. It is observed that the vertical temperature gradient in the tide/river runoff simulation is higher than it is in the excluded tide/river runoff simulation resulting in a colder SST in the tide/river runoff simulation. However, this is not followed by a higher SSS, as generally observed for an enhanced upwelling and as also observed in section A. Again, the relatively lower subsurface salinity maximum in the excluded tide/river runoff simulation contributes significantly in reducing the SSS (Figure 5.32). Furthermore, the occurrence of an enhanced vertical mixing induced by the interaction between tidal forcing and the rough bottom topography is observed in section B. This is indicated by the relatively uniform temperature and salinity within the water column between 134 and 136.6 ° E.

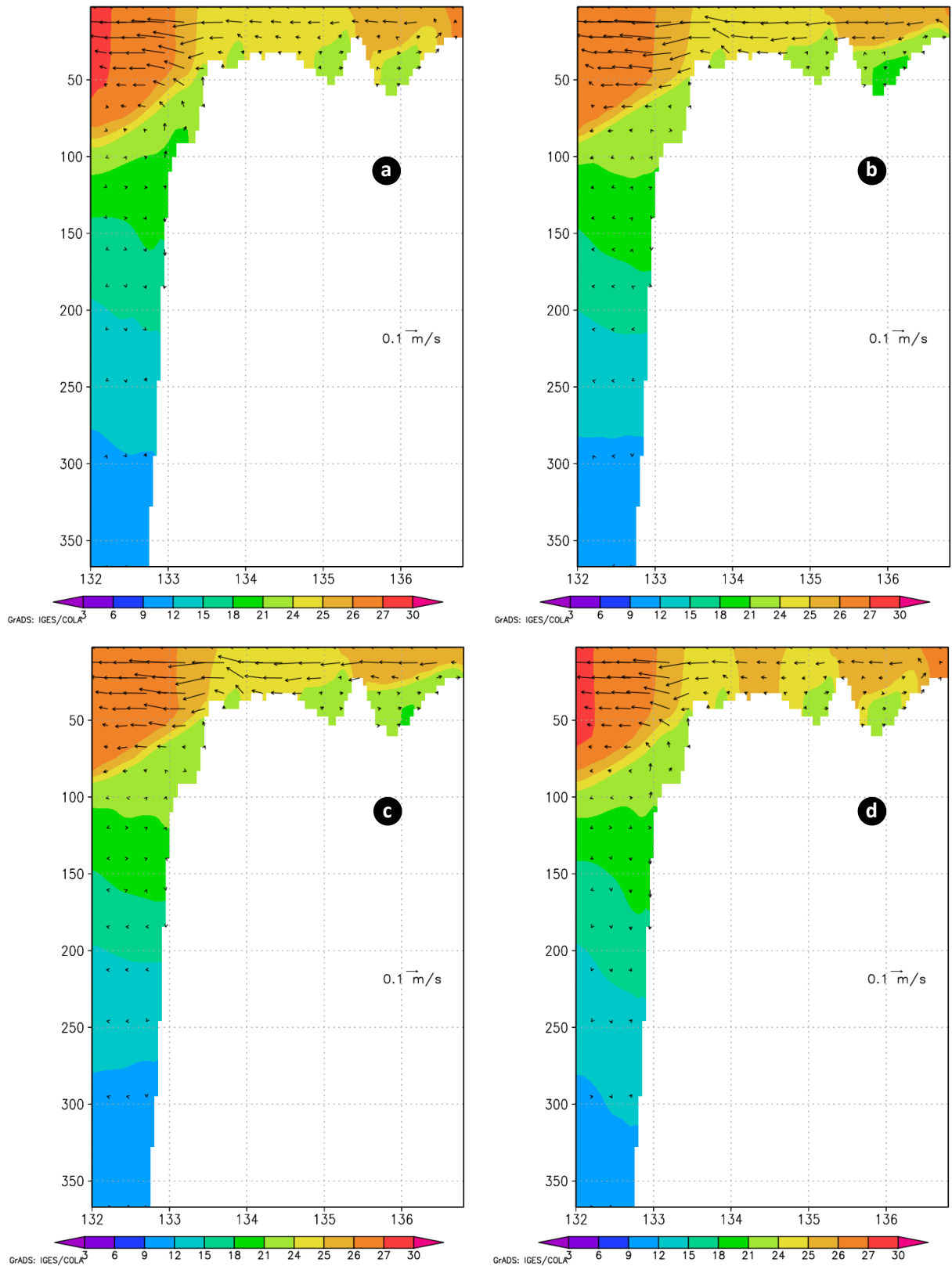


Figure 5.31: The vertical profile of u-w velocity (where u-velocity is in m/s and w-velocity is in $\times 10^{-3}$ m/s) and temperature ($^{\circ}\text{C}$) (the background) along the section B (7.35°S and $132^{\circ}\text{E} - 138^{\circ}\text{E}$) in the period of July 2004 for the cases of: a) the WRT; b) the WO; c) the WR; d) the WT.

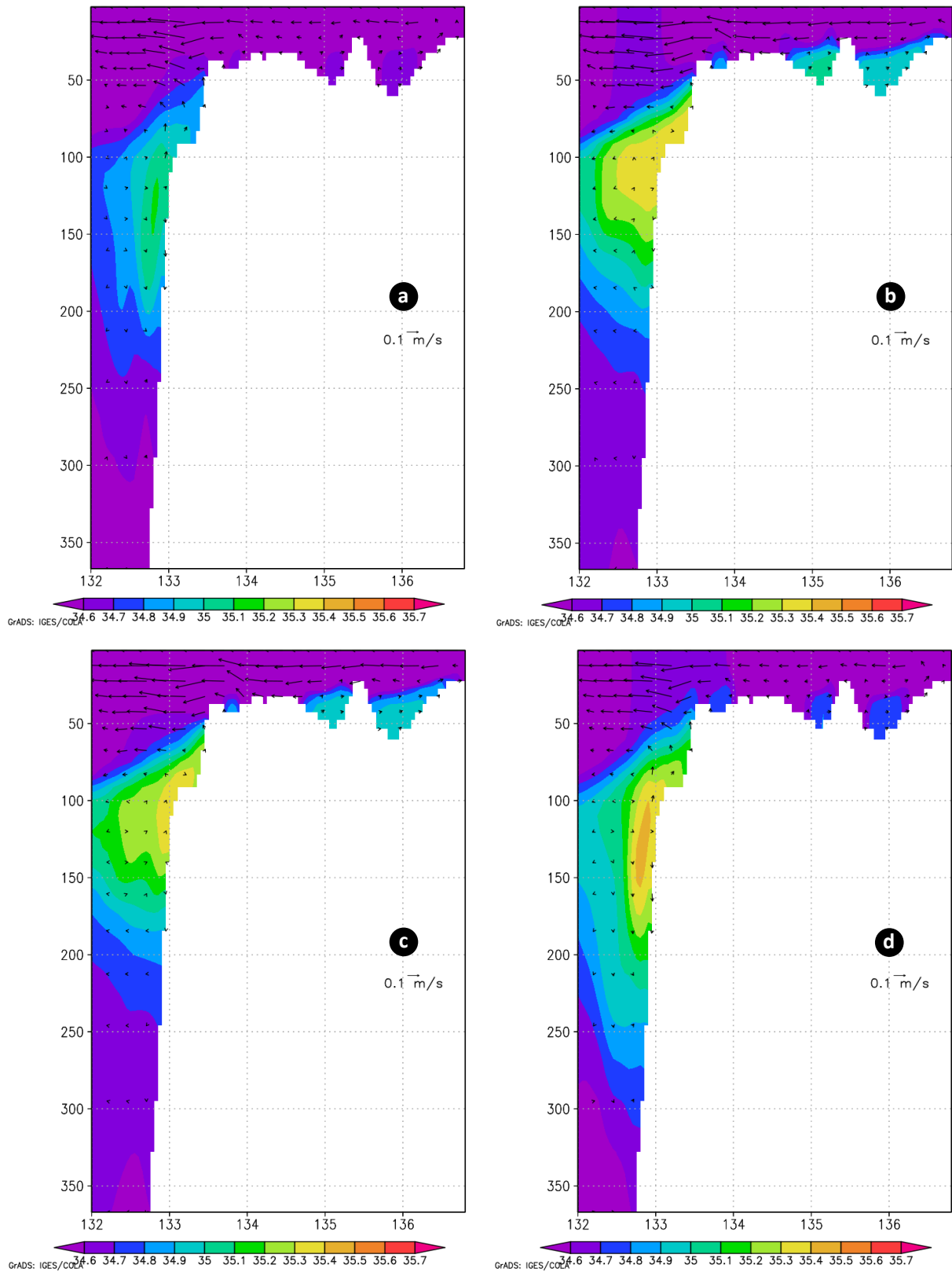


Figure 5.32: The vertical profile of u-w velocity (where u-velocity is in m/s and w-velocity is in $\times 10^{-3}$ m/s) and salinity (the background) along the section B (7.35° S and 132° E - 138° E) in the period of July 2004 for the cases of: a) the WRT; b) the WO; c) the WR; d) the WT.

5.4.5 Vertical Profile along the Section C

The simulation results show that the residual currents within the water column along section C in the tide inclusion simulation are generally much smaller than those in the tide exclusion simulation (Figure 5.33 or 5.34). It is estimated that the tidal forcing tends to weaken the residual surface currents by about 0.035 m/s (60%) in the zonal direction and about 0.013 m/s (24%) in the meridional direction. As a consequence of this, the upwelling intensity in the tide inclusion simulation is generally smaller than the upwelling in the tide exclusion simulation. By considering the same wind forcing applied in the two simulations (tide and no-tide), the results suggests that the enhanced vertical eddy viscosity (see section 5.5), that modify significantly the vertical viscosity force (see also section 6.1.2.3), is the main factor in reducing the residual currents around section C. These weaker currents subsequently weaken the upwelling around the Papua Coast. This condition is one of the reasons why less salinity and higher temperature are found in the upper layers of the Sahul shelf in the tide inclusion simulation, compared to those in the tide exclusion simulation (see also Figures 5.33 and 5.34). Furthermore, it is suggested that the less salinity is also caused by the subsurface water masses geostrophically transported from the Northern Aru Basin to the Sahul Shelf (see also Figures 5.29 or 5.30). In addition, the enhanced vertical eddy viscosity results in a lower vertical temperature/salinity stratification within the water column at section C (Figures 5.33 and 5.34).

In the subsurface, the currents in the two simulations are mainly directed to the eastward with the lower intensity in the tide simulation compared to the one in the tide exclusion simulation (Figure 5. 33). It is suggested that the eastward subsurface currents are generated by the geostrophic balance (see also the section 6.3.1) as a result of the relatively higher SSH in the north of section C in the two simulations compared to the SSH in the southern section. The latter is indicated by a negative horizontal pressure gradient force in the meridional direction along section C (Figures 6. 2 and 6.4). The relatively higher SSH in the northern section C is mainly caused by the interaction between the northward surface transport and the blocking of Papua Coast. These eastward subsurface currents are also induced by the subsurface currents of Northern Aru Basin, which is relatively strong, that are transported geostrophically (see also section 6.1.2.1) and then intrude into Sahul continental Shelf through the Aru Chanel (see also Figure 5.29). It is suggested that these two generations are the main reasons why the subsurface currents around section C is relatively stronger than the surface currents.

Furthermore, the results show that the upwelling center is more concentrated at the bottom slope. The result suggests that the upwelling is not only induced by the offshore surface transport but also by the climbing effect generated by an interaction between the onshore subsurface transport and the bottom slope. Flowing from deep to shallow water, the zonal tidal flow is rectified by the topography and forced up

Similar to that sections A and B, the influence of river runoff is generally indicated by the relatively low salinity in the WRT/WR case compared to the WT/VO case within the upper water column of section C. Furthermore, the results show that the river runoff contributes to the enhancement of the residual surface currents around the Sahul Shelf. As a consequence of this, the eastward subsurface currents and upwelling around this section are generally increased, which can be observed by comparing the current vectors between the simulations (VO/WT case with WR/WRT case) (Figure 5.33). As will be discussed in section 6.2, the stronger currents are mainly induced by the modifications of vertical eddy viscosity and horizontal pressure gradient force.

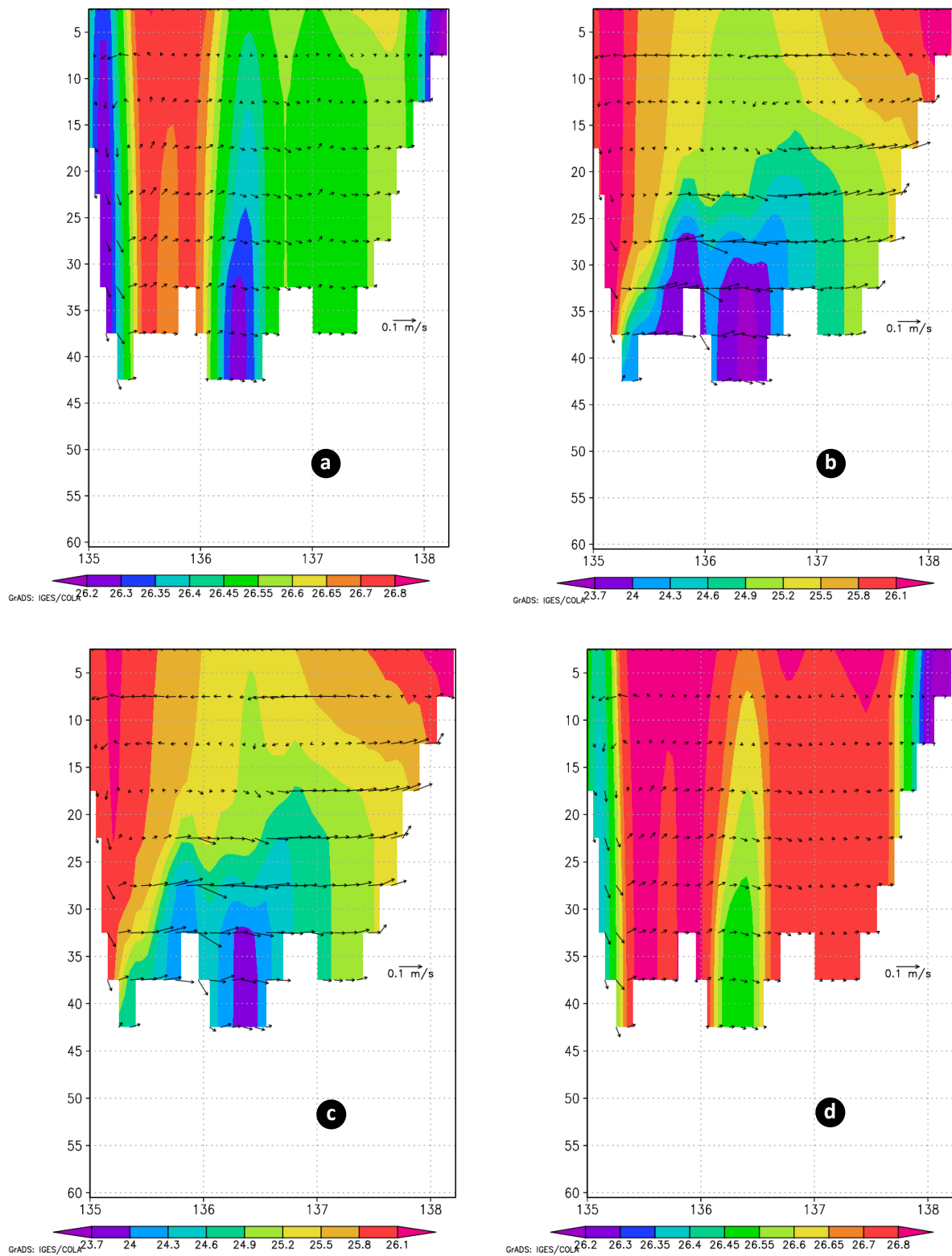


Figure 5.33: The vertical profile of u-w velocity (where u-velocity is in m/s and w-velocity is in $\times 10^{-3}$ m/s) and temperature ($^{\circ}\text{C}$) (the background) along the section C (6.0°S and $135^{\circ}\text{E} - 138.5^{\circ}\text{E}$) in the period of July 2004 for the cases of: a) the WRT; b) the WO; c) the WR; d) the WT.

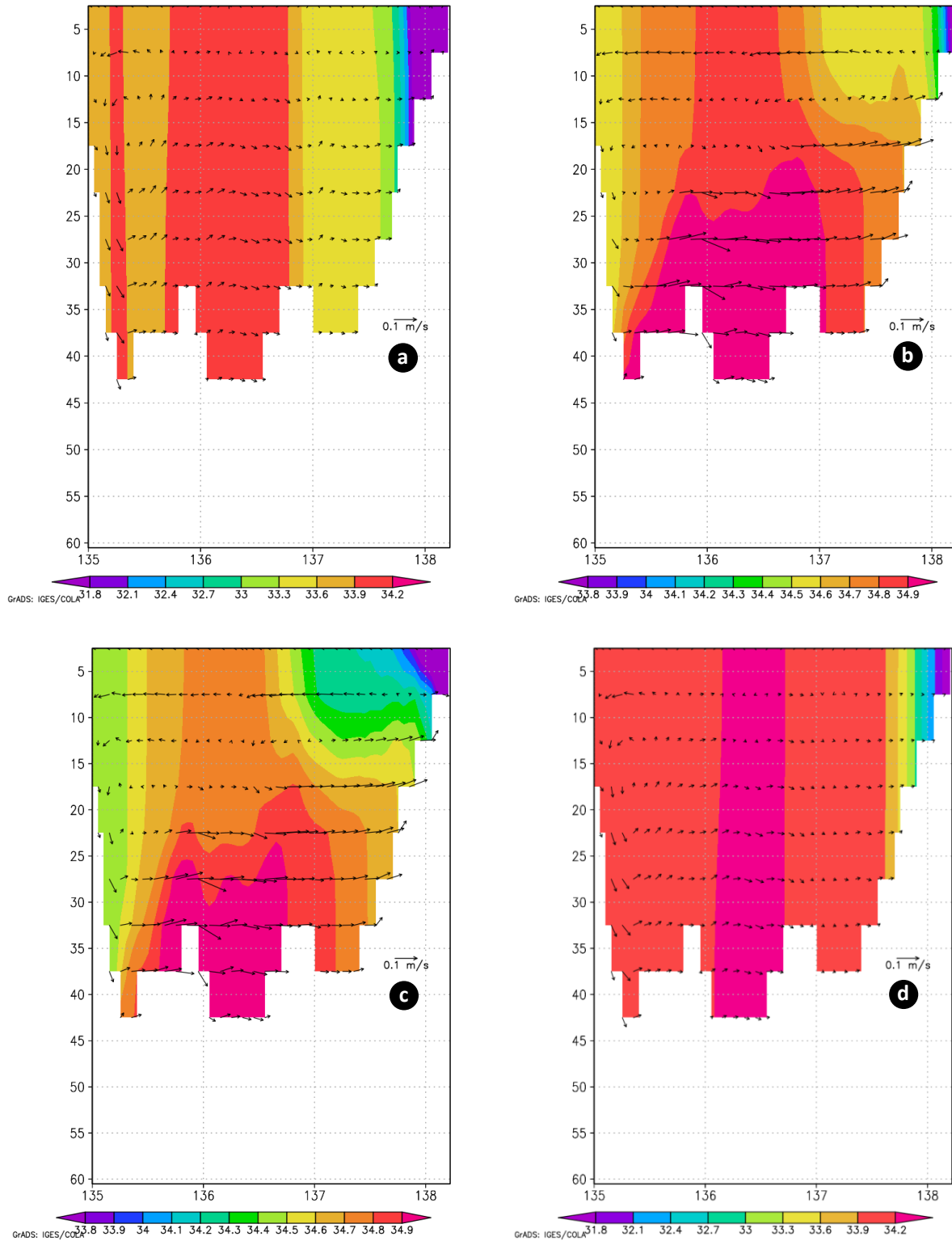


Figure 5.34: The vertical profile of u-w velocity (where u-velocity is in m/s and w-velocity is in $\times 10^{-3}$ m/s) and salinity (the background) along the section C (6.0°S and $135^{\circ}\text{E} - 138.5^{\circ}\text{E}$) in the period of July 2004 for the cases of: a) the WRT; b) the WO; c) the WR; d) the WT.

5.5 Vertical Viscosity Coefficient

In the three simulations, the viscosity at the surface layer in section B is relatively larger than in other areas (Figures 5.35a, 5.35b and 5.35c). It is suggested that this high viscosity is induced by the relatively high magnitude of high wind stress exposing to this area (Figure 5.2). However, it is observed that tidal forcing modifies vertical viscosity. In general, nonlinear interaction between tidal currents and bottom topography tends to enhance vertical mixing as can be identified by the relatively high vertical viscosity around the bottom. The results suggest that tidal mixing in section C is relatively stronger than in Sections A and B, while tidal mixing in Section B is relatively lower than in section A (Figures 5.36 - 5.38). Due to the relatively stronger tidal mixing in and shallow depth of section C, the vertical viscosity in the surface water is significantly modified. Here, it is observed that the vertical viscosity at the surface water in the tide inclusion simulation is higher than that in the tide exclusion simulation (Figures 5.35a, 5.35b and 5.35d). In contrast, due to relatively weak tidal mixing in and significant depth of Sections A and B, tidal mixing generally contributes little to the viscosity of the surface layer. Furthermore, it is observed that, over the Northern Aru Islands (section A), tidal forcing generally reduces the viscosity of the surface layer. The findings suggest that enhanced upwelling intensity induced by tidally-driven circulation cell (see also section 5.4.3 and Appendix A) could prevent weakening stratification due to tidal mixing. A significant change is observed around the Northern Aru headland, where the upwelling observed is relatively stronger than in the surrounding area (Figure 5.35). Similarly, along section B, enhanced upwelling tends to reduce the vertical viscosity of the upper layers, albeit with less of a change than in Section A. It is suggested that this condition is related to the weaker intensity of tidally-induced upwelling in Section B (see also section 5.4.4 and Appendix A).

Meanwhile, enhanced stratification due to river runoff leads to reduced A_v ($\Delta A_v > 0$), which is mostly observed in the Northern Arafura Sea (Figure 5.35e).

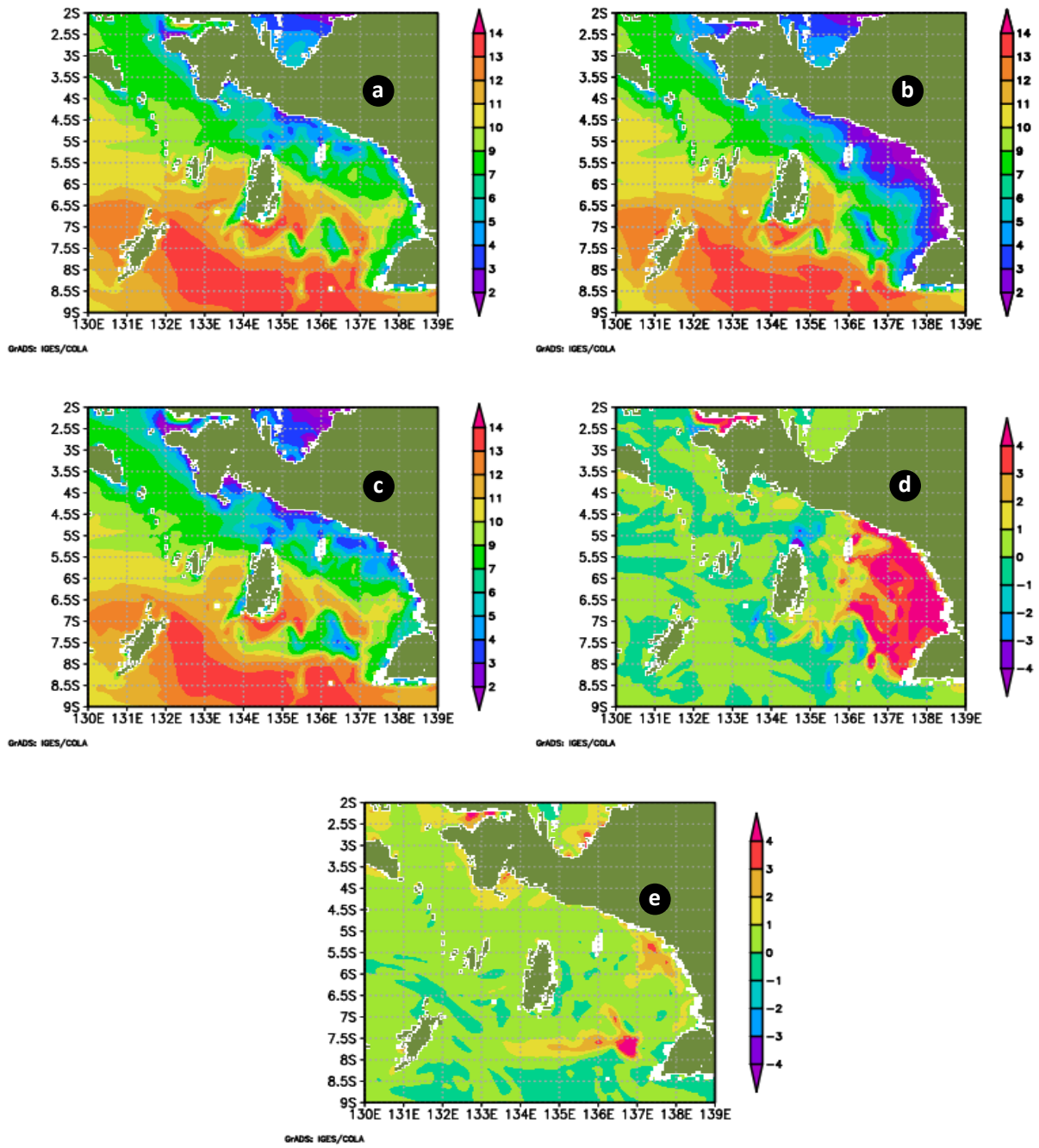


Figure 5.35: Vertical viscosity coefficient ($\times 1000 \text{ m}^2 \text{ s}^{-1}$) in the surface layer around the Northern Arafura Sea for: a) WT case, b) WO case and c) WTR case. The Av difference between: d) the WT and WO cases (WT - WO), e) WT and WTR cases (WT - WTR).

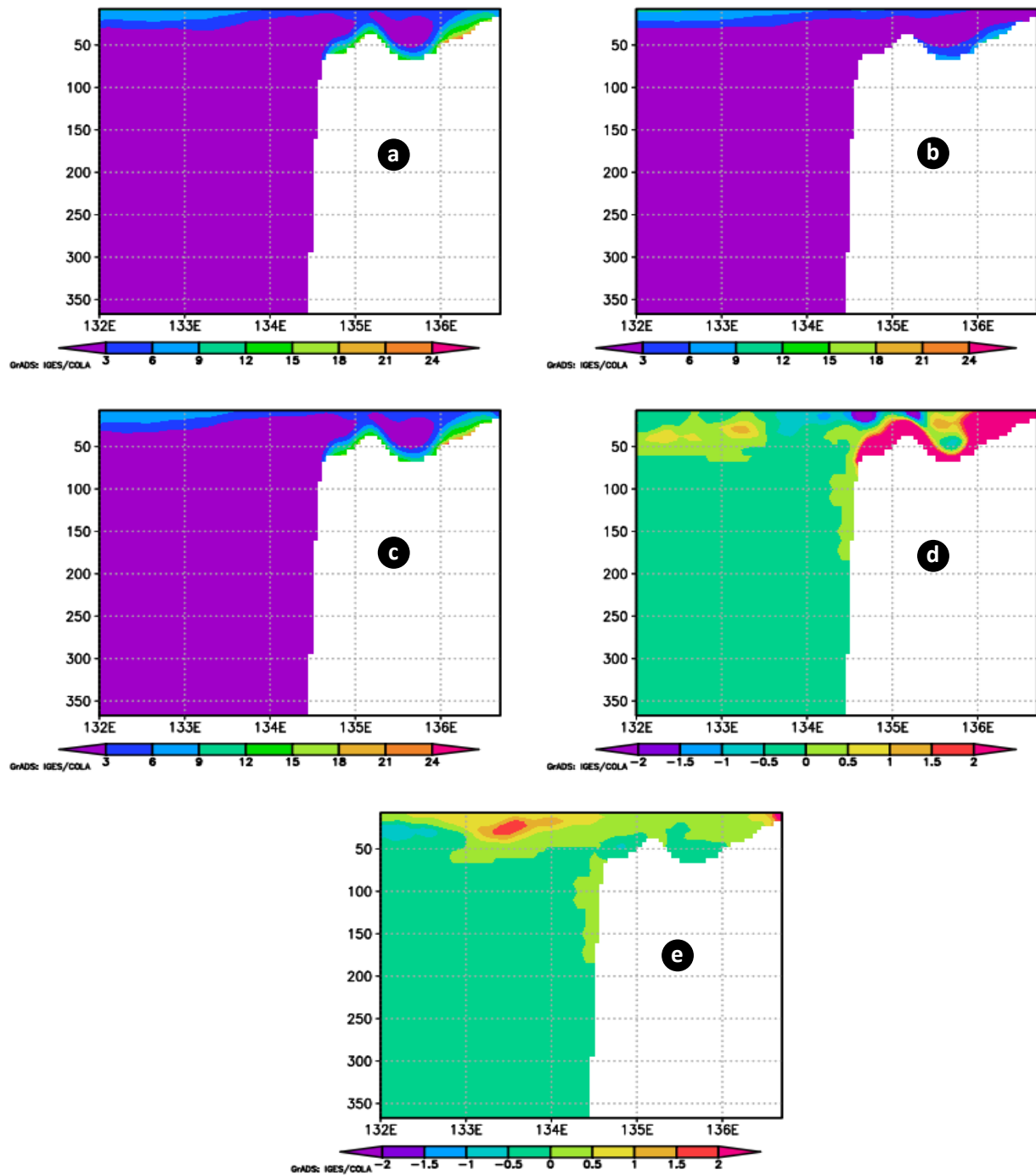


Figure 5.36: Vertical viscosity coefficient ($\times 1000 \text{ m}^2\text{s}^{-1}$) around Section A for: a) WT case, b), WO case and c) WTR case. The A_v difference between: d) the WT and WO cases (WT - WO), e) the WT and WTR cases (WTR - WT).

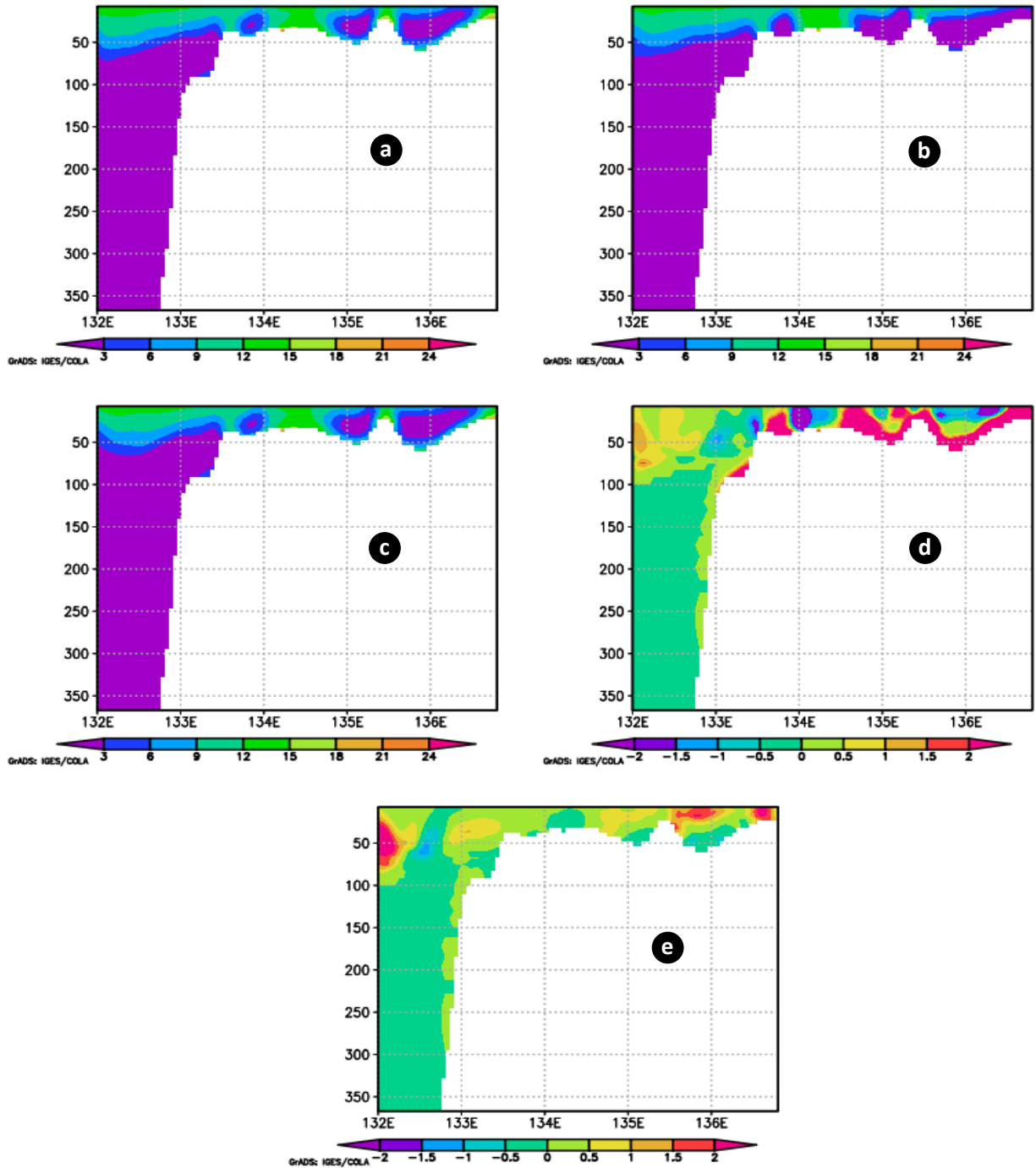


Figure 5.37: Vertical viscosity coefficient ($\times 1000 \text{ m}^2\text{s}^{-1}$) around Section B for: a) WT case, b), WO case and c) WTR case. The A_v difference between: d) the WT and WO cases (WT - WO), e) the WT and WTR cases (WTR - WT).

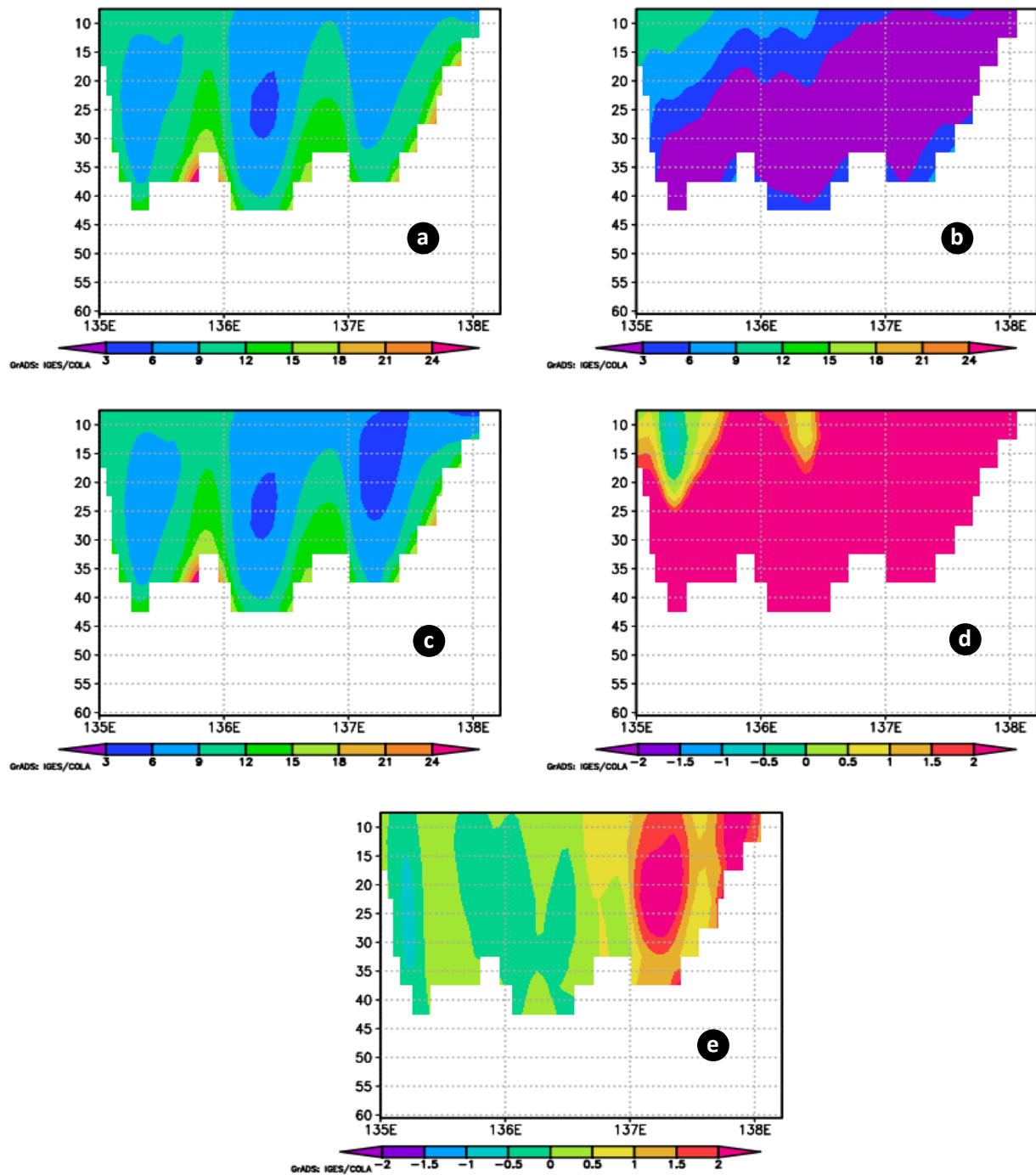


Figure 5.38: Vertical viscosity coefficient ($\times 1000 \text{ m}^2\text{s}^{-1}$) around Section C for: a) WT case, b), WO case and c) WTR case. The A_v difference between: d) the WT and WO cases (WT - WO), e) the WT and WTR cases (WTR - WT).

5.6 Internal Tide and Mixing

Internal tides have been observed in some regions of the Indonesian Sea such as Lombok Strait, Halmahera Sea, Sangihe Strait, Sulu Strait, Makassar Strait and Luzon Strait (Mitnik et al., 2000; Aiki et al., 2011; Sari Ningsih, 2008; Susanto et al., 2005; Matthees et al., 2011; Robertson and Field, 2005,2008; Kartadikaria, 2011; Nugroho, 2017). The internal tides can be identified by observing vertical velocity and temperature profiles. The ripple-like pattern of vertical velocity is one of indications of the existence of the internal waves, as reported by Arbic et al. (2010). In this simulation, a relatively strong ripples can be detected at about 200 m depth whereby largest signals are observed around the Sulawesi and Halmahera Seas (Figure 5.39). The propagation of internal wave can also be observed by using Hovmoller diagram. The transect line chosen is located around the Sulawesi and Halmahera Seas (Figure 5.40). The results indicate that the waves travel at about 1.8 m/s and 3.1 m/s in the Sulawesi and Halmahera Seas respectively. These internal tides generate upwelling and downwelling that bring the lower-cold water to the upper layer and vice versa.

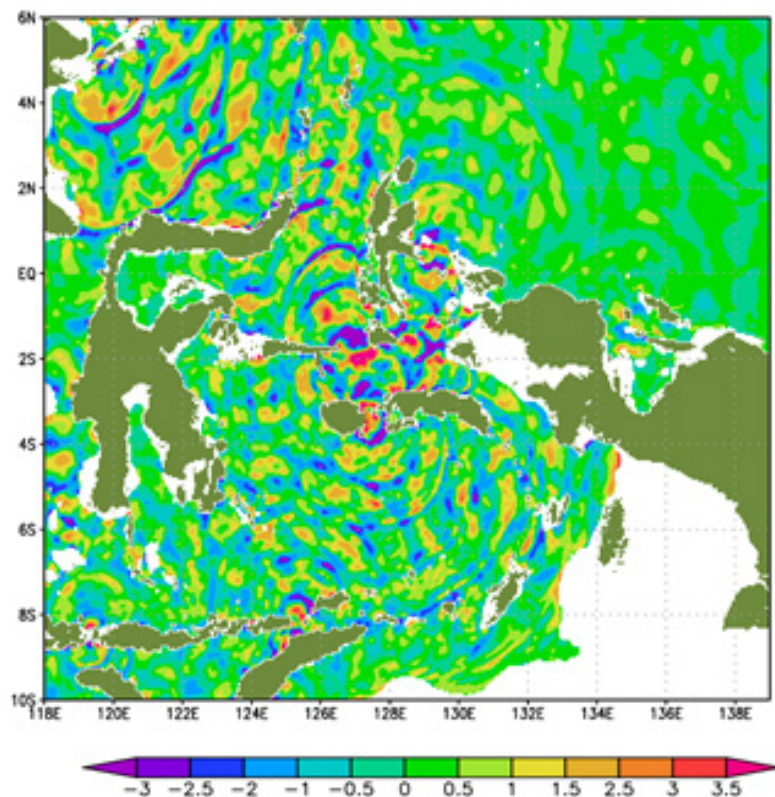


Figure 5.39: The Instantaneous vertical velocity (m/s) at about 200 m depth in the Eastern Indonesian Seas in the 2004 period

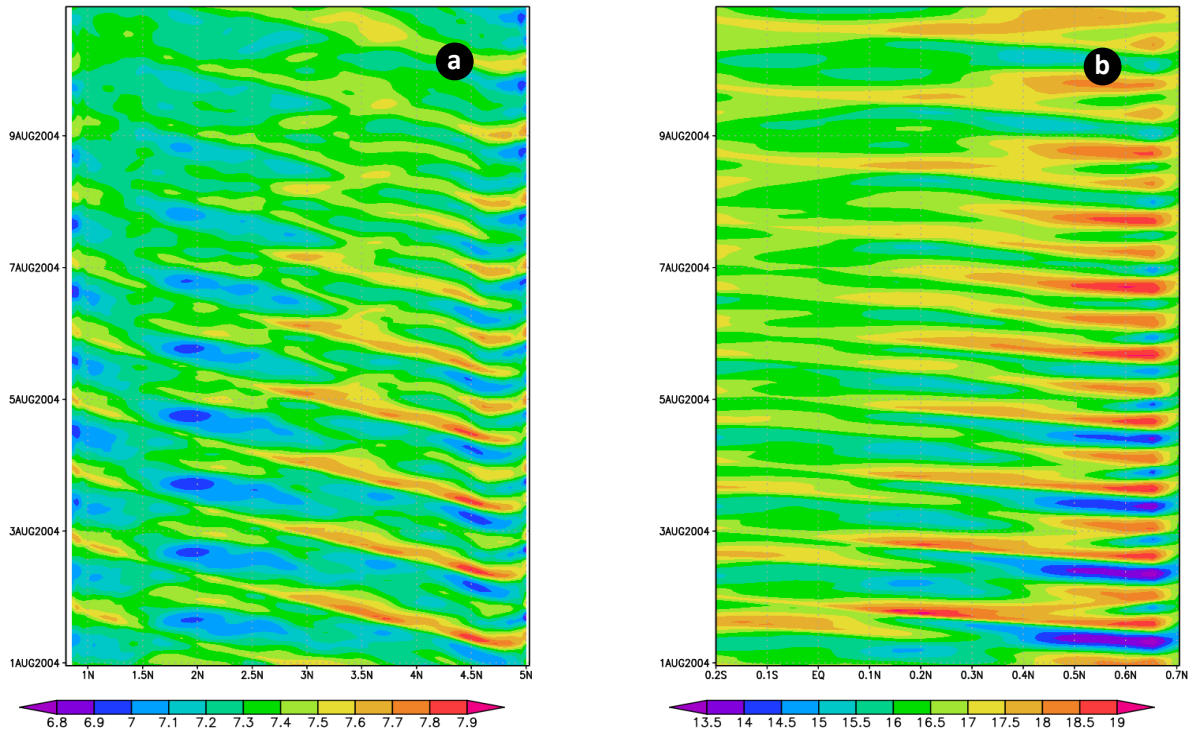


Figure 5.40: Hovmoller diagram of temperature ($^{\circ}\text{C}$); at about 650 m depth along $0.8^{\circ} - 5^{\circ}\text{N}$ at 120°E in the Sulawesi Sea (a) and at about 200 m depth along $-0.2^{\circ} - 0.7^{\circ}\text{N}$ at 129.15°E in the Halmahera Sea (b) in the 2004 period

6. Momentum Analysis: The interaction of Tide and River Runoff with Wind-Driven Upwelling

In this chapter, the mean of momentum components in tide exclusion simulation (WO), the tide inclusion simulation (WT), and tide-river runoff inclusion simulation (WRT) is calculated for 28 days to explain the dynamic process of wind-driven circulation and its interaction with tidal forcing and river runoff during period of the wind-driven upwelling (July 2004) in the selected areas (sections A, B and C) of the northern Arafura Sea.

6.1 Interaction between Tidal Forcing and Wind-Driven Circulation during Wind-Driven Upwelling

6.1.1 Horizontal Distribution of Momentum Balance

In ideal conditions (no lateral boundaries), as a result of south-westerly winds (Figure 5.2) and the influence of the Coriolis force, the surface currents of the northern Arafura Sea should be directed westward (about 45 degrees to the left out of the wind). However, the results show that surface currents in the selected areas are mostly directed north-westward, which is almost in the same direction as wind (see also Figures 5.2 and 5.24). This suggests that the deflected currents are mainly induced by a pressure gradient due to interactions between surface Ekman transport and islands, as discussed in detail below.

Effect of wind on the upwelling

Around the Northern Aru Islands (part of section A), the zonal momentum balance equation in the WO case shows a dominant geostrophic balance, as indicated by the pressure gradient force (PGF_x , which represents the summation of barotropic- and baroclinic- PGF_x) being of relatively higher magnitude than the nonlinear advection (ADV_x) and vertical viscosity (VVI_x) terms. The summation of PGF_x , ADV_x and VVI_x terms is balanced by the Coriolis force (COR_x), the direction of which is opposite to that of the PGF_x term (Figure 6.1). This balance correlates with northward meridional residual currents (see also Figure 5.24), as also indicated by the negative value of the COR_x term (see also Figure 6.1). The results suggest that the relatively high PGF_x term is induced by convergence flow across the Sahul Channel (located between Northern Aru Islands and Papua; see Figure 5.24). This convergence flow is mainly

caused by currents from the Western Aru Coast that are transported geostrophically to the channel (Figure 5.24). As a consequence, the sea surface of this area is relatively higher than in surrounding areas, inducing a slope that generates a relatively high PGF_x term ($PGF_x > 0$) which is directed eastward around the Northern Aru Islands (Figure 6.1). Then, under Coriolis influence, northward currents are then generated. Meanwhile, a dominant Ekman balance is identified in the meridional direction, as indicated by the VVI_y term being of relatively higher magnitude than the PGF_y and ADV_y terms (Figure 6.2). The summation of the PGF_y , ADV_y and VVI_y terms is balanced by the COR_y term, the direction of which is opposite that of the VVI_y (Figure 6.1). This balance is correlated to the westward residual currents (Figure 5.24), as also indicated by the negative value of the COR_y term (Figure 6.1).

Around the Southern Aru Islands (part of section B), the surface-layer momentum balance equation in the zonal and meridional directions in the WO case is characterized by the dominance of the geostrophic (rather than Ekman) equation (Figures 6.1 and 6.2). This condition is indicated by the PGF term being of relatively higher magnitude than the VVI term. Meanwhile, the magnitude of the ADV term is lower than that of the PGF and VVI terms. The summation of the PGF , VVI , and ADV terms is balanced by the Coriolis force, the direction of which is opposite that of the PGF term. This study suggests that the relatively higher PGF term over section B is induced mainly by the spatial variation of wind stress around the Arafura and Banda Seas, with relatively stronger wind stress being found across section B (Figure 5.2). Relatively stronger wind stress is also indicated by the VVI term being of relatively higher magnitude over Section B than surrounding (Figures 6.1 and 6.2). As a consequence of this, relatively stronger currents (Figure 5.39) and lower sea levels (Figure 4.2) are generally observed over section B. This study shows that the low sea level creates a slope, which results in the PGF term being relatively high over Section B. The results suggest that, in the zonal direction, the geostrophic flow tends to cancel out the Ekman flow, as indicated by the opposite directions of the PGF_x and VVI_x terms. In contrast, in the meridional direction, the PGF_y and VVI_y terms reinforce each other, as indicated by their shared direction. The summation of these terms is balanced by a Coriolis term that is of higher magnitude than around the Northern Aru Islands, a situation related to the western surface currents being stronger around the Southern Aru Islands than the around Northern Aru Islands.

Near the Western Papua Coast (part of section C), the PGF term also contributes significantly to the momentum balance in the WO case. In the meridional direction, the

momentum balance equation in this area is characterized by a dominant Ekman balance, as indicated by the balance of the VVI_y and COR_y terms (Figure 6.2). In this area, the PGF_y term significantly modifies the Ekman transport, while the contribution of the ADV_y term is relatively smaller. This balance correlates with the westward surface currents (see also Figure 5.24), as indicated by $COR_y < 0$. This pattern is generally also found in the zonal direction in the same area. Meanwhile, near the western border (the Eastern Aru Coast), the zonal momentum balance equation is dominated by the geostrophic balance. This study suggests that the relatively higher PGF_x term near the western border is induced by water masses that, having been transported westward, pile up around the Eastern Aru Coast. Under Coriolis influence, the net pressure gradient force then induces northward currents around the Western Aru Coast (see also Figure 5.24), as indicated by $COR_x < 0$ (Figure 6.2).

The influence of tides on the wind driven upwelling

The above patterns are generally also observed in the WT case. However, it is observed that the nonlinear advection (ADV) term contributes much more significantly to the momentum balance equation in both zonal and meridional directions in the WT case, as observed mostly around the headland, the bump, and the continental slope of the Aru Channel (Figures 2.2, 6.3 and 6.4). Here, the relatively high ADV term is mostly balanced by a relatively high PGF. This balance represents nonlinear interaction between tidal flow and bottom topography, as related to residual current generation that induces upwelling over the Northern Aru headland and circulation cells across the continental slope of the Aru Channel (as discussed in Appendix A).

Furthermore, tidal forcing modifies the VVI term over the surface, as can be observed by comparing the WT and WO cases (Figures 6.1 - 6.6). Significant change between the two simulations is found over section C, a fact related to the significantly higher Av difference between the two simulations (as discussed in section 5.5). It is observed that the VVI term in the WT case in this area is mostly lower than in the WO case, which is mostly indicated by $VVI_x > 0$ and $VVI_y < 0$ (Figures 6.5 and 6.6). In general, relatively higher vertical viscosity results in higher interfacial stress within the water column (Figure not shown). Consequently, by considering the same wind forcing in the WT and WO cases, the vertical viscous force (the VVI term, representing interfacial stress differences between two adjacent layers; see also section 3.5) in the surface water is relatively lower in the WT case than in the WO case. This lower VVI term is suggested as the main factor inducing lower residual surface currents over section C. Meanwhile, the relatively smaller Av difference around the Northern and Southern

Aru Islands (see also section 5.5) results in a smaller difference in the VVI term than that around the Sahul Shelf.

It is additionally observed that the tidally induced mixing (see also sections 5.4.3 and 5.6) contributes considerably to the modification of the PGF terms over sections A and B. Over section A, it is observed that tidal mixing contributes to modify the PGF term so that PGF_y term at the surface layer, which is dominated by barotropic- PGF_y , in the tide inclusion simulation is mostly in the same direction as VVI_y term. Meanwhile, in the tide exclusion simulation, the PGF_y term is generally opposite (and has a lower magnitude than) VVI_y term (Figures 6.2 and 6.4). Consequently, by considering the relatively similar values of the VVI_y term in the two simulation, the results show that the summation of VVI_y and PGF_y terms in the meridional direction is balanced by the COR_y term being higher in the WT case than in the WO case. The higher COR_y term is related to stronger westward currents in TW case than that in the WO case, as discussed in section 5.4.1. Conversely, over the section B tidal forcing generally contributes to a weakening of the geostrophic components in the meridional direction ($\Delta PGF < 0$, $\Delta COR > 0$ Figure 6.6), indicating that zonal surface currents are weaker in the TW case than in WO case (see also section 5.4.1).

Over section C, the simulation results also show that tidal mixing modifies the PGF and ADV terms considerably in the zonal and meridional directions (Figures 6.1–6.6). Similar to the WO case, in the WT case the PGF terms in the zonal and meridional directions are mostly in the opposite direction to the VVI term. However, it is found that the summation of VVI_x , PGF_x , and ADV_x terms in the zonal direction around the western Aru Coast is generally balanced by a lower COR_x term in the WT case than in the WO case. This lower COR_x term indicates weaker northward residual currents (see also Figure 5.24). Meanwhile, around the western coast of Papua, the summation of the VVI_x , PGF_x , and ADV_x terms in zonal direction is generally balanced by a COR_x term ($COR_x < 0$) in the WT case that is in the opposite direction to the COR_y term ($COR_y > 0$) in the WO case; this indicates that meridional residual currents in the WT and WO cases are in the opposite direction. Here, the negative COR_x term is related to the northward surface currents (see also Figures 5.24b and 5.24d). It is further observed that the magnitude of meridional surface currents is relatively smaller in the WT case than in the WO case. In the meridional direction, the summation of the VVI_y , PGF_y , and ADV_y terms over section C are mostly balanced by a lower COR_y term, indicating that westward residual surface currents are weaker in the WT case than in the WO case.

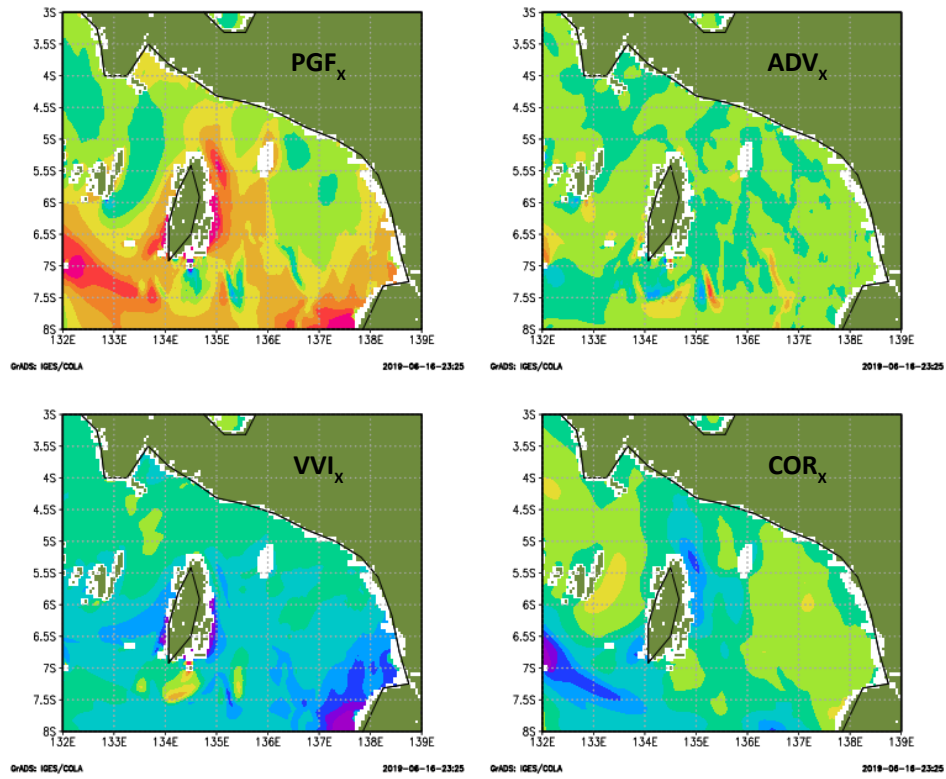


Figure 6.1: Momentum components in the zonal direction in water surface ($z = 1$) for the WO case during the period of July 2004 (28 days) ($\times 10^{-3} \text{ ms}^{-2}$).

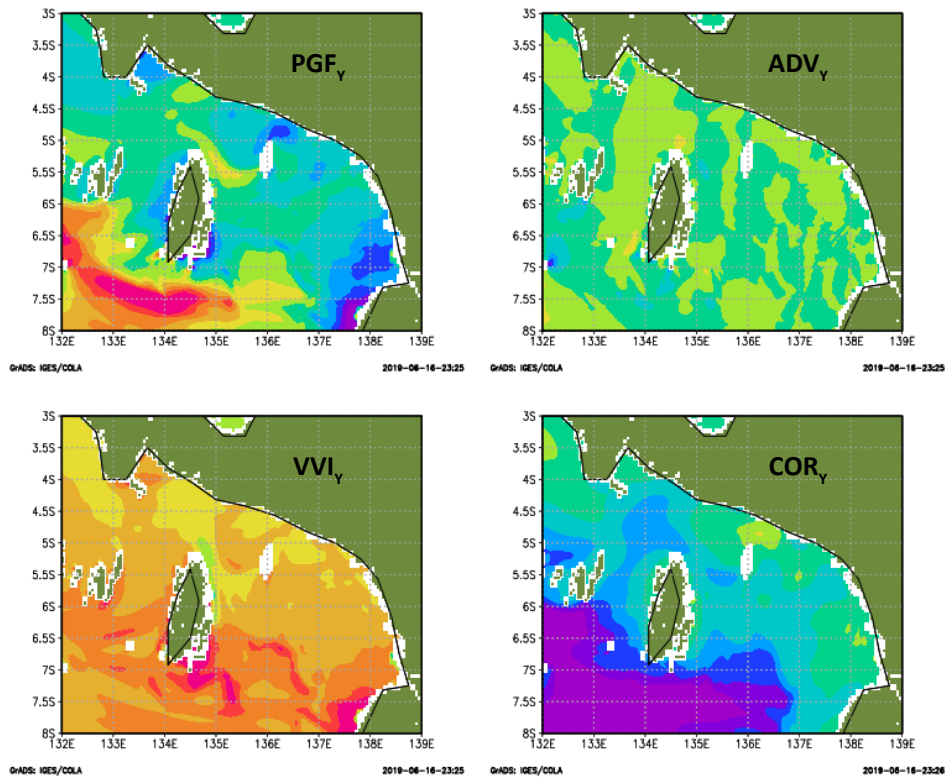


Figure 6.2: Momentum components in the meridional direction in water surface ($z = 1$) for the WO case during the period of July 2004 (28 days) ($\times 10^{-3} \text{ ms}^{-2}$).

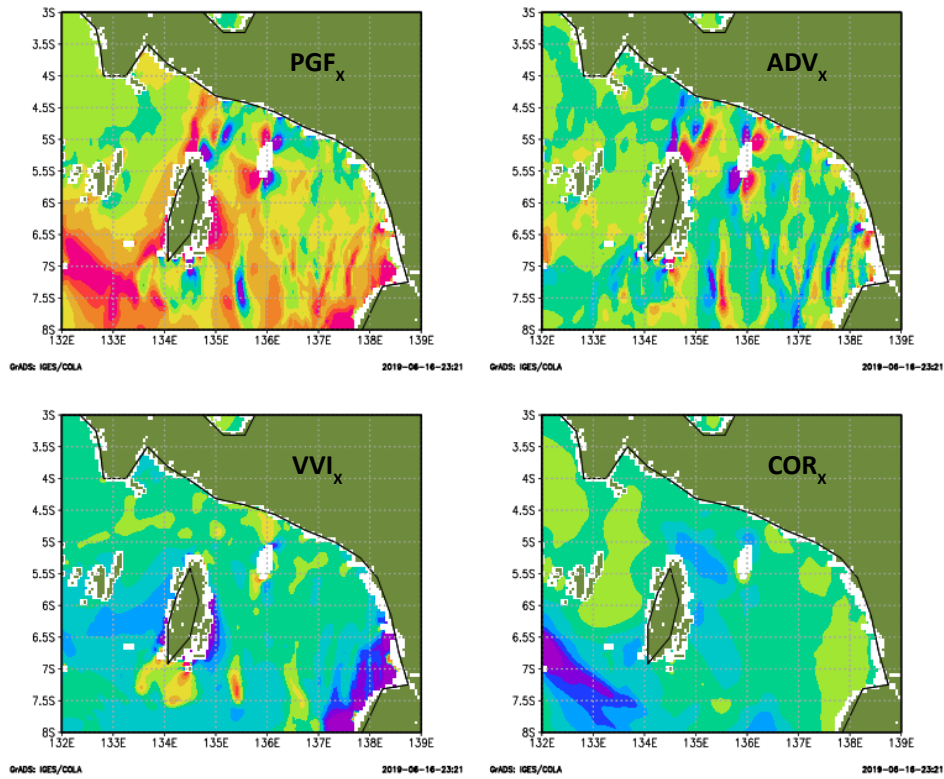


Figure 6.3: Momentum components in the zonal direction in water surface ($z = 1$) for the WT case during the period of July 2004 (28 days) ($\times 10^{-3} \text{ ms}^{-2}$).

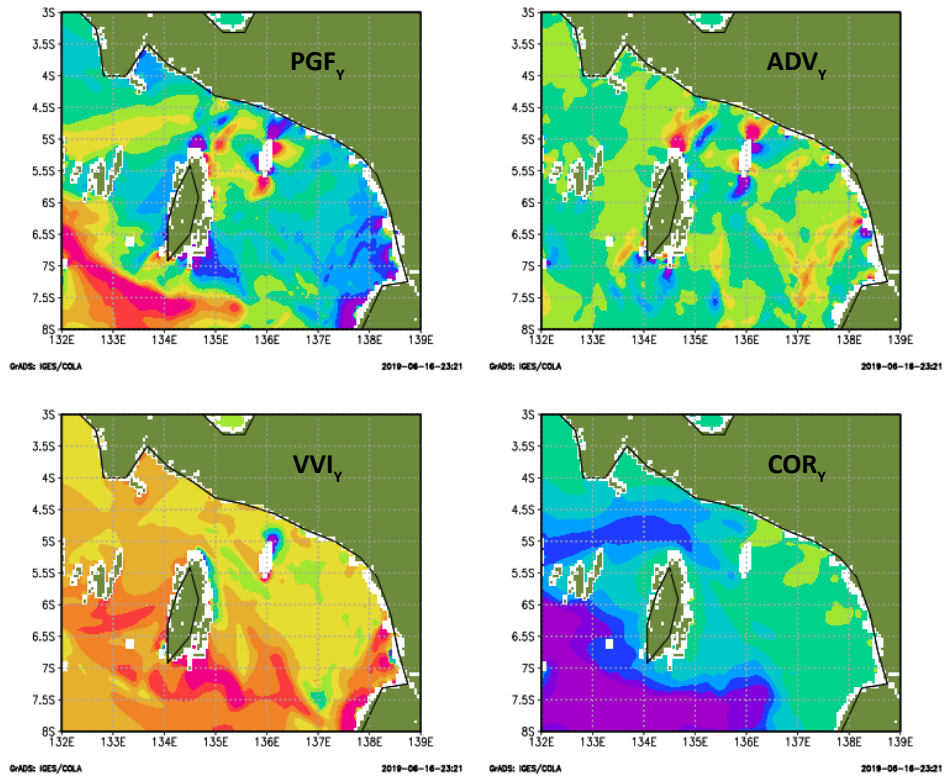


Figure 6.4: Momentum components in the meridional direction in water surface ($z = 1$) for the WT case during the period of July 2004 (28 days) ($\times 10^{-3} \text{ ms}^{-2}$).

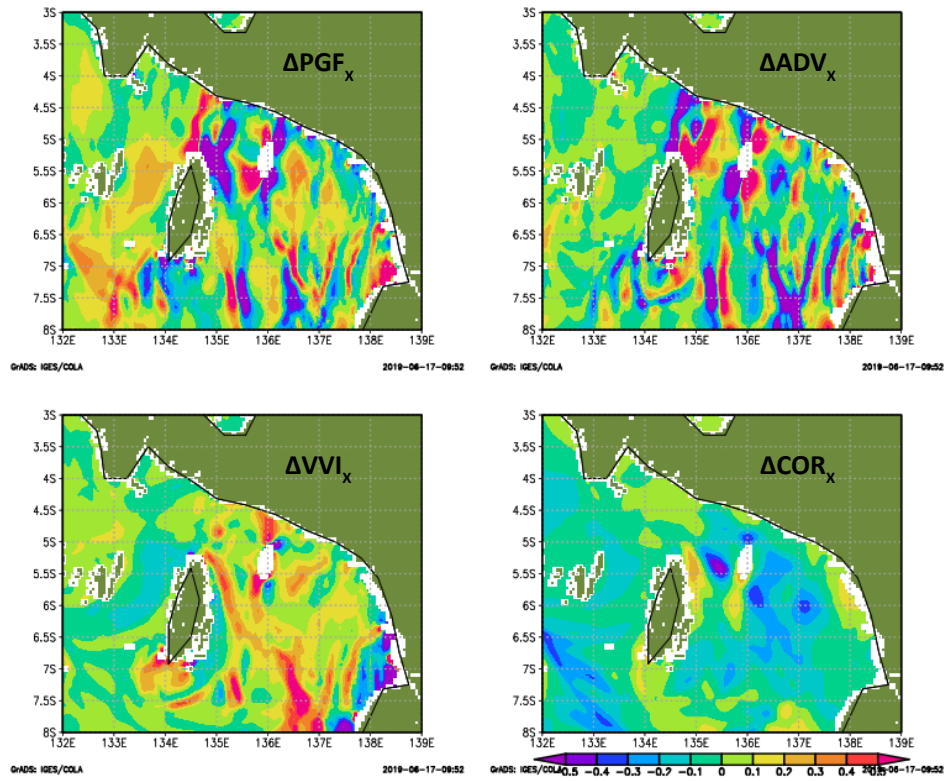


Figure 6.5: The difference of momentum components in the zonal direction in water surface ($z = 1$) between the WT and WO cases (WT-WO) during the period of July 2004 (28 days) ($\times 10^{-3} \text{ ms}^{-2}$).

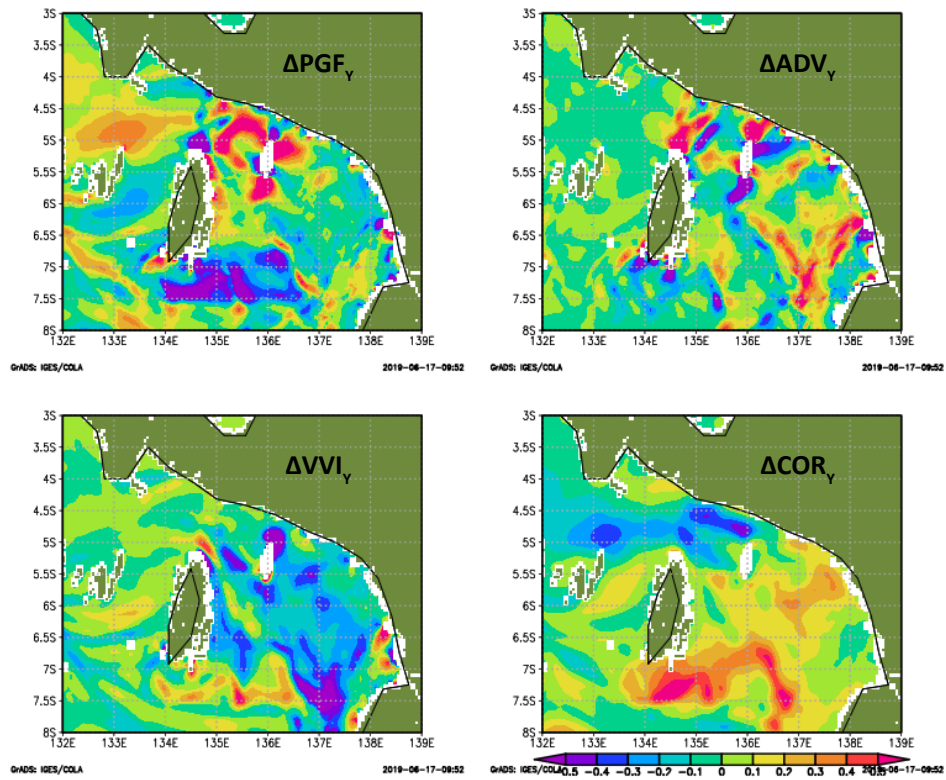


Figure 6.6: The difference of momentum components in the meridional direction in water surface ($z = 1$) between the WT and WO cases (WT-WO) during the period of July 2004 (28 days) ($\times 10^{-3} \text{ ms}^{-2}$).

6.1.2 Vertical Profile of Momentum Balance

6.1.2.1 Section A

Owing to the effect of the wind on water surface circulation (see also in Figure 5.2), a dominant Ekman balance is generally observed in the meridional direction within the upper 20 m of the surface layer along section A in the WO case (Figures 6.7 and 6.8). This is well-correlated with the westward offshore surface currents across Section A, as shown in Figures 5.44b and 5.44d. An Ekman balance is generally also observed in the zonal direction in the same area. However, as discussed in the previous section, the relatively high PGF_x term contributes significantly to the disruption of the Ekman transport, as observed over the northern Aru Headland (4.8°S/134.6°W). In the deeper layer (the interior), the momentum balance in the zonal and meridional directions shows a dominant geostrophic balance, which is well correlated with south-eastward currents (see also Figures 5.27, 5.28, and 5.29). Considering the uniform vertical structure of the horizontal barotropic pressure gradient force (PGFT) within the water column, it can be concluded that the vertical structure of the horizontal baroclinic pressure gradient force (PGFC) contributes significantly to the formation of the vertical structure of subsurface currents along section A. Therefore, the relatively high PGF term at a depth of approximately 60 m is supposed to be the main factor responsible for the maximum velocity around this layer (Figure 5.44), and its intensity is dependent on the density of the ITF water mass (see also Section 5.3.3).

This pattern of momentum balance across section A is generally also found in the WT case. However, a significant difference is observed over the continental slope and the bump, as indicated by the relatively higher magnitude of the PGF and ADV terms (Figures 6.9 - 6.12). This pattern is related to the nonlinear interactions of the tidal flow and bottom topography, as discussed in section Appendix A, that induces circulation cells across the slope and upwelling over the bump. It is also observed that tidally enhanced vertical mixing contributes to a reduced PGF term in the subsurface layer, which is the main factor responsible for subsurface currents between the depth of 20 and 150 m being weaker in the tide inclusion simulation than in the tide exclusion simulation. Furthermore, significant difference is also observed in the bottom topography (Figures 6.11 and 6.12). It is found that the VVI term in the tide inclusion simulation is generally larger than that in the tide exclusion simulation. This condition is related to the relatively higher interfacial stress induced by tidally enhanced vertical mixing within the water column and the near-zero bottom stress value.

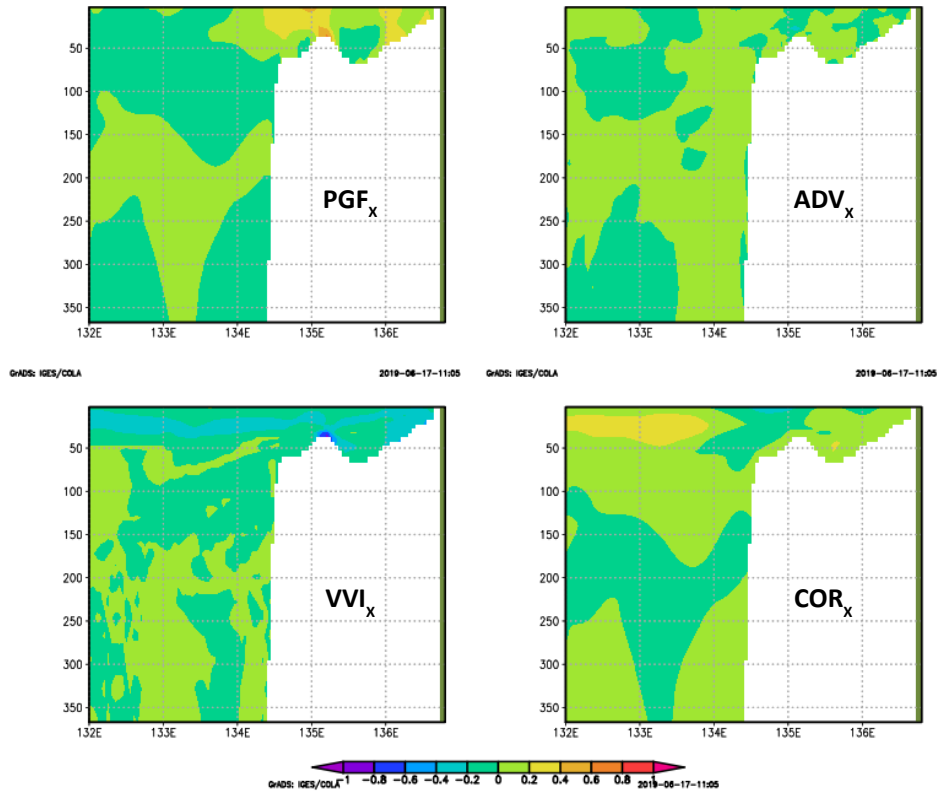


Figure 6.7: Momentum components in the zonal direction along the section A for the WO case during the period of July 2004 (28 days) ($\times 10^{-3} \text{ ms}^{-2}$).

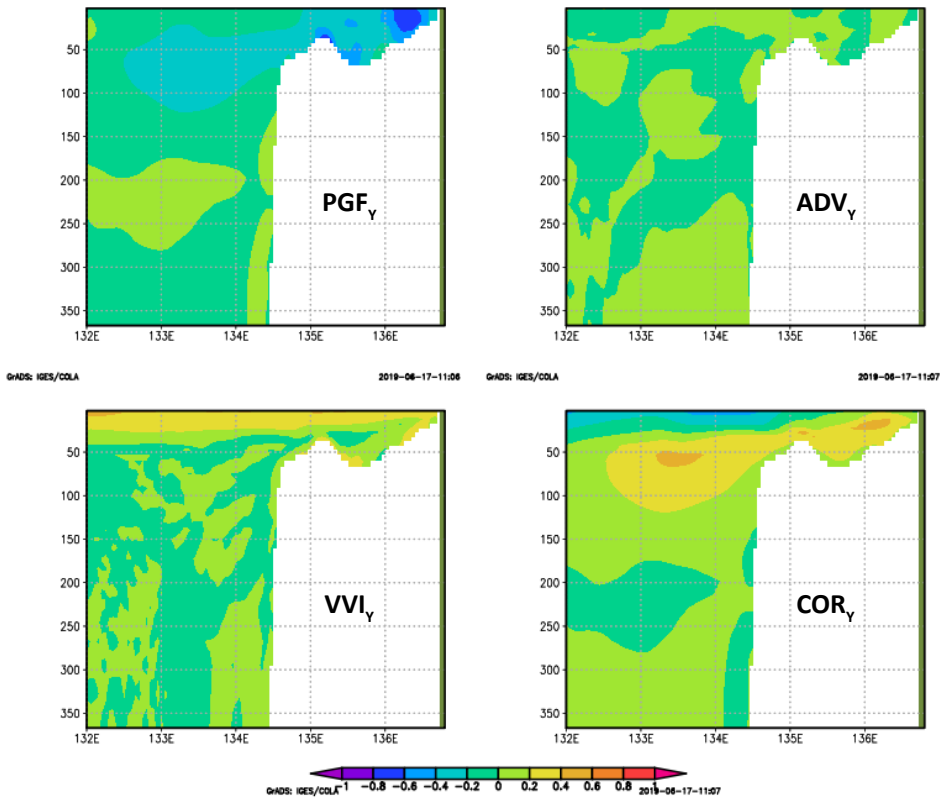


Figure 6.8: Momentum components in the meridional direction along the section A for the WO case during the period of July 2004 (28 days) ($\times 10^{-3} \text{ ms}^{-2}$).

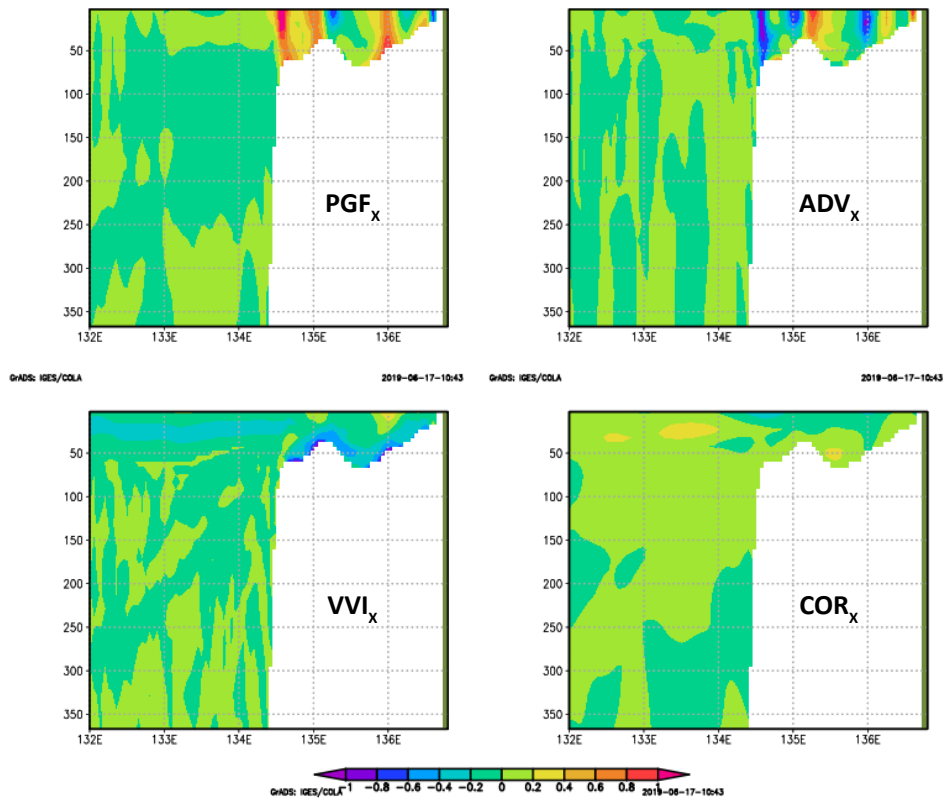


Figure 6.9: Momentum components in the zonal direction along the section A for the WT case during the period of July 2004 (28 days) ($\times 10^{-3} \text{ ms}^{-2}$).

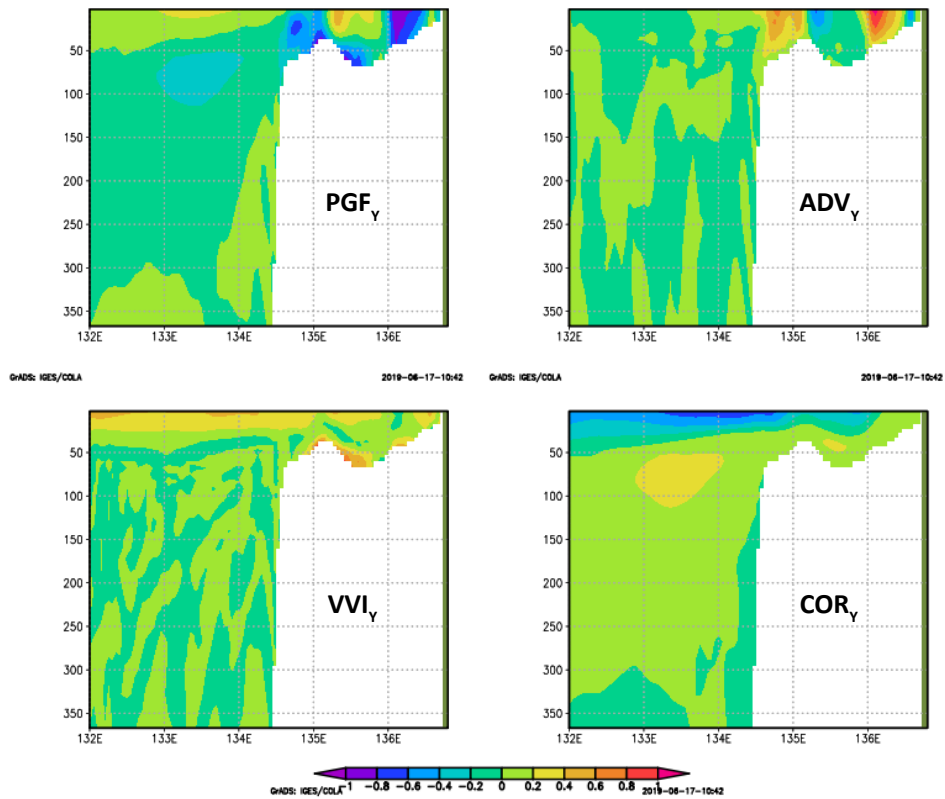


Figure 6.10: Momentum components in the meridional direction along the section A for the WT case during the period of July 2004 (28 days) ($\times 10^{-3} \text{ ms}^{-2}$).

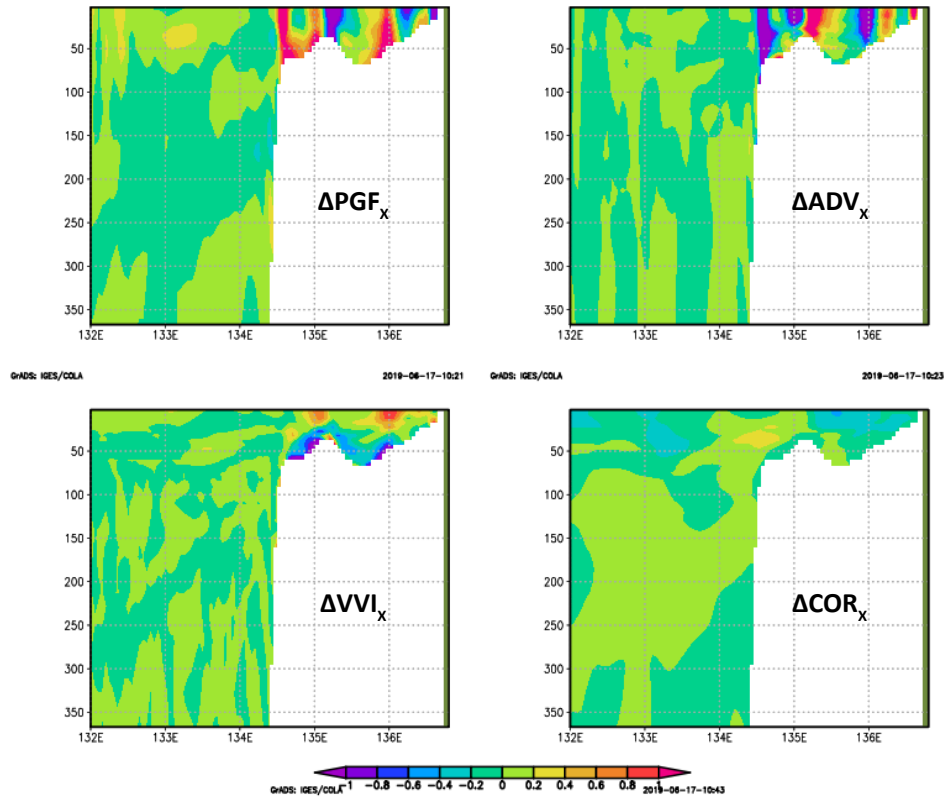


Figure 6.11: The difference of momentum components in the zonal direction along the section A between the WT and WO cases (WT-WO) during the period of July 2004 (28 days) ($\times 10^{-3} \text{ ms}^{-2}$).

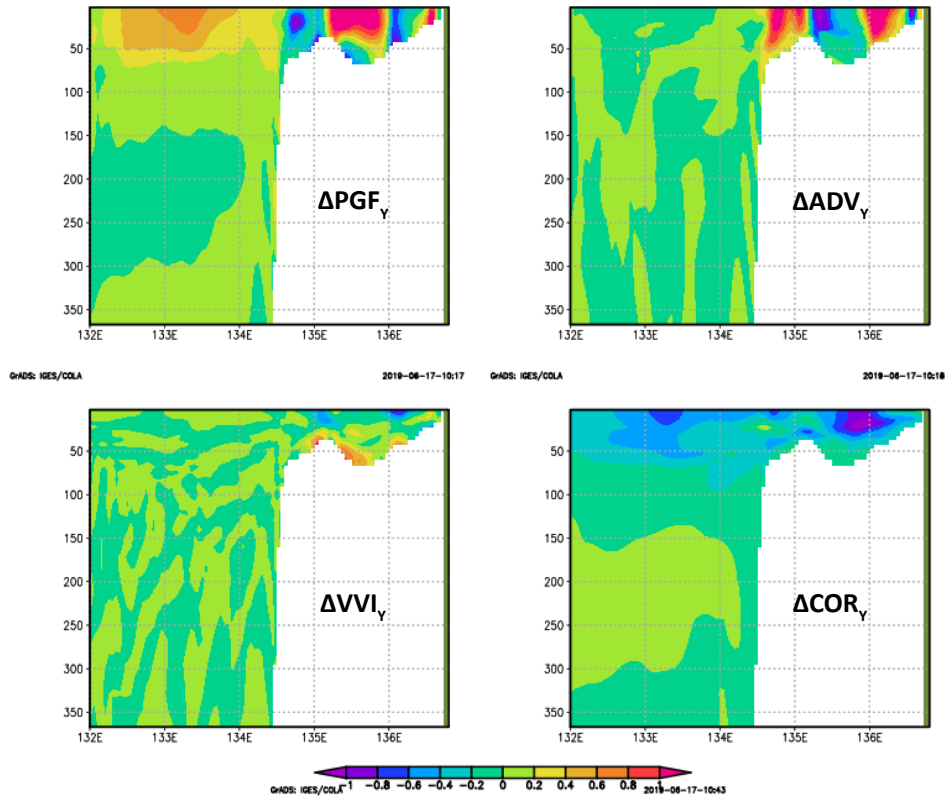


Figure 6.12: The difference of momentum components in the meridional direction along the section A between the WT and WO cases (WT-WO) during the period of July 2004 (28 days) ($\times 10^{-3} \text{ ms}^{-2}$).

6.1.2.2 Section B

Over the continental slope of section B, the dominant geostrophic balance in the meridional direction in the WO case is found in the entire water column. By considering the uniform vertical structure of the horizontal barotropic pressure gradient force in the meridional direction ($PGFT_y$) within the water column, it can be concluded that the horizontal baroclinic pressure gradient force in the meridional direction ($PGFC_y$) contributes significantly to the modification of the vertical structure of the PGF_y term ($PGFC_y + PGFT_y$), weakening the PGF term in deeper layers. It is also found that as a result of wind over the water surface, the VVI_y term contributes significantly to the momentum balance within 20 m of the upper layer. This reinforces the PGF_y term and, under the Coriolis force, generates relatively strong westward (offshore) surface currents. Below this layer (>20 m depth), the PGF_y term is mostly directed northward. Under Coriolis influence, it generates westward subsurface currents that are in the same direction as the surface currents (indicated by $COR_y < 0$). Only a few parts of this layer have a negative PGF_y term, which is directed southward to generate (under Coriolis force) onshore currents. The results suggest that the westward subsurface currents are the main factor canceling the onshore (eastward) currents induced by the Ekman surface transport and suppressing upwelling (see also section 5.4.4).

Similarly, in the zonal direction in the WO case, a dominant geostrophic balance is also found in the entire water column over the continental slope, while the magnitude of the VVI_x and ADV_x terms are relatively lower than that of the PGF_x term. Above 100 m depth, it is observed that the PGF_x term is mostly directed eastward ($PGF_x > 0$). Here, the Ekman transport tends to weaken the geostrophic transport as the direction of the VVI_x and ADV_x terms are opposite that of the PGF_x term. The summation of PGF_x , VVI_x , and ADV_x terms is balanced by a negative COR_x term, indicating northward currents. Due to the presence of a continental slope in meridional direction (see also Figure 2.2), these relatively strong northward currents contribute significantly to the upwelling of the subsurface water. In the deeper layer (100–200 m depth), the PGF_x term is negative, and thus its direction is opposite that of the PGF term in the upper layer (above 100 m). Again, this indicates the strong influence of the baroclinic- PGF_x term in producing the total pressure gradient force. The negative- PGF_x term, under Coriolis force, in this layer is related to eastward currents (see also Figures 5.27 and 5.31).

Over the continental slope of section B, the inclusion of tidal forcing in the simulation generally leads to the PGF_y term having a considerably reduced magnitude in the depth above

100 m around the continental slope; changes in the VVI and ADV terms are relatively smaller (Figures 6.17 and 6.18). Under the influence of the Coriolis effect, the lower PGF_y term generally leads to weaker offshore currents above depths of 100 m. The results show that, in the deeper layer (>100 m in depth), the modification of the PGF_y , ADV_y , and VVI_y terms is balanced by the COR_y term, and as such there are more areas with a COR term > 0. This indicates more onshore currents. This is suggested to intensify upwelling around the slope, as indicated by upward-sloping isotherms in the onshore direction being steeper in the WT case than in the WO case (as discussed in Section 5.4.4). The results suggest that the stronger upwelling in this area is also induced by northward currents, driven by the PGF_y term above 100 m in depth, under Coriolis effect, being stronger in the WT case than in the WO case.

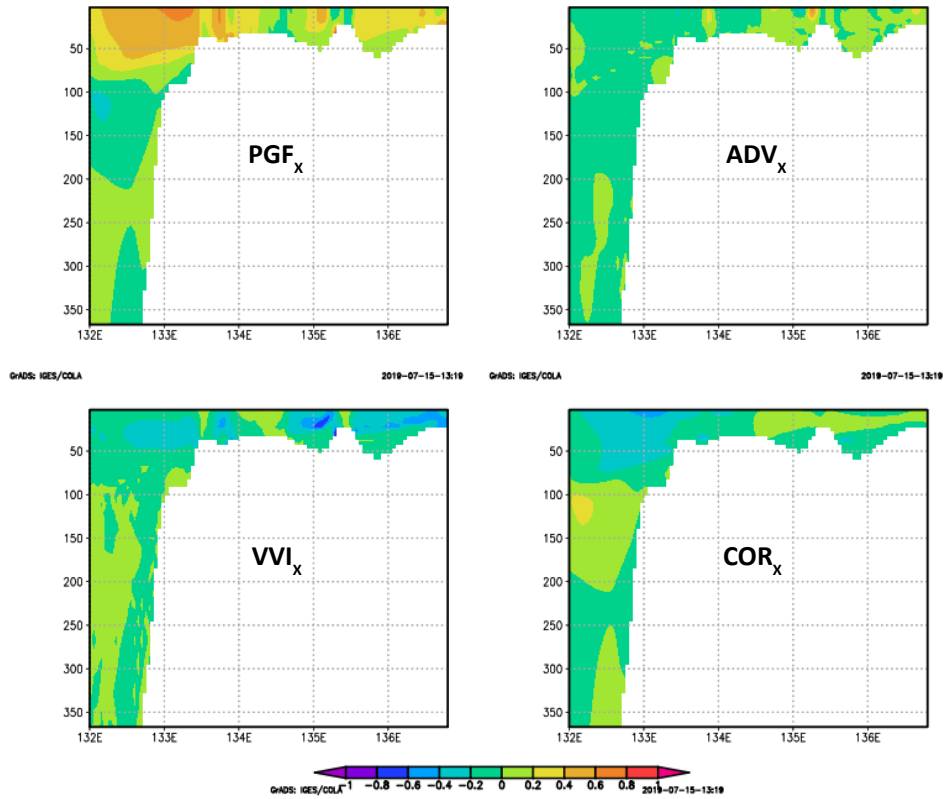


Figure 6.13: Momentum components in the zonal direction along the section B for the WO case during the period of July 2004 (28 days) ($\times 10^{-3} \text{ ms}^{-2}$).

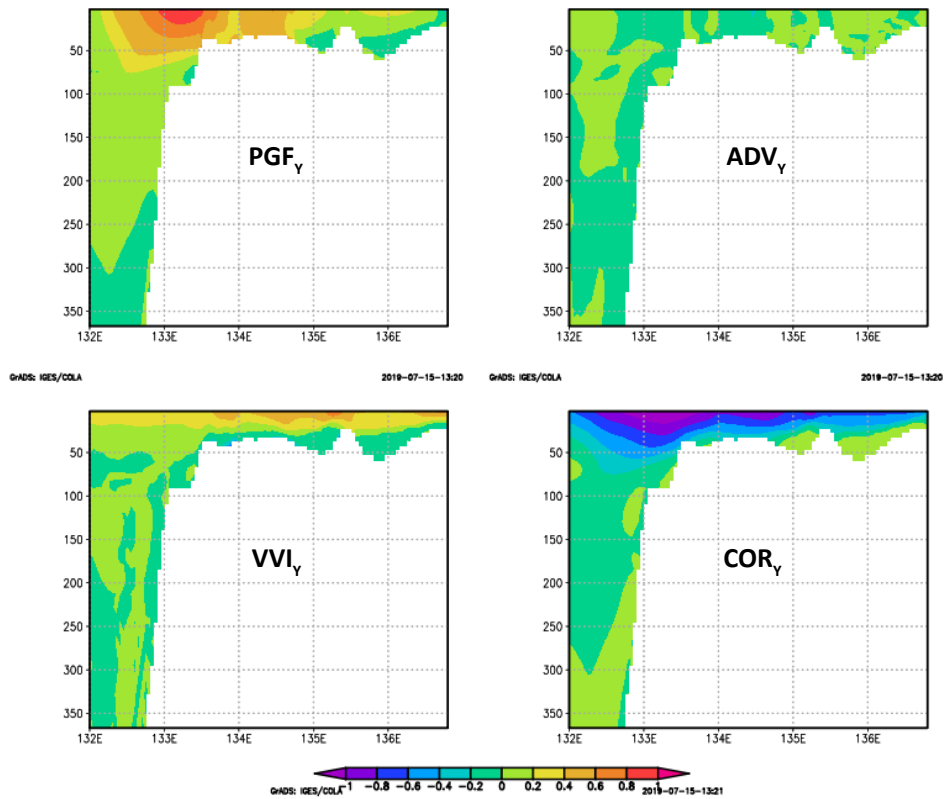


Figure 6.14: Momentum components in the meridional direction along the section B for the WO case during the period of July 2004 (28 days) ($\times 10^{-3} \text{ ms}^{-2}$).

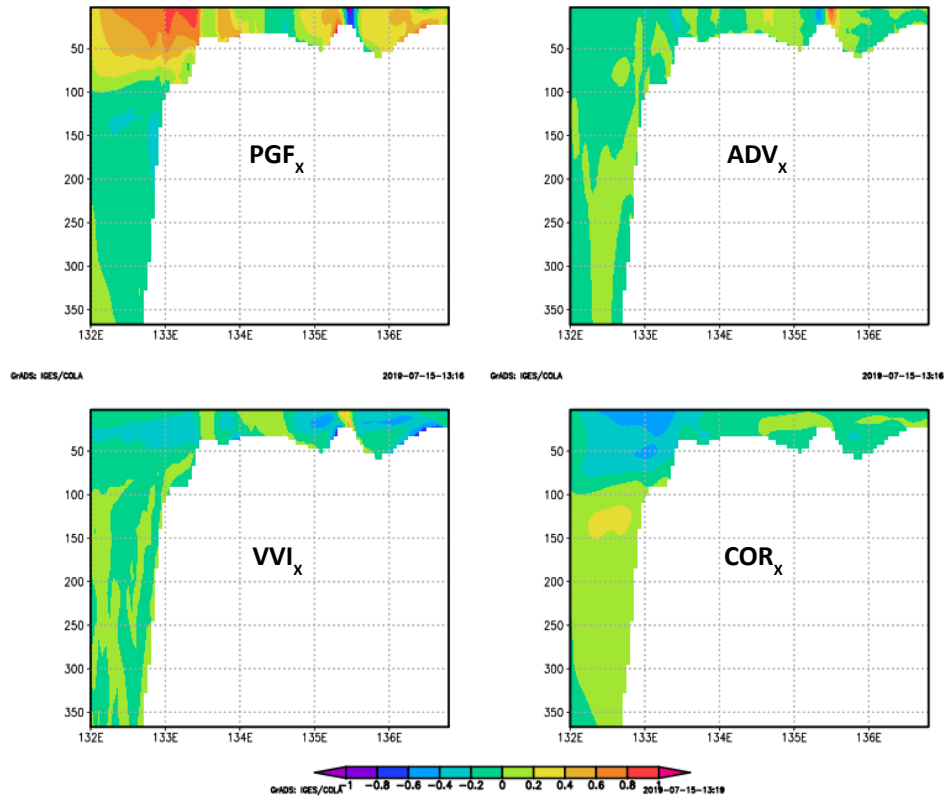


Figure 6.15: Momentum components in the zonal direction along the section B for the WT case during the period of July 2004 (28 days) ($\times 10^{-3} \text{ ms}^{-2}$).

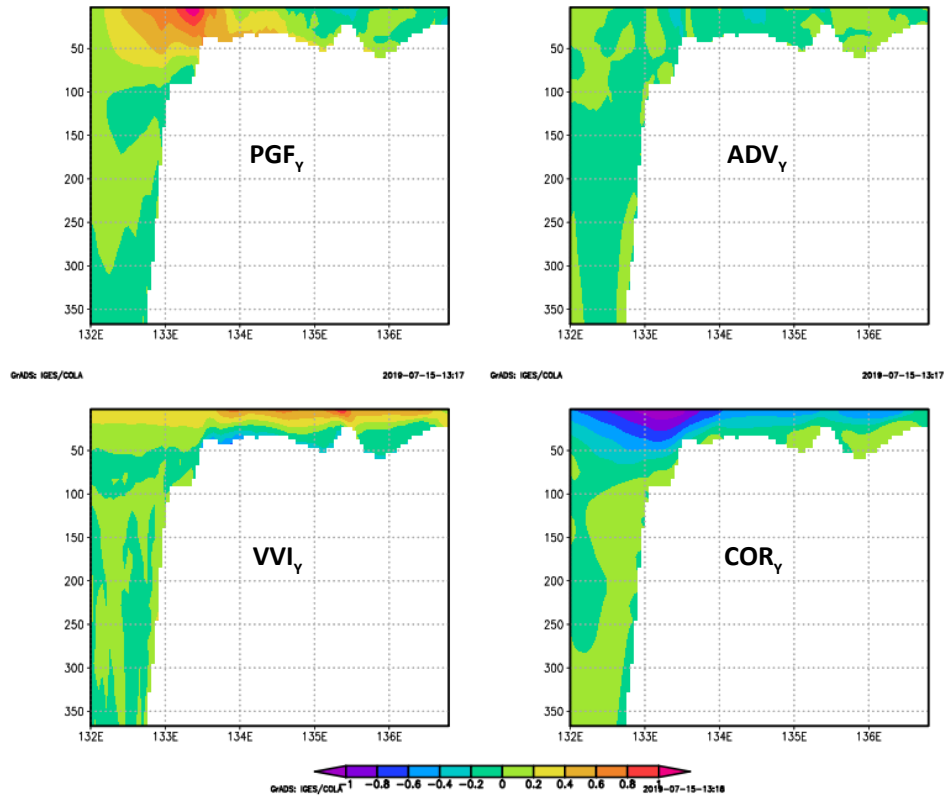


Figure 6.16: Momentum components in the meridional direction along the section B for the WT case during the period of July 2004 (28 days) ($\times 10^{-3} \text{ ms}^{-2}$).

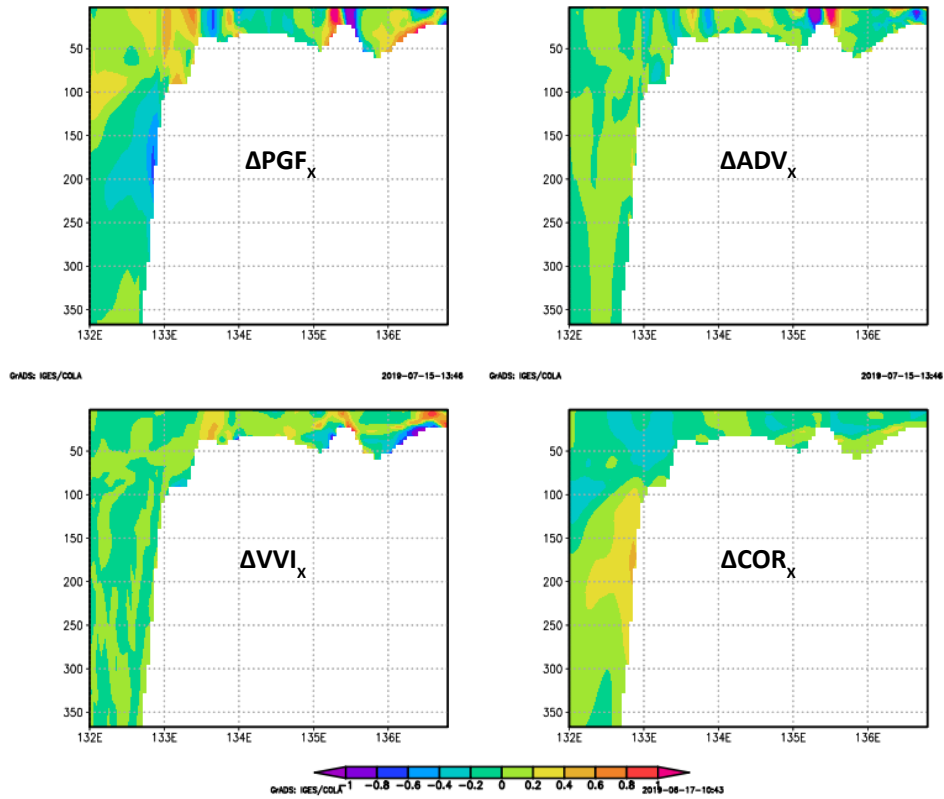


Figure 6.17: The difference of momentum components in the zonal direction along the section B between the WT and WO cases (WT-WO) during the period of July 2004 (28 days) ($\times 10^{-3} \text{ ms}^{-2}$).

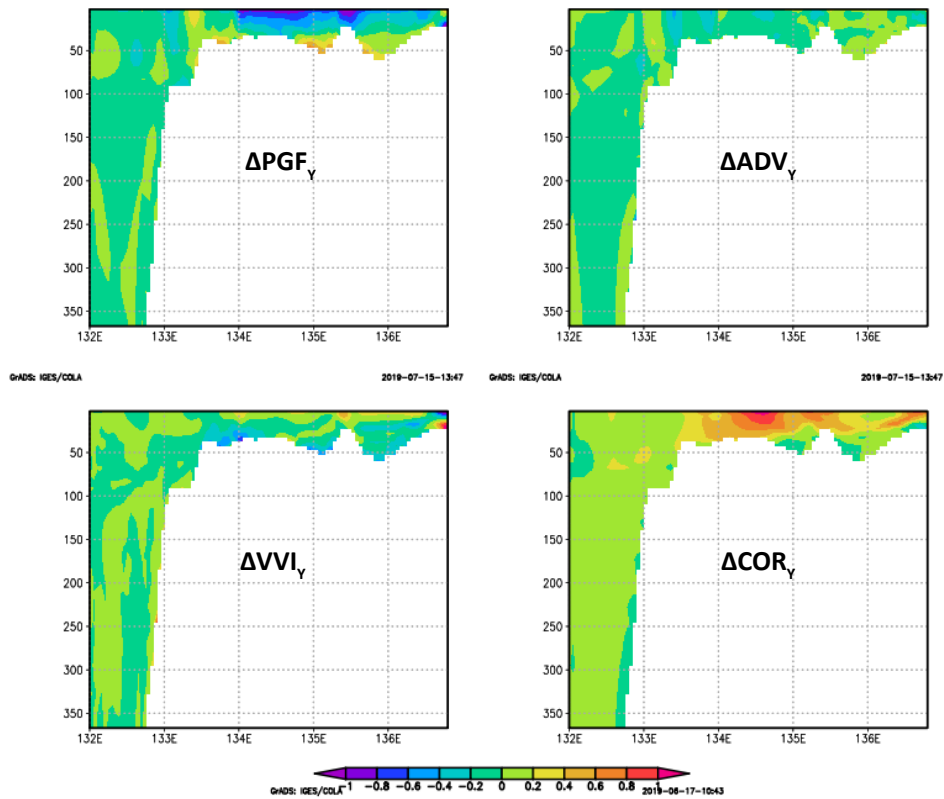


Figure 6.18: The difference of momentum components in the meridional direction along the section B between the WT and WO cases (WT-WO) during the period of July 2004 (28 days) ($\times 10^{-3} \text{ ms}^{-2}$).

6.1.2.3 Section C

Near the eastern border of section C, the dominant Ekman balance in the zonal direction, which is significantly disturbed by the PGF term in the WT and WO cases, is found not only in the upper layer but also in the entire water column. Meanwhile, the dominant geostrophic balance is mostly found within the water column near the western border of section C (Figures 6.19 and 6.21). In the meridional direction, the dominant Ekman balance in this area is only identified in the upper layer (Figures 6.20 and 6.22). Below this layer, the momentum balance equation is principally characterized by a geostrophic balance.

As discussed in section 5.5, the impacts of tide forcing in weakening vertical stratification is mostly observed within the water column of section C. As a consequence of this, the results show that, the VVI term in the zonal and meridional directions is generally larger near the bottom in the tide inclusion simulation than in the tide exclusion simulation. Meanwhile, the VVI term in the zonal and meridional directions in the upper layer is generally lower in the tide inclusion simulation than in the tide exclusion simulation (Figures 6.19–6.24). Larger values of the ADV term are generally found in the zonal and meridional directions within the water column of section C in the WT case than in the WO case. Similar to the surface layer (discussed in section 6.1.1), tidal mixing contributes considerably to the modification of the PGF term in the subsurface layer. Around the coast of Papua, it is found that the PGF_x term is relatively higher in the WT case than in the WO case (Figures 6.19, 6.21 and 6.23). Considering the opposite directions of the PGF and VVI terms, the results show that the higher magnitudes of the PGF_x , ADV_x and VVI_x terms is balanced by a lower COR_x term (Figures 6.19, 6.21 and 6.23). This condition suggests that the change in the PGF term dominates the VVI term and as in the WO case, the results also show the dominance of the Ekman balance in the WT case. The lower COR_x term correlates with southward subsurface currents being weaker in the WT case. Meanwhile, the PGF_y in the lower layer is relatively lower in the WT case than in the WO case (Figure 6.24). Here, by considering the opposite directions of the PGF_y and VVI_y terms and the dominant geostrophic balance in the WT and WO cases, the results show that the lower magnitude of the PGF_y term and higher magnitudes of the ADV_y and VVI_y terms are balanced by COR_y term ($\Delta COR_y < 0$) being lower in the WT case than in the WO case. The lower COR_y term is correlated with eastward subsurface currents being lower in the WT case than in the WO case (Figure 6.24). The lower cross circulation along the western border of Section C indicates that upwelling is less intensive in the WT case than in the WO case.

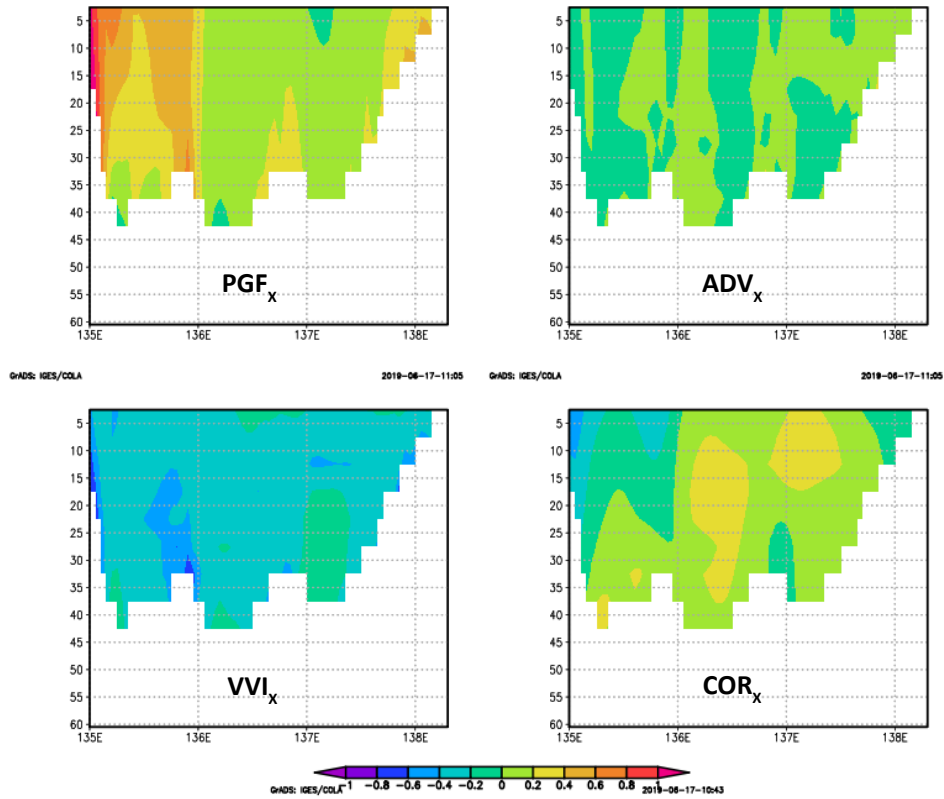


Figure 6.19: Momentum components in the zonal direction along the section C for the WO case during the period of July 2004 (28 days) ($\times 10^{-3} \text{ ms}^{-2}$).

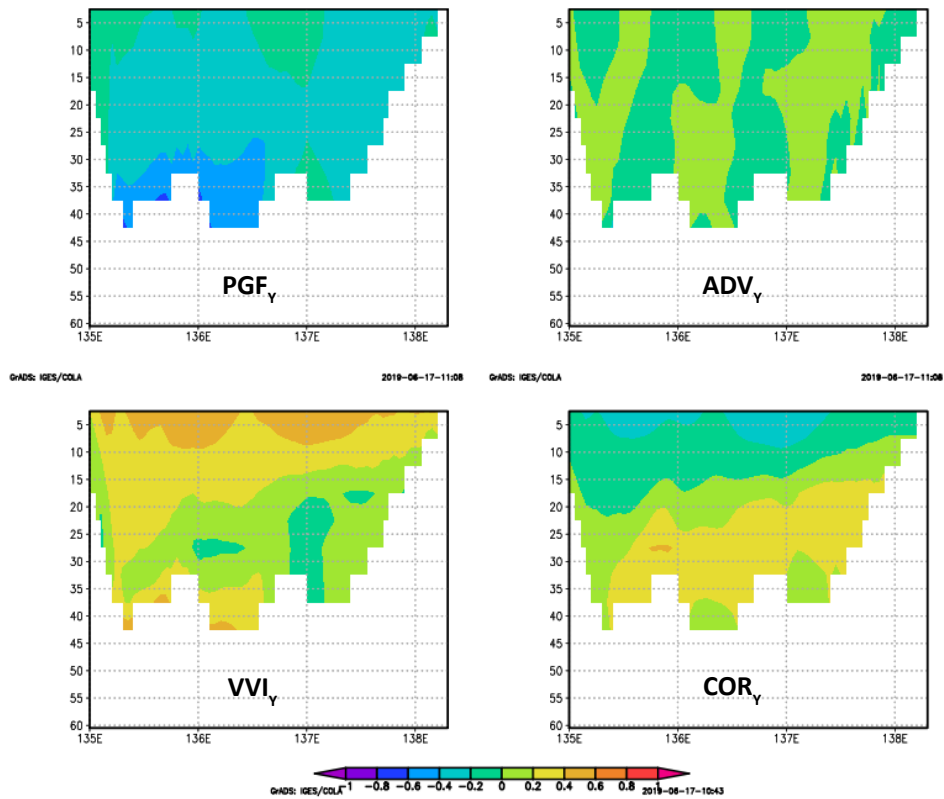


Figure 6.20: Momentum components in the meridional direction along the section C for the WO case during the period of July 2004 (28 days) ($\times 10^{-3} \text{ ms}^{-2}$).

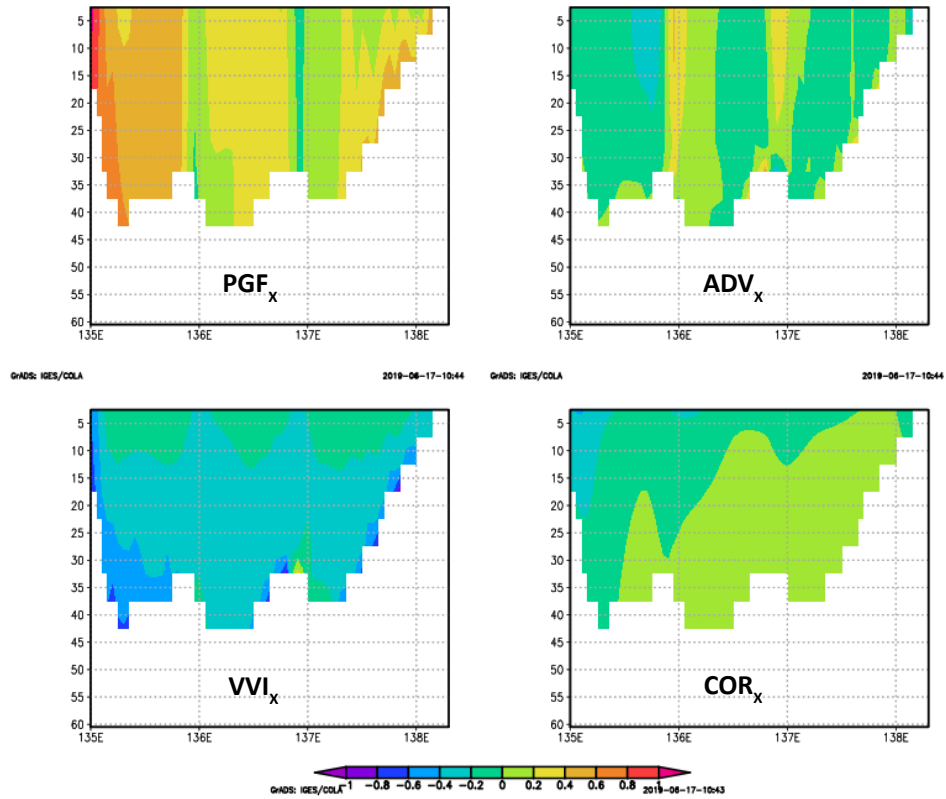


Figure 6.21: Momentum components in the zonal direction along the section C for the WT case during the period of July 2004 (28 days) ($\times 10^{-3} \text{ ms}^{-2}$).

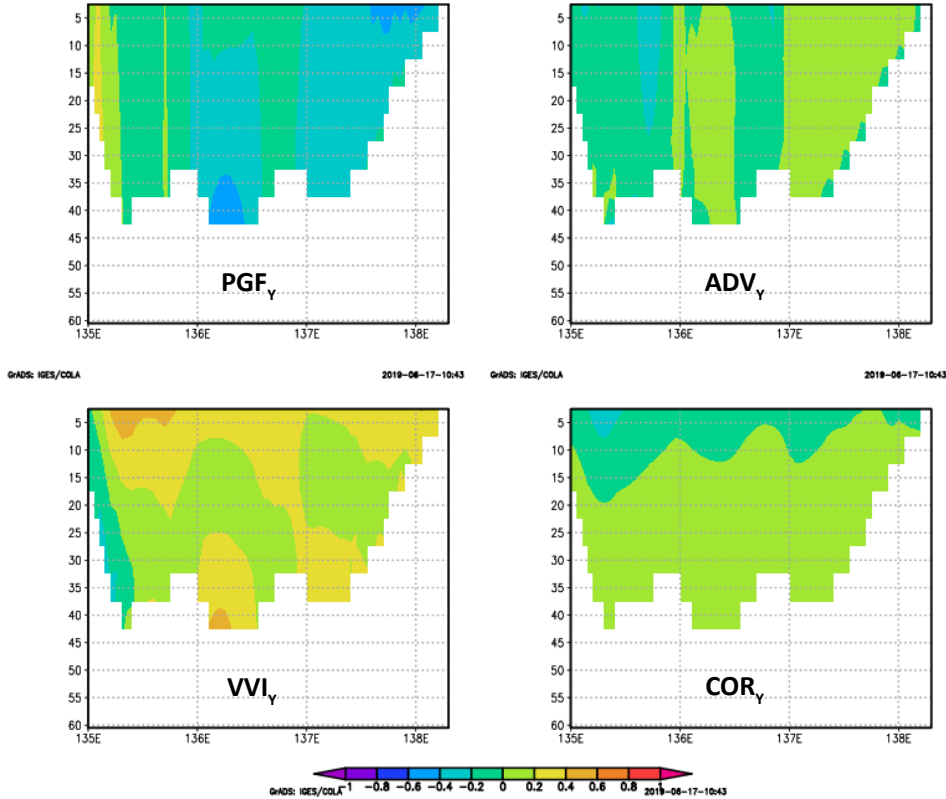


Figure 6.22: Momentum components in the meridional direction along the section C for the WO case during the period of July 2004 (28 days) ($\times 10^{-3} \text{ ms}^{-2}$).

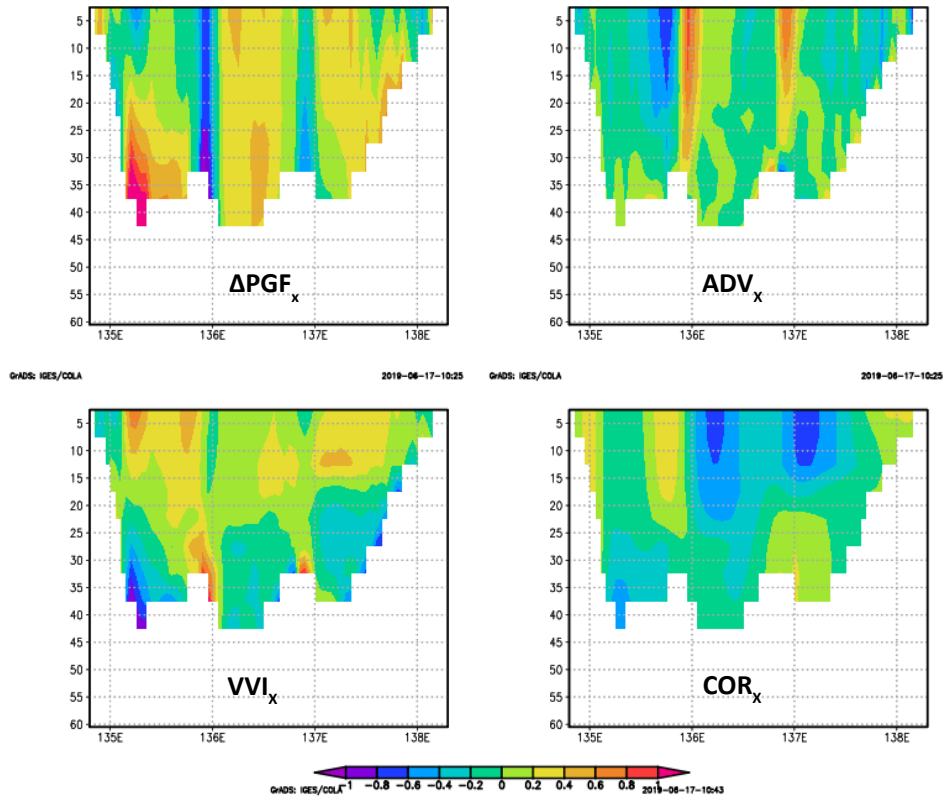


Figure 6.23: The difference of momentum components in the zonal direction along the section C between the WT and WO cases (WT-WO) during the period of July 2004 (28 days) ($\times 10^{-3} \text{ ms}^{-2}$).

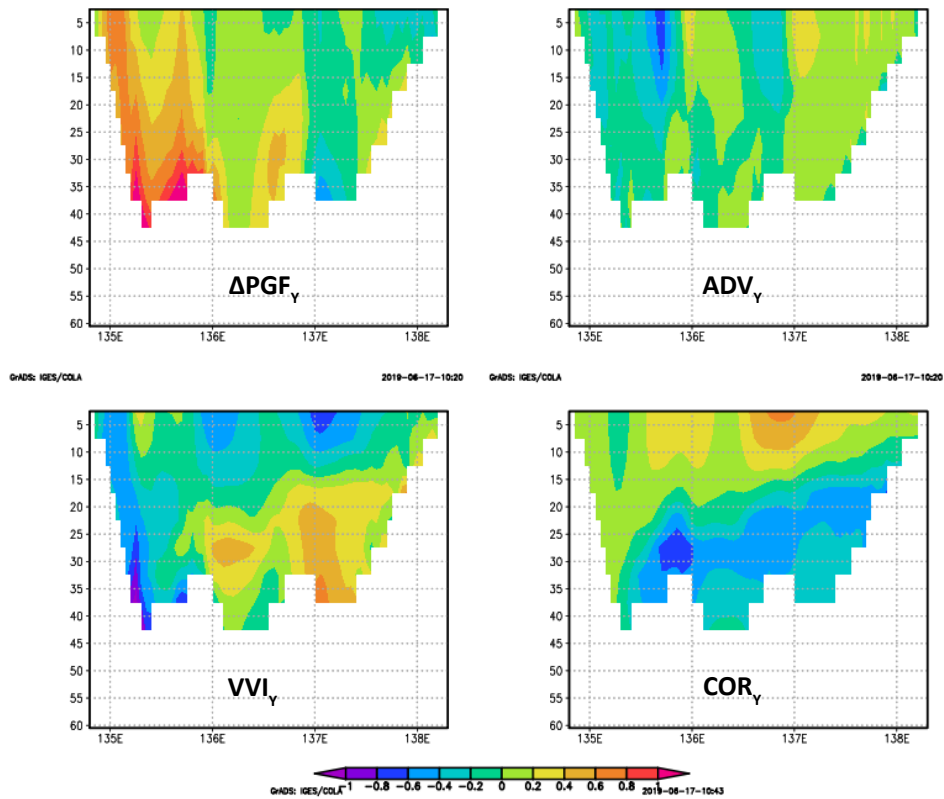


Figure 6.24: The difference of momentum components in the meridional direction along the section C between the WT and WO cases (WT-WO) during the period of July 2004 (28 days) ($\times 10^{-3} \text{ ms}^{-2}$).

6.2 Interaction between River Runoff and Tide–Wind Driven Circulation during Wind–Driven Upwelling

In contrast to tide exclusion simulation (the WO case), which show significant difference of momentum balance structures to the WT case, the river-tide inclusion simulation (the WRT case) has structures similar to those of the tide inclusion simulation (the WT case). However, the magnitude of each momentum component shows a reasonable difference (Figures 6.25 - 6.29). In general, the river runoff tends to enhance the vertical density stratification and, subsequently, to weaken the vertical eddy viscosity coefficient (see also section 5.5). In the surface water, the lower viscosity generally leads to a weakening of the interfacial stress and reduces the surface Ekman depth. By considering the same wind forcing applied in the two simulations, the reduced interfacial stress in the WRT case leads to the enhancement of the VVI term as observed in the upper layer (< 15 m depth) where most of the wind's frictional energy (then is called as the plume layer) is trapped; this is generally observed over sections A, B and C. However, in the relatively shallow water as observed around the western coast of Papua (southern section C), increased stratification leads to a lower VVI term. This condition indicates that the velocity shear in this area contributes more to the determination of viscous force than the vertical viscosity coefficient (see also section 3.5). It is suggested that, in the upper layer, the higher stratification induced by river runoff leads to higher velocity shear, which then increase interfacial stress. Consequently, the surface-level VVI term is less in WRT case than that in the WT case. In the zonal direction, an increase VVI term is indicated by positive values ($\Delta VVI_x > 0$) while in the meridional direction negative values ($\Delta VVI_y < 0$) are found (Figures 6.25 and 6.26). The reverse patterns are generally true. In general, the river runoff also contributes considerably to the modification of the PGF term; the modification of the ADV term is relatively smaller than VVI and PGF term.

The following discussion will focus more on the momentum balance in the meridional direction which is related to the cross-shelf circulation in inducing upwelling across the continental slope of sections A, B and C. In section A, the river runoff contributes to the considerable modification of PGF_y and ADV_y terms in the upper layer, with changes being comparable to the change in the VVI_y term (Figures 6.26 and 6.27). The results show that the changes to the VVI_y , PGF_y and ADV_y terms in the WRT case are balanced by a considerably higher COR_y term ($\Delta COR > 0$, see Figures 6.25 and 6.26); this, in turn, indicates stronger residual surface currents in the zonal direction. In the lower layer of section A (below depth of

approximately 15 m), increased stratification generally leads to the weakening of the VVI_y term ($\Delta VVI_y > 0$) and enhancement of the PGF_y term ($\Delta PGF_y > 0$). These are balanced by a higher COR_y term (Figure 6.27), which indicates the stronger compensating flows beneath the plume that induce colder surface water temperature (as discussed in section 5.4.3; see also Figures 5.24a and 5.24d).

In section B, in addition to enhancing the VVI_y term, the river runoff also enhances the PGF_y term in the upper layer; meanwhile, changes in the ADV_y term are relatively smaller than those in the PGF and VVI terms (Figures 6.4 and 6.29). By considering the unidirectionality of the PGF_y and VVI_y terms, the results show that the enhancement of the PGF_y and VVI_y terms in the WRT case are balanced by a significantly higher COR_y term than in the WT_y case. It is also found that the modification of the COR_y term in section B is larger than in sections A and B. Below the plume layer of section B (20 – 100 m depth), considerable changes in the VVI_y and PGF_y terms are also found (Figure 6.28). The changes are identified as being balanced by a relatively lower COR_y term ($\Delta COR_y > 0$) than in the WT case, indicating that westward subsurface are weaker. The results suggest that these lower subsurface currents are related to the more subsurface waters (below the plume layer) being upwelled to the upper layers, as induced by the stronger surface Ekman currents. Consequently, the SST around this area is colder (see also Figures 5.31a and 5.31d). As discussed in section 6.1.1.2, the relatively high PGF term over the slope of section A leads to stronger offshore currents in the upper layers (within 100 m), which cancels out the onshore currents induced by Ekman surface currents. By considering continuity conservation around the slope, it can be concluded that the stronger surface Ekman currents will induce stronger onshore currents, which subsequently reduces the offshore subsurface currents that arise geostrophically from pressure gradient due to spatial variations in wind stress (as discussed in section 6.1.1). In the deeper layer (between 100 and 200 m depth), the stronger onshore currents arise geostrophically are identified, as indicated by the higher magnitude of the PGF_y ($\Delta PGF_y < 0$) and Coriolis ($\Delta COR_y > 0$) terms.

Comparing the WRT and WT cases, the results again show that the river runoff mostly contributes to the considerable enhancement of the PGF_y term in the upper layer of the western border of section C while changes in the ADV_y term are relatively smaller (Figures 6.4 and 6.29). Even though the PGF_y term tends to reduce the Ekman surface transport as indicated by the opposite directions of the VVI_y and PGF_y terms, the results show that the higher magnitudes of the VVI_y and PGF_y terms in the WRT case ($\Delta VVI < 0$, $\Delta PGF < 0$) are

balanced by the considerably higher COR_y term ($\Delta COR_y > 0$) (Figures 6.25 and 6.26), indicating the stronger residual surface currents in the zonal direction. This condition suggests that the change in the VVI_y term dominates the PGF_y term. The enhanced surface currents in the WRT case generate considerably stronger compensating flow as indicated by the relatively higher COR_y term ($\Delta COR_y < 0$) that results in colder surface water around the western coast of Papua (see also Figures 5.24a and 5.24b).

In the WRT case, the increased surface transport in the zonal direction driven by river runoff generally generates a higher SSH around the western border of section C than in the river runoff exclusion simulation. This is indicated by the relatively higher PGF term directed to eastward ($\Delta PGF_x < 0$) (Figure 6.25). It is also observed that the river runoff contributes to the enhancement of the VVI term ($\Delta VVI_x < 0$). By considering the opposite directions of the PGF_x and VVI_x terms, it is found that the change of these terms is balanced by the COR_x term ($\Delta COR_x > 0$) being moderately higher in the WRT case than in the WT case. This higher COR_x term indicates that there are the stronger northward currents near the western Aru coast that brings relatively colder surface water (see also Figures 5.25a and 5.25d).

The stronger cross circulation as observed across sections A, B, and C indicates that there are more subsurface waters upwelled in the surface due to river runoff. Stronger upwelling is also indicated by relatively colder temperature in the river runoff inclusion simulations than that of the river runoff exclusion simulations as discussed in section 5.4.1.

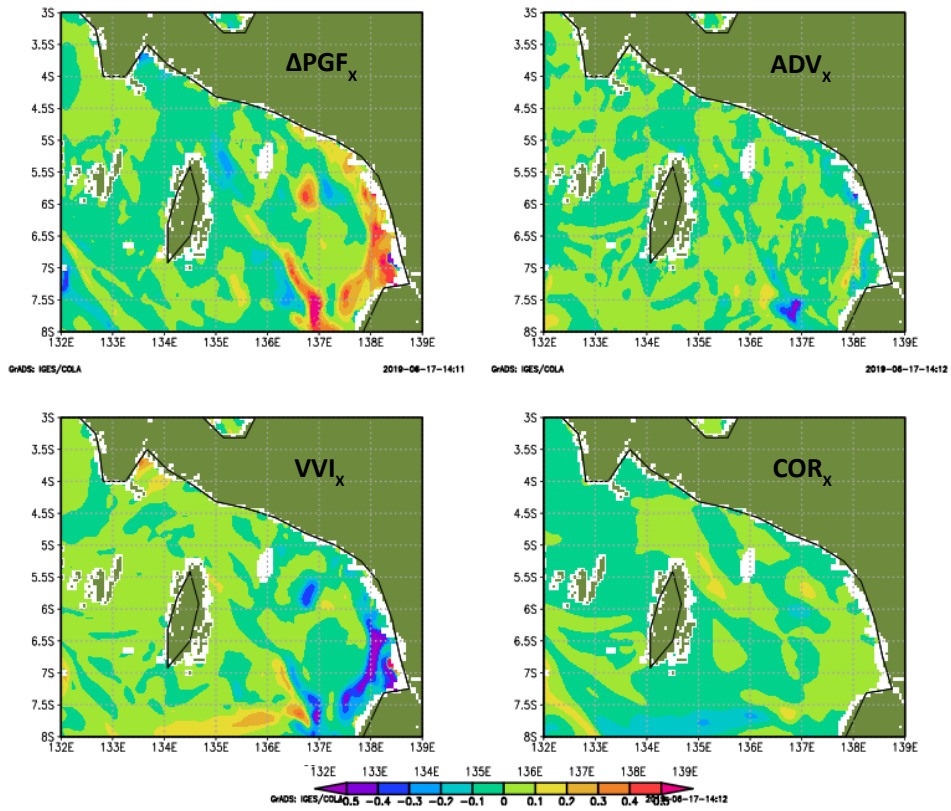


Figure 6.25: The difference of momentum components in the zonal direction in water surface ($z = 1$) between the WT and WO cases (WT-WRT) during the period of July 2004 (28 days) ($\times 10^{-3} \text{ ms}^{-2}$).

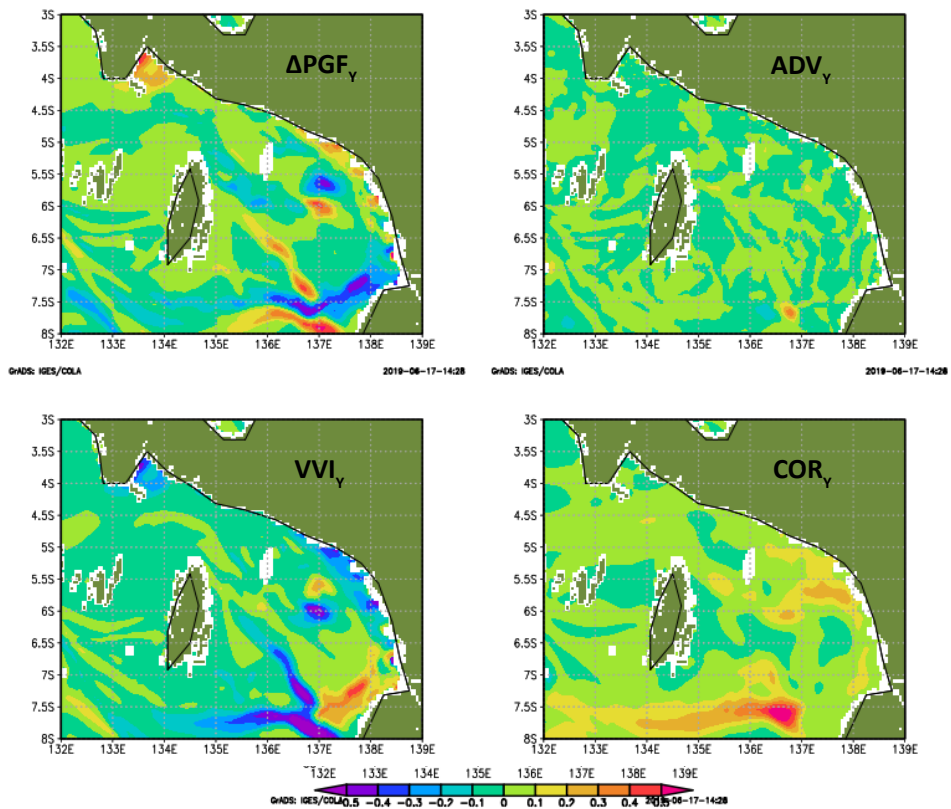


Figure 6.26: The difference of momentum components in the meridional direction in water surface ($z = 1$) between the WT and WO cases (WT-WRT) during the period of July 2004 (28 days) ($\times 10^{-3} \text{ ms}^{-2}$).

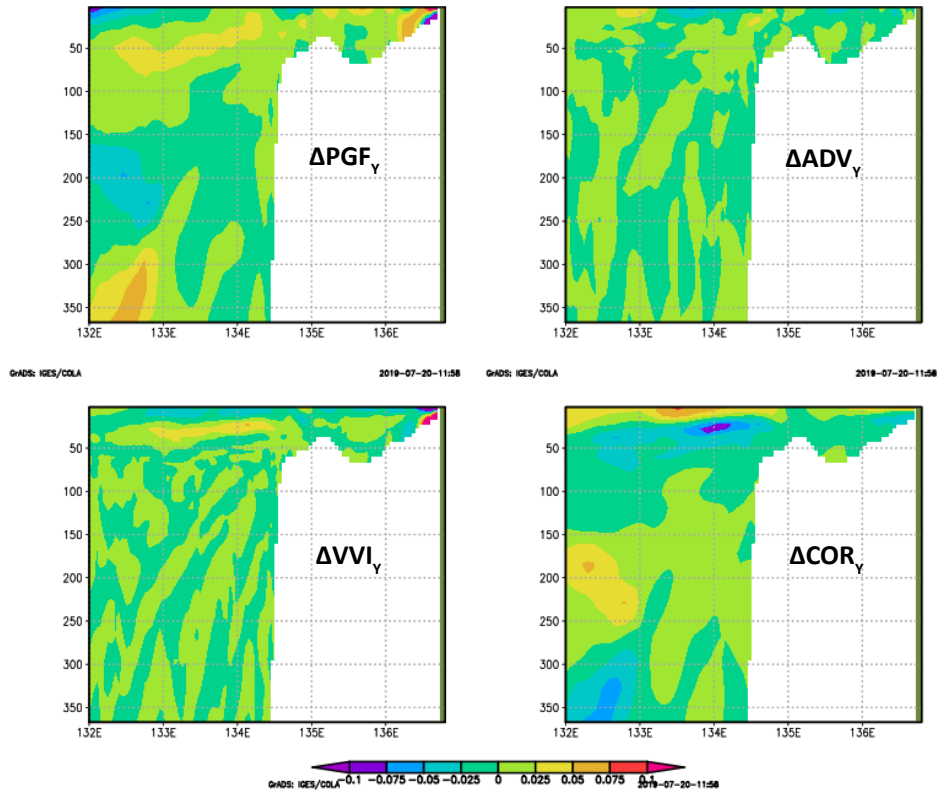


Figure 6.27: The difference of momentum components in the meridional direction along the section A between the WT and WRT cases (WT-WRT) during the period of July 2004 (28 days) ($\times 10^{-3} \text{ ms}^{-2}$)

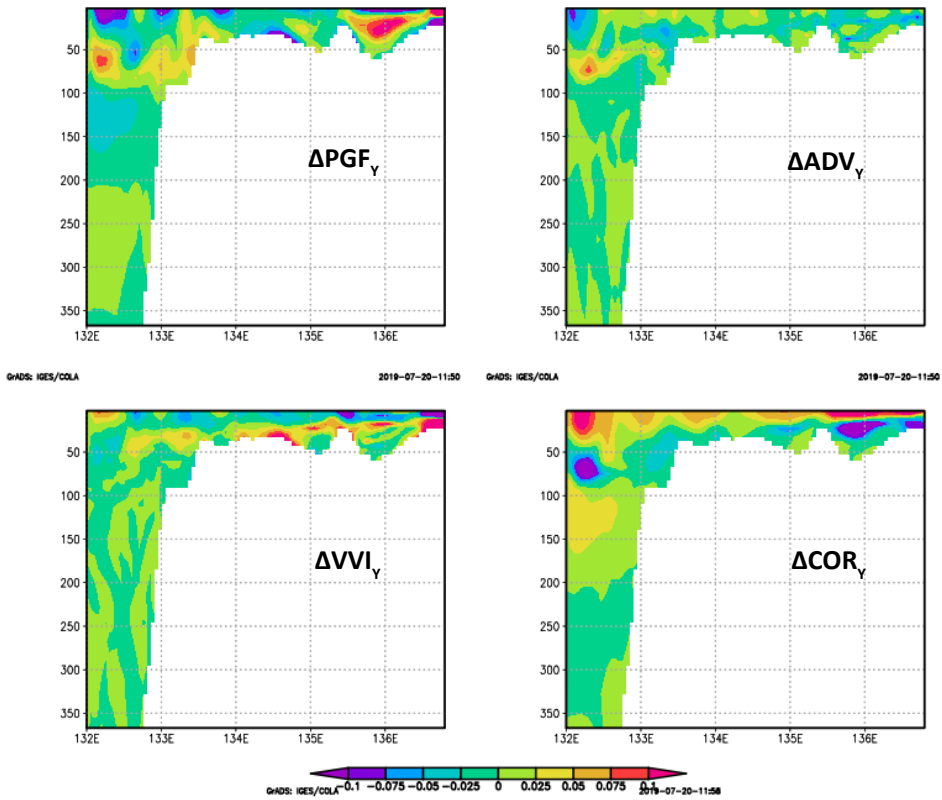


Figure 6.28: The difference of momentum components in the meridional direction along the section B between the WT and WRT cases (WT-WRT) during the period of July 2004 (28 days) ($\times 10^{-3} \text{ ms}^{-2}$).

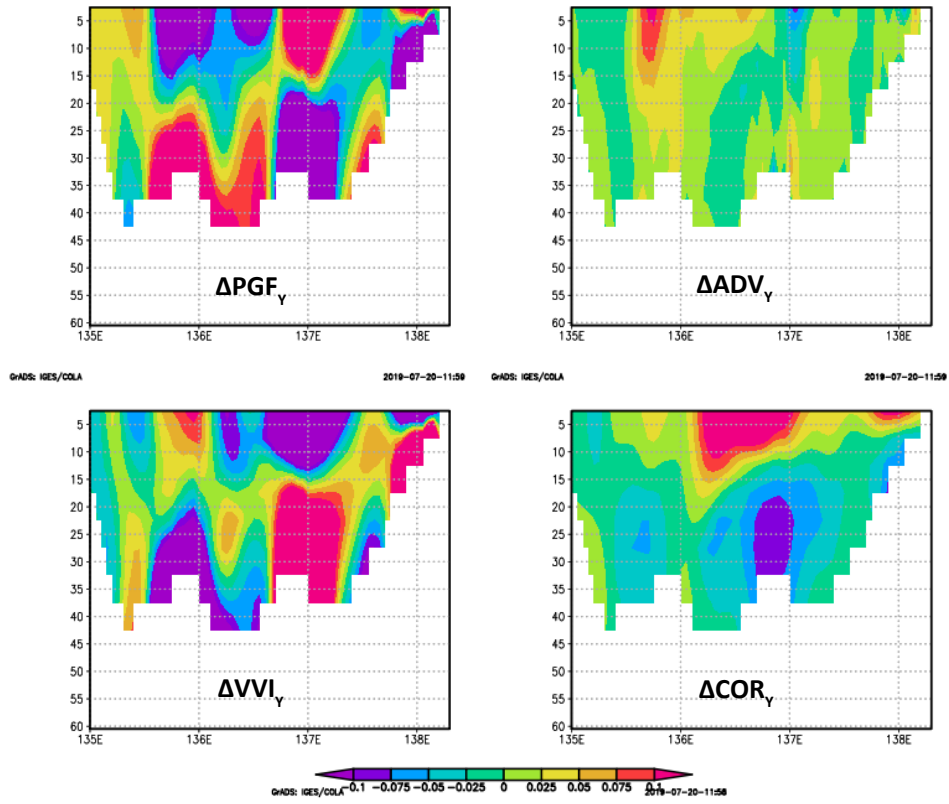


Figure 6.29: The difference of momentum components in the meridional direction along the section C between the WT and WTR cases (WT-WRT) during the period of July 2004 (28 days) ($\times 10^{-3} \text{ ms}^{-2}$).

7. Upwelling Variability in the Northern Arafura and Banda Seas

In this section, upwelling intensity during Normal, El Niño, La Niña conditions, as well as extreme IOD events are identified by observing the physical conditions in the Northern Arafura and the Banda Seas. The years 1990 and 1993 are chosen to represent the “normal” condition, with the Oceanic Niño Index (ONI) and IOD being less than the threshold of $|-/+ 0.5|$. El Niño condition will be represented by the years of 1991, 1997, and 2002, while relatively strong La Niña conditions will be represented by the periods of 1998–2000, 2007–2008, and 2010–2011. Finally, 1994 is selected to represent a strong positive IOD event. Upwelling intensity can be identified by SST and SSS anomalies; negative anomalies are indicated by lower-than-average SST/SSS, while positive anomalies are indicated by higher-than-average SST/SSS. In this study, the average SST and SSS is calculated based on simulation data obtained between 1990 and 2014. A positive upwelling intensity is usually represented by a negative SST anomaly/positive SSS anomaly, and vice versa

7.1 Normal Condition

The results show that upwelling intensity was lower in 1990 than in 1993. The SST anomaly in 1993 was relatively low, about -2.5°C , while the anomaly in 1990 was higher (about -1.23°C) (Figure 7.1). In contrast, the SSS anomaly in 1993 was higher (by about 0.1) than in 1990. It is also observed that wind stress magnitude during the southeast monsoon (May–October) was higher by about 0.0064 N/m^2 in 1993 than in 1990 (Figure 7.2). Wind stress in 1990 was about -0.062 N/m^2 in the zonal direction and 0.059 N/m^2 in the meridional direction, while in 1993 it was about -0.068 N/m^2 in the zonal direction and 0.062 N/m^2 in the meridional direction. The ONI index during the southeast monsoon throughout these two periods was $+0.35$, and negative IOD event occurs in both periods with a value less than -0.5 (Figure 7.3). Therefore, this study suggests that, under normal conditions (ONI and IOD $< |-/+ 0.5|$), the stronger wind stress is a dominant factor in inducing stronger upwelling in 1993 than in 1990.

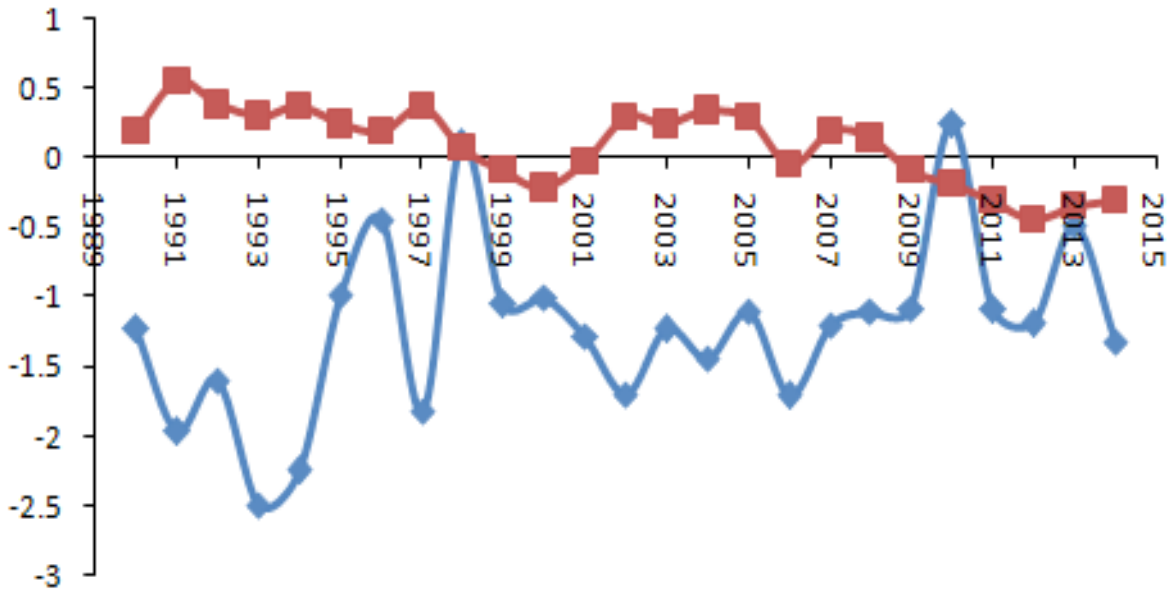


Figure 7.1: The average sea surface temperature (°C) (blue) and salinity (red) anomalies derived from HAMSOM simulation during the south east monsoon in the period between 1990 and 2014 in the Northern Arafura and Band Seas (from 130° E - 137° E and from 4°S to 8°S).

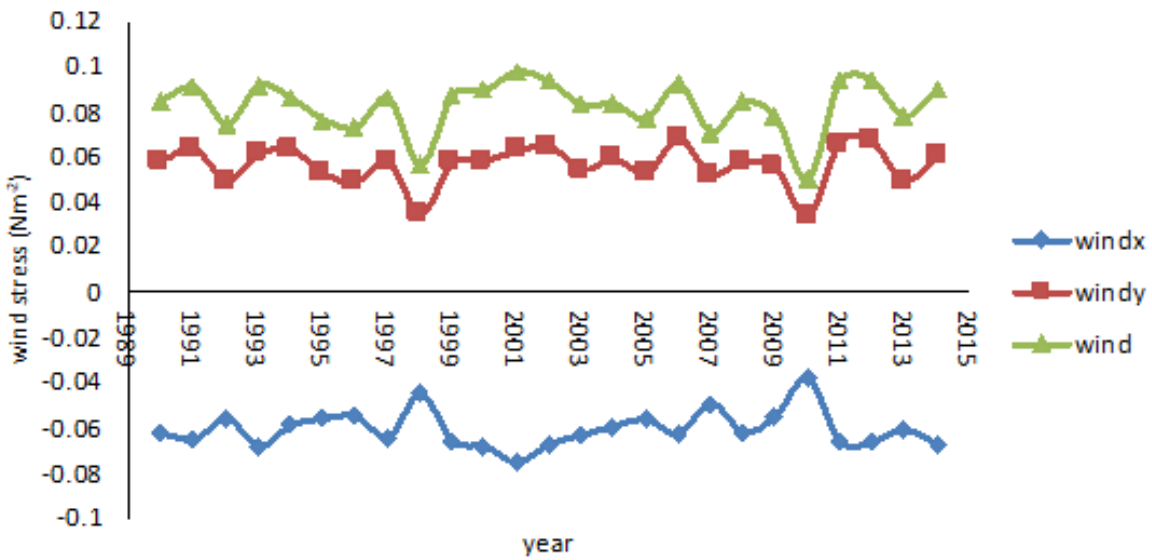


Figure 7.2: The average wind stress (Nm⁻²) in; zonal direction (blue), meridional direction (red) and resultant (light blue) derived from NCEP in the period between 1990 and 2014 in the Northern Arafura and Band Seas (from 130° E - 137° E and from 4°S to 8°S)..

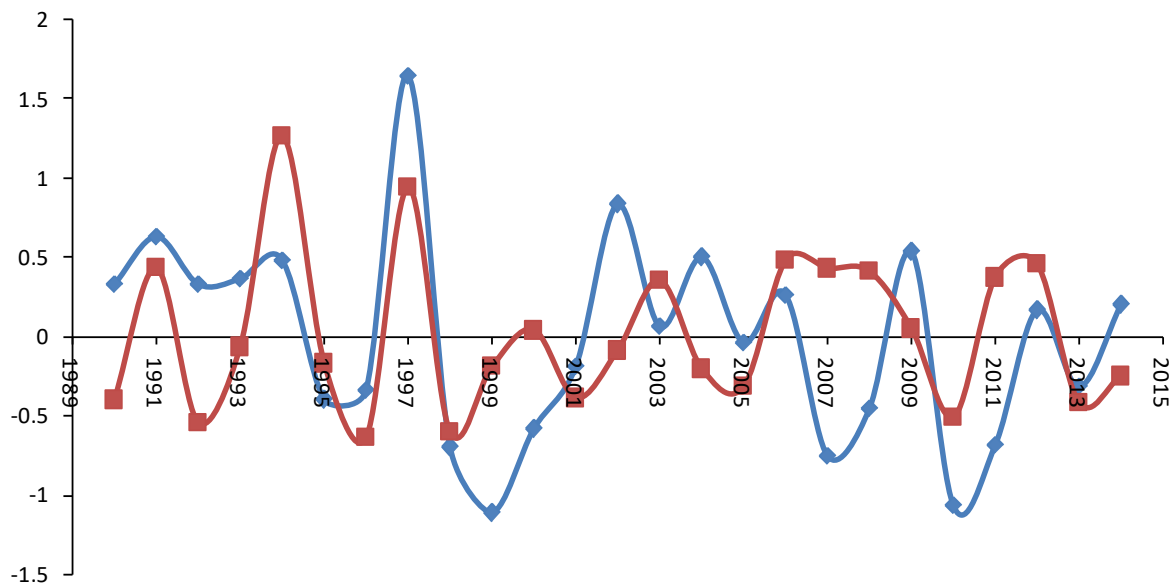


Figure 7.3: The average ONI (blue) and IOD (red) in the period between 1990 and 2014 in the Northern Arafura and Band Seas (from 130° E - 137° E and from 4°S to 8°S).

7.2 La Niña

Relatively weak upwelling is observed during La Niña, indicated by SST anomalies being relatively higher and SSS anomalies being relatively lower than in normal and El Niño conditions. During La Niña, the SST anomaly usually varies between -1.21°C and 0.24°C , while the SSS anomaly varies between -0.31 and 0.19 (Figure 7.1). This study suggests that the relatively low SSS anomaly around the research area is not only influenced by the weaker upwelling intensity induced by La Niña but also by the availability of more fresh water (Figure 7.4) during La Niña periods, which generally induces more precipitation, and local forcing. More than $19,000 \text{ m}^3/\text{s}$ of fresh water is available during the La Niña period, which is more than average during El Niño ($<10,000 \text{ m}^3/\text{s}$) and normal periods (between $10,000 \text{ m}^3/\text{s}$ and $19,000 \text{ m}^3/\text{s}$)—except when compared to the 2012 and 2013 periods (Figure 7.4). Although normal-ENSO conditions and normal-IOD phases usually result in less rainfall (and thus less available fresh water) than during La Niña, in 2012 and 2013 between $20,000 \text{ m}^3/\text{s}$ and $22,000 \text{ m}^3/\text{s}$ was available (i.e. higher than during La Niña). This indicates that the higher availability of fresh water during these two periods is not influenced by La Niña, but local forcing. The relatively high availability of fresh water is also indicated by the SSS being relatively lower than during other periods.

The important role of La Niña in inducing higher SST can also be observed by comparing the physical conditions between 2008 and 2011. It is found that the La Niña intensity and wind stress magnitude during the southeast monsoon in the 2008 period (-0.45 and 0.085

N/m²) were lower than during the 2011 period (-0.7 and 0.094N/m²), while the IOD in those periods were similar, at about +0.4 (Figures 5.25 and 5.26). Normally, stronger wind stress leads to lower SST anomalies. In contrast, the SST anomaly in 2011 was relatively higher than in the 2008 period (about -1.09°C as compared to -1.11°C). Therefore, the study suggests that a stronger La Niña in 2011 weakened the wind-driven upwelling, as indicated by the SST anomaly being higher in this period than in 2008.

The results also show that the highest SST anomaly (about 0.24°C) was observed in 2010 when a strong La Niña (at about -1.07), strong negative IOD events (at about -0.51), and relatively low wind stress occurred together in the Arafura Sea (Figure 7.3). In contrast, a relatively low SSS (about -0.19) was observed in this period, indicating that much more fresh water resulted from precipitation and river runoff induced by La Niña and the negative IOD event. In 2010, wind stress of about -0.038 N/m² in the zonal direction and 0.033 N/m² in the meridional direction is observed, relatively lower than in other periods (Figure 7.2). In 1998, La Niña and negative IOD events also occurred together, though with a lower La Niña intensity and slightly higher negative IOD indexes. Furthermore, it is observed that the SSS anomaly was higher in 1998 than in 2010 which indicates that more fresh water was available in 2010 (as shown in Figure 7.4). It is suggested that the lower availability of fresh water in 1998 was an effect of the weaker La Niña. It is also observed that, unlike in 2010, south-easterly winds were stronger in 1998. Wind stress in 1998 reached about -0.044 N/m² in the zonal direction and 0.035 N/m² in the meridional direction. The results therefore suggest that higher south-easterly winds and weaker La Niña led to stronger upwelling, as indicated by lower SST and higher SSS anomalies. The SST and SSS anomalies in 1998 were about 0.1 °C and 0.06, respectively.

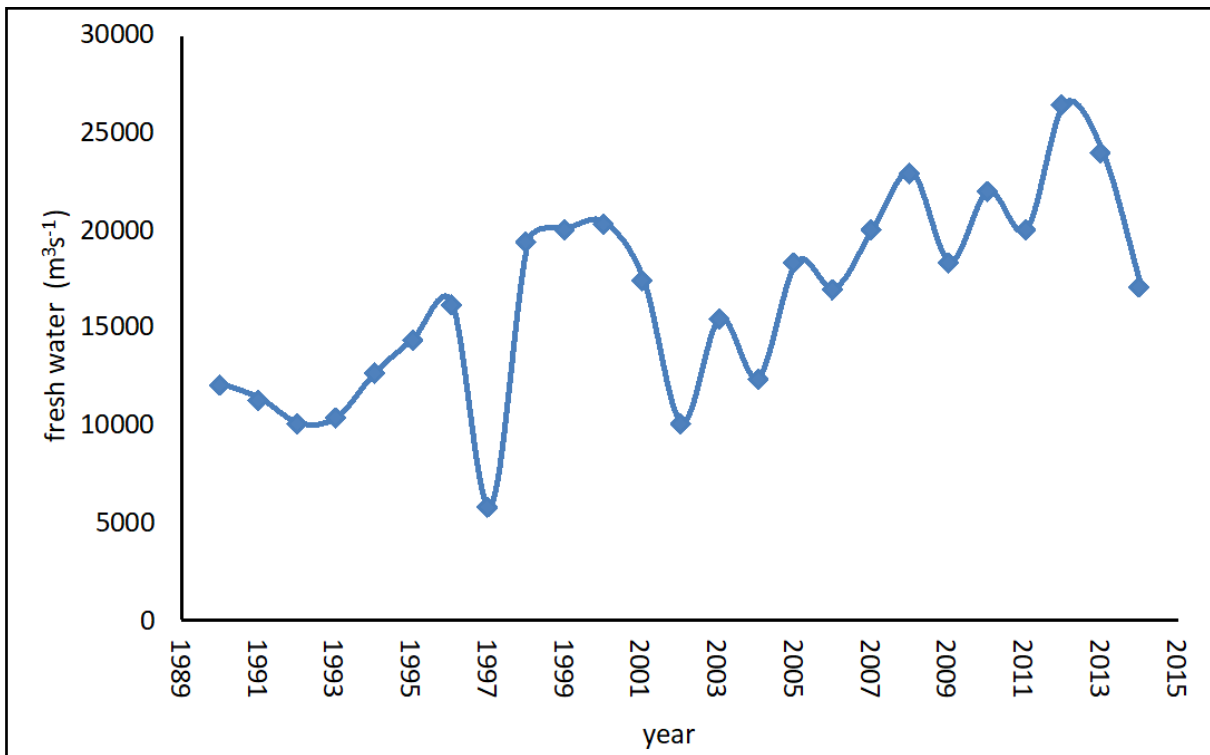


Figure 7.4: The average fresh water rate (m^3/s) in the period between 1990 and 2014 in the Northern Arafura and Banda Seas (from 130°E - 137°E and from 4°S to 8°S).

Furthermore, according to the observations, much stronger upwelling was identified in other La Niña periods (1999, 2000, 2007 and 2011) than in 1998 and 2010. The data shows that, except for 1999, La Niña was weaker in the other periods than in 2010, while the IOD events in the other periods were under normal-IOD conditions (Figure 7.3). In contrast, the south-easterly winds in the Northern Arafura and the Banda Seas blew much stronger in the other La Niña periods than in the 1998 and 2010 periods. Wind stresses ranged from 0.071 to 0.090 N/m^2 in the other periods, while wind stress magnitudes were respectively about 0.050 and 0.057 N/m^2 in 1998 and 2010 (Figure 7.3). The study therefore suggests that relatively weaker La Niña and stronger winds contributed to lower SST and higher SSS anomalies in 2000, 2007, and 2011, when the SST varied between -1.21°C and -1.06°C while the SSS ranged from -0.31 to 0.19 (Figure 7.1). The intensities of La Niña in 1999 and 2010 were similar (about -1.1). However, it is observed that the SST was lower (-1.06°C) and SSS was higher (-0.1), respectively, in 1999 than in 2010 (0.24°C and -0.2). These conditions indicate that other factors, i.e. local wind forcing and IOD, have more of an effect on the physical processes around the Aru Basin. As can be seen in Figures 7.2 and 7.3, the wind stress and the negative IOD (0.088 N/m^2 and -0.2) in the year 1999 were respectively higher (0.078 N/m^2) and lower (-0.51) than in 2010.

7.3 El Niño

In contrast to La Niña periods, stronger upwelling is generally observed during El Niño periods (1991, 1997, and 2002), as indicated by the relatively low SST and high SSS anomalies; SST anomalies vary between -1.97°C and -1.70°C , while SSS anomalies range from 0.29 to 0.54. El Niño's role in inducing lower SST anomalies can be observed by comparing the wind stress and SST between 1997 (El Niño) and 2011 (La Niña). Wind stress during the southeast monsoon in 1997 was about -0.064 N/m^2 in the zonal direction and about 0.058 N/m^2 in the meridional direction, while in 2011 the wind stress was about -0.066 N/m^2 in the zonal direction and about 0.066 N/m^2 in the meridional direction. Stronger wind stress generally corresponds to cooler SST (lower SST anomaly). However, the stronger wind stress in 2011 generated higher SST (-1.09°C) than in 1997 (-1.82°C). Therefore, this study suggests that a shallowing of the thermocline induced by El Niño played an important role in strengthening the intensity of upwelling in 1997.

El Niño's influence on wind-driven upwelling intensity can also be observed by comparing the anomalies between the 2002 and 1991/1997 periods. In 2002, upwelling intensity was relatively lower than in other El Niño periods, as indicated by the relatively high SST and low SSS (about -1.70°C and 0.29, respectively), even though wind stress during this period was higher than during other El Niño periods. Wind stress during the southeast monsoon in 2002 was about -0.067 N/m^2 in the zonal direction and about 0.065 N/m^2 in the meridional direction, while wind stress was about $-0.065/-0.064 \text{ N/m}^2$ in the zonal direction and about $0.064/0.058 \text{ N/m}^2$ in the meridional direction during the years 1991/1997. However, it is observed that the ONI and IOD indexes during this period were lower than during other El Niño periods. Therefore, this study suggests that ENSO and IOD played important roles in intensifying upwelling intensity in 1991 and 1997.

The influence of positive IOD events on the SST and SSS anomalies can also be observed by comparing the conditions in 1991 and 1994. The results show that wind stress was higher in 1991 than in 1994, while the positive ONI was lower in 1994 than in 1991. Normally, higher wind stress and ONI generates lower SST and SSS anomalies. However, unexpectedly, the SST and SSS anomalies in the 1994 period were about -2.25°C and 0.37, respectively, while in 1991 they were -1.97°C and 0.54. This indicates that the strong positive IOD in 1994 was the main factor generating the low SST that brought colder subsurface waters to the surface, while the salinity was reduced due to precipitation and river runoff that might be related to the lower ONI index.

Conclusion

HAMSOM has proven as a useful tool to simulate the response of surface water conditions in the Northern Arafura and Banda Seas (BAS) during the monsoon season. Relatively lower SST and higher SSS were observed in the BAS area during the southeast monsoon (May–October) than during northwest monsoon (December–March). The average sea surface temperature and salinity during the southeast monsoon are about 26.91°C and 34.0, respectively, while they are respectively about 29.45 °C and 33.9 during the northwest monsoon. The simulation shows that the physical and dynamic conditions in the research area are influenced not only by local conditions but also by regional conditions.

For local conditions, discussion has shown that tidal forcing and river runoff influence wind-driven upwelling around the Northern Arafura Sea during the southeast monsoon. Three sections (near the Northern Aru Islands [section A], the Southern Aru Islands [section B], and the Saul Shelf [section C]) were selected for observation. The simulation shows that Ekman surface currents are main factors inducing upwelling over the slopes of sections A, B, and C. In section B, the horizontal pressure gradient—mainly induced by spatial variation of wind stress—contributes significantly to canceling out the onshore subsurface currents and subsequently reduce upwelling; as such, upwelling is relatively less intense in section B than in section A, despite relatively higher wind stress levels. The relatively weaker wind stress in section C leads to a relatively lower upwelling intensity than in other sections.

It is found that tidal forcing generally leads to the enhancement of upwelling over sections A and B. Over the continental slope of section A, enhanced upwelling in the tide simulation is induced mainly by the formation of circulation cells and residual currents around the Northern Aru headland due to nonlinear interaction between tidal flow and topography. This nonlinear interaction can be identified by the nonlinear advection in the tide inclusion simulation being relatively higher than in the tide exclusion simulation. Over the continental slope of section B, the enhanced upwelling is associated with the modified horizontal pressure gradient due to tidal mixing so that a stronger onshore subsurface flow is identified between 50 and 200 m depth. In contrast, tidal forcing generally weakens upwelling over section C; as such, the temperature and salinity in the tide inclusion simulation are respectively higher and lower than in the tide exclusion simulation. The weakened upwelling over section C is caused by the relatively low residual currents toward off the Papua Coast, induced by relatively higher viscosity due to tidal mixing.

River runoff not only contributes to lower the salinity in the investigated areas, but also enhances the westward offshore surface currents and subsequent upwelling in all sections. By considering the same wind force in the river runoff inclusion and exclusion simulations, it can be concluded that the enhanced surface currents are related to enhanced stratification, which results in weaker vertical eddy coefficients and interfacial stress. The vertical viscous force in the surface water layers is subsequently enhanced, as observed across all sections.

The influences of the Southwestern Pacific Ocean, ENSO, and IOD events on the Northern Arafura Sea have been identified to have the largest impact on the region condition in the Northern Arafura Sea. The influence of the Southwestern Pacific Ocean on the Northern Arafura Sea is indicated by the presence of a salinity maximum (more than 34°C), as brought by relatively strong currents (known as the ITF) within the thermocline layer. These water masses mainly enter through the Halmahera and Seram Seas before intruding into the Aru Basin (part of the Northern Arafura Sea).

In addition, HAMSOM can also be used to investigate and analyze upwelling variations around the Arafura and Banda Seas as a response to ENSO and IOD. It is found that El Niño/La Niña contribute to the enhancement/weakening of upwelling intensities induced mainly by local wind forcing around the Arafura and Banda Seas. It is also observed that positive/negative IOD plays an important role in enhancing/weakening the intensity of upwelling.

List of Abbreviations

| | |
|--------|--|
| ACCEL | : Acceleration |
| AVISO | : Archiving, Validation and Interpretation of Satellite Oceanographic data |
| BAS | : Banda and Northern Arafura Seas |
| COR | : Coriolis Force |
| EIS | : Eastern Indonesian Seas |
| ENSO | : El Niño Southern Oscillation |
| HE | : Halmahera Eddies |
| HADV | : Horizontal nonlinear advection; |
| HAMSOM | : Hamburg Shelf Ocean Model |
| HVI | : Horizontal Viscosity |
| IOD | : Indian Ocean Dipole |
| ITF | : Indonesian Throughflow |
| MC | : Mindanau Current |
| MODIS | : Moderate-resolution Imaging Spectroradiometer |
| NCEP | : National Centers for Environmental Prediction |
| NECC | : North Equatorial Counter Current |
| NGCC | : New Guinea Coastal Current |
| ONI | : Oceanic Niño Index |
| WO | : Wind Only |
| WR | : Wind-River Runoff |
| WRT | : Wind-River Runoff- Tidal Forcing |
| WT | : Wind-Tidal Forcing |
| PGF | : Pressure Gradient Force |
| SSH | : Sea Surface Height |
| SSS | : Sea Surface Salinity |
| SST | : Sea Surface Temperature |
| SWPO | : South Western Pacific Ocean |
| SWPS | : South Western Pacific Subtropical Salinity Maximum |
| VADV | : Vertical Nonlinear Advection |
| VVI | : Vertical Viscosity |

List of Figure

| | |
|---|----|
| Figure 1: The horizontal distributions of chlorophyll-a (gC/m^2) derived from MODIS (http://icdc.cen.uni-hamburg.de) during the northwest monsoon (December 2004) (above) and during the southeast monsoon (July 2004) (below) around the Banda and Arafura Seas | 2 |
| Figure 2. 1 : Topography (meters) of the model area. The red box with Red-line (Section A), Green-line (Section B), and Yellow-line (Section C) indicates the region this paper is mostly concerned with (in the section 5.3). The red solid circles represent the river locations. | 6 |
| Figure 2. 2: Topography in the Sahul Shelf (meters) | 7 |
| Figure 4.1: SSHs (meter) overlaid by baroclinic (left) and barotropic (right) surface currents (m/s) during the south-east monsoon reproduced by HAMSOM (left) and AVISO (right). | 24 |
| Figure 4.2: SSHs (meter) overlaid by baroclinic (left) and barotropic (right) surface currents during the north-west monsoon reproduced by HAMSOM (left) and AVISO (right). | 24 |
| Figure 4.3: Time-series comparing measured tides (blue lines) with tides from the hydrodynamic model (red lines) at a) Ambon (July 2004) b) Benoa (September 2004) c) Davau (July 2004) d) Tawau (July 2004). | 26 |
| Figure 4.4: The values of SST ($^{\circ}\text{C}$) from MODIS (red color) and HAMSOM simulation (blue color) in the period of between 2003 and 2014 in the Banda and Northern Arafura Seas | 27 |
| Figure 4.5: Averaged SST ($^{\circ}\text{C}$) over the period 2003-2014 comparison between the HAMSOM (left) and MODIS (right) during southeast monsoon. | 28 |
| Figure 4.6: Comparison of HAMSOM simulation (red line) and INSTANT observation (blue line) of zonal and meridional velocities at 50 m depth in Lombok, Makassar, Ombai straits and Timor Passage. | 31 |
| Figure 4.7: Comparison of HAMSOM simulation (red line) and INSTANT observation (blue line) of zonal and meridional velocities at 150 m depth in the Lombok, Makassar, Ombai Straits and Timor Passage | 32 |
| Figure 4.8: TS-diagram derived from HAMSOM simulations and global observation data (EN4) in the 2004 period in the selected areas: the WRT case (red), the WO case (yellow), the WR case (blue), the WT case (green) and the global data of EN4 (cyan). | 34 |
| Figure 5.1: Monthly average wind stress (Nm^{-2}) in the Arafura and Banda Seas (BAS) (from 130°E - 137°E and from 4°S to 8°S) between January and December, derived from the NCEP data in the periods between 1990 and 2014: in zonal direction (blue line), in meridional direction (red line) and the resultant of zonal and meridional directions (light green line). | 37 |
| Figure 5.2: The horizontal distribution of seasonally average wind stress vectors (Nm^{-2}) and their magnitudes (background) derived from NCEP data in the periods between 1990 and 2014 during the; a) southeast monsoon (May-October), b) transition I (November), c) northwest monsoon (December-March) and transition II (April). | 37 |
| Figure 5.3: Monthly average of precipitation (P), evaporation (E)) derived from NCEP data and river runoff (R) derived from WaterGAP Global Hydrology Model in the periods between 1990 and 2014 in the Arafura and Banda Seas (BAS) (from 130°E - 137°E and from 4°S to 8°S): P(light green), E(blue), R(red), P+E (purple) and P+E+R (light blue). | 38 |
| Figure 5.4: Monthly average SST ($^{\circ}\text{C}$) (red) and SSS (blue) in the BAS (from 130°E - 137°E and from 4°S to 8°S) between January and December, derived from the HAMSOM simulation between 1990 and 2014. | 39 |

| | |
|---|----|
| Figure 5.5: Horizontal distribution of average SST (°C) and SSS (a and b) overlaid by surface currents during the northwest monsoon (February) in the BAS, derived from the HAMSOM simulation between 1990 and 2014..... | 40 |
| Figure 5.6: Horizontal distribution of average SST (°C) and SSS (a and b) overlaid by surface currents during the southwest monsoon (July) in the BAS, derived from the HAMSOM simulation between 1990 and 2014..... | 40 |
| Figure 5.7: Horizontal distribution of average temperature (°C) (a) and salinity (b) overlaid by subsurface currents at about 130 m during the northwest monsoon (February) in the BAS, derived from the HAMSOM simulation between 1990 and 2014..... | 43 |
| Figure 5.8: Horizontal distribution of average temperature (°C) (a) and salinity (b) overlaid by subsurface currents at about 130 m during the southeast monsoon (July) in the BAS, derived from the HAMSOM simulation between 1990 and 2014..... | 43 |
| Figure 5.9: The vertical profile of average velocities (m/s) along the section of 0.5 °N and from 128.5 °E to 130°E for zonal (a) and meridional (b) flow directions during the northwest monsoon (February), derived from the HAMSOM simulation between 1990 and 2014..... | 44 |
| Figure 5.10: The vertical profile of average velocities (m/s) along the section of 0.5 °N and from 128.5 °E to 130°E for zonal (a) and meridional (b) flow directions during the southeast monsoon (July), derived from the HAMSOM simulation between 1990 and 2014..... | 44 |
| Figure 5.11: Tidal surface currents and w-velocity ($\times 10^{-3}$ m/s) (the background) for barotropic mode (TOBT) around the Northern Arafura Sea at a) maximum flood and b) maximum ebb. | 46 |
| Figure 5.12: Tidal surface currents and w-velocity ($\times 10^{-3}$ m/s) (the background) for baroclinic mode (TOBC) around the Northern Aru Arafura Sea at a) maximum flood and b) maximum ebb. | 46 |
| Figure 5.13: Zonal tidal currents (m/s) in the upper layer ($z=2$) at points: a) 4.8°S/ 134.6°E (section A), c) 7.35°S/ 133.1°E (section B), e) 6°S/137°E (section C) for the barotropic mode; b) 4.8°S/134.6°E (Section A), d) 7.35°S/ 133.1°E (section B), f) 6°S/ 137°E (section C) for the baroclinic mode..... | 48 |
| Figure 5.14: Momentum components in zonal(left) and meridional(right) directions at selected points during maximum flood at $z = 2$ for barotropic mode ($\times 10^{-3} \text{ ms}^{-2}$). Legend: Barotropic-PGF (Red), baroclinic-PGF (Green), ADV (Blue), VVI (light blue), COR (yellow), ACC (Orange)..... | 51 |
| Figure 5.15: Momentum components in zonal(left) and meridional(right) directions at selected points during maximum flood at near bottom for barotropic mode ($\times 10^{-3} \text{ ms}^{-2}$). Legend: Barotropic-PGF (Red), baroclinic-PGF (Green), ADV (Blue), VVI (light blue), COR (yellow), ACC (Orange)..... | 52 |
| Figure 5.16: Momentum components around the Northern Arafura Sea in the zonal direction at maximum flood at $z = 2$ for the barotropic mode ($\times 10^{-2} \text{ ms}^{-2}$). | 53 |
| Figure 5.17: Momentum components around the Northern Arafura Sea in the meridional direction at maximum flood at $z = 2$ for the barotropic mode ($\times 10^{-2} \text{ ms}^{-2}$). | 54 |
| Figure 5.18: Momentum components around the Northern Arafura Sea in the zonal direction at maximum ebb at $z = 2$ for the barotropic mode ($\times 10^{-2} \text{ ms}^{-2}$). | 55 |
| Figure 5.19: Momentum components around the Northern Arafura Sea in the meridional direction at maximum ebb at $z = 2$ for barotropic mode ($\times 10^{-2} \text{ ms}^{-2}$). | 56 |
| Figure 5.20: Vertical profile of u-w velocity, where u-velocity is in m/s and w-velocity is in $\times 10^{-3}$ (m/s). The background represents w-velocity ($\times 10^{-3}$ m/s) for barotropic mode (TOBT) around the Northern Aru Island (section A) at a) maximum flood and b) maximum ebb..... | 58 |

| | |
|--|----|
| Figure 5.21: Vertical profile of u-w velocity, where u-velocity is in m/s and w-velocity is in $\times 10^{-3}$ (m/s). The background represents the w-velocity ($\times 10^{-3}$ m/s) for the baroclinic mode (TOBC) around the Northern Aru Island (section A) at a) maximum flood and b) maximum ebb. | 58 |
| Figure 5.22: Vertical profile of u-w velocity, where u-velocity is in m/s and w-velocity is in $\times 10^{-3}$ (m/s). The background represents the w-velocity ($\times 10^{-3}$ m/s) for the barotropic mode (TOBT) around the Southern Aru Island (section B) at a) maximum flood and b) maximum ebb. | 59 |
| Figure 5.23: Vertical profile of u-w velocity, where u-velocity is in m/s and w-velocity is in $\times 10^{-3}$ (m/s). The background represents the w-velocity ($\times 10^{-3}$ m/s) for the baroclinic mode (TOBC) around the Southern Aru Island (section B) at a) maximum flood and b) maximum ebb. | 59 |
| Figure 5.24: Surface currents and the SST ($^{\circ}\text{C}$) (the background) in the period of July 2004 for the cases of: a) the WRT; b) the WO; c) the WR; d) the WT. | 63 |
| Figure 5.25: Surface currents and the SSS (the background) in the period of July 2004 for the cases of: a) the WRT; b) the WO; c) the WR; d) the WT. | 64 |
| Figure 5.26: Subsurface currents and temperature ($^{\circ}\text{C}$) (the background) at 130 m depth in the period of July 2004 for the cases of: a) the WRT; b) the WO; c) the WR; d) the WT. | 66 |
| Figure 5.27: Subsurface currents and salinity (the background) at 130 m depth in the period of July 2004 for the cases of: a) the WRT; b) the WO; c) the WR; d) the WT. | 67 |
| Figure 5.28: Subsurface currents and density ($+1000 \text{ kg/m}^3$) (the background) at 60 m depth in which the maximum velocities are generally found within the water column along the section A in the period of July, 2004 for the cases of: a) the WRT; b) the WR. | 68 |
| Figure 5.29: The vertical profile of u-w velocity (where u-velocity is in m/s and w-velocity is in $\times 10^{-3}$ m/s) and temperature ($^{\circ}\text{C}$) (the background) along the section A (4.8°S and $131^{\circ}\text{E} - 136^{\circ}\text{E}$) in the period of July 2004 for the cases of: a) the WRT; b) the WO; c) the WR; d) the WT. | 72 |
| Figure 5.30: The vertical profile of u-w velocity (where u-velocity is in m/s and w-velocity is in $\times 10^{-3}$ m/s) and salinity (the background) along the section A (4.8°S and $131^{\circ}\text{E} - 136^{\circ}\text{E}$) in the period of July 2004 for the cases of: a) the WRT; b) the WO; c) the WR; d) the WT. | 73 |
| Figure 5.31: The vertical profile of u-w velocity (where u-velocity is in m/s and w-velocity is in $\times 10^{-3}$ m/s) and temperature ($^{\circ}\text{C}$) (the background) along the section B (7.35°S and $132^{\circ}\text{E} - 138^{\circ}\text{E}$) in the period of July 2004 for the cases of: a) the WRT; b) the WO; c) the WR; d) the WT. | 76 |
| Figure 5.32: The vertical profile of u-w velocity (where u-velocity is in m/s and w-velocity is in $\times 10^{-3}$ m/s) and salinity (the background) along the section B (7.35°S and $132^{\circ}\text{E} - 138^{\circ}\text{E}$) in the period of July 2004 for the cases of: a) the WRT; b) the WO; c) the WR; d) the WT. | 77 |
| Figure 5.33: The vertical profile of u-w velocity (where u-velocity is in m/s and w-velocity is in $\times 10^{-3}$ m/s) and temperature ($^{\circ}\text{C}$) (the background) along the section C (6.0°S and $135^{\circ}\text{E} - 138.5^{\circ}\text{E}$) in the period of July 2004 for the cases of: a) the WRT; b) the WO; c) the WR; d) the WT. | 80 |
| Figure 5.34: The vertical profile of u-w velocity (where u-velocity is in m/s and w-velocity is in $\times 10^{-3}$ m/s) and salinity (the background) along the section C (6.0°N and $135^{\circ}\text{E} - 138.5^{\circ}\text{E}$) in the period of July 2004 for the cases of: a) the WRT; b) the WO; c) the WR; d) the WT. | 81 |
| Figure 5.35: Vertical viscosity coefficient ($\times 1000 \text{ m}^2\text{s}^{-1}$) in the surface layer around the Northern Arafura Sea for: a) WT case, b) WO case and c) WTR case. The A_v difference between: d) the WT and WO cases (WT - WO), e) WT and WTR cases (WT - WTR). | 83 |

| | |
|---|-----|
| Figure 5.36: Vertical viscosity coefficient ($\times 1000 \text{ m}^2\text{s}^{-1}$) around Section A for: a) WT case, b), WO case and c) WTR case. The Av difference between: d) the WT and WO cases (WT - WO), e) the WT and WTR cases (WTR - WT). | 84 |
| Figure 5.37: Vertical viscosity coefficient ($\times 1000 \text{ m}^2\text{s}^{-1}$) around Section B for: a) WT case, b), WO case and c) WTR case. The Av difference between: d) the WT and WO cases (WT - WO), e) the WT and WTR cases (WTR - WT). | 85 |
| Figure 5.38: Vertical viscosity coefficient ($\times 1000 \text{ m}^2\text{s}^{-1}$) around Section C for: a) WT case, b), WO case and c) WTR case. The Av difference between: d) the WT and WO cases (WT - WO), e) the WT and WTR cases (WTR - WT). | 86 |
| Figure 5.39: The Instantaneous vertical velocity (m/s) at about 200 m depth in the Eastern Indonesian Seas in the 2004 period | 87 |
| Figure 5.40: Hovmoller diagram of temperature ($^{\circ}\text{C}$); at about 650 m depth along $0.8^{\circ} - 5^{\circ}\text{N}$ at 120°E in the Sulawesi Sea (a) and at about 200 m depth along $-0.2^{\circ} - 0.7^{\circ}\text{N}$ at 129.15°E in the Halmahera Sea (b) in the 2004 period..... | 88 |
| Figure 6.1: Momentum components in the zonal direction in water surface ($z = 1$) for the WO case during the period of July 2004 (28 days) ($\times 10^{-3} \text{ ms}^{-2}$) | 93 |
| Figure 6.2: Momentum components in the meridional direction in water surface ($z = 1$) for the WO case during the period of July 2004 (28 days) ($\times 10^{-3} \text{ ms}^{-2}$) | 93 |
| Figure 6.3: Momentum components in the zonal direction in water surface ($z = 1$) for the WT case during the period of July 2004 (28 days) ($\times 10^{-3} \text{ ms}^{-2}$). | 94 |
| Figure 6.4: Momentum components in the meridional direction in water surface ($z = 1$) for the WT case during the period of July 2004 (28 days) ($\times 10^{-3} \text{ ms}^{-2}$). | 94 |
| Figure 6.5: The difference of momentum components in the zonal direction in water surface ($z = 1$) between the WT and WO cases (WT-WO) during the period of July 2004 (28 days) ($\times 10^{-3} \text{ ms}^{-2}$) . | 95 |
| Figure 6.6: The difference of momentum components in the meridional direction in water surface ($z = 1$) between the WT and WO cases (WT-WO) during the period of July 2004 (28 days) ($\times 10^{-3} \text{ ms}^{-2}$). | 95 |
| Figure 6.7: Momentum components in the zonal direction along the section A for the WO case during the period of July 2004 (28 days) ($\times 10^{-3} \text{ ms}^{-2}$) | 97 |
| Figure 6.8: Momentum components in the meridional direction along the section A for the WO case during the period of July 2004 (28 days) ($\times 10^{-3} \text{ ms}^{-2}$). | 97 |
| Figure 6.9: Momentum components in the zonal direction along the section A for the WT case during the period of July 2004 (28 days) ($\times 10^{-3} \text{ ms}^{-2}$) | 98 |
| Figure 6.10: Momentum components in the meridional direction along the section A for the WT case during the period of July 2004 (28 days) ($\times 10^{-3} \text{ ms}^{-2}$) | 98 |
| Figure 6.11: The difference of momentum components in the zonal direction along the section A between the WT and WO cases (WT-WO) during the period of July 2004 (28 days) ($\times 10^{-3} \text{ ms}^{-2}$) . | 99 |
| Figure 6.12: The difference of momentum components in the meridional direction along the section A between the WT and WO cases (WT-WO) during the period of July 2004 (28 days) ($\times 10^{-3} \text{ ms}^{-2}$) . | 99 |
| Figure 6.13: Momentum components in the zonal direction along the section B for the WO case during the period of July 2004 (28 days) ($\times 10^{-3} \text{ ms}^{-2}$) | 102 |

| | |
|---|-----|
| Figure 6.14: Momentum components in the meridional direction along the section B for the WO case during the period of July 2004 (28 days) ($\times 10^{-3} \text{ ms}^{-2}$) . | 102 |
| Figure 6.15: Momentum components in the zonal direction along the section B for the WT case during the period of July 2004 (28 days) ($\times 10^{-3} \text{ ms}^{-2}$). | 103 |
| Figure 6.16: Momentum components in the meridional direction along the section B for the WT case during the period of July 2004 (28 days) ($\times 10^{-3} \text{ ms}^{-2}$) . | 103 |
| Figure 6.17: The difference of momentum components in the zonal direction along the section B between the WT and WO cases (WT-WO) during the period of July 2004 (28 days) ($\times 10^{-3} \text{ ms}^{-2}$) . | 104 |
| Figure 6.18: The difference of momentum components in the meridional direction along the section B between the WT and WO cases (WT-WO) during the period of July 2004 (28 days) ($\times 10^{-3} \text{ ms}^{-2}$) . | 104 |
| Figure 6.19: Momentum components in the zonal direction along the section C for the WO case during the period of July 2004 (28 days) ($\times 10^{-3} \text{ ms}^{-2}$). | 106 |
| Figure 6.20: Momentum components in the meridional direction along the section C for the WO case during the period of July 2004 (28 days) ($\times 10^{-3} \text{ ms}^{-2}$). | 106 |
| Figure 6.21: Momentum components in the zonal direction along the section C for the WT case during the period of July 2004 (28 days) ($\times 10^{-3} \text{ ms}^{-2}$). | 107 |
| Figure 6.22: Momentum components in the meridional direction along the section C for the WO case during the period of July 2004 (28 days) ($\times 10^{-3} \text{ ms}^{-2}$). | 107 |
| Figure 6.23: The difference of momentum components in the zonal direction along the section C between the WT and WO cases (WT-WO) during the period of July 2004 (28 days) ($\times 10^{-3} \text{ ms}^{-2}$) . | 108 |
| Figure 6.24: The difference of momentum components in the meridional direction along the section C between the WT and WO cases (WT-WO) during the period of July 2004 (28 days) ($\times 10^{-3} \text{ ms}^{-2}$) . | 108 |
| Figure 6.25: The difference of momentum components in the zonal direction in water surface ($z = 1$) between the WT and WO cases (WT-WRT) during the period of July 2004 (28 days) ($\times 10^{-3} \text{ ms}^{-2}$) . | 112 |
| Figure 6.26: The difference of momentum components in the meridional direction in water surface ($z = 1$) between the WT and WO cases (WT-WRT) during the period of July 2004 (28 days) ($\times 10^{-3} \text{ ms}^{-2}$) . | 112 |
| Figure 6.27: The difference of momentum components in the meridional direction along the section A between the WT and WRT cases (WT-WRT) during the period of July 2004 (28 days) ($\times 10^{-3} \text{ ms}^{-2}$) | 113 |
| Figure 6.28: The difference of momentum components in the meridional direction along the section B between the WT and WRT cases (WT-WRT) during the period of July 2004 (28 days) ($\times 10^{-3} \text{ ms}^{-2}$) . | 113 |
| Figure 6.29: The difference of momentum components in the meridional direction along the section C between the WT and WTR cases (WT-WRT) during the period of July 2004 (28 days) ($\times 10^{-3} \text{ ms}^{-2}$) . | 114 |
| Figure 7.1: The average sea surface temperature ($^{\circ}\text{C}$) (blue) and salinity (red) anomalies derived from HAMSOM simulation during the south east monsoon in the period between 1990 and 2014 in the Northern Arafura and Band Seas (from $130^{\circ} \text{ E} - 137^{\circ} \text{ E}$ and from 4°S to 8°S). | 116 |
| Figure 7.2: The average wind stress (Nm^{-2}) in; zonal direction (blue), meridonal direction (red) and resultant (light blue) derived from NCEP in the period between 1990 and 2014 in the Northern Arafura and Band Seas (from $130^{\circ} \text{ E} - 137^{\circ} \text{ E}$ and from 4°S to 8°S). | 116 |
| Figure 7.3: The average ONI (blue) and IOD (red) in the period between 1990 and 2014 in the Northern Arafura and Band Seas (from $130^{\circ} \text{ E} - 137^{\circ} \text{ E}$ and from 4°S to 8°S). | 117 |

| | |
|--|-----|
| Figure 7.4: The average fresh water rate (m^3/s) in the period between 1990 and 2014 in the Northern Arafura and Banda Seas (from 130° E - 137° E and from 4° S to 8° S). | 119 |
| Figure A.1: Tidal residual currents (m/s) and w -velocity ($\times 10^{-3} \text{ m/s}$) (background) at $z = 2$ for a) TOBT b) TOBT-NADV c) TOBT-Half d) TOBC around the Northern Arafura Sea. The residual currents are obtained by averaging over 28 days. | 139 |
| Figure A.2: The vertical profile of u - w velocity, where u -velocity is in m/s and w -velocity is in $\times 10^{-3} (\text{m/s})$. The background represents w -velocity ($\times 10^{-3} \text{ m/s}$) along section A for a) TOBT b) TOBT-NADV c) TOBT-Half d) TOBC. The residual currents are obtained by averaging over 28 days. | 140 |
| Figure A.3: The vertical profile of u - w velocity, where u -velocity is in m/s and w -velocity is in $\times 10^{-3} (\text{m/s})$. The background represents w -velocity ($\times 10^{-3} \text{ m/s}$) along section B for a) TOBT b) TOBT-NADV c) TOBT-Half d) TOBC. The residual currents are obtained by averaging over 28 days..... | 141 |
| Figure A.4: Momentum components in the zonal direction in section A for the TOBT case averaged over 28 days ($\times 10^{-3} \text{ ms}^{-2}$). | 143 |
| Figure A.5: Momentum components in the meridional direction in section A for the TOBT case averaged over 28 days ($\times 10^{-3} \text{ ms}^{-2}$) | 143 |
| Figure A.6: Momentum components in the zonal direction in section A for the TOBC case averaged over 28 days ($\times 10^{-3} \text{ ms}^{-2}$) | 144 |
| Figure A.7: Momentum components in the meridional direction in section A for the TOBC case averaged over 28 days ($\times 10^{-3} \text{ ms}^{-2}$) | 144 |
| Figure A.8: The difference of momentum components in the zonal direction in section A between the TOBT and TOBC cases (TOBT-TOBC) averaged over 28 days ($\times 10^{-3} \text{ ms}^{-2}$)..... | 145 |
| Figure A.9: The difference of momentum components in the meridional direction in section A between the TOBT and TOBC cases (TOBT-TOBC) averaged over 28 days ($\times 10^{-3} \text{ ms}^{-2}$)..... | 145 |
| Figure A.10: Momentum components in the zonal direction in section B for the TOBT case averaged over 28 days ($\times 10^{-3} \text{ ms}^{-2}$) | 146 |
| Figure A.11: Momentum components in the meridional direction in section B for the TOBT case averaged over 28 days ($\times 10^{-3} \text{ ms}^{-2}$)..... | 146 |
| Figure A.12: Momentum components in the zonal direction in section B for the TOBC case averaged over 28 days ($\times 10^{-3} \text{ ms}^{-2}$) | 147 |
| Figure A.13: Momentum components in the meridional direction in section B for the TOBC case averaged over 28 days ($\times 10^{-3} \text{ ms}^{-2}$)..... | 147 |
| Figure A.14: The difference of momentum components in the zonal direction in section B between the TOBT and TOBC cases (TOBT-TOBC) averaged over 28 days ($\times 10^{-3} \text{ ms}^{-2}$)..... | 148 |
| Figure A.15: The difference of momentum components in the meridional direction in section B between the TOBT and TOBC cases (TOBT-TOBC) averaged over 28 days ($\times 10^{-3} \text{ ms}^{-2}$)..... | 148 |

References

- Adisanjaya, N. M., 2010. Potensi Produksi Sumberdaya Ikan di Perairan Laut Indonesia dan Permasalahannya. [cited in 6 May 2018]. Available at: <http://www.eafm-indonesia.net/public/files/penelitian/5ae09-POTENSI,-PRODUKSI-SUMBERDAYA-IKAN-DI-PERAIRAN-LAUT-INDONESIA-DAN-PERMASALAHANNYA.pdf>
- Aldrian, E. and Susanto R. D., 2003. Identification of three dominant rainfall regions within Indonesia and their relationship to sea surface temperature. *International Journal Climatology*, 23, 1435-1452.
- Allen, J.S., Newberger, P.A. and Federiuk, J., 1995. Upwelling circulation on the Oregon continental shelf. Part 1: response to idealized forcing. *J. Phys. Oceanogr.* 25, 1843–1866.
- Ashok, K., Z. Guan, and T. Yamagata, 2001. Impact of the Indian Ocean Dipole on the relationship between the Indian Monsoon rainfall and ENSO. *Geophys. Res. Lett.*, 26, 4499–4502.
- Austin, J. A., and Lentz S., 2002. The inner shelf response to winddriven upwelling and downwelling. *J. Phys. Oceanogr.*, 32, 2171– 2193.
- Backhaus, J. O., 1983. A semi-implicit scheme for shallow water equations for applications to shelf sea modelling. *Continental Shelf Research*, 2, 243-254.
- Backhaus, J. O., 1985. A three-dimensional model for the simulations of shelf sea dynamics. *Deutsche Hydrographische Zeitschrift*, 38, 165-187.
- Berdeal, B., Hickey, I.B.M., and Kawase, M., 2002. Influence of wind stress and ambient flow on high discharge river plume. *J. Geophys. Res.* 107 (C9), 3130.
- CEA, 2016. "Indonesia Fisheries: 2015 Review." Prepared for The David and Lucile Packard Foundation.
- Chao, S.Y., 1988. Wind-driven motion of estuarine plumes. *J. Phys. Oceanogr.* 18, 1144–1166.
- Chen, C., Beardsley, R. C., 1995. A numerical study of stratified tidal rectification over finite-amplitude banks. Part I: Symmetric banks. *Journal of Physical Oceanography*, 25. Jg., Nr. 9, S. 2090-2110.
- Clancy, R. M., Kaitala, J. E. and Zambresky, L. F., 1986. The Fleet Numerical Oceanography Center Global Spectral Ocean Wave Model. *Bulletin of the American Meteorological Society*, 67, 498-512.
- Cushman-Roisin, B. and Beckers, J.M, 2011. *Introduction to Geophysical Fluid Dynamics: Physical and Numerical Aspects*, 2nd ed.; Academic Press: Cambridge, MA, USA.
- Döll, P., Kaspar, F. and Lehner, B., 2003. A global hydrological model for deriving water availability indicators: model tuning and validation. *J. Hydrol.* 270, 105–134
- Egbert GD, Bennett AF and Foreman MGG., 1994. TOPEX/POSEIDON tides estimated using a global inverse model. *J of Geophysical Research* 99: 24821-24852.
- Egbert GD and Erofeeva SY., 2002. Efficient inverse modeling of barotropic ocean tides. *J. Atmos. Oceanic Technol* 19: 183-204.

- Ekman, V. W., 1905. On the influence of the earth's rotation on ocean currents. *Archives of Mathematics, Astronomy and Physics*, 2 (11), 1-53.
- Ffield, A. and Gordon, A. L., 1992. Vertical mixing in the Indonesian thermocline. *J. Phys. Oceanogr.* 22, 1984-1995.
- Ffield, A., and Gordon A. L., 1996. Tidal mixing signatures in the Indonesian seas. *J. Phys. Oceanogr.*, 26, 1924–1937.
- Fung, I.Y., Harrison, D.E. and Lacis, A.A., 1984. On the variability of the net longwave radiation at the ocean surface. *Reviews of Geophysics* 22, 177–193.
- Gan, J., Li. L., Wang D., and Guo X., 2009. Interaction of a river plume with coastal upwelling in the northeastern South China Sea, *Cont. Shelf Res.*, 29, 728 – 740, doi:10.1016/j.csr.2008.12.002.
- Geyer, W. R., and Signell, R., 1990. Measurements of tidal flow around a headland with a ship-board acoustic Doppler current profiler. *Journal of Geophysical Research: Oceans*, 95(C3), 3189-3197.
- Gieskes, W. W. C., Kraay, G. W., Nontji, A., Setiapermana, D. and Sutomo, 1990. Monsoonal differences in primary production in the eastern Banda Sea (Indonesia). *Netherlands Journal of Sea Research*, 25,473-483.
- Gordon, A. L. and Susanto, R. D., 2001. Banda Sea surface-layer divergence. *Ocean Dynamics Journal*, 52:2-10.
- Gordon, A. L., 2005. Oceanography of the Indonesian seas and their throughflow, *Oceanography*, 18, 14 – 27.
- Gordon, A. L., Susanto R. D., Ffield A., Huber B. A., Pranowo W., and Wirasantosa S., 2008. Makassar Strait throughflow, 2004 to 2006, *Geophys. Res. Lett.*, 35, L24605, doi:10.1029/2008GL036372.
- Gordon, A. L., Sprintall, J., Van Aken, H. M., Susanto, R. D., Wijffels, S., Molcard, R., Ffield, A., Pranowo, W. and Wirasantosa, S., 2010. The Indonesian throughflow during 2004-2006 as observed by the INSTANT program. *Dynamics of Atmosphere and Oceans*, 50 : 115-128.
- Gordon, A. L., Huber B. A., Metzger E. J., Susanto R. D., Hurlburt H. E., and Adi T. R., 2012. South China Sea throughflow impact on the Indonesian throughflow, *Geophys. Res. Lett.*, 39, L11602, doi:10.1029/2012GL052021.
- Hein, H., 2007. Vietnam upwelling—Analysis of the upwelling and related processes in the coastal area of south vietnam, Ph.D. thesis, Univ. of Hamburg, Hamburg, Germany.
- Hein, B., 2013. Processes of stratification and destratification in the Mekong ROFI — seasonal and intraseasonal variability. (Ph.D. Thesis) University Hamburg, University of Hamburg (<http://ediss.sub.uni-hamburg.de/volltexte/2013/6369/>).

- Hickey, B.M., Pietrafesa, L.J., Jay, D.A. and Boicourt, W.C., 1998. The Columbia river plume study: subtidal variability in the velocity and salinity fields. *J. Geophys. Res.* 103, 10,339–10,368.
- Huthnance, J. M., 1973. Tidal current asymmetries over the Norfolk Sandbanks. *Estuarine and Coastal Marine Science*, 1. Jg., Nr. 1, S. 89-99.
- Huthnance, J. M., 1981. On mass transports generated by tides and long waves. *Journal of Fluid Mechanics*, 102. Jg., S. 367-387.
- Hutter, K. and Jöhnk, K., 2004. *Continuum Methods of Physical Modeling*. Springer, Berlin, 635 pp.
- Huang, D., 1995. *Modelling Studies of Barotropic and Baroclinic Dynamics in the Bohai Sea*. Berichte aus dem Zentrum für Meeres- und Klimaforschung, Nr. 17.
- Ilahude, A.G., Komar, Mardanis, 1990. On the hydrology and productivity of the northern Arafura Sea. *Neth. J. Sea Res.* 24, 573 – 583.
- Ilahude, A.G., and Gordon A.L., 1996. Thermocline Stratification Within the Indonesian seas. *Journal of Geophysical Research* 101(C5):12,401– 12,409.
- Iskandar, I., 2010. Seasonal and interannual patterns of sea surface temperature in Banda Sea as revealed by self-organizing map. *Continental shelf research*, 30, 1136-1148.
- Jungclaus, J.H., Botzet, M., Haak, H., Keenlyside, N., Luo, J.-J., Latif, M., Marotzke, J., Mikolajewicz, U., Roeckner, E., 2006. Ocean circulation and tropical variability in the coupled model ECHAM5/MPI-OM. *Journal of Climate* 19, 3952–3972.
- Kämpf, J., 2009. *Ocean modeling for beginners—using open-source software*. Springer, New York.
- Kämpf, J., 2016. On the majestic seasonal upwelling system of the Arafura Sea, *J. Geophys. Res. Oceans*, 121, 1218–1228, doi:10.1002/2015JC011197.
- Kalnay, E., et al., 1996. The NCEP/NCAR Reanalysis 40-year Project. *Bulletin American Meteorology Society* 19, 3952-3972.
- Kida, S. and Richards K. J., 2009. Seasonal sea surface temperature variability in the Indonesian seas. *J. Geophys. Res.* 114, C06016, doi:10.1029/2008JC005150.
- Kilpatrick, K. A., Podestá, G., Walsh, S., Williams, E., Halliwell, V., Szczodrak, M., Evans, R., 2015. A decade of sea surface temperature from MODIS. *Remote Sensing of Environment*, 165, 27-41. DOI: 10.1016/j.rse.2015.04.023.
- Kirincich, A. R., Barth J. A., Grantham B. A., Menge B. A., and Lubchenco J., 2005. Wind-driven inner-shelf circulation off central Oregon during summer, *J. Geophys. Res.*, 110, C10S03, doi:10.1029/2004JC002611.
- Koch-Larrouy, A., Madec G., Bouruet-Aubertot P., Gerkema T., Bessie`res L., and Molcard R., 2007. On the transformation of Pacific Water into Indonesian Throughflow Water by internal tidal mixing, *Geophys. Res. Lett.*, 34, L04604, doi:10.1029/2006GL028405

- Koch-Larrouy, A., Madec, G., Iudicone, D., Atmadipoera, A. and Molcard, R., 2008. Physical processes contributing to the water mass transformation of the Indonesian Throughflow. *Ocean Dynamics*, 58:275–288.
- Kochergin V. P., 1987. Three-dimensional prognostic models. In: Three-dimensional coastal ocean models, N. S. Heaps, editor, American Geophysical Union, Washington D.C., Coastal and Estuarine Science, 4, 201-208.
- Kondo, J., 1975. Air-Sea bulk transfer coefficients in diabatic conditions. *Boundary-Layer Meteorology* 9, 91–112.
- Kurapov, A. L., Allen J. S., and Egbert G. D., 2010. Combined effects of wind-driven upwelling and internal tide on the continental shelf, *J. Phys. Oceanogr.*, 40, 738-756, doi: 10.1175/2009JPO4183.1.
- Lee, S. H., & Beardsley, R. C., 1999. Influence of stratification on residual tidal currents in the Yellow Sea. *Journal of Geophysical Research: Oceans*, 104(C7), 15679-15701.
- Lentz, S.J., 2001. The influence of stratification on the wind-driven cross-shelf circulation over the north Carolina shelf. *J. Phys. Oceanogr.* 23, 2749–2760.
- Lentz, S. J. and Chapman, D. C., 2004. The Importance of Nonlinear Cross-Shelf Momentum Flux during Wind-Driven Coastal Upwelling. *Journal of Physical Oceanography*. 34, 2444-2457.
- Loder, J. W., Wright, D. G., 1985. Tidal rectification and frontal circulation on the sides of Georges Bank. *Journal of Marine Research*, 43. Jg., Nr. 3, S. 581-604.
- Ludewig, E., 2013. Influence of offshore wind farms on atmosphere and ocean dynamics. Dissertation Universität Hamburg.
- Lü, X., F. Qiao, Xia C., and Yuan Y., 2007. Tidally induced upwelling off Yangtze River estuary and in Zhejiang coastal waters in summer, *Sci. China, Ser. D*, 50, 462 – 473, doi:10.1007/s11430-007-2050-0.
- Luyten, P.J., Jones, J.E., Proctor, R., Tabor, A., Tett., P., Wild-Allen, K., 1999. COHERENS—a coupled hydrodynamical-ecological model for regional and Shelf Seas: user documentation. MUMM Report, Management Unit of the Mathematical Models of the North Sea, pp. 1–914.
- Maas, L. R. M., Zimmerman, J. T. F., 1989a. Tide-topography interactions in a stratified shelf sea I. Basic equations for quasi-nonlinear internal tides. *Geophysical & Astrophysical Fluid Dynamics*, 45. Jg., Nr. 1-2, S. 1-35.
- Maas, L. R. M.; Zimmerman, J. T. F., 1989b. Tide-topography interactions in a stratified shelf sea II. Bottom trapped internal tides and baroclinic residual currents. *Geophysical & Astrophysical Fluid Dynamics*, 45. Jg., Nr. 1-2, S. 37-69.

- Magaldi, M. G., Özgökmen, T. M., Griffa, A., Chassignet, E. P., Iskandarani, M., & Peters, H., 2008. Turbulent flow regimes behind a coastal cape in a stratified and rotating environment. *Ocean Modelling*, 25(1-2), 65-82.
- Marsland, S.J., Haak, H., Jungclaus, J.H., Latif, M., Roske, F., 2003. The Max-Planck-Institute global Ocean/sea ice model with orthogonal curvilinear coordinates. *Ocean Modelling* 5, 91–127.
- Mayer, B., Damm P. E., Pohlmann T., and Rizal S., 2010. What is driving the ITF? An illumination of the Indonesian throughflow with a numerical nested model system, *Dyn. Atmos. Oceans*, 50, 301–312, doi:10.1016/j.dynatmoce.2010.03.002.
- Mayer, B., and Damm P. E., 2012. The Makassar Strait throughflow and its jet, *J. Geophys. Res.*, 117, C07020, doi:10.1029/2011JC007809.
- Mazé, R., 1998. Tidal rectification: Friction or not friction?. *Journal of physical oceanography*, 1998, 28. Jg., Nr. 7, S. 1333-1345.
- Miller, G. R., 1996. The flux of tidal energy out of the deep oceans. *J Geophys. Res.*, 71, 2845-2489.
- Pohlmann, T., 1987. Three dimensional circulation model of the South China Sea, in *three Dimensional Models of Marine and Estuarine Dynamics*, edited by J. N. B. Jamart, pp 245 – 268, Elsevier, Amsterdam.
- Pohlmann, T., 1991. Untersuchung hydro- and thermo-dynamischer Prozesse in der Nordsee mit einem dreidimensionalen numerischen Modell. *Berichte aus dem Zentrum für Meeres- und Klimaforschung der Universität Hamburg*, Nr. 23.
- Pohlmann, T., 1996a. Calculating the development of the thermal vertical stratification in the north sea with a three-dimensional baroclinic circulation model, *Cont. Shelf Res.*, 16(2), 163 – 194.
- Pohlmann, T., 1996b. Calculating the annual cycle of the vertical eddy viscosity in the North Sea with a three-dimensional baroclinic shelf sea circulation model. *Cont. Shelf Res.*, Vol. 16, No. 2: 147 – 161.
- Pohlmann T., 2006. A meso-scale model of the central and southern North Sea: consequences of an improved resolution. *Cont Shelf Res* 26: 2367–2385.
- Putri, M. R., 2005. Study of ocean climate variability (1959–2002) in the eastern Indian Ocean, Java Sea and Sunda Strait using the HAMburg Shelf Ocean model, *Dissertation, Univ. Hamburg*, 104 pp.
- Ray, R. D., and Susanto R. D., 2016. Tidal mixing signatures in the Indonesian seas from high-resolution sea surface temperature data, *Geophys. Res. Lett.*, 43, doi:10.1002/2016GL069485.
- Rennie, S.E., Largier, J.L., Lentz, S.J., 1999. Observations of a pulsed buoyancy current downstream of Chesapeake Bay. *J. Geophys. Res.* 104, 18,227–18,240.

- Robinson, I. S., 1981. Tidal vorticity and residual circulation. *Deep Sea Research Part A. Oceanographic Research Papers*, 1981, 28. Jg., Nr. 3, S. 195-212.
- Robertson, R., and Field A., 2008. Baroclinic tides in the Indonesian seas: Tidal fields and comparisons to observations, *J. Geophys. Res.*, 113, C07031, doi:10.1029/2007JC004677.
- Rooth, C., 1972. A linearized bottom friction law for large-scale oceanic motions. *J. Phys. Oceanogr.*, 2, 509–510.
- Saji, N. H., Goswami B. N., Vinayachandran P. N., and Yamagata T., 1999. A dipole mode in the tropical Indian Ocean. *Nature* 401, 360-363.
- Sandstrom, H., and Oakey N. S., 1995. Dissipation in internal tides and solitary waves. *J. Phys. Oceanogr.*, 25, 604–614.
- Sheng, J., Wang, L., 2004. Numerical study of tidal circulation and nonlinear dynamics in Lunenburg Bay, Nova Scotia. *Journal of Geophysical Research: Oceans*, 109. Jg., Nr. C10.
- Shinoda, T., Han W., Metzger E. J., and Hurlburt H., 2012. Seasonal variation of the Indonesian throughflow in Makassar Strait, *J. Phys. Oceanogr.*, 42, 1099–1123, doi:10.1175/JPO-D-11-0120.1.
- Signell, R. P., Geyer, W. R., 1991. Transient eddy formation around headlands. *Journal of Geophysical Research: Oceans*, 1991, 96. Jg., Nr. C2, S. 2561-2575.
- Sprintall, J., Wijffels, S., Gordon, A. L., Field, A., Molcard, R., Dwi Susanto., R., Soesilo, I., Sopaheluwakan, J., Surachman, Y. and van Aken, H. M., 2004. INSTANT: new international array to measure the Indonesian throughflow. *Eos* 85 (39), 369-376.
- Sjöberg, B., and Stigebrandt A., 1992. Computations of the geographical distribution of the energy flux to mixing processes via internal tides and the associated vertical circulation in the ocean. *Deep-Sea Res.*, 39, 269-291.
- Sprintall, J., Gordon, A. L., Koch-Larrouy, A., Lee, T., Potemra, J. T., Pujiana and K., Wijffels, S. E., 2014. The Indonesian seas and their role in the coupled ocean–climate system. *Nature Geosci.* 7, 487–492 (2014).
- Su, J., and Pohlmann T., 2009. Wind and topography influence on an upwelling system at the eastern Hainan coast, *J. Geophys. Res.*, 114, C06017, doi:10.1029/2008JC005018.
- Sulistiyo, B., Adi, T. M., Triyono, 2013. Karakteristik Sumberdaya Laut Arafura & Pesisir Baratdaya Papua. <http://pusriskel.litbang.kkp.go.id/index.php/en/publikasi/buku-a-technical-documentation?download=1389%3Abukudayadukunglautarafurapesisirpapua>.
- Susanto, R. D., Field A., Gordon A. L., and Adi T. R., 2012. Variability of Indonesian throughflow within Makassar Strait, 2004–2009, *J. Geophys. Res.*, 117, C09013, doi:10.1029/2012JC008096.
- Tomczak, M. and Godfrey, 2001. *Regional Oceanography: an Introduction*. Pergamon 1994. Retrieved Jan., 2015, from <http://www.es.flinders.edu.au/~mattom/regoc/pdfversion.htm>.

- van Haren, H. and Gostiaux L., 2012. Detailed internal wave mixing observed above a deep-ocean slope. *Journal of Marine Research* 70:173–197, <http://dx.doi.org/10.1357/002224012800502363>.
- Venayagamoorthy, S. K. and Fringer, O. B., 2006. Numerical simulations of the interaction of internal waves with a shelf break. *Phys. Fluids* 18(7), 076603.
- Wang D-R., Yang Y., Wang J., Bai X., 2015. A modeling study of the effects of river runoff, tides, and surface wind-wave mixing on the eastern and western Hainan upwelling systems of the South China Sea. *China Ocean Dyn.* <https://doi.org/10.1007/s10236-015-0857-3>
- Wetsteyn, F. J., Ilahude A. G. and Baars M. A., 1990. Nutrient distribution in the upper 300 m of the eastern Banda Sea and northern Arafura Sea during and after the upwelling season, August 1984 and February 1985, *Proc. Snellius-II Symp., Neth. J. Sea Res.*, 25, 449–464.
- Wunsch, C., 1971. Note on some Reynolds stress effects of internal waves on slopes. *Deep-Sea Res.*, 18, 583–591.
- Wyrтки, 1958. The water exchange between the Pacific and the Indian Oceans in relation to upwelling processes. *Ins. Mar. Res.*, Djakarta. *Proc. Ninth Pac. Sci. Congr.* 16, 61 – 65.
- Wyrтки, 1961. *Scientific Results of Marine Investigations of the South China Sea and the Gulf of Thailand 1959-1961*, Naga Report vol. 2, The University of California.
- Zijlstra, J. J., Baars, M. A., Tijssen, S. B., Wetsteyn, F. J., Witte, J. IJ., Ilahude, A. G. and Hadikusuma, 1990. Monsoonal effects on the hydrography of the upper waters (<300 M) of the eastern Banda sea and Northern Arafura sea, with special reference to vertical transport process. *Netherland journal of sea research*, 25 (4): 431-447.
- Zimmermann, J. T. F., 1979. On the Euler-Lagrange transformation and the Stokes' drift in the presence of oscillatory and residual currents. *Deep Sea Research Part A. Oceanographic Research Papers*, 26. Jg., Nr. 5, S. 505-520.

Acknowledgments

I would like to express my sincere gratitude toward as my supervisor PD. Dr. Thomas Pohlmann for encouragement, helpful comments, criticisms and suggestions. I also would like to thank Dr. Bernhard Mayer for the scientific support and discussions for this work. Many thanks go to Dr. Mutiara Rachmat Putri (Bandung Institute of Technology) for her helpful advice.

I am also thankful to Deutscher Akademischer Austauschdienst (DAAD) for financing this work. I am also very grateful to Indonesian Institute of Sciences (LIPI) for allowing and supporting my study leave.

Many thanks should be given all the colleagues of the Institute of Oceanography (IFM) Hamburg for their technical and scientific supports. Thanks to the DAAD-IGSP-2014 and FSDH Families for their support and warm friendship since my stays in Hamburg.

This work is dedicated to my beloved wife Pipit Pitriana, my sons, Mizan Ilman Ramadhan and Nahyan Ilzam Ahlami, my parents, Abdussamad Abbas and Hamidah, in-laws, Uji Sanudji and Dede Painem, my brothers and my sisters. Thank you for your love, prayers and support throughout this research.

Appendix A

A. Residual Tidal Currents Generation and Momentum Balance around the Northern Arafura Sea

This section will focus on the role of primary nonlinear terms (i.e. advection and bottom friction) in generating tidal residual currents over the headland of the Aru Islands and Sahul Shelf Slope connecting the Aru Islands with Papua by comparing averaged currents over 28 days using tide only-barotropic (TOBT), tide only-barotropic-without advection term TOBT-NADV), and tide only-barotropic-with halved friction (TOBT-Half) cases. The influence of stratification on tidal circulation (baroclinic mode/TOBC) will be also discussed.

The results show relatively strong residual currents around the Northern Aru Islands in TOBT mode. In the horizontal profile, residual currents directed away from the headland are observed around the headland of the Northern Aru Islands and a bank located between the Aru Islands and Papua at about $5.25^{\circ}\text{S}/136^{\circ}\text{E}$ (Figure 5.24a). These residual currents are induced by the separation flow, as discussed in the previous section, and induce upwelling around the headlands. Removing the nonlinear advection of momentum, the residual currents around the headland and slope change significantly. Here, the residual currents are reduced, resulting in reduced upwelling intensity (Figures 5.24a and 5.24b). Meanwhile, in the vertical profile, at least two circulation cells are formed around the continental slope in the TOBT case (Figure 5.25a). After removing the nonlinear advection of momentum (TOBT-NADV case), circulation cells are not formed along the slope; rather, vertical velocity is directed mostly upward, with relatively lower intensity. In the TOBT-NADV case, considerably weaker residual currents are also identified around the Southern Aru Islands. These results confirm some findings in other areas (Chen et al., 1985; Dyke, 1987; Shen and Wang, 2004); for example, in Lunenburg Bay, Nova Scotia, Shen and Wang (2004), found that the excluding nonlinear term from momentum significantly reduces residual currents.

Near the western coast of Papua, where the water is relatively shallow, the residual currents are similar in the TOBT and TOBT-NADV cases. This study suggests that the residual currents around this area, which are relatively smaller than those in section A, are mostly induced by nonlinear bottom friction.

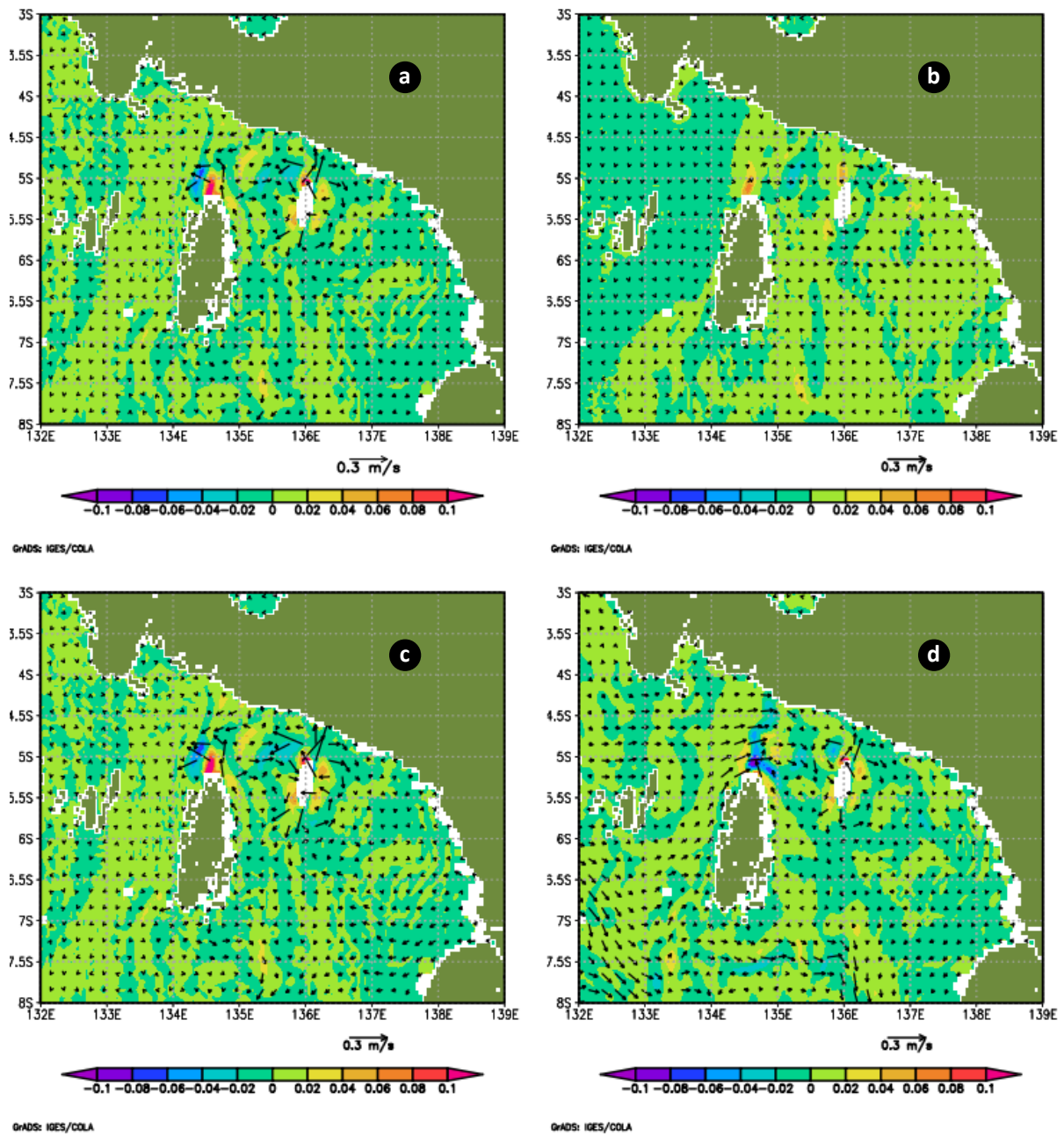


Figure A.1: Tidal residual currents (m/s) and w-velocity ($\times 10^{-3}$ m/s) (background) at $z = 2$ for a) TOBT b) TOBT-NADV c) TOBT-Half d) TOBC around the Northern Arafura Sea. The residual currents are obtained by averaging over 28 days.

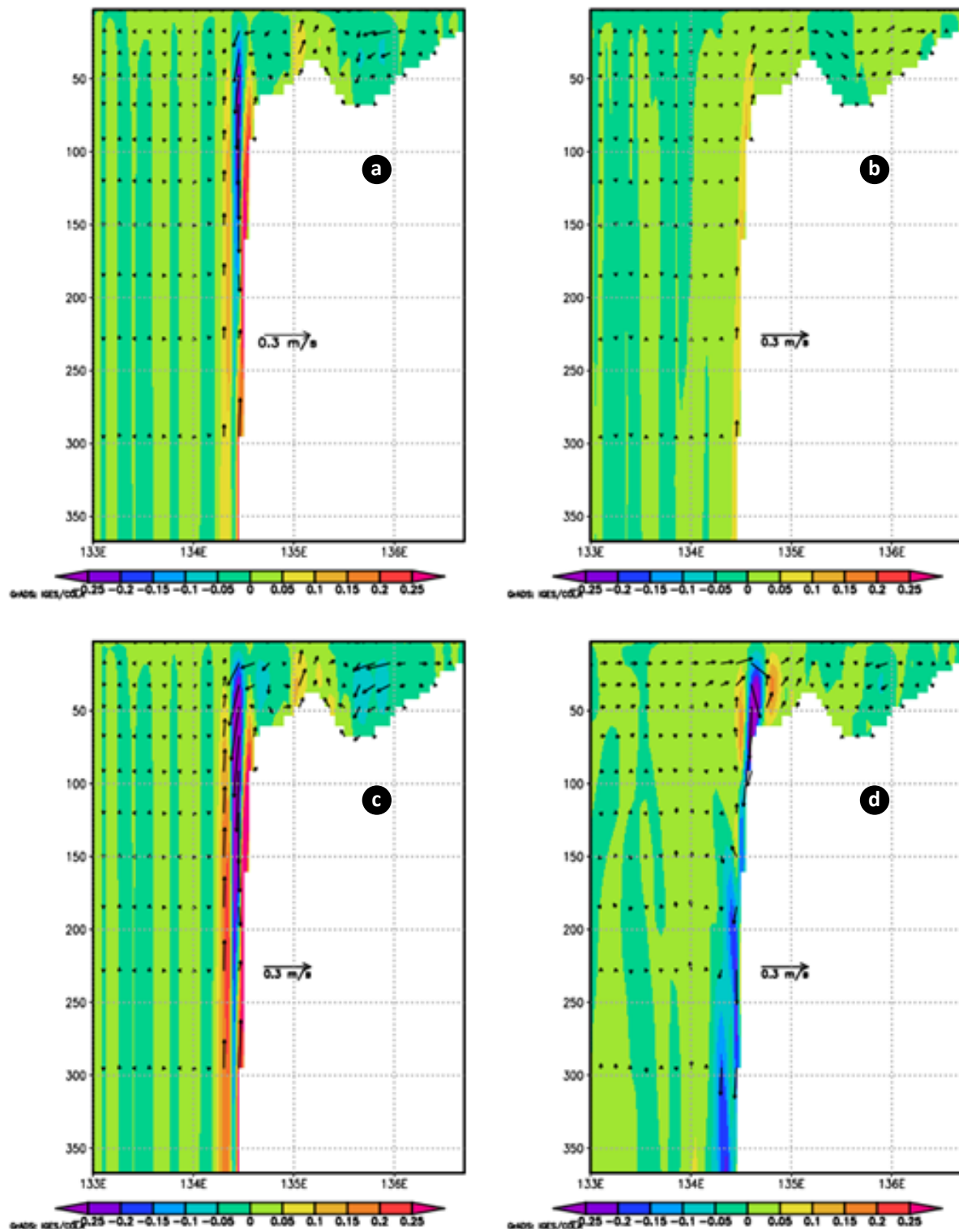


Figure A.2: The vertical profile of u-w velocity, where u-velocity is in m/s and w-velocity is in $\times 10^{-3}$ (m/s). The background represents w-velocity ($\times 10^{-3}$ m/s) along section A for a) TOBT b) TOBT-NADV c) TOBT-Half d) TOBC. The residual currents are obtained by averaging over 28 days.

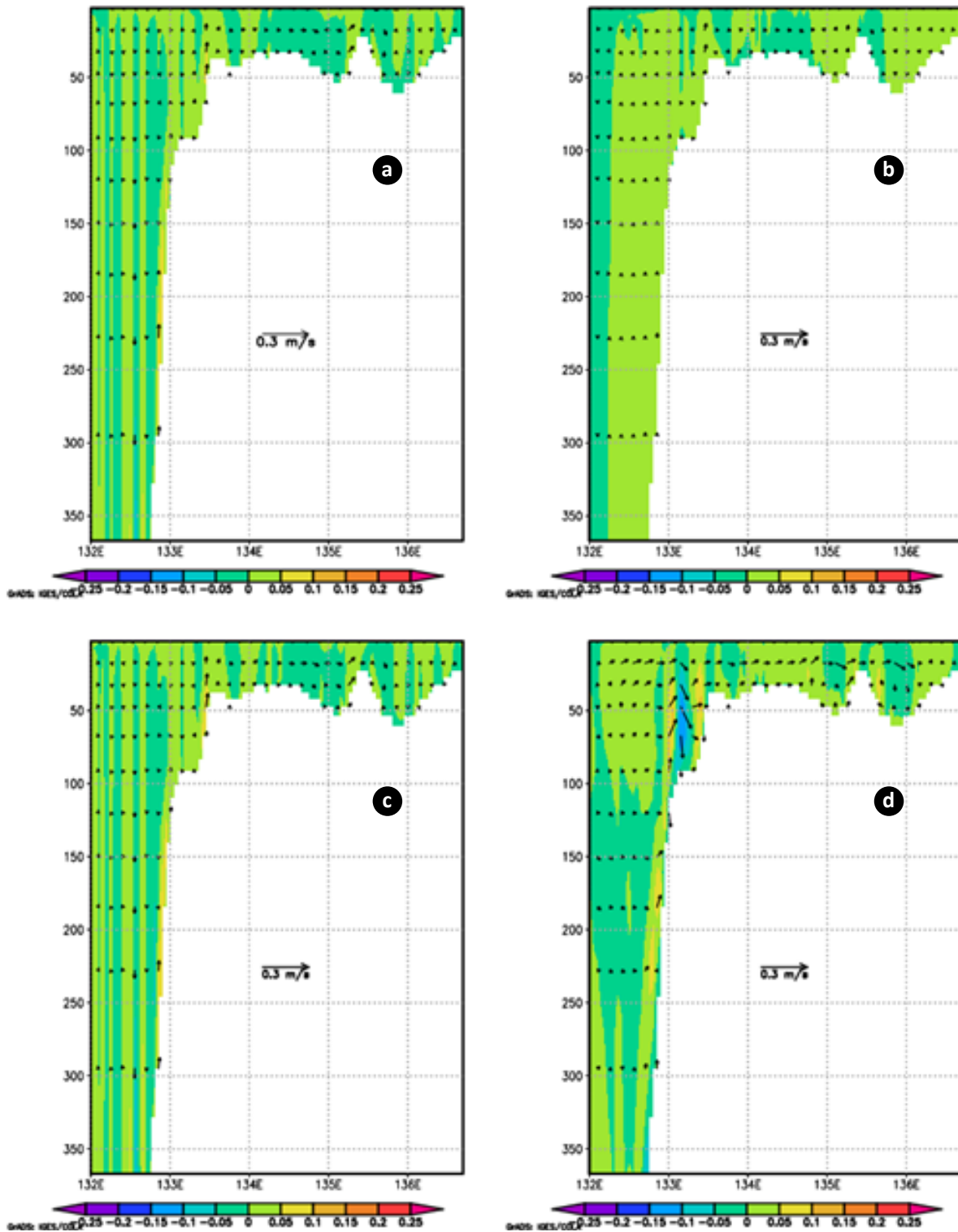


Figure A.3: The vertical profile of u-w velocity, where u-velocity is in m/s and w-velocity is in $\times 10^{-3}$ (m/s). The background represents w-velocity ($\times 10^{-3}$ m/s) along section B for a) TOBT b) TOBT-NADV c) TOBT-Half d) TOBC. The residual currents are obtained by averaging over 28 days

To observe the role of nonlinear bottom friction in generating residual currents, a simplified case was designed by halving the bottom friction (TOBT-Half); bottom friction could not be removed from the calculation without compromising the stability of the mode. This

case shows residual currents around the headland, slope, and western coast of Papua that resemble those of the TOBT case, but are relatively stronger.

When stratification is added, the residual currents over the continental slope of sections A and B are modified significantly. It is observed that, in these areas, stratification generally suppresses turbulence, and as such the VVI term around the bottom of the continental slope in the TOBC mode is lower than in the TOBT mode (Figures 5.27–5.38). It is also found that the tide-induced front formed in this area generates a horizontal density gradient, and as such modifies the SSH and PGF terms. Stratification also reduces nonlinear advection, as indicated by the mode having a lower ADV term than the TOBC. Furthermore, the results show that change is dominated by the ADV and PGF terms; changes in the VVI and COR terms are relatively smaller (Figures 5.31, 5.32, 5.37 and 5.38). Across the continental slope of section A, these changes lead to a modified vertical current structure; as such, while there are at least two circulation cells in the TOBT case, only one circulation cell is observed around the continental slope in the TOBC case (Figures 5.25a and 5.25d). In the surface layer, the modification of momentum components due to stratification contributes to the modification of horizontal currents. As such, in the TOBC mode the zonal surface currents along the continental slope of section A flow opposite to the surface currents of the TOBT mode, while the location of upwelling and downwelling centers are shifted (Figures 5.24a and 5.24b). Meanwhile, over the continental slope of section B, stratification leads to a relatively strong circulation cell (Figure 5.26a); in the TOBT mode, only a small cell was observed (Figure 5.26d).

Momentum components related to the influence of stratification on residual tidal current generation in section C are not discussed here as the influence is relatively small. This condition may be attributed to the region's relatively shallow depth, which induces well mixing.

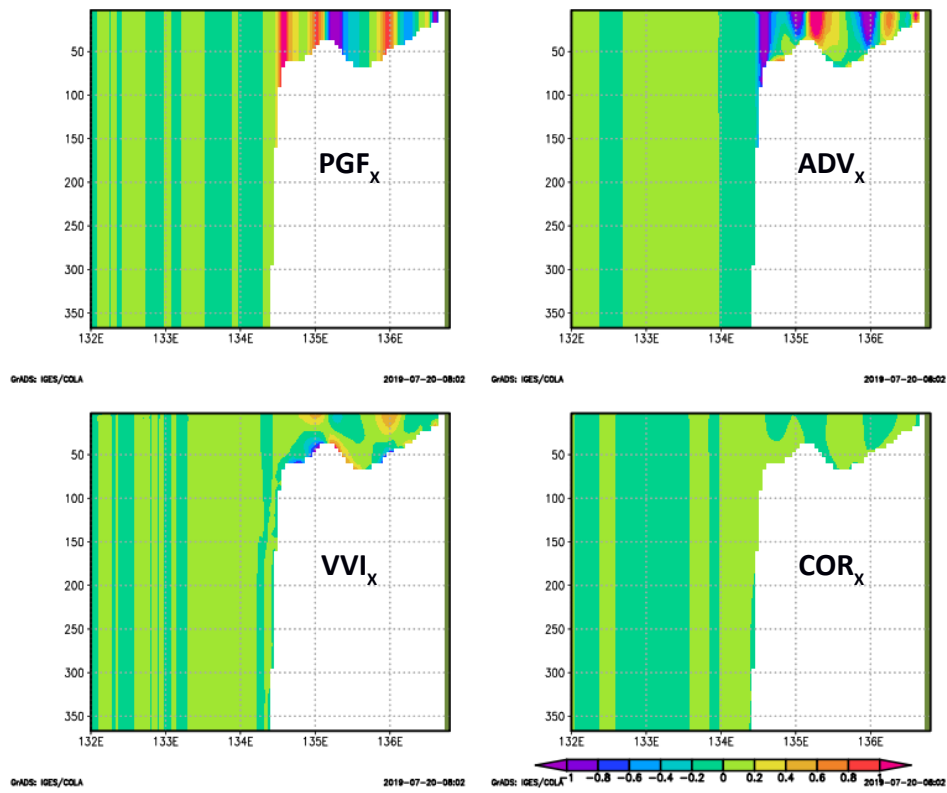


Figure A.4: Momentum components in the zonal direction in section A for the TOBT case averaged over 28 days ($\times 10^{-3} \text{ ms}^{-2}$).

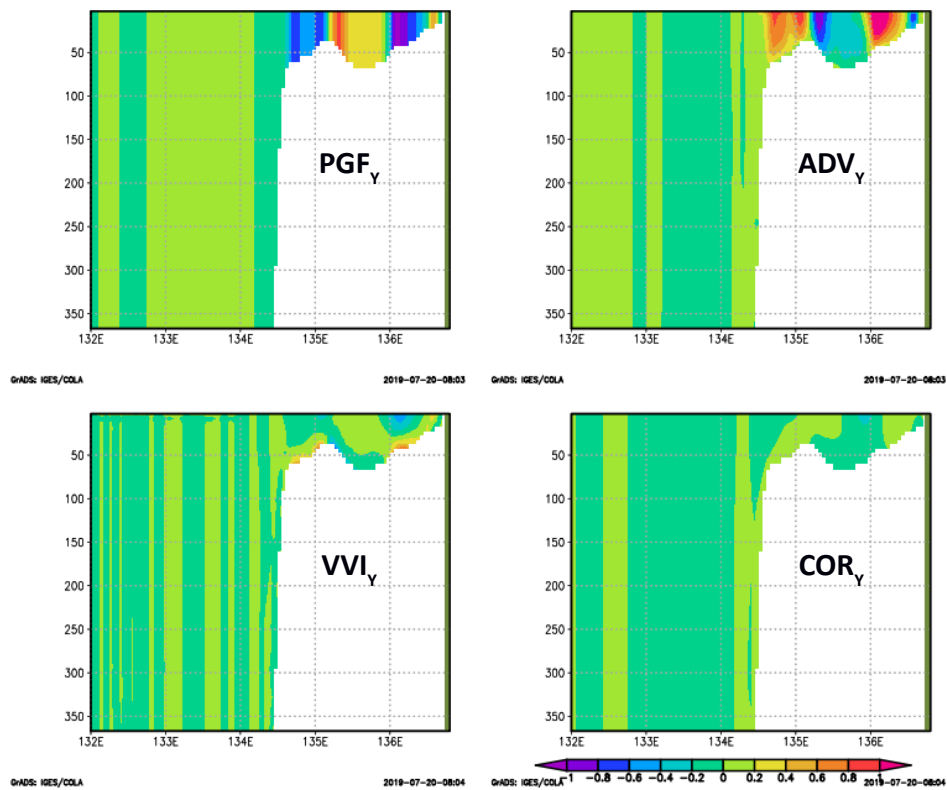


Figure A.5: Momentum components in the meridional direction in section A for the TOBT case averaged over 28 days ($\times 10^{-3} \text{ ms}^{-2}$).

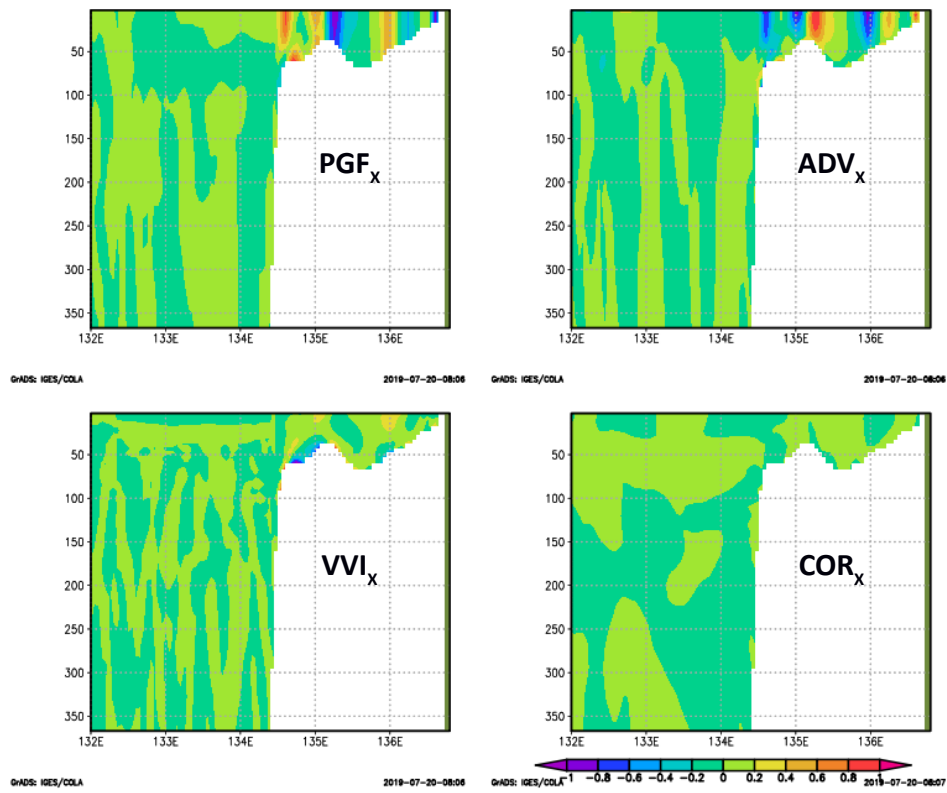


Figure A.6: Momentum components in the zonal direction in section A for the TOBC case averaged over 28 days ($\times 10^{-3} \text{ ms}^{-2}$)

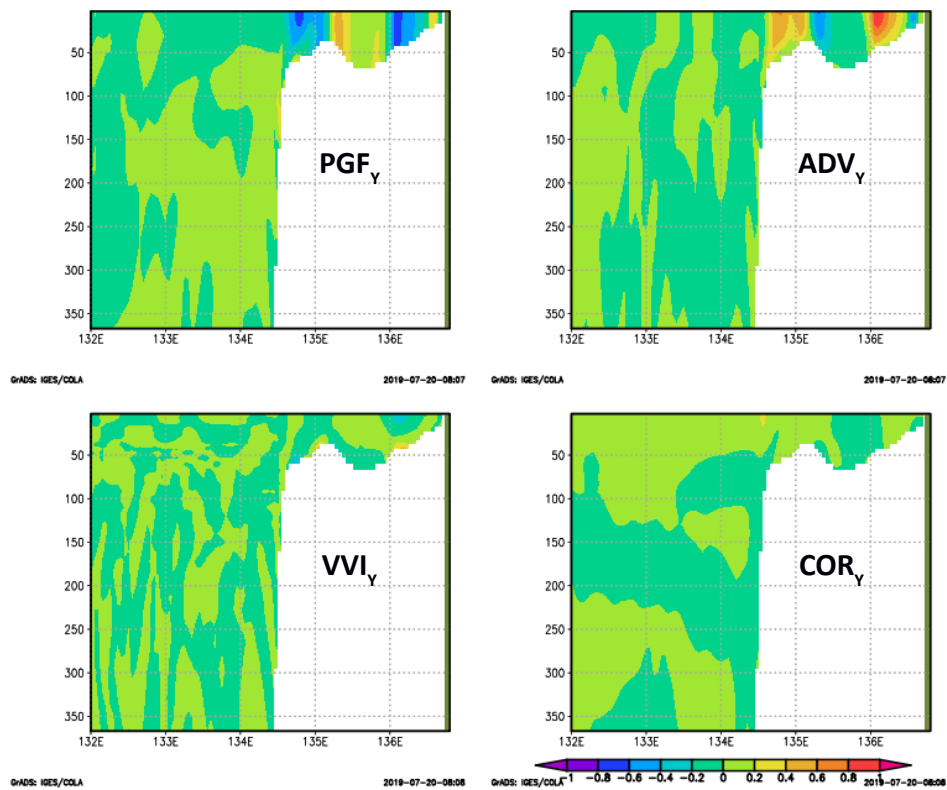


Figure A.7: Momentum components in the meridional direction in section A for the TOBC case averaged over 28 days ($\times 10^{-3} \text{ ms}^{-2}$)

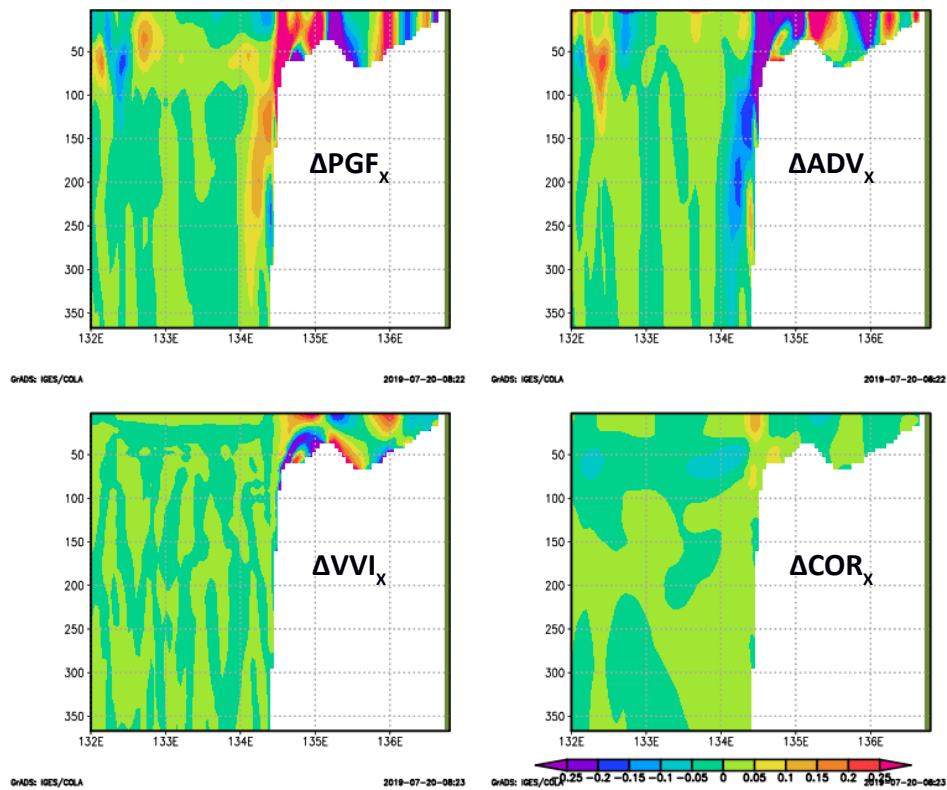


Figure A.8: The difference of momentum components in the zonal direction in section A between the TOBT and TOBC cases (TOBT-TOBC) averaged over 28 days ($\times 10^{-3} \text{ ms}^{-2}$)

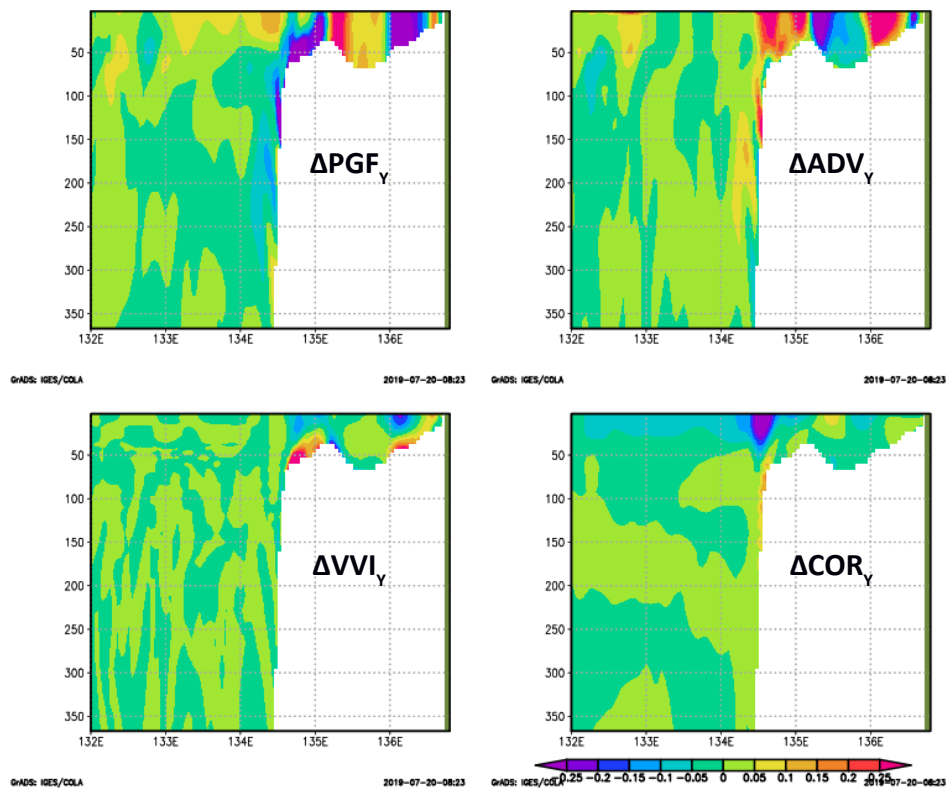


Figure A.9: The difference of momentum components in the meridional direction in section A between the TOBT and TOBC cases (TOBT-TOBC) averaged over 28 days ($\times 10^{-3} \text{ ms}^{-2}$)

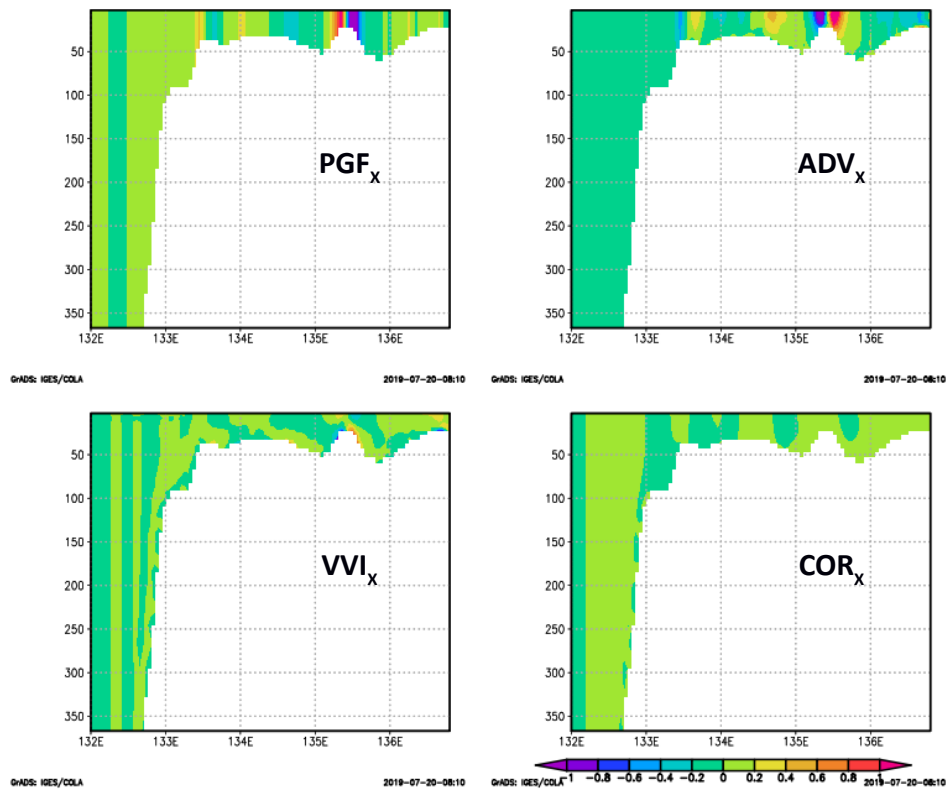


Figure A.10: Momentum components in the zonal direction in section B for the TOBT case averaged over 28 days ($\times 10^{-3} \text{ ms}^{-3}$)

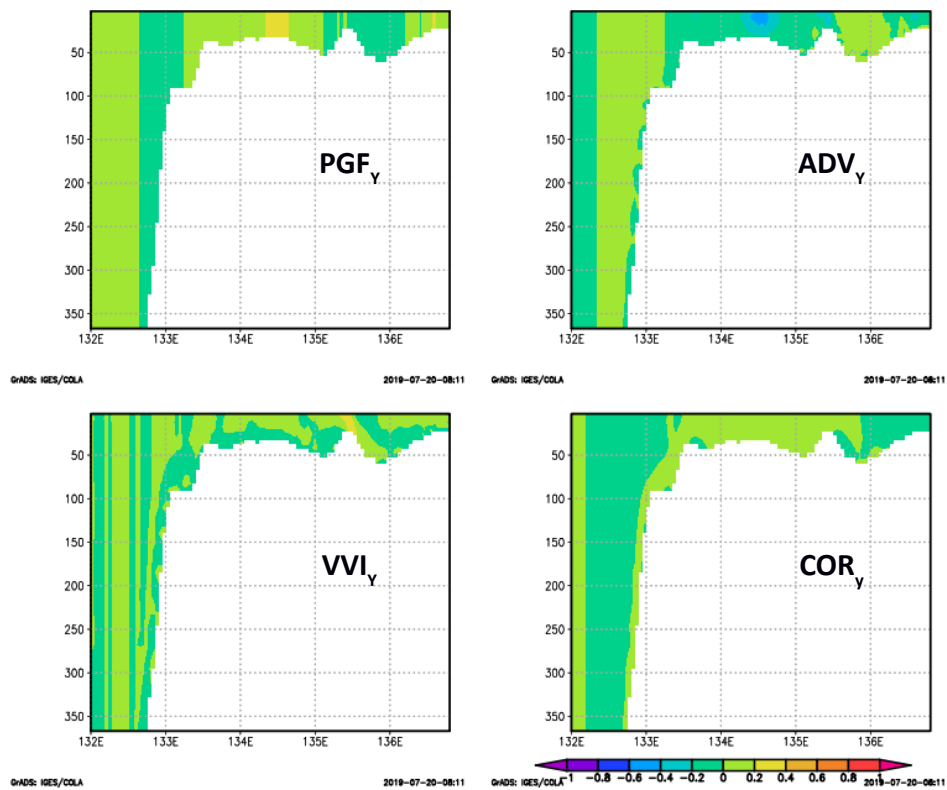


Figure A.11: Momentum components in the meridional direction in section B for the TOBT case averaged over 28 days ($\times 10^{-3} \text{ ms}^{-2}$)

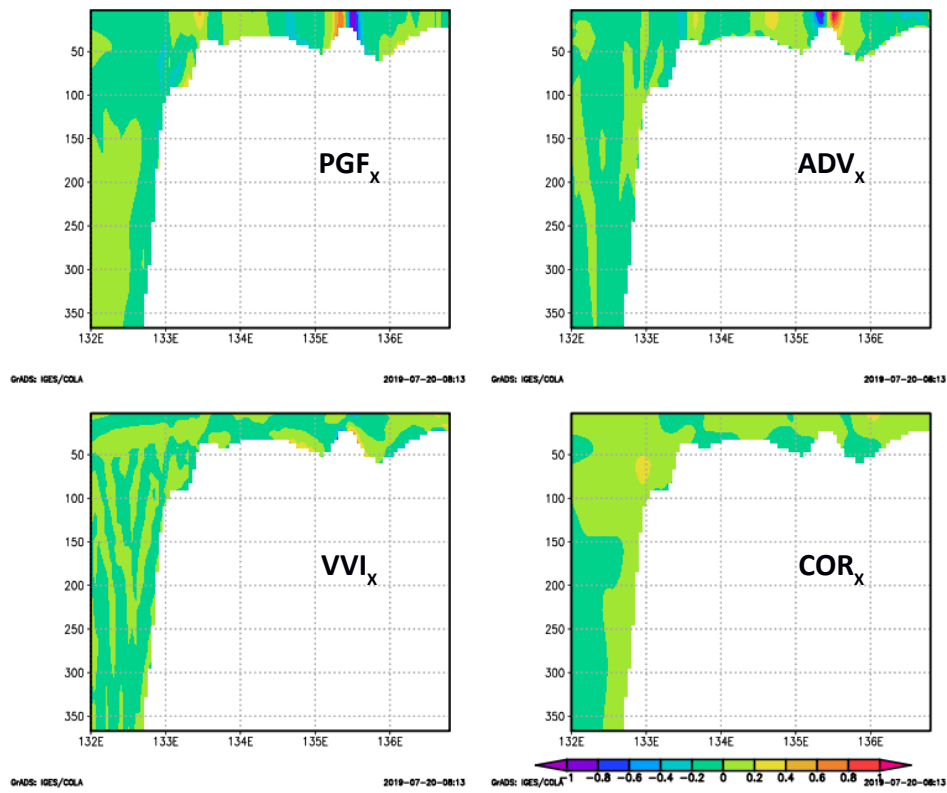


Figure A.12: Momentum components in the zonal direction in section B for the TOBC case averaged over 28 days ($\times 10^{-3} \text{ ms}^{-2}$)

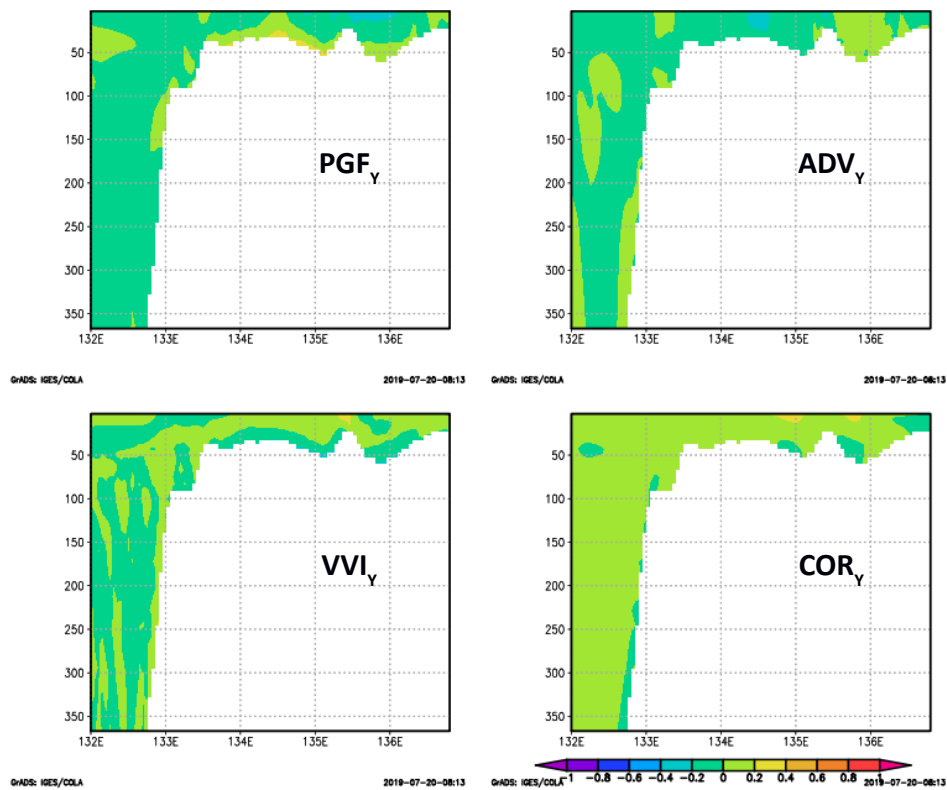


Figure A.13: Momentum components in the meridional direction in section B for the TOBC case averaged over 28 days ($\times 10^{-3} \text{ ms}^{-2}$)

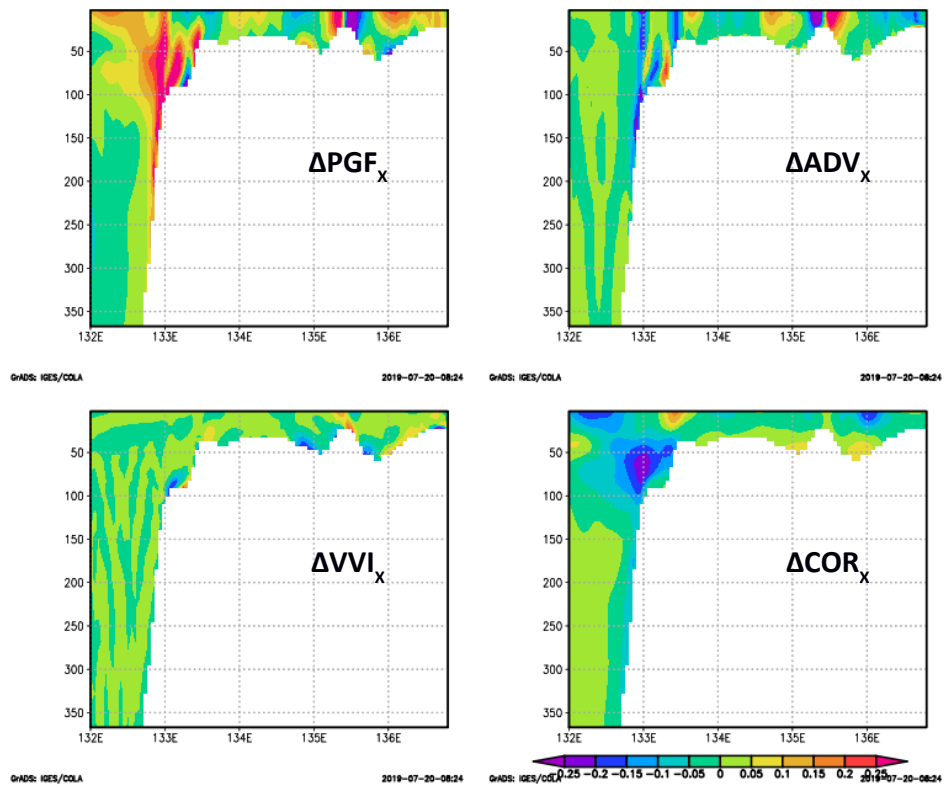


Figure A.14: The difference of momentum components in the zonal direction in section B between the TOBT and TOBC cases (TOBT-TOBC) averaged over 28 days ($\times 10^{-3} \text{ ms}^{-2}$)

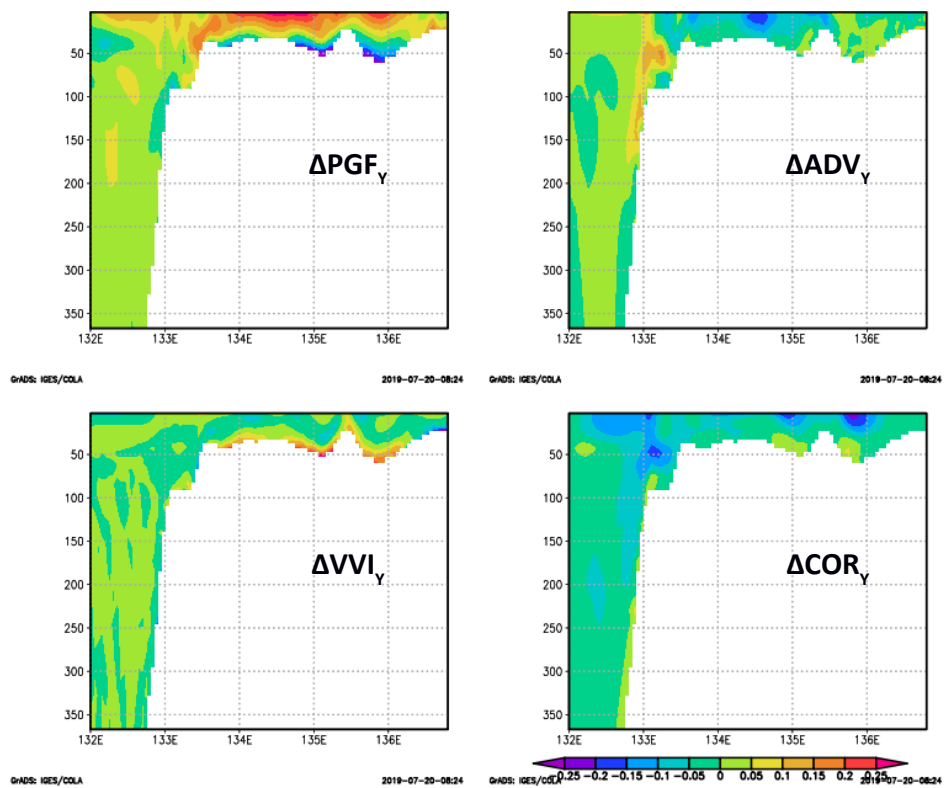


Figure A.15: The difference of momentum components in the meridional direction in section B between the TOBT and TOBC cases (TOBT-TOBC) averaged over 28 days ($\times 10^{-3} \text{ ms}^{-2}$)

Versicherung an Eides statt

Hiermit versichere ich an Eides statt, dass ich die vorliegende Dissertation mit dem Titel: “Upwelling and Related Processes in the Banda and Northern Arafura Seas“ selbstständig verfasst und keine anderen als die angegebenen Hilfsmittel – insbesondere keine im Quellenverzeichnis nicht benannten Internet-Quellen – benutzt habe. Alle Stellen, die wörtlich oder sinngemäß aus Veröffentlichungen entnommen wurden, sind als solche kenntlich gemacht. Ich versichere weiterhin, dass ich die Dissertation oder Teile davon vorher weder im In- noch im Ausland in einem anderen Prüfungsverfahren eingereicht habe und die eingereichte schriftliche Fassung der auf dem elektronischen Speichermedium entspricht.

Hamburg, 2019

